NASA Technical Memorandum 106320

Microgravity Vibration Isolation Technology: Development To Demonstration

Carlos M. Grodsinsky
Lewis Research Center
Cleveland, Ohio

September 1993

NASA

Microgravity Vibration Isolation Technology: Development to Demonstration

Abstract

by

Carlos Mauricio Grodsinsky

The low gravity environment provided by space flight has afforded the science community a unique arena for the study of fundamental and technological sciences. However, the dynamic environment observed on space shuttle flights and predicted for Space Station Freedom has complicated the analysis of prior "microgravity" experiments and prompted concern for the viability of proposed space experiments requiring long term, low gravity environments. Thus, isolation systems capable of providing significant improvements to this random environment have been developed. This dissertation deals with the design constraints imposed by acceleration sensitive, "microgravity" experiment payloads in the unique environment of space.

A theoretical background for the inertial feedback and feedforward isolation of a payload was developed giving the basis for two experimental active inertial isolation systems developed for the demonstration of these advanced active isolation techniques. A prototype six degree of freedom digital active isolation system was designed and developed for the ground based testing of an actively isolated payload in three horizontal degrees of freedom. A second functionally equivalent system was built for the multi-dimensional testing of an active inertial isolation system in a reduced gravity environment during low gravity aircraft trajectories.

These multi-input multi-output control systems are discussed in detail with estimates on acceleration noise floor performance as well as the actual performance acceleration data. The attenuation performance is also given for both systems demonstrating the advantages between inertial

and non-inertial control of a payload for both the ground base environment and the low gravity aircraft acceleration environment.

A future goal for this area of research is to validate the technical approaches developed to the 0.01 Hz regime by demonstrating a functional active inertial feedforward/feedback isolation system during orbital flight. A NASA IN-STEP flight experiment has been proposed to accomplish this goal, and the expected selection for the IN-STEP program has been set for July of 1993.

Acknowledgments

The author wishes to acknowledge the contribution of Dr. G. V. Brown, research scientist at NASA Lewis Research Center Structural Dynamics Division, for his technical advice and support.

Thanks also go to Dr. R. Quinn, research advisor, for his technical support and guidance through both my M.S. and Ph.D.

The author would like to dedicate this work to the fond memory of Joseph F. Lubomski who was an inspiration and a good friend through out the course of this research project.

Table of Contents

List of Figures

List of Tables

I. Introduction

1.1 "Microgravity" Facts and Fiction

From the beginning of the space program, humans have been intrigued by the phenomenon of weightlessness. Development of more accurate theories for physical and chemical laws have been possible through the study of experimental results when the effects of gravity can be substantially reduced or eliminated. A permanent weightless research environment will one day be provided within the orbiting Space Station Freedom. However, for many scientific applications, earthbound methods are being employed to simulate the idealized condition of weightlessness with the aim of improving upon current theories.

A variety of tools are available to provide weightless conditions for materials, fluid physics, and basic physical phenomena research. Numerous freefall methods have been developed to provide short duration periods of near-weightlessness, or "microgravity". Drop tubes and towers have produced "microgravity" duration's of one to ten seconds. Aircraft flying parabolic trajectories have generated periods of low gravity for about 15 to 20 seconds. Sounding rockets and, of course, on-orbit launch vehicles have also been used. Each technique has benefit and liability tradeoffs associated with it such as available test duration versus cost per test. Also, all techniques have specific limitations on the degree of ideal weightlessness which they provide. Each facility is typically categorized by the duration of DC or "Quasi-Steady" gravity levels achieved. However, each facility has vibro-acoustic responses which typically are well above a microgravity and, more specifically, manned orbital facilities have acceleration magnitudes at low frequencies well above any earth bound laboratory acceleration environments [1]. This section will focus on the long duration on-orbit facilities using measurements of the shuttle acceleration environment and estimates of the future Space Station Freedom environment.

Interest in vibration isolation for microgravity experiments has increased within the microgravity science community as the space shuttle flight program has progressed and the small, but significant, levels of residual acceleration on the shuttle have become more widely recognized and documented [2,3]. These residual accelerations result form several sources characteristic of the orbiting carrier and the orbital environment. Very-low-frequency (dc to 10^{-3} Hz) accelerations due to drag, tidal effects, and gravity gradients contribute microgravity acceleration levels, $g = 10^{-6} g_o$ where $g_o = 9.81$ m/s^2. Orbiter thruster activity can contribute 10^{-4} to 10^{-2} g/g_o accelerations with significant duration, but these can be predicted and controlled. The most significant and troublesome contribution to most experimental payloads is the moderate-frequency (10^{-3} to 10.0 Hz) dynamic spectrum of accelerations having magnitudes in the range 10^{-5} to 10^{-2} g's. This dynamic background is primarily due to random excitations from manned activity on the orbiter as well as small thruster firings for orbit keeping maneuvers. However, orbiter structural dynamics and flight systems also contribute observable intermittent and resonant accelerations to the environment as the orbiter interacts with its dynamic mechanical and thermal environment [4]. To categorize the disturbances which are present in the space shuttle and which will be present on Space Station Freedom, the accelerations are grouped into three frequency ranges: (1) quasi-static external disturbances, (2) low-frequency vibrations, and (3) medium- to high-frequency disturbances. The first category includes aerodynamic drag, gravity gradient effects, and photon pressure accelerations acting directly on the orbiter. The second category includes excitations of the large flexible space structures due to crew motion, spacecraft attitude control, and robotic arms. The third category includes disturbances due to on-board equipment such as pumps and motors having a frequency range of about 10 Hz and higher. The range of accelerations observed on several shuttle missions or estimated for the accessible orbit is given in Table 1.1 [2,3,5].

Source	Acceleration, g/g_o	Frequency, Hz
Quasi-steady or constant cycle		
Aerodynamic drag	10^{-7}	0 to 10^{-3}
Light pressure	10^{-8}	0 to 10^{-3}
Gravity gradient	10^{-7}	0 to 10^{-3}
Periodic		
Thruster fire (orbital)	2×10^{-2}	9
Crew motion	2×10^{-3}	5 to 20
Ku-band antenna	2×10^{-4}	17
Nonperiodic		
Thruster fire (attitude)	10^{-4}	1
Crew pushoff	10^{-4}	1

Table 1.1: Acceleration Disturbances

The evolution of the Freedom Station design has led to potential limitations on long-term, low-gravity experimentation in this environment. It is now obvious that most of the true "microgravity" experiments will require isolation from this random milli-g environment if reproducible and useful results are to be expected. The Space Station Freedom will have many of the same excitation sources as are present on the Shuttle. However, SSF will be a much larger, more flexible structure and, hence, will be more modally dense and more easily excited. The present Space Station Design has over 100 modes below a Hertz which will not only complicate the isolation of these low frequency disturbances but will also dictate an acceleration environment with more energy at lower frequencies than presently exhibited on the Shuttle orbiter. The low frequency regime for many microgravity experimenters appears to be the most critical according to the g-jitter sensitivity analyses which have proliferated over the past several years [6].

To specifically address the measured acceleration environments on-board the Space Shuttle and expected on the Space Station Freedom, a plot is presented showing areas of expected magnitudes of accelerations in certain frequency bands. Figure 1.1 from a NASA SSF study represents the expected levels of excitations which will be present on Freedom. These magnitude and frequency depiction's of disturbances do not represent the structural response of the Freedom Station or the Space Shuttle to expected forcing functions. However, the expected disturbances do fall above the "microgravity" requirement curve shown, superimposed on this plot. The measured acceleration environment of the Space Shuttle falls below this line in Figure 1.1, however measurements have shown that there is orbiter response at certain fundamental frequencies between 3 and 10 Hz [7]. The fundamental frequencies expected for the Freedom Station are well below 1 Hz which are expected for such a large flexible structure which leads to concern about the experimental environment.

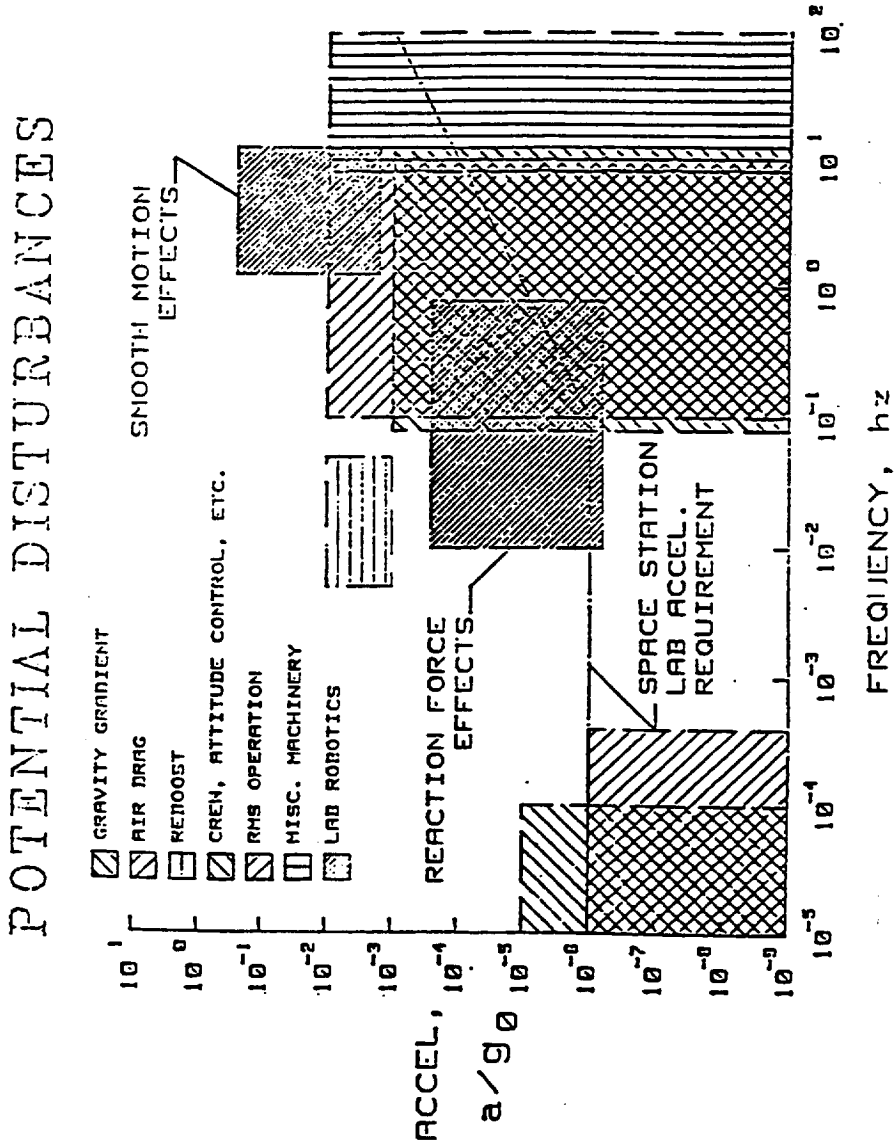

Figure 1.1: SSF Potential Disturbances

1.2 Motivation for Active Vibration Isolation Solutions

The evolution of the Space Station design and the documented Space Shuttle acceleration environment has led to potential limitations on long term, low gravity experimentation in these environments. It is now obvious that most of the true microgravity experiments will require isolation from this random milli-g environment if reproducible and useful results are to be expected. An effective isolation system must be designed with a resonance frequency below $1/\sqrt{2}$ times the lowest excitation frequency of interest. Because a large part of the transient disturbances have a frequency range from milli-Hz to 1 Hz, it is extremely difficult to design passive isolation systems for this environment. This difficulty is due to the absence of materials which have useful ranges of both low-modulus (providing low frequency) and appropriate damping (to avoid large amplitude oscillation). Two stage passive isolators can decrease the frequency range, however limited damping leads to potentially unstable systems in the random excitation environment [8].

Passive isolation systems require extremely low stiffness for the isolation of small disturbance frequencies for typical values of mass associated with microgravity space experiments. In contrast, when there are direct disturbances to a payload a small value of stiffness is not desirable because of space limitations to accommodate large displacements. Thus, there is a trade off, and an effective design would need to compensate for both direct disturbances, if present, and low frequency base disturbances. Active systems offer significant advantages over passive systems in the orbital acceleration environment. This is due to the extremely small stiffnesses needed to isolate against such low frequency base disturbances and the added capability needed to adapt to direct disturbances for the optimal isolation of a payload. In addition, since the responses to these two excitations require conflicting solutions, a closed loop system is required for the inertial control of the isolated payload [9,10].

Active systems require sensing of motion or position, and a feedback or feedforward control loop, or both, to counteract mechanical excitation and to minimize motion of an isolated body. Such systems introduce the complexity of a high-gain control system, but offer significant advantages in versatility and performance [11]. To achieve a broad spectrum of isolation, both feedforward and feedback control loops are used referencing the isolated payload to an inertial frame rather than to the dynamic support.

1.3 Uniqueness of Active Inertial Isolation Research

The purpose of this thesis is to complete and expand on the development of a general theoretical approach to the formidable problem of isolating against low frequency disturbances and maintaining accelerations below extremely low levels. The primary contributions of this work were to develop the general understanding of active inertial feedback and feedforward control of an isolated payload and to further this understanding by developing a six degree-of-freedom active vibration isolation system and experimental hardware in order to demonstrate these theoretical inertial isolation control techniques. This research will lead to the use of digital active control of dependent multi-degrees of freedom in order to inertially reference a payload needing an extremely stable platform. The developmental and demonstration hardware developed constitute two six degree of freedom testbed active isolation platforms with the unique capability of demonstrating and verifying multiple control approaches for the low frequency isolation problem. These multi-degree of freedom platforms give the control designer the availability of twelve inertial sensors and six relative sensors for the various states which would be utilized in a classical or modern control design. These input sensors are digitized and can be used in what ever control algorithm is designed dependent on the isolation requirements generated for a specific attached payload. The two systems developed were a six degree of freedom 12 bit laboratory prototype and a high fidelity 16 bit low gravity aircraft demonstration

system. A classical active spring-mass-damper control and an inertial feedforward multi-degree of freedom controller were demonstrated and compared to the theoretical predictions for such an approach. The inertial feedback compensation techniques were not demonstrated in six degrees of freedom because of the straightforward nature of the controller and will be used at a later date for the full verification of a hybrid control approach during a proposed NASA Office of Advanced Concepts and Technology (OACT) In-Space Technology Experiment.

1.4 An Overview of the Active "Microgravity" Payload Isolation Field

In 1987 the Microgravity Science and Applications Division, of the Office of Space Science and Applications, organized Advanced Technology Development (ATD) programs in order to develop the enabling technologies needed for the use of Space Station Freedom as a viable microgravity experimental platform. One of these development programs was a Vibration Isolation Technology (VIT), ATD. This technology development program grew because of increased awareness that the acceleration disturbances present on the Space Transportation System (STS) orbiter are detrimental to many microgravity experiments proposed for STS, and in the future, Space Station Freedom (SSF). During the beginning of the VIT ATD a large gap existed between the necessary acceleration requirements for many experiments and the actual acceleration environment achieved on the Shuttle orbiter. A VIT workshop was held to bring the users together with industry and university technologists to establish a dialogue between the two groups to better define needs and requirements. The results of the technology requirements definition phase were then used to focus vibration isolation technology development on the critical needs of vibration sensitive microgravity experiments.

An international Vibration Isolation Technology for Microgravity Science and Applications Symposia and Workshop was held in April of 1991 as a culmination of the technology requirements

definition phase of the VIT project. This Symposia/workshop was to present and evaluate the efforts of the various international organizations involved in VIT research, and to formulate plans to develop mutually beneficial cooperative efforts in the pursuit of VIT technology developments. This workshop was also used to evaluate and shape NASA's future efforts in the VIT area, specific to MSAD's technology involvement [12].

A summary of the various groups and their contributions to the field follow with their respective innovations and primary accomplishments. Internationally there are two groups outside of the U. S. who have done research in the area of "microgravity" vibration isolation, the European Space Agency and NASDA. The European's began a research effort at the University of North Wales. D. I. Jones, A. R. Owens, and R. G. Owen developed a Microgravity Isolation Mount (MGIM) which is a Columbus rack-based facility designed to provide active vibration isolation for sensitive experimental payloads. The control basis for this work was done using the feedback of relative position and velocity to control a payload through a soft suspension system. This work was experimentally verified in only one dimension and again used no inertial feedback or feedforward stabilization of the payload for the base cancellation of disturbances or the ability to control direct disturbances should they exist. The NASDA program in microgravity vibration isolation is very extensive and can be summarized in the general study of both passive and active devices to improve the microgravity environment. They have studied the use of acceleration feedback and have done low gravity aircraft tests in three degrees of freedom with some limited success. [12]

The national arena consists of basically four groups who have fabricated and demonstrated experimental hardware for the active isolation of sensitive payloads specific to the orbital "microgravity" environment. These groups consisted of Honeywell Satellite Systems Operation, Satcon Technology, and a A. VonFlotow at MIT. Each group designed a six degree of freedom active isolation system with different capabilities and limitations. The Honeywell Satellite Systems group designed and fabricated a Magnetic Isolation System (MIS) based on the control of attractive

electromagnets referenced to relative sensors. The MIS was laboratory tested in 1986, and provided superior six-dof isolation, with close to unit transmissibility below the break frequency of about 4 Hz and fifth-order isolation roll-off above [13]. This isolation system was the first of its kind. However, it was limited in low frequency isolation bandwidth and did not incorporate the advantages of inertially referencing the isolated payload. The Satcon Technology approach consisted of a six-dof Lorentz force actuated active isolation payload utilizing a cubic gap-error nonlinear feedback controller. This experimental package was only demonstrated in three-dof and does not utilize inertial stabilization of the payload. The Lorentz force actuators have advantages in their bi-directionality and linear force to control current capability however, they are limited in force per unit power as compared to attractive actuators. In addition, it is difficult to design a six degree of freedom system having minimal cross axis coupling using Lorentz actuators. The final group at MIT, Dr. A. VonFlotow et al., developed a six degree of freedom system using piezoelectric polymer material as the actuation devices. This experimental hardware was only demonstrated in three degrees of freedom but did include the capability of direct inertial feedback which is advantageous as discussed in a 1989 ASME 12th biannual Mechanical Vibration and Noise conference publication entitled "Low Frequency Vibration Isolation Technology for Microgravity Space Experiments" [8]. However, the performance of the system was degraded by the force and bandwidth limitations of the actuation devices [14].

II. Theoretical Developments in Active Inertial Isolation

2.1 Single DOF Inertial Isolation Approaches

The active isolation systems described in this section are effective at frequencies above 0.01 to 0.1 Hz. This constraint arises not from technology limitations, but from practical limitations on the stroke needed to isolate against very low frequency disturbances. Volume constraints in the Shuttle and in the future Freedom Station manned environments limit the stroke of any support system. For example, aerodynamic drag will act on a solar-pointing station with a frequency equal to that of the orbital frequency (about 90 min. per orbit). Although drag is a function of the atmospheric conditions during a specific mission, an average g of 10^{-7} will be used. Thus, the distance Freedom Station would travel under such an acceleration would be $2(a/\omega^2)$, or 1.5 m (4.7 ft), where $\omega = 2\pi/(90x60)$ rad/sec and $a = (9.81\ m/sec^2)x(10^{-7}\ g/g_o)$, assuming null initial velocity. Thus, an isolated payload would be forced to follow such a large spacecraft displacement, but be active in a much smaller region. This active region would depend on the volume constraints of a payload in the Shuttle or in the Freedom Station microgravity module.

The following one dimensional baseline cases assume the use of an attractive electromagnet and a Lorentz force actuator, respectively, and can be analyzed as spring-mass-damper systems. It is assumed that the spring and damper characteristics for the attractive electromagnet and the damping characteristics for the Lorentz actuator are actively controlled and translated in to actuator response by a control law dependent on the response characteristics desired. Using an attractive electromagnetic actuator, one can produce forces in only one direction. Therefore, to achieve a push-pull configuration one needs to use two opposing electromagnets acting on an armature. Figure 2.1 illustrates the two general magnetic actuator configurations: the attractive electromagnet and the

Lorentz force actuator. For the attractive electromagnetic actuators, the force produced by one magnet is proportional to the square of the current and inversely proportional to the square of the gap. Figure 2.2 shows the magnetic circuit actuator's squared dependence on current. Because of these nonlinear characteristics, a bias current linearization technique is used. Thus, the bias current i_b is used to produce a nearly linear control law such that, for small disturbances about this current, the control force produced can be assumed linear. In order to control this system, one must close a control loop around position and velocity feedback signals with a bias current. Other nonlinearities due to hysteresis and saturation arise between magnetic flux and input coil current, but are not significant with proper care of the magnetic circuit design.

In contrast, the Lorentz actuator can produce forces bi-directionally. The force produced by a Lorentz actuator is a vector quantity equal to the cross product of current and magnetic field. Therefore, depending on the direction of current flow in the coil, one can produce a force in either a positive or negative direction. Because of this actuator's linear dependence on control current, linearization is not needed, and it is open-loop stable. The Lorentz actuator thus has advantages over the magnetic circuit actuator, but requires more power to produce a certain force than does the magnetic circuit configuration. However, the forces needed to control a payload in the "weightless" environment of space are small, and this inefficiency is not as limiting as on Earth.

The basic concept behind these active feedback isolation techniques is to sense position, velocity, and acceleration, or velocity and acceleration, and then to drive an actuator 180^{O} out of phase with this signal in order to cancel a disturbance to the payload. If there is knowledge about certain disturbances, a feedforward loop can anticipate an excitation and react without an error signal. Thus, the optimal isolation system for microgravity experiments to known and sensed orbiter disturbances requires inertial isolation of the experiment using a feedforward/feedback type controller. Such a controller does not circumvent the need for relative information of the payload in

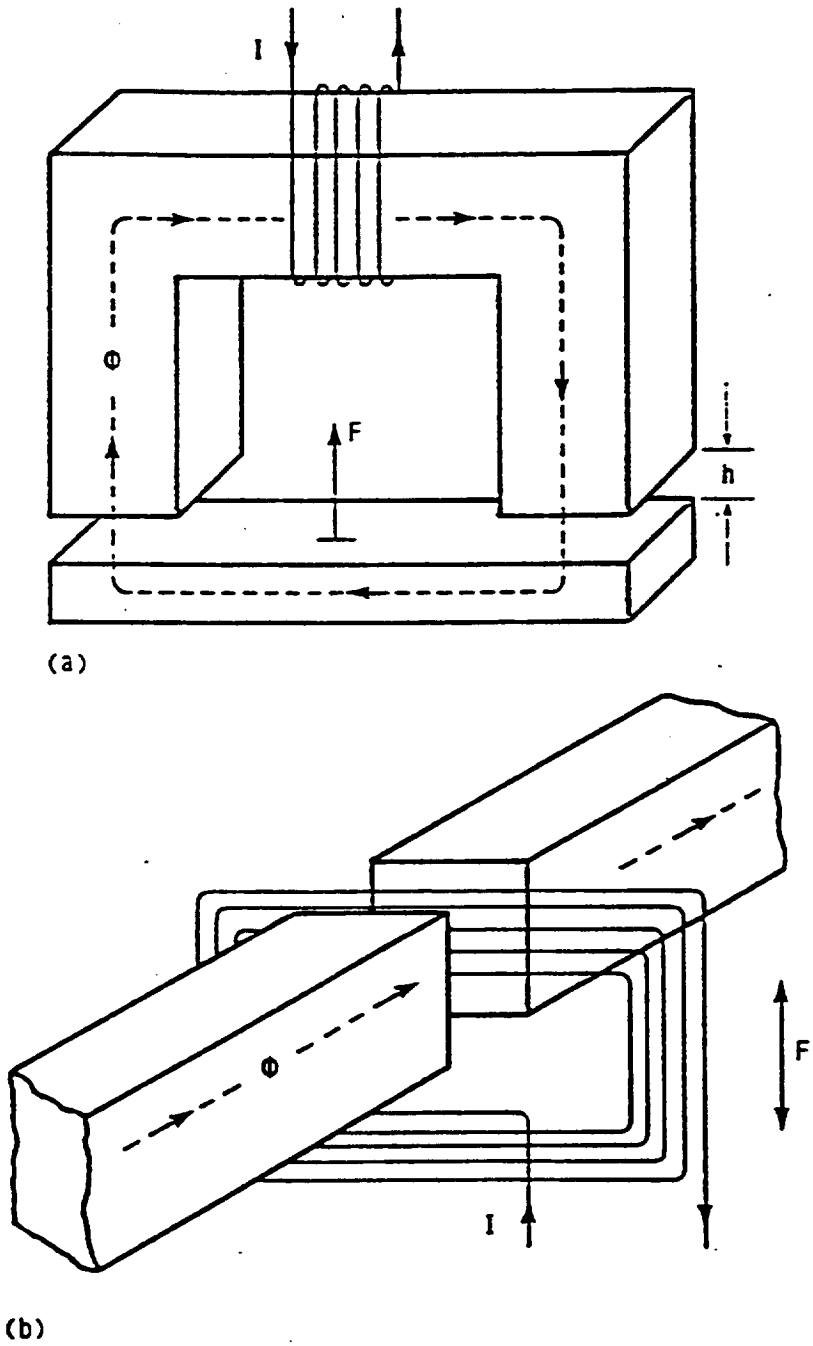

(a) Attractive electromagnetic actuator.
(b) Lorentz force actuator.
Figure 2.1: general magnetic actuator configurations.

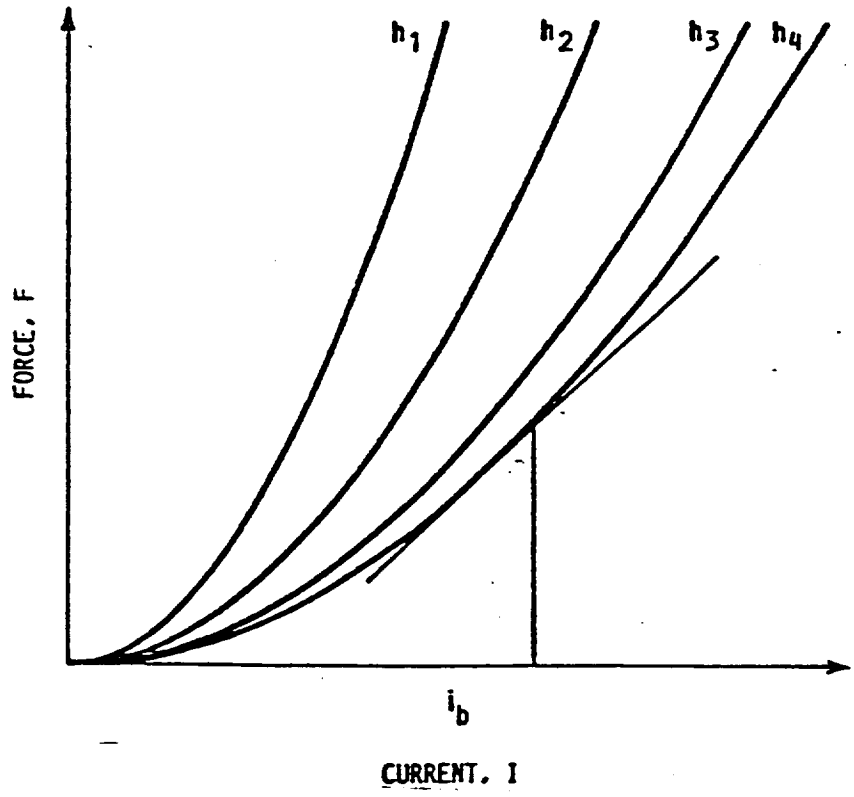

Figure 2.2: squared dependence of magnetic-circuit actuator on current. (i_b is bias current; gap $h_1 < h_2 < h_3 < h_4$)

order to follow the large motion disturbances without exceeding boundary conditions (i.e., volume constraints). These active isolation techniques can be implemented by using either analog or digital control schemes to close the feedback and feedforward control loops.

2.1.1 Formulations for Baseline Inertial Control Cases

The responses of a magnetic circuit isolator and a Lorentz electromagnet in one degree of freedom can be evaluated by their transmissibility's and effectiveness in isolating against both base and direct disturbances. These transmissibilities and effectiveness functions are given with a brief description of their formulation. (Appendix B gives a detailed analysis of the transmissibility and effectiveness formulations and their results for a variety of feedback inertial control schemes as well as for feedforward transmissibility functions with bandwidth error estimates.) First, the responses, or transmissibilities, of the various control approaches are generated for harmonic base excitations by using the active isolation system's differential equations of motion. These equations of motion are formulated by using Newton's first and second laws, where the base displacement, u, is actually a time function, so that u = u(t). The same is implied for a directly applied force such that, in actuality, F = F(t).

In order to demonstrate the advantages of isolating a payload by the various feedforward/feedback controller designs a simple one degree of freedom spring-mass-damper system, shown in Figure 2.3, is analyzed where F_s is a servo force proportional to certain feedback or feedforward inertial control signals. This force is achieved by referencing an actuator to the appropriate signal of an accelerometer, or the integrals of this signal, either attached to the support structure of the mass or the mass itself. The general equation of motion for this system is:

$$m\ddot{x} + c(\dot{x} - \dot{u}) + k(x - u) + F_s = 0. \tag{2.1}$$

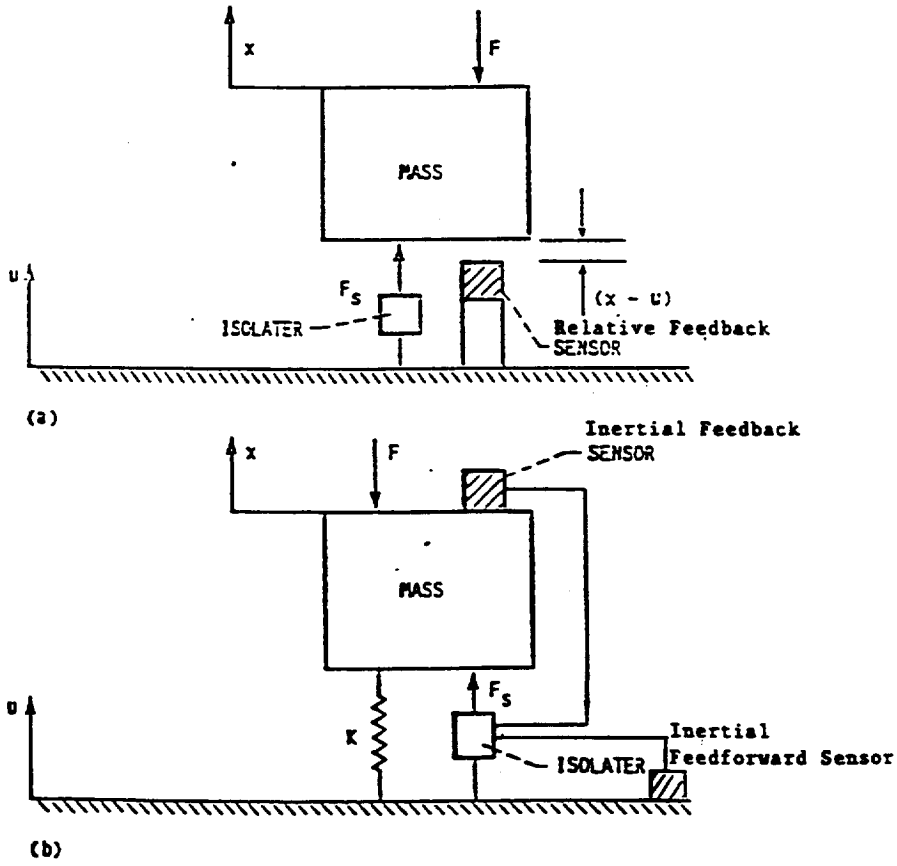

(a) Relative feedback system.
(b) Inertial feedback and feedforward systems.
Figure 2.3: physical representation of active isolation systems.

The servo force will be defined in two distinct inertial isolation control approaches to investigate the isolation characteristics of these feedback and feedforward controllers. These definitions will be represented as F_{siff} and F_{sifb}, where F_{siff} is defined as a servo force referenced to the inertial position and velocity of the support structure giving an inertial feedforward controller, and F_{sifb} is defined as the servo force referenced to the acceleration and the inertial velocity of the isolated mass giving an inertial feedback controller. In order to depict the effect of these different control approaches on the transmissibility or effectiveness of the controller to reject base disturbances the transmissibility function for both inertial cases will be solved. Therefore, beginning with the general equation of motion and substituting the defined servo force representations,

$$F_{sifb} \equiv G_{afb}\ddot{x} + G_{vfb}\dot{x} \tag{2.2}$$

and,

$$F_{siff} \equiv G_{piff}u + G_{viff}\dot{u}, \tag{2.3}$$

the controller equations of motion for the feedback and feedforward controllers become:

$$m\ddot{x} + k(x-u) + G_{afb}\ddot{x} + G_{vfb}\dot{x} = 0 \tag{2.4}$$

and,

$$m\ddot{x} + c(\dot{x}-\dot{u}) + k(x-u) + G_{piff}u + G_{viff}\dot{u} = 0, \tag{2.5}$$

respectively. If one assumes monochromatic motion of the base structure, one can write the displacement u as $A\sin\omega t$, where A is the displacement amplitude. Rearranging terms and using the following definitions, the viscous damping factors $\xi = c/2m\omega_n$, $\xi_{vfb} = G_{vifb}/2m\omega_n$, $\xi_{vff} = G_{viff}/2m\omega_n$, a direct acceleration feedback term, $G_{aifb}/m = G_{afb}$, and an inertial feedforward term, $G_{piff}/m = \omega_{np}^2$,

equations (2.4) and (2.5) can be put into vibration notation [15] as follows:

$$\ddot{x}(1+G_{afb}) + 2\xi_{vfb}\omega_n\dot{x} + \omega_n^2 x = \omega_n^2 u, \tag{2.6}$$

and

$$\ddot{x} + 2\xi\omega_n\dot{x} + \omega_n^2 x = u(\omega_n^2 - \omega_{np}^2) + \dot{u}2\omega_n(\xi - \xi_{vff}). \tag{2.7}$$

If one takes the Laplace transforms of x and u, equations (2.6) and (2.7) become:

$$(s^2(1+G_{fb})+2\xi_{fb}\omega_n s+\omega_n^2)X(s)=\omega_n^2 U(s), \tag{2.8}$$

and

$$(s^2+2\xi\omega_n s+\omega_n^2)X(s)=U(s)\left[(\omega_n^2-\omega_{ff}^2)+s2\omega_n(\xi-\xi_{ff})\right]. \tag{2.9}$$

Taking the frequency response and calculating the magnitude of the transfer function one arrives at the following equations, which give the frequency response transfer function or transmissibility of the isolated payload to a harmonic base disturbance for both feedback and feedforward cases respectively.

$$\left|\frac{X(j\omega)}{U(j\omega)}\right|=\sqrt{\frac{1}{\left(1-(1+G_{fb})\left(\frac{\omega}{\omega_n}\right)^2\right)^2+\left(2\xi_{fb}\frac{\omega}{\omega_n}\right)^2}}, \tag{2.10}$$

and

$$\left|\frac{X(j\omega)}{U(j\omega)}\right|=\sqrt{\frac{\left(1-\left(\frac{\omega_{ff}}{\omega_n}\right)^2\right)^2+\left(\left(2\frac{\omega}{\omega_n}\right)(\xi-\xi_{ff})\right)^2}{\left(1-\left(\frac{\omega}{\omega_n}\right)^2\right)^2+\left(2\xi\frac{\omega}{\omega_n}\right)^2}}. \tag{2.11}$$

Equations (2.10) and (2.11) depict the feedback and feedforward inertial isolation approaches for attenuating base excitations. In the previous formulations the spring and damper elements were assumed constant. However, if an umbilical is used in the payload it most likely can not be represented by a simple stiffness and damping factor. In addition, if the isolated payload is not passively mounted but actively controlled by an attractive magnetic suspension system it has the advantages of a closed loop active control system where the relative spring and viscous elements are variables dependent on controller loop gains. The feedback and feedforward transfer function

equations depict ideal conditions where the inertial sensors are not bandwidth limited and have infinite resolution, which of course is not the case in any realistic experimental system. Therefore, the actual performance will be dictated by the noise floor and bandwidth of the control system.

To demonstrate the advantages of inertial feedback and feedforward active isolation the previous transfer functions will be plotted with only one control term in the equations depicting the physical characteristics of the system and its response to the attenuation of base disturbances. Taking equation (2.10) and plotting the response for simple acceleration feedback, Figure 2.4 illustrates the advantage of inertially increasing the dynamic mass of the isolated payload thus, forcing the transfer function to the left or effectively lowering the corner frequency of the system. Figure 2.5 shows the feedback transfer function equation (2.10) with only inertial velocity feedback. These curves show the response of the system to increased velocity feedback determined from the integration of an inertial sensor signal. The advantage of active inertial damping derived from an inertial reference on the payload is the removal of the resonant response, broadening and smoothing the transition between the low-frequency and high-frequency regions, while reducing both the transmission and the response, particularly in the low-frequency range of interest. The effect of such a system for large values of velocity feedback gain can be understood by noting that it is equivalent to having a passive damper attached between the isolated mass and a virtual inertial reference. As the inertial damping is increased, the isolated mass becomes more and more tightly coupled to the (motionless) ideal inertial reference. In other words, the stronger the viscous term the better the attenuation. This type of response is not seen in the pure suspension case because the velocity term was determined from the derivative of a relative position sensor.

To describe the inertial feedforward cancellation approach one can simply analyze the numerator of equation (2.11) and compare it to the typical single degree of freedom spring mass damper transfer function. The feedforward terms are simply added to cancel out the relative stiffness and damping terms to theoretically attempt an infinite attenuation of base disturbances. This can not

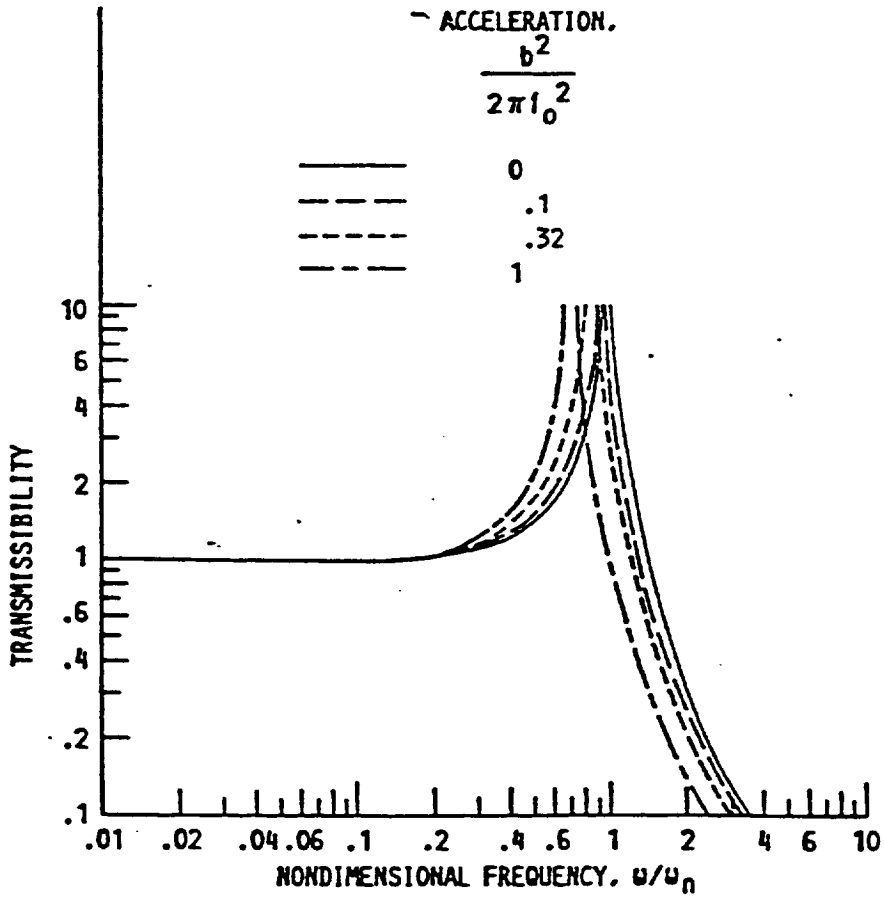

Figure 2.4: inertial acceleration feedback transmissibility curves.

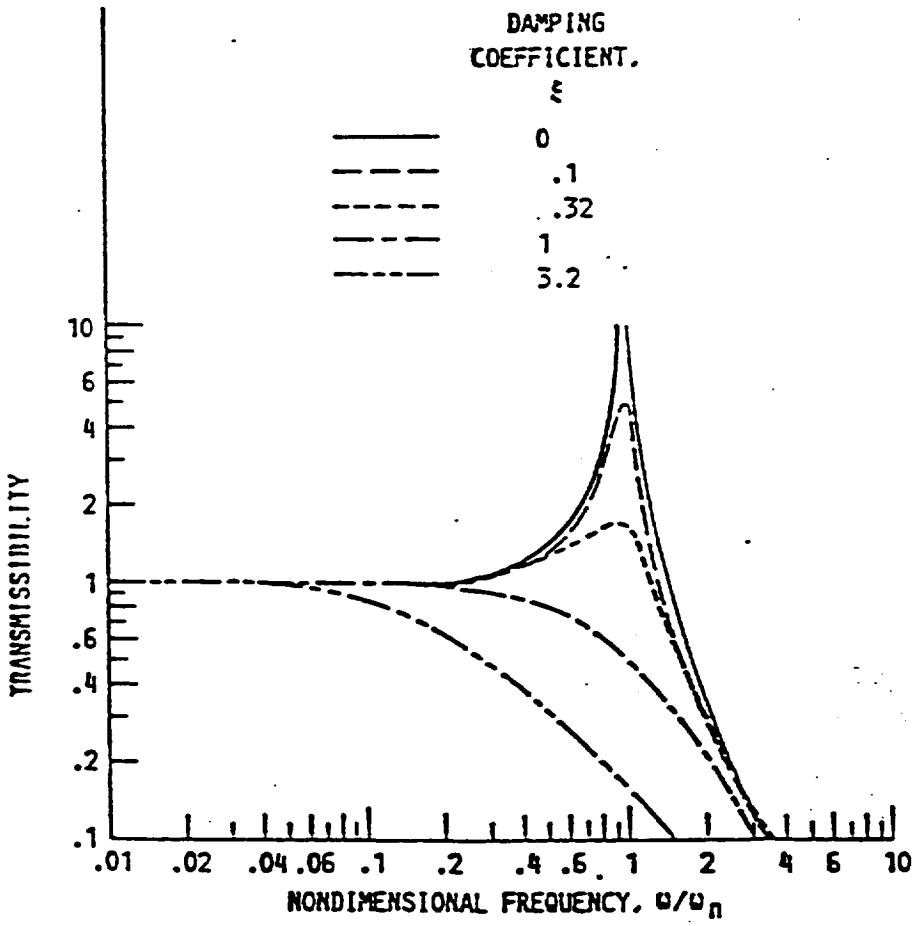

Figure 2.5: inertial damping transmissibility curves.

be achieved because of noise floor and bandwidth limitations on the feedforward control loops. However, an increase in roll off and overall attenuation can be achieved as will be demonstrated by the performance of the actual hardware designed.

2.2 Six DOF Formulation for Development and Demonstration Hardware

For the development and demonstration system hardware designs, attractive electromagnetic actuators were used as the control force devices. Since the attractive magnets are open loop unstable and must be stabilized by an appropriate amount of relative position feedback, one first must demonstrate the relative feedback control approach for a simplified single degree of freedom system upon which the multi-dimensional case will be formulated.

2.2.1 Generic Actuator Control Equation

Consider the single DOF system shown in Figure 2.6, where m and k_1 are the mass of the experimental payload and umbilical stiffness, respectively. The umbilical stiffness k_1 represents a flexible connection between the experimental payload and the base, which may be necessary for various functions like the supply of power, cooling fluid, etc.. The base acceleration $\ddot{u}$ represents the acceleration of the support structure. The control force is provided by the attractive magnetic actuator. It is well known [16] that the magnetic force f is related to the coil current I as follows:

$$f = \mu_o A_f N^2 \frac{I^2}{h^2} = G\frac{I^2}{h^2}, \tag{2.12}$$

where h, μ_o, A_f, and N are air gap, permeability of free space, magnetic pole face area, and the number of coil turns, respectively.

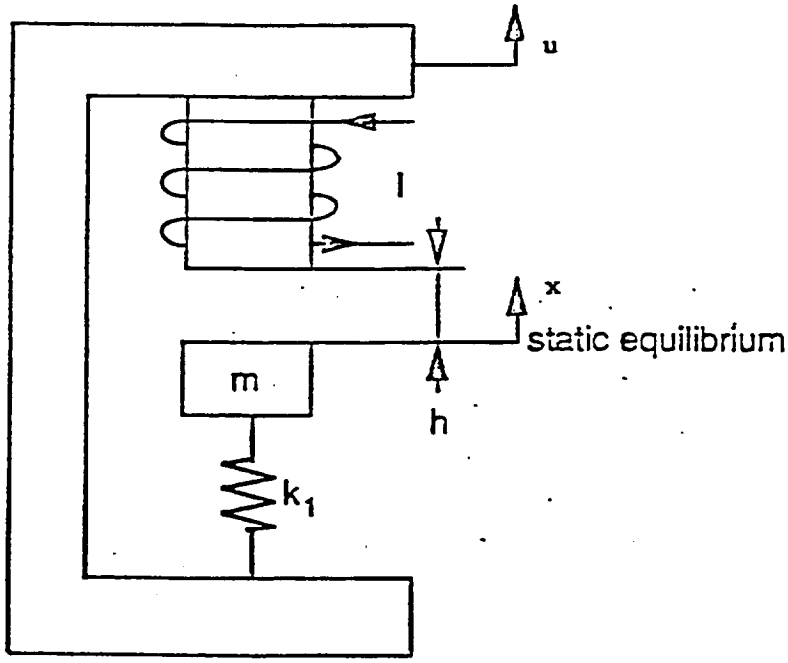

Figure 2.6: single degree of freedom system with magnetic actuator.

If h_o is the desired air gap at static equilibrium, the coil current I_s will be governed by the following static equilibrium equation.

$$mg + k_1\Delta = G\frac{I_s^2}{h_o^2}, \tag{2.13}$$

where Δ is the static deflection in the spring.

If x(t) is the dynamic displacement of the mass measured from the equilibrium position, the differential equation of motion is represented as,

$$m\ddot{x} + k_1(x-u) = \hat{f}(t), \tag{2.14}$$

where

$$\hat{f}(t) = f - mg - k_1\Delta, \tag{2.15}$$

and

$$f = G\frac{(I_s+i)^2}{(h_o-(x-u))^2} f = G\frac{(I_s+i)^2}{(h_o-(x-u))^2}. \tag{2.16}$$

In equation (2.16), i is the incremental current which is small relative to I_s. Since the relationship between f and i is nonlinear, a linearized relationship is used from the binomial expansion of equation (2.16) around the current i as follows:

$$f = G\frac{I_s^2}{h_o^2} + 2G\frac{I_s}{h_o^2}i + 2G\frac{I_s^2}{h_o^3}(x-u). \tag{2.17}$$

From equations (2.13) - (2.17),

$$m\ddot{x} + k_{eff}(x-u) = 2G\frac{I_s}{h_o^2}i, \tag{2.18}$$

where

$$k_{eff} = k_1 - 2G\frac{I_s^2}{h_o^3}. \tag{2.19}$$

Depending on the values of k_1, I_g, h_o, and G, it is possible that k_{eff} can be negative. If one assumes there is no umbilical the negative stiffness from the linearized electromagnetic circuit is most commonly referred to as the negative magnetic field stiffness which forces the controller current to be at least proportional to a relative displacement feedback signal in order to produce a closed-loop stable system. For the controller design, the control input now becomes $2G(I_g/h_o^2)i$.

Since the linearization approach is strictly valid for a small perturbation around the equilibrium position, one could directly treat $\hat{f}(t)$ as the control input; and then determine the corresponding coil current using equation (2.15) and (2.16) as follows:

$$(I_g + i) = G^{-1/2}(h_o - (x-u))(\hat{f} + mg + k_1\Delta)^{1/2}. \tag{2.20}$$

Hence, for the controller one could either consider the exact relationship (2.15) and (2.16) or the linearized system (2.19). Appendix C gives a more detailed explanation of the linearized approach including a viscous term and solving for the effective stiffness and damping of an attractive magnetic suspension system, assuming no umbilical connection.

2.2.2 Formulation of Six DOF Equations of Motion for General Isolation System

The following two figures and the subsequent mathematical formulations are given as representative of hardware systems built for the demonstration of active inertial feedforward isolation techniques. The systems built are generally represented in the following section where the actuation of either system was accomplished through three actuation pod locations giving the ability to actuate and control the isolated payload in six degrees of freedom. A specific experimental description of the developed isolation system will be given in the experimental section of this dissertation.

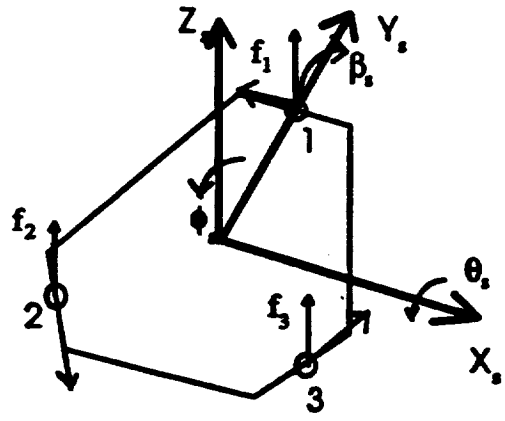

Figure 2.7: Six Degree of Freedom System

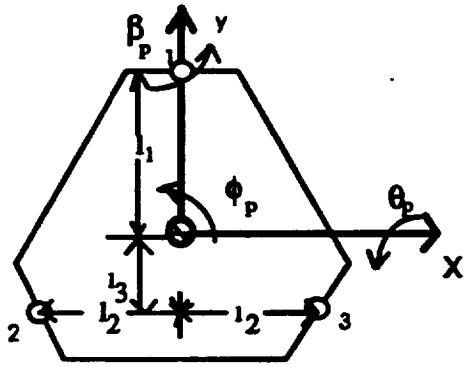

Figure 2.8 Top View of Isolation System

Referring to Figures 2.7 and 2.8 the xyz coordinate axes are chosen such that they are principal axes of the rigid body at the center of mass of the payload. The parameters f_1, f_2, and f_3, are the control forces in the appropriate dimensions for actuator pod locations one, two, and three, respectively. These forces provide the necessary static equilibrium forces as well as the appropriate negative feedback stabilization forces to counteract the negative spring rates associated with the attractive magnetic circuits. Let m represent the mass of the platform and let I_z, I_x, and I_y be the moments of inertia of the platform about the z, x, and y, axes. Twelve attractive type magnetic actuators provide control forces at the actuator pod locations 1, 2, and 3.

If x, y, and z are the dynamic displacements of the center of mass of the payload in a global xyz directions and ϕ, β, and θ are the angular displacements about the x, y, and z axes, respectively, the equations of motion can be expressed on the basis of Newton's and Euler's laws as follows.

$$m\ddot{z}_p + (k_{m1v} + k_{m2v} + k_{m3v})z_r = \hat{f}_{1v} + \hat{f}_{2v} + \hat{f}_{3v}$$

$$m\ddot{x}_p + (-k_{m1h} + k_{m2h}\frac{1}{2} + k_{m3h}\frac{\sqrt{3}}{2})x_r = -\hat{f}_{1h} + \hat{f}_{2h}\frac{1}{2} + \hat{f}_{3h}\frac{\sqrt{3}}{2}$$

$$m\ddot{y}_p + (-k_{m2h}\frac{\sqrt{3}}{2} + k_{m3h}\frac{1}{2})y_r = -\hat{f}_{2h}\frac{\sqrt{3}}{2} + \hat{f}_{3h}\frac{1}{2}$$

$$I_x\ddot{\phi}_p + (k_{m1h} + k_{m2h} + k_{m3h})l_1\phi_r = (\hat{f}_{1h} + \frac{1}{2}\hat{f}_{1h} + \frac{\sqrt{3}}{2}\hat{f}_{1h})l_1$$

$$I_x\ddot{\theta}_p + (k_{m1v}l_1 - k_{m2v}l_3 - k_{m3v}l_3)\theta_r = \hat{f}_{1v}l_1 - \hat{f}_{2v}l_3 - \hat{f}_{3v}l_3$$

$$I_y\ddot{\beta}_p + (k_{m2v} - k_{m3v})l_2\beta_r = (\hat{f}_{2v} - \hat{f}_{3v})l_2$$

. (2.21) - (2.27)

The $\hat{f}$ actuator control forces are based on a linearized control law for an attractive magnetic circuit as defined in the previous section. In this mathematical representation of the equations of motion for the six DOF case the $k_{m's}$ represent the negative spring rates associated with the linearized attractive magnetic circuits, where for this general representation there are no umbilical connections assumed. The bias forces associated with the linearization techniques account for the residual acceleration of gravity in the vertical dimensions and thus, as stated previously, since equations (2.21) - (2.27) represent the dynamic equations of motion, all static or equilibrium terms have been canceled appropriately.

The actuator control forces will be defined as follows, in a vertical and horizontal dimension, specific to their respective actuator pod locations 1, 2, and 3. Referencing Figure 2.7, the linearized vertical and horizontal actuator forces will be defined as follows:

$$\begin{pmatrix} f_{1v} \\ f_{2v} \\ f_{3v} \\ f_{1h} \\ f_{2h} \\ f_{3h} \end{pmatrix} = \begin{pmatrix} G_{1v}\frac{I_{1sv}^2}{h_{o1v}^2} + 2G_{1v}\frac{I_{1sv}}{h_{o1v}^2}i_{1v} + 2G_{1v}\frac{I_{1sv}^2}{h_{o1v}^3}v_{1r} \\ G_{2v}\frac{I_{2sv}^2}{h_{o2v}^2} + 2G_{2v}\frac{I_{2sv}}{h_{o2v}^2}i_{2v} + 2G_{2v}\frac{I_{2sv}^2}{h_{o2v}^3}v_{2r} \\ G_{3v}\frac{I_{3sv}^2}{h_{o3v}^2} + 2G_{2v}\frac{I_{3sv}}{h_{o3v}^2}i_{3v} + 2G_{3v}\frac{I_{3sv}^2}{h_{o3v}^3}v_{3r} \\ G_{1h}\frac{I_{1sh}^2}{h_{o1h}^2} + 2G_{1h}\frac{I_{1sh}}{h_{o1h}^2}i_{1h} + 2G_{1h}\frac{I_{1sh}^2}{h_{o1h}^3}h_{1r} \\ G_{2h}\frac{I_{2sh}^2}{h_{o2h}^2} + 2G_{2h}\frac{I_{2sh}}{h_{o2h}^2}i_{2h} + 2G_{2h}\frac{I_{2sh}^2}{h_{o2h}^3}h_{2r} \\ G_{3h}\frac{I_{3sh}^2}{h_{o3h}^2} + 2G_{3h}\frac{I_{3sh}}{h_{o3h}^2}i_{3h} + 2G_{3h}\frac{I_{3sh}^2}{h_{o3h}^3}h_{3r} \end{pmatrix} \tag{2.28}$$

The actuator constants G_{1v} - G_{3v}, and G_{1h} - G_{3h}, and the actuator relative position displacements v_{1r} - v_{3r}, and h_{1r} - h_{3r}, will be defined for the general case as in the equations of motion (2.21) - (2.27). The actuator constants for an attractive magnetic actuator were given in section 2.2.1. These constants will be referenced to each actuator pod location 1, 2, and 3 as shown in Figures 2.7 and 2.8.

Figure 2.7 is a perspective view of a prototype system developed for laboratory demonstrations. From this view each actuator pod location can be broken into two components having a coordinate relation with the global $x_S y_S z_S$ axes as follows.

$$
\begin{aligned}
i_1 &= -X_s \\
j_1 &= Z_s \\
i_2 &= -\frac{\sqrt{3}}{2}Y_s + \frac{1}{2}X_s \\
j_2 &= Z_s \\
i_3 &= \frac{\sqrt{3}}{2}Y_s + \frac{1}{2}X_s \\
j_3 &= Z_s
\end{aligned}
$$

(2.29) - (2.34)

These two dimensional actuator coordinates will be defined as local vertical and horizontal components. Therefore the actuator constants will be defined with these local vertical and horizontal coordinates as subscripts. Thus, the actuator constants are defined as follows:

$$
\begin{pmatrix} G_{1v} \\ G_{2v} \\ G_{3v} \\ G_{1h} \\ G_{2h} \\ G_{3h} \end{pmatrix} = \begin{pmatrix} 2\mu_o N_{1v}^2 A_{f1v} \\ 2\mu_o N_{2v}^2 A_{f2v} \\ 2\mu_o N_{3v}^2 A_{f3v} \\ 2\mu_o N_{1h}^2 A_{f1h} \\ 2\mu_o N_{2h}^2 A_{f2h} \\ 2\mu_o N_{3h}^2 A_{f3h} \end{pmatrix}, \tag{2.35}
$$

where the constants μ_o, A_f, and N are defined in section 2.2.1. Referring to Figures 2.7 and 2.8 the possible relative displacements which can be realized by the rigid body motion of the suspended payload or the support structure will result in the following definitions of relative displacements from the equilibrium position, defined by the nominal equilibrium air gaps h_{o1v} - h_{o3v}, and h_{o1h} - h_{o3h}. Therefore, for small relative angles, the relative displacements at the actuator locations 1, 2, and 3 for the vertical and horizontal directions are as follows:

$$\begin{pmatrix} v_{1r} \\ v_{2r} \\ v_{3r} \\ h_{1r} \\ h_{2r} \\ h_{3r} \end{pmatrix} = \begin{pmatrix} (z-Z_s)+l_1(\theta_p-\theta_s) \\ (z-Z_s)-l_3(\theta_p-\theta_s)+l_2(\beta_p-\beta_s) \\ (z-Z_s)-l_3(\theta_p-\theta_s)-l_2(\beta_p-\beta_s) \\ -(x-X_s)+l_1(\phi_p-\phi_s) \\ (x-X_s)\frac{1}{2}-(y-Y_s)\frac{\sqrt{3}}{2}+l_1(\phi_p-\phi_s) \\ (x-X_s)\frac{1}{2}+(y-Y_s)\frac{\sqrt{3}}{2}+l_1(\phi_p-\phi_s) \end{pmatrix} \tag{2.36}$$

The two systems built will be distinguished from each other as a laboratory prototype and low gravity flight test hardware, respectively. The only major difference between these two systems was the large one g bias operational environment during laboratory experiments. This condition dictated a large bias current in the vertical actuators to support the weight of the payload, thus giving a large negative spring rate requiring a certain amount of relative position feedback, an order of magnitude greater than the horizontal actuators. This of course was not the case during the parabolic flights, since for approximately 10 - 20 seconds the isolated payload was off loaded. Now that the closed-loop stabilization equations for the multi-dimensional case have been formulated one can begin to theoretically represent the incremental control current i as the summation of various control signals representing the relative feedback and inertial feedforward control approaches.

2.2.3 Control Signal Theoretical Formulation

As depicted in section 2.2.1, for the signal dimensional case, a linearized closed-loop attractive magnetic circuit is controlled by an incremental current i typically represented as being proportional to relative displacement and velocity, giving an effective positive stiffness and a

damping term for the simple one dimensional case (See Appendix C). In line with this formulation, the magnetic circuits for the three dimensional case can be analyzed by assuming there is minimal coupling due to non-symmetric stator-armature gap displacements, and that the average force produced by a specific actuator pair is aligned with the centerline of the attractive magnet and perpendicular to the pole face of the actuator, for small angular displacements and translational motion. Therefore, the incremental control current will be defined in the global coordinate system referenced to the relative rigid body motions and the inertial parameters of the support structure. These globally defined control currents will then be defined in the appropriate actuator local coordinates for the control of the isolated payload. The incremental control current i will be defined in the fixed rigid body coordinates as follows:

$$\begin{pmatrix} i_x \\ i_y \\ i_z \\ i_\theta \\ i_\beta \\ i_\phi \end{pmatrix} = \begin{pmatrix} -C_{xr}(x_p - X_s) - C_{\dot{x}r}(\dot{x}_p - \dot{X}_s) + D_{xi}X_s + D_{\dot{x}i}\dot{X}_s \\ -C_{yr}(y_p - Y_s) - C_{\dot{y}r}(\dot{y}_p - \dot{Y}_s) + D_{yi}Y_s + D_{\dot{y}i}\dot{Y}_s \\ -C_{zr}(z_p - Z_s) - C_{\dot{z}r}(\dot{z}_p - \dot{Z}_s) + D_{zi}Z_s + D_{\dot{z}i}\dot{Z}_s \\ -C_{\theta r}(\theta_p - \theta_s) - C_{\dot{\theta}r}(\dot{\theta}_p - \dot{\theta}_s) + D_{\theta i}\theta_s + D_{\dot{\theta}i}\dot{\theta}_s \\ -C_{\beta r}(\beta_p - \beta_s) - C_{\dot{\beta}r}(\dot{\beta}_p - \dot{\beta}_s) + D_{\beta i}\theta_s + D_{\dot{\beta}i}\dot{\beta}_s \\ -C_{\phi r}(\phi_p - \phi_s) - C_{\dot{\phi}r}(\dot{\phi}_p - \dot{\phi}_s) + D_{\phi i}\phi_s + D_{\dot{\phi}i}\dot{\phi}_s \end{pmatrix}. \tag{2.37}$$

The previous set of equations (2.37) represent the control current formulations for the respective body fixed xyz coordinates where the control coefficients are defined as the relative displacement feedback gains $C_{xr,yr,zr,\theta r,\beta r,\phi r}$ (amps/m), the relative velocity feedback gains $C_{\dot{x}r,\dot{y}r,\dot{z}r,\dot{\theta}r,\dot{\beta}r,\dot{\phi}r}$ (amps sec/m), and the inertial feedforward gains, $D_{xi,yi,zi,\theta i,\beta i,\phi i}$ (amps/m), and $D_{\dot{x}i,\dot{y}i,\dot{z}i,\dot{\theta}i,\dot{\beta}i,\dot{\phi}i}$ (amps sec/m), respectively. This set of equations represents a typical active relative feedback control where the relative effective stiffness and damping can be digitally controlled. In addition the inertial feedforward terms are introduced into the control equations to attempt the

cancellation of base mechanical excitations due to the mass being referenced to its support environment through the relative isolation parameters, which are needed in order to have a closed loop stable system as well as defining the systems equilibrium position. If one were to define the control equations for inertial feedback as in a previous section for the one dimensional active isolation problem, the control currents can be represented as follows:

$$\begin{pmatrix} i_{x_p b} \\ i_{y_p b} \\ i_{z_p b} \\ i_{\theta_p b} \\ i_{\beta_p b} \\ i_{\phi_p b} \end{pmatrix} = \begin{pmatrix} -C_{x_p}(x_p - X_s) - C_{\dot{x}_p}(\dot{x}_p - \dot{X}_s) - E_{\ddot{x}_p}\dot{x}_p - E_{\bar{\ddot{x}}_p}\bar{\ddot{x}}_p \\ -C_{y_p}(y_p - Y_s) - C_{\dot{y}_p}(\dot{y}_p - \dot{Y}_s) - E_{\ddot{y}_p}\dot{y}_p - E_{\bar{\ddot{y}}_p}\bar{\ddot{y}}_p \\ -C_{z_p}(z_p - Z_s) - C_{\dot{z}_p}(\dot{z}_p - \dot{Z}_s) - E_{\ddot{z}_p}\dot{z}_p - E_{\bar{\ddot{z}}_p}\bar{\ddot{z}}_p \\ -C_{\theta_p}(\theta_p - \theta_s) - C_{\dot{\theta}_p}(\dot{\theta}_p - \dot{\theta}_s) - E_{\ddot{\theta}_p}\dot{\theta}_p - E_{\bar{\ddot{\theta}}_p}\bar{\ddot{\theta}}_p \\ -C_{\beta_p}(\beta_p - \beta_s) - C_{\dot{\beta}_p}(\dot{\beta}_p - \dot{\beta}_s) - E_{\ddot{\beta}_p}\dot{\beta}_p - E_{\bar{\ddot{\beta}}_p}\bar{\ddot{\beta}}_p \\ -C_{\phi_p}(\phi_p - \phi_s) - C_{\dot{\phi}_p}(\dot{\phi}_p - \dot{\phi}_s) - E_{\ddot{\phi}_p}\dot{\phi}_p - E_{\bar{\ddot{\beta}}_p}\bar{\ddot{\beta}}_p \end{pmatrix}. \tag{2.38}$$

Here the inertial feedback coefficients $E_{\ddot{x}_p,\ddot{y}_p,\ddot{z}_p,\ddot{\theta}_p,\ddot{\beta}_p,\ddot{\phi}_p}$, and $E_{\bar{\ddot{x}}_p,\bar{\ddot{y}}_p,\bar{\ddot{z}}_p,\bar{\ddot{\theta}}_p,\bar{\ddot{\beta}}_p,\bar{\ddot{\phi}}_p}$ are defined as the inertial acceleration and velocity feedback terms having (amps-sec^2/m) and (amps-sec/m) units, respectively.

Using the actuator constants for the actuation locations 1, 2, and 3 one can define the control forces, $\hat{f}$, for these locations by defining the incremental control currents in the appropriate local actuator coordinates as follows:

$$\begin{pmatrix} \hat{f}_{1v} \\ \hat{f}_{2v} \\ \hat{f}_{3v} \\ \hat{f}_{1h} \\ \hat{f}_{2h} \\ \hat{f}_{3h} \end{pmatrix} = \begin{pmatrix} C_{1v}(i_z + i_\theta) \\ C_{2v}\frac{l_1}{2l_3}(i_z - i_\theta + i_\beta) \\ C_{3v}\frac{l_1}{2l_3}(i_z - i_\theta - i_\beta) \\ C_{1h}(-i_x + i_\phi) \\ C_{2h}(\frac{1}{2}i_x - \frac{\sqrt{3}}{2}i_y + \frac{1}{2}i_\phi) \\ C_{2h}(\frac{\sqrt{3}}{2}i_x + \frac{1}{2}i_y + \frac{\sqrt{3}}{2}i_\phi) \end{pmatrix} \tag{2.39}$$

The constants $C_{1v,2v,3v}$ and $C_{1h,2h,3h}$ are the actuator constants defined by the following relationships formulated in section 2.2.1.

$$\begin{pmatrix} C_{1v} \\ C_{2v} \\ C_{3v} \\ C_{1h} \\ C_{2h} \\ C_{3h} \end{pmatrix} = \begin{pmatrix} 2G_{1v}\frac{I_{1xv}}{h_{01v}^2} \\ 2G_{2v}\frac{I_{2xv}}{h_{02v}^2} \\ 2G_{3v}\frac{I_{3xv}}{h_{03v}^2} \\ 2G_{1h}\frac{I_{1xh}}{h_{01h}^2} \\ 2G_{2h}\frac{I_{2xh}}{h_{02h}^2} \\ 2G_{3h}\frac{I_{3xh}}{h_{03h}^2} \end{pmatrix} \tag{2.40}$$

Using these equations the equations of motion can be put into matrix form in order to calculate the theoretical transfer functions. The control currents as represented in equations (2.39) have been assumed to be in general dependent on an appropriate stable controller. For the remainder of this dissertation it will be assumed that the control currents defined in equations (2.37) are used

giving the relative feedback/inertial feedforward controller which is experimentally demonstrated in the laboratory and Learjet hardware.

Six differential equations of motion have been developed which describe the motion of a payload isolated by attractive magnetic actuators at three planar points incorporating the center of mass of the system. In summary these equations are (2.21) through (2.27) where the appropriate constants and control forces are defined in local coordinates from equations (2.39). If the six degrees of freedom are truly decoupled, the system response will be only due to inputs in the appropriate directions. This however, is not likely and there is some coupling between degrees of freedom because of the non-orthogonality of the attractive magnetic circuits. This non-orthogonality is very small, however, and will be assumed negligible.

III. Design and Development of Active Inertial Isolation Systems

The experimental hardware designed and developed for active low frequency isolation consisted of a ferromagnetic isolated payload actuated at three pod locations. Each actuation pod consisted of three or four attractive magnetic actuators arranged to produce an effective push-pull configuration in two dimensions giving the actuation capability of six DOF on the ferromagnetic platform. Figure 3.1 shows a layout of the laboratory prototype system where the isolated payload was of a hexagonal design fabricated from angle iron and welded together to the dimensions shown in Figure 3.2.

The relative and inertial motion of both systems, (i.e. the displacement of the isolated payload with respect to its support environment and the acceleration of either the payload or the support), are measured using eddy current probes and proof-mass accelerometers, respectively. These signals are then run through signal conditioning circuits consisting of filters and gain adjustments. The gain adjustments are introduced to take advantage of the full scale range of the analog-to-digital conversion. For the relative signals, one does not want to roll off the response at dc because the package is required to follow the low frequency motion of the orbiter due to rattle space constraints being limited to 1 to 3 cm (.394 to 1.2 in). This can be achieved by an integral action in the feedback controller. However, the accelerometer signals for the feedback or feedforward control need to be rolled-off at the lower frequencies because of this same limitation.

The low-pass filters are provided because the payload, naturally being mechanically attenuated at higher frequencies, is limited in acceleration performance by the active control system noise floor. In addition to the physical control considerations for the band-pass and low-pass filters employed, one must consider the frequency response, noise floor, and linearity of the control sensors. The sensor response will limit the system performance and resolution. Shaping the control

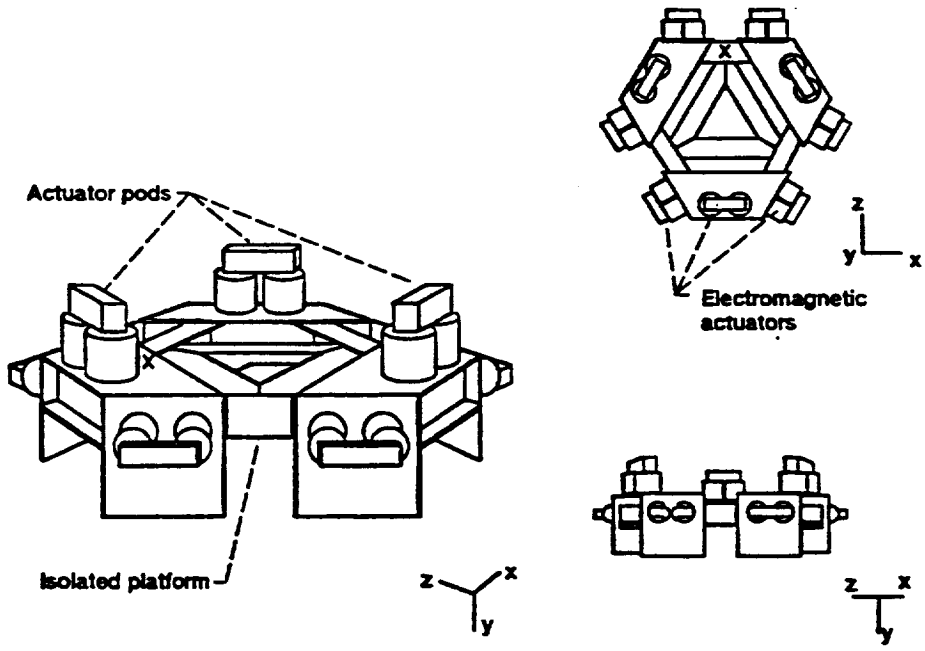

Figure 3.1: Prototype Active Vibration Isolation System Layout.

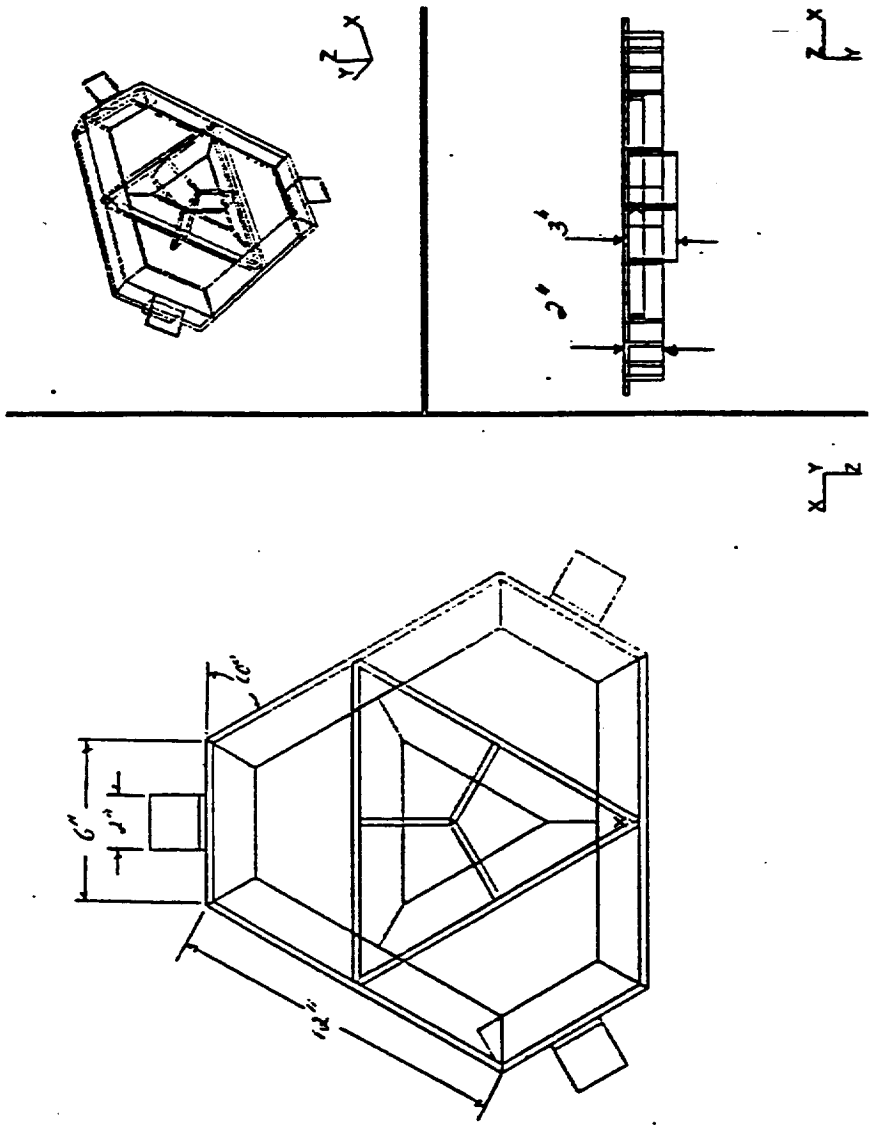

Figure 3.2: Prototype System's Ferromagnetic Isolated Payload.

bandwidth of the system can increase overall system performance, as defined by a broad-band acceleration noise floor measurement on the controlled payload.

The mechanical design considerations for such systems reflect typical hardware design practices for any space born payloads. However, there are a few considerations concerning the structural response of the payload and support structure which are important for the performance of any isolation system. These concerns should be addressed to take full advantage of performance capabilities and limitations of the active control system. One should design the support and payload structure to have their structural modes above the controller bandwidth. If there are excited payload modes within the frequency range of interest, the active relative feedback loops could potentially become feedforward loops driving the system unstable. In addition, the noise floor performance of the system will be limited by the excited modes of the structure. These factors will effect sensor locations where co-location of the control sensors with the actuation device is most desirable. Therefore, the structural dynamics of the support and payload are critical for observability considerations.

The layout of the system is also important, especially for orbiter designs, because all volume taken by the isolation system is subtracted from the total experimental volume available. In designing a six DOF concept one must begin by understanding the dynamic environment in which such a system is to perform. Once the isolation requirements are established, the physical limits of the system DOF can be defined which will then dictate the actuator/payload configuration. Once these isolation system requirements are established, the full system concept is limited only by the total size, power, and mass constraints of the orbital carrier.

3.1 Closed Loop Control of Active Attractive Electromagnetic Isolation Systems

3.1.1 Sensor Descriptions and Placements

In order to describe the control of a generic payload the equations of motion for a general attractive electromagnetic suspension system were developed and the controller currents described referenced to the relative and inertial rigid body dynamics of the isolation system. These control states must be measured by transducers and used as the control inputs in order to control the incremental current to the actuators. In order to assess the extent to which a disturbance effects the isolated platform or to control the platform's motion, motion sensors are mounted on the platform or the support structure producing a voltage output that is proportional to the motion experienced at the sensor location. This section is intended to give insight into the concepts underlying the use of motion sensors in the stabilization and control of a platform.

There are a wide variety of sensors available for measuring motion. Sensors which produce voltages proportional to linear position, velocity and acceleration are common, as are their rotational counterparts. A detailed description of the mechanical and electrical technology employed in these sensors is varied, dependent on the specific sensor, and is beyond the scope of this dissertation, but it is important to address the issues which affect the selection of the control sensors for this application. Some of the important issues are:

(1) inertial verses non-inertial measurement

(2) frequency response and sensor dynamics

(3) noise floor and parasitic sensitivities

(4) sensor placement.

3.1.1.1 Inertial Verses Non-inertial Measurement

Motion sensors can be grouped into two general categories: (1) inertial and (2) non-inertial. An inertial motion sensor provides a measurement of the motion with respect to an inertial reference

frame, while a non-inertial motion sensor measures motion with respect to a non-inertial reference frame. Examples of inertial motion sensors include accelerometers and rate sensors (rate sensors measure linear or angular velocity). Examples of non-inertial sensors include Linear Variable Differential Transformers (LVDT), capacitance probes, eddy current probes, inductive probes etc.

To demonstrate the difference between inertial and non-inertial sensors, consider two simple applications of an LVDT. First, in the configuration shown in Figure 3.3, mass M is supported by a spring K and viscous damper C. The vertical motion u, of the base causes the motion x, of the mass M. The LVDT in this configuration measures the relative position of mass M, and the base, x - u. This is a non-inertial measurement because a given voltage output corresponds to a unique displacement x with respect to a fixed reference frame attached to the base. In contrast, consider the configuration shown in Figure 3.4. The quantities M, K, C, x and u are as described previously. A smaller mass m, supported by spring k, is mounted in a housing, which is in turn mounted on top of mass M. The LVDT now measures the relative displacement of mass m, and the housing, x_f - x. The LVDT in this configuration also provides an approximate measure of the inertial acceleration of mass M assuming that $\sqrt{K/m}$ >> frequencies of interest. Regardless of the motion of the base, a change in the inertial velocity of mass M will cause motion of the smaller mass m, and thus a non-zero output from the LVDT. The housing fixture containing the non-inertial LVDT sensor and mass m, is functioning as an inertial sensor for the mass M.

The difference between these two configurations is of fundamental importance in stabilization applications. Suppose that a control system is implemented in each of the two configurations above, such that actuation forces F_s act on the mass M, and are dependent on the output of the LVDT. If the purpose of the controller is to hold the LVDT output at zero as the motion of the base disturbs the system, then in Figure 3.3 the mass M will follow, or "track" the motion of the base. This behavior is undesirable, particularly when the disturbances are seismic, and originate from the base. In Figure 3.4 the output of the LVDT is zero when the mass M is stationary with respect to

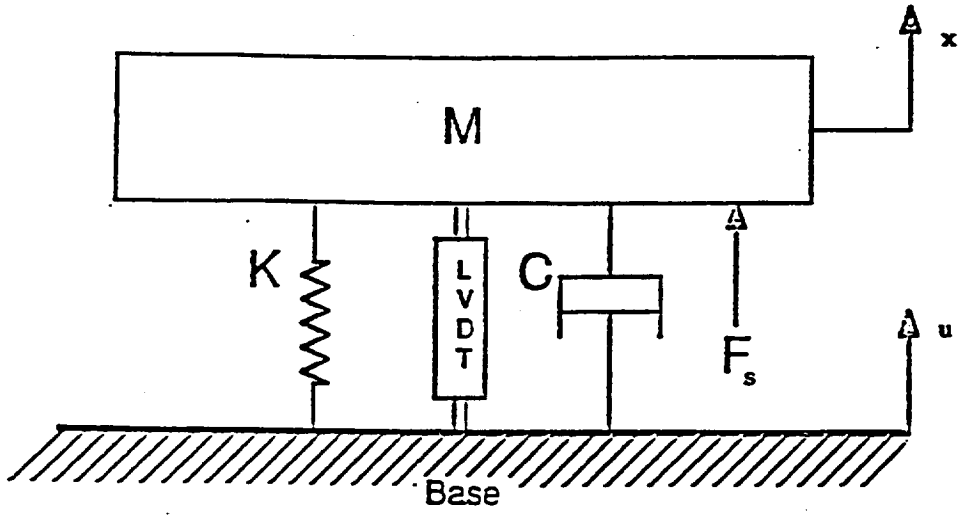

Figure 3.3: LVDT sensor measurment in non-inertial configuration.

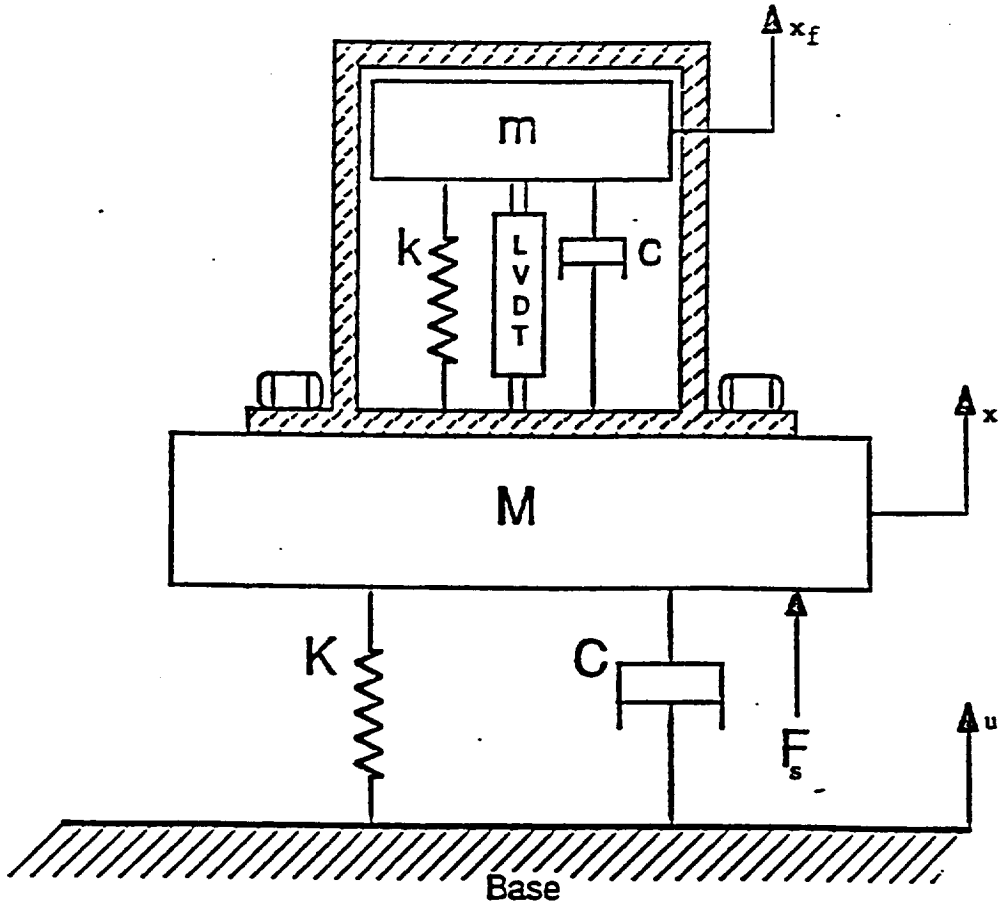

Figure 3.4: LVFT sensor measurement in inertial configuration.

inertial space (experiences no acceleration), regardless of the motion of the base. The mass M is in this case, inertially isolated from the seismic motion of the base. This behavior is far more suitable for stabilization applications. Following this line of reasoning if the housing was attached to the base structure the voltage output of the LVDT would be proportional to the inertial motion of the base. In this case if a servo force F_s were to be referenced to this signal and the stiffness and damping coefficients are known, motion of the base could be effectively canceled. In essence the mass M would seem to be in motion to an observer on the base however, in actuality, the base would be in motion and the mass M would be inertially fixed.

3.1.1.2 Frequency Response and Sensor Dynamics of Inertial Sensors

Inertial motion sensors (accelerometers and inertial rate devices) have performance characteristics which vary with the frequency of input excitation. Mathematically, the frequency response of a sensor is described by its transfer function. In general the transfer function is a complex value dependent on frequency. The magnitude and phase of the sensor response to the input excitation are typically plotted separately as a function of frequency [17]. The magnitude of the frequency response is typically sufficient to describe the important features of the sensor dynamics. The phase information may become important in the stability of a control system which employs the sensor in a control loop.

The magnitude function is the ratio of the amplitude of the output to the amplitude of the input excitation as functions of frequency. If the sensor is intended to measure velocity, then the ratio of output voltage to the input velocity excitation should ideally be flat over the frequency range of the sensor. Therefore, if the magnitude of the transfer function from input to output for the sensor is constant over the operating range, then the sensor response is said to be flat.

An inertial motion sensor can only exhibit a flat response over some finite frequency range. Above and below the operating frequency range (generally the flat portion of the magnitude function) the response is attenuated, or "rolled off". Figure 3.5 shows a sensor magnitude function exhibiting a flat response over the region from about 1.0 Hz to about 300.0 Hz. On either side of the flat region the response is attenuated. A highpass filter is often used to roll off the response at low frequencies. The reason for this is two fold. In this application the inertial sensors are used to cancel out the excitation effect of a base motion disturbance, however, the practicality of this is limited to certain volume constraints as was discussed earlier. Therefore, the sensor response must be rolled-off at the lower frequencies. In addition, electrical noise in the signal conditioning circuitry is proportional to the reciprocal of the frequency, and thus increases with decreasing frequency. This effect, called flicker noise, degrades the low frequency performance of the sensor and therefore, an effective flat bandpass filter must be designed in conjunction with the appropriate inertial sensor in order to have a flat response of the sensor circuitry configuration in the control bandwidth of interest [18]. The highpass filter truncates the response in the degraded region so that only the reliable portion of the sensor response appears in the sensor output. At high frequencies, inertial masses employed in accelerometers cannot respond "fast enough" dynamically to measure the motion above a certain frequency. In fact, an accelerometer which operates on the principle shown in Figure 3.4 is a second-order spring-mass mechanical system, and has a magnitude function which behaves like a low-pass filter. In essence, the magnitude response of the accelerometer will be flat at frequencies well below the sensor natural frequency $\sqrt{K/M}$. (Damping can extend the range up to about $0.6\sqrt{K/M}$.)

The shape of the magnitude function can be complicated, containing multiple regions of varying slopes. The magnitude function of the accelerometer used in this application will be studied later and it will be shown that this function is not flat in any frequency range. However, this sensor is still quite useful. As will be demonstrated in the results section of this dissertation. See Appendix D for a detailed description of transfer function determination.

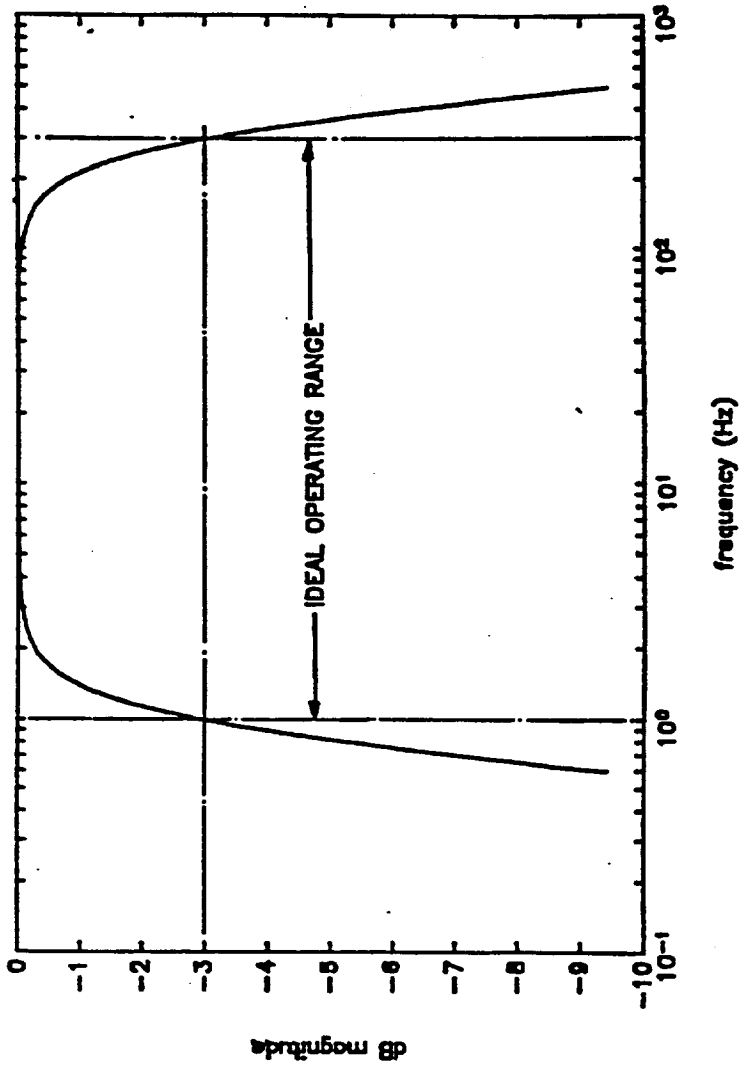

Figure 3.5: Typical sensor transfer function magnitude plot.

3.1.1.3 Noise Floor and Parasitic Sensitivity

As mentioned earlier, an inertial motion sensor is limited in the range of excitation frequencies that it can be used to measure reliably. In addition, a given sensor can only measure excitations which fall within a limited range of amplitudes. The smallest change in the measured quantity which a sensor is capable of measuring accurately is called the sensor resolution. A motion sensor can reliably measure any excitation which falls within this range of amplitudes bounded at one end by the resolution of the sensor, and bounded at the other end by the amplitude which would result in the maximum output range of the sensor. If the excitation acting on the sensor location is too large (i.e. has too large an amplitude), then the sensor will saturate, creating an output which is usually equal to the maximum output voltage of the sensor. If the excitation is too weak (i.e. has an amplitude smaller than the resolution of the sensor), then factors such as static electric fields and magnetic interference which are not related to the excitation of interest (called noise) have more influence on the output of the sensor than the excitation. This situation leads to a poor correlation between the excitation and the sensor output. In order to measure large excitations, sensor components are generally made stiffer, and the electronics less sensitive therefore, the amplitude range of the sensor is very important to consider in that the sensor noise floor must be at least an order of magnitude less than the smallest excitation amplitude of interest and that the largest amplitude expected is within the amplitude range of the sensor used.

The measurement of motions having very small amplitudes is difficult. Particularly in stabilization applications where disturbances tend to be very small, it is important to quantify accurately, the resolution of the sensor. Most accelerometer manufacturers publish values of the sensitivity and maximum allowable impact for the various models they produce. The sensitivity is merely the value of the magnitude function in the flat portion of the curve [19]. When there is no flat portion on the curve, sensors are often calibrated by experimentally fitting a straight line through data

showing the sensor voltage output as a function of the magnitude of the input. The slope of this line is also the sensitivity of the sensor, and is equivalent to the definition given previously. The units of the sensitivity are output per unit input.

It would seem logical that one could measure as low an amplitude excitation as desired, as long as the sensitivity of the sensor were high enough. Unfortunately, even an accelerometer with a very high sensitivity will fail to provide an accurate measurement when the excitation becomes sufficiently small due to its noise performance. In addition, the amplitude at which the measurement breaks down varies with frequency. What is needed is a plot of the amplitude at which the measurement provided by a sensor breaks down versus frequency. This function is called the incoherent power spectrum, and is obtained using signal processing techniques [20]. Only the signal processing concepts required in the analysis of interest will be mentioned.

The incoherent power spectrum may be obtained for a given sensor using the following technique [20]. Two identical sensors, sensor x and sensor y, are placed in a quiet environment, and are mounted rigidly to one another so that the sensitive axes of the sensors are coincident. Records of sensor output versus time are obtained for both sensors simultaneously. Autocorrelation functions $R_{xx}(\tau)$ and $R_{yy}(\tau)$ and the crosscorrelation function $R_{xy}(\tau)$ are calculated from the time histories of the output from sensors x and y. These functions are defined below, and are described in more detail in Appendix D.

$$R_{xx}(\tau) = E\{x(t)x(t+\tau)\}$$
$$R_{yy}(\tau) = E\{y(t)y(t+\tau)\} \qquad (3.1)$$
$$R_{xy}(\tau) = E\{x(t)y(t+\tau)\}$$

In these expressions, the operator E{ } represents the expected value, or the arithmetic mean of the quantities enclosed in the brackets (see Appendix D). The autospectral density and cross-spectral density functions are calculated from the autocorrelation and crosscorrelation functions using the Fourier transform. These functions are defined below, and are described in detail in Appendix D.

$$G_{xx}(j\omega) = \frac{1}{\pi(bw)} \int_{\omega_i}^{\omega_f} R_{xx}(\tau) \exp(-j\omega\tau) d\tau$$

$$G_{yy}(j\omega) = \frac{1}{\pi(bw)} \int_{\omega_i}^{\omega_f} R_{yy}(\tau) \exp(-j\omega\tau) d\tau \qquad (3.2)$$

$$G_{xy}(j\omega) = \frac{1}{\pi(bw)} \int_{\omega_i}^{\omega_f} R_{xy}(\tau) \exp(-j\omega\tau) d\tau,$$

where $G_{xx}(j\omega)$, $G_{yy}(j\omega)$ are the autospectral densities of the autocorrelation function for sensors x and y while $G_{xy}(j\omega)$ is the crosspectral density of the crosscorrelation function for the two sensors. In the previous expressions:

bw	=	bandwidth of interest, $\omega_f - \omega_i$ (rad/s)
j	=	complex operator = $\sqrt{-1}$
ω	=	frequency (rad/s)
ω_i	=	lowest frequency of interest (rad/s)
ω_f	=	highest frequency of interest (rad/s).

The functions in equations (3.1) and (3.2) are then used to calculate the coherence function $\gamma^2_{xy}(\omega)$ as shown below.

$$\gamma^2_{xy} = \frac{|G_{xy}(j\omega)|^2}{G_{xx}(j\omega) G_{yy}(j\omega)} \qquad (3.3)$$

The coherence function is fundamental to signal processing. It is a complex-valued function which is a measure of the agreement between the two signals, x(t) and y(t), as a function of frequency. Notice that if the auto-spectral density functions for the two sensor outputs, $G_{xx}(j\omega)$ and $G_{yy}(j\omega)$ are equal, then $|G_{xy}(j\omega)|^2 = |G_{xx}(j\omega)|^2 = |G_{yy}(j\omega)|^2$, and the coherence function is equal to unity

over the frequency band. The value of the magnitude of the coherence function is always within the region

$$0 \le \left|\gamma_{xy}^2\right| \le 1$$

and a coherence magnitude of unity implies a perfect agreement between the two signals x and y.

Suppose that a shock is imparted to the configuration consisting of the two sensors mounted back-to-back. Provided that both sensors are functioning, they should both sense the excitation and generate similar outputs at the time of the excitation. Now suppose that shocks similar to the one described above are occurring frequently, and have pronounced frequency components between 100 and 200 Hz. When a Fast Fourier Transform (FFT) is performed on the sensor time histories, and the auto-spectral and cross-spectral densities are calculated from the FFT, the auto-spectra and cross-spectra associated with the two sensors will both show regions of elevated energy between 100 and 200 Hz. What is not so predictable is that removing the shock environment does not completely eliminate the sensor output. Small residual motion and electrical noise will cause some sensor signal.

Unlike motion or an excitation which causes similar outputs from both sensors, electrical noise is random in nature. It is statistically unlikely that the two sensors will produce noise-induced voltage outputs that are the same at any given instant in time. The two sensor outputs due to excitations will tend to agree, while those induced by noise will typically disagree. The two effects can be separated using the coherence function.

The energy that both signals have in common is (subject to statistical probability) caused by motion input, and is called the coherent power. The coherent power for both sensor outputs is presented below in terms of the coherence. The coherent power for sensor x is given by

$$P_{cx}(j\omega) = \gamma_{xy}^2 G_{xx}(j\omega). \tag{3.4}$$

The coherent power for sensor y is given by

$$P_{cy}(j\omega) = \gamma_{xy}^2 G_{yy}(j\omega). \tag{3.5}$$

Notice that the coherent power is not necessarily the same for both sensor outputs. It follows then that the incoherent power, or that energy in the signals induced by noise, is the energy that is left over. The incoherent power for sensor x is given by

$$P_{icx}(j\omega) = (1-\gamma_{xy}^2)G_{xx}(j\omega). \tag{3.6}$$

The incoherent power for sensor y is given similarly by

$$P_{icy}(j\omega) = (1-\gamma_{xy}^2)G_{yy}(j\omega). \tag{3.7}$$

The areas under the incoherent power spectra are called the cumulative powers of the incoherent power spectra $P_{icx}(j\omega)$ and $P_{icy}(j\omega)$.

$$P_{cum\_ic\_x(j\omega)} = \int_{\omega_l}^{\omega_h} P_{icx}(j\omega)d\omega \tag{3.8}$$

$$P_{cum\_ic\_y(j\omega)} = \int_{\omega_l}^{\omega_h} P_{icy}(j\omega)d\omega \tag{3.9}$$

If the signal x has units of volts, then the cumulative power has units of volts^2. The square root of the cumulative power is called the root-mean-square (rms) of the spectrum. The spectrum rms of the signal x has units of volts. Although there are other measures of the noise floor of a motion sensor, the rms of the incoherent power spectrum is a good measure of the noise floor. It is a good general practice to select a sensor which has a noise floor at least one order of magnitude lower than the smallest quantity to be measured in the bandwidth of interest.

One of the problems with highly sensitive inertial sensors is that they tend to sense motions that they are not intended to sense. For example, a rotational velocity sensor will have some sensitivity to linear motion. This undesired response is called cross-axis, or parasitic sensitivity. The amount of parasitic sensitivity that a sensor exhibits can be assessed using the coherence function. The coherent power is first calculated for a set of two sensors as described. Then the two sensors are mounted so that the sensitive axes are orthogonal to one another. The coherent power for the sensors is calculated again for the sensors in this configuration. The rms of the coherent power spectra in

both configurations (in axis and orthogonal mounting) are calculated. The ratio of the two rms values gives the percentage of parasitic sensitivity. A good motion sensor should exhibit very low parasitic sensitivity.

3.1.1.4 Sensor Placement

It is good practice to place the sensor as close as possible to the point at which a measurement of the motion is desired. But often, the geometry or some other constraint makes this difficult. In these cases it is important to be aware of the dynamic effects of placing a sensor at a location away from the axis of motion along which a measurement is required.

Consider a platform as shown in Figure 3.6. The reference frame is fixed to the center of gravity of the platform labeled, "CG". The positive conventions are shown for translation and rotation. An accelerometer is mounted at a point P, away from the center of gravity, whose position with respect to the center of gravity is specified by the vector $\bar{r}$. Taking into account all six degrees of freedom (three translations and three rotations), the acceleration experienced at the sensor location P, is given by the relation [21],

$$\bar{a}_p = \bar{a}_{cg} + (\bar{\alpha} \times \bar{r}) + (\bar{\omega} \times \bar{\omega} \times \bar{r}). \tag{3.10}$$

In this equation (3.10), $\bar{a}_p$ is the acceleration of point P, $\bar{a}_{cg}$ is the acceleration of the center of gravity of the platform, $\bar{\alpha}$ is the angular acceleration vector of the platform, and $\bar{\omega}$ is the angular velocity vector of the platform. Expanded into components, the angular acceleration and angular velocity vectors may be described in their respective component directions as follows:

$$\begin{aligned} \bar{\alpha} &= \alpha_x \hat{i} + \alpha_y \hat{j} + \alpha_z \hat{k} \\ \bar{\omega} &= \omega_x \hat{i} + \omega_y \hat{j} + \omega_z \hat{k}, \end{aligned} \tag{3.11}$$

where $\hat{i}, \hat{j}$ and $\hat{k}$ are the unit vectors along the x, y, and z axes respectively. Placed at the point P, the accelerometer measures not only the acceleration of the center of gravity, but also the acceleration

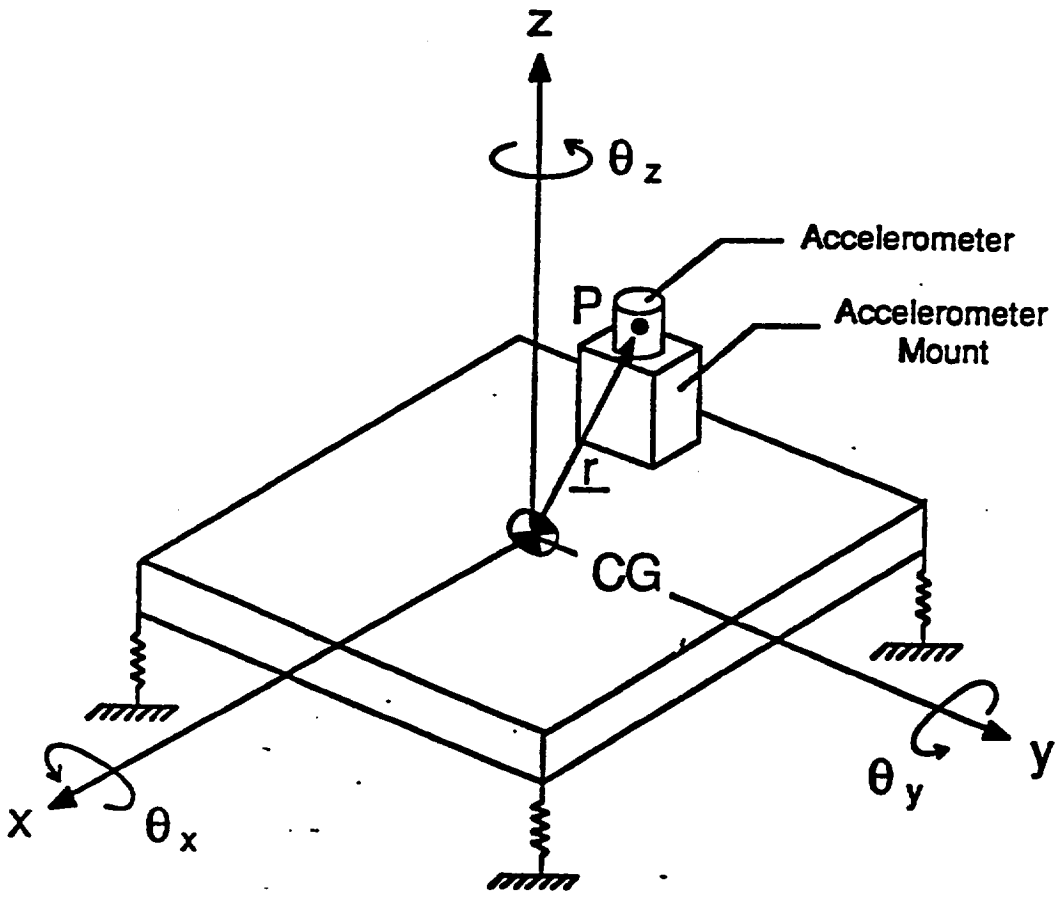

Figure 3.6: Inertial sensor mounted off-axis.

terms associated with the rotational acceleration and the rotational velocity crossed with the vector position of P. The acceleration of point P can be formulated with all the component vector terms as follows:

$$\begin{aligned}\bar{a}_p = \bar{a}_{cg} &+ \left[(\omega_x\omega_y - \alpha_z)r_y + (\alpha_y + \omega_x\omega_z)r_z - (\omega_y^2 + \omega_z^2)r_x\right]\hat{i} \\ &+ \left[-(\omega_x^2 + \omega_z^2)r_y + (\omega_y\omega_z - \alpha_x)r_z + (\alpha_y + \omega_x\omega_y)r_x\right]\hat{j} \\ &+ \left[(\alpha_x + \omega_y\omega_z)r_y - (\omega_x^2 + \omega_y^2)r_z + (\omega_x\omega_y - \alpha_y)r_x\right]\hat{k}\end{aligned} \quad , \qquad (3.12)$$

where r_X, r_Y, and r_Z, are the components of the vector r from the cg to the accelerometer location at point P. If the sensitive axis of the accelerometer is oriented along the z-axis, and the accelerometer has low parasitic sensitivity to motion in the other orthogonal axes, then the terms in the first two brackets of equation (3.12) can be ignored. The terms in the third bracket must be examined carefully by substituting into the terms the "worst case" values of the angular acceleration and the angular velocity that may occur. If the result obtained by taking the sum of all the bracketed terms is significantly above the noise floor of the sensor, then the terms cannot be ignored.

There was one type of inertial sensor used in the control systems described in this dissertation. This accelerometer is a proof-mass type accelerometer from Sunstrand Corporation. The specific accelerometer used is discussed in the next section with reference to the design issues highlighted in this section and some comparisons are given regarding the noise floor of the accelerometer used as compared to other types of inertial sensors available.

3.1.2 Sunstrand QA-2000 Accelerometer

The Sunstrand QA-2000 transducer is an inertial, linear accelerometer which functions on an electromagnetic principle. Figure 3.7 provides an illustration of the operating principle behind this proof-mass accelerometer. The inertial mass is composed of a magnetized material, and thus

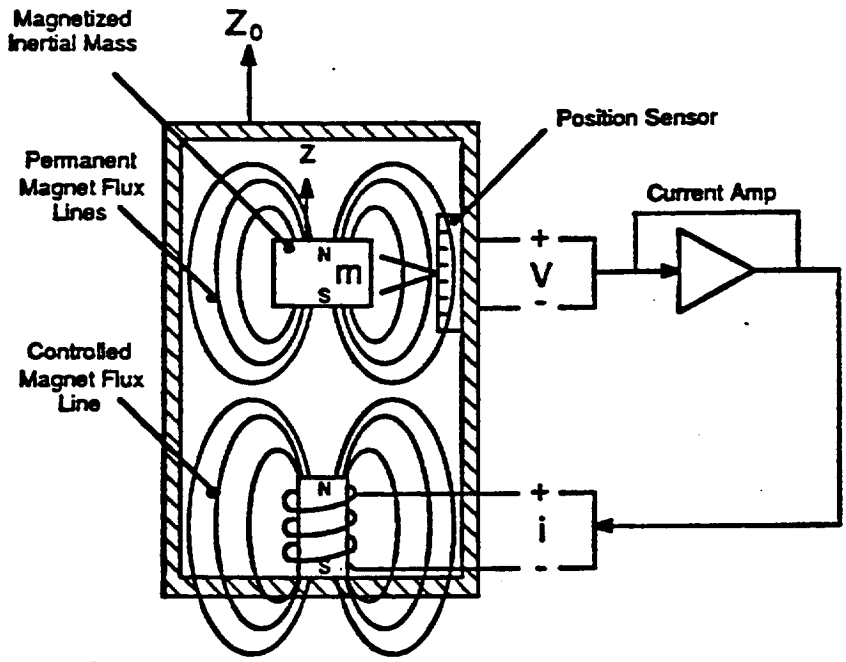

Figure 3.7: Conceptual illustration of QA-2000 operating principle.

produces a magnetic field. An opposing magnetic field, controlled by varying the current in a coil, supports the inertial mass due to the repulsive force between the permanent and controlled magnetic fields. The current in the coil is continuously adjusted in a closed loop, such that the repulsive magnetic force restores the relative displacement to a null reading. By altering the current in the coil, the inertial mass is held fixed with respect to the sensor case (to within some tolerance). Therefore, the current required to maintain this condition, is at all times proportional to the acceleration of the case. The voltage drop across a resistor in the coil circuit is used to determine the voltage signal, which is proportional to the current by Ohm's law.

The frequency response of this sensor type was generated as defined in section 3.1.1.2 and is shown in Figure 3.8. The peaks at high frequencies were caused by the test apparatus, and not by the sensor itself. The phase loss however, is caused by the sensor, but is not limiting since the controller bandwidth will be rolled-off. The noise floor of the QA-2000 was also measured as described in section 3.1.1.3 over a limited frequency band. The measured noise floor is presented in Figure 3.9.

The performance goal for these vibration isolation systems in orbit is presented in Figure 3.10. It is desirable to employ a sensor having a noise floor that is at least an order of magnitude below the smallest disturbance to be rejected. Thus, if at some frequency the performance goal is 1 micro-g, then the level of the noise floor should be at most , 0.1 micro-g. This requirement specifies a performance curve for the sensor noise. In Figure 3.10 an orbital isolation platform performance goal, the sensor noise goal, and the noise floors for a variety of inertial sensor is presented on the same plot for comparison. As shown in Figure 3.10 the Sunstrand QA-2000 exhibits an acceptable noise floor.

3.1.3 Bently Eddy Current Displacement Probes

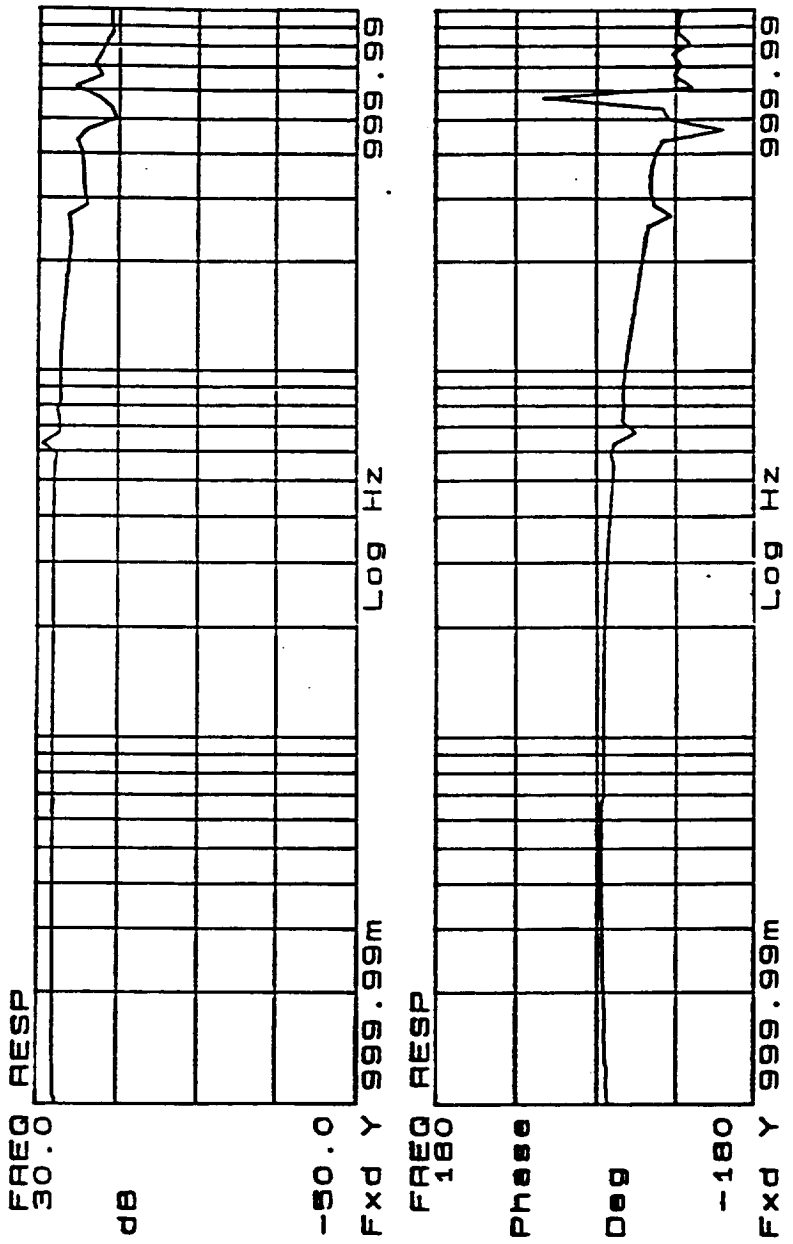

Figure 3.8: Bode plots of the QA-2000 frequency response.

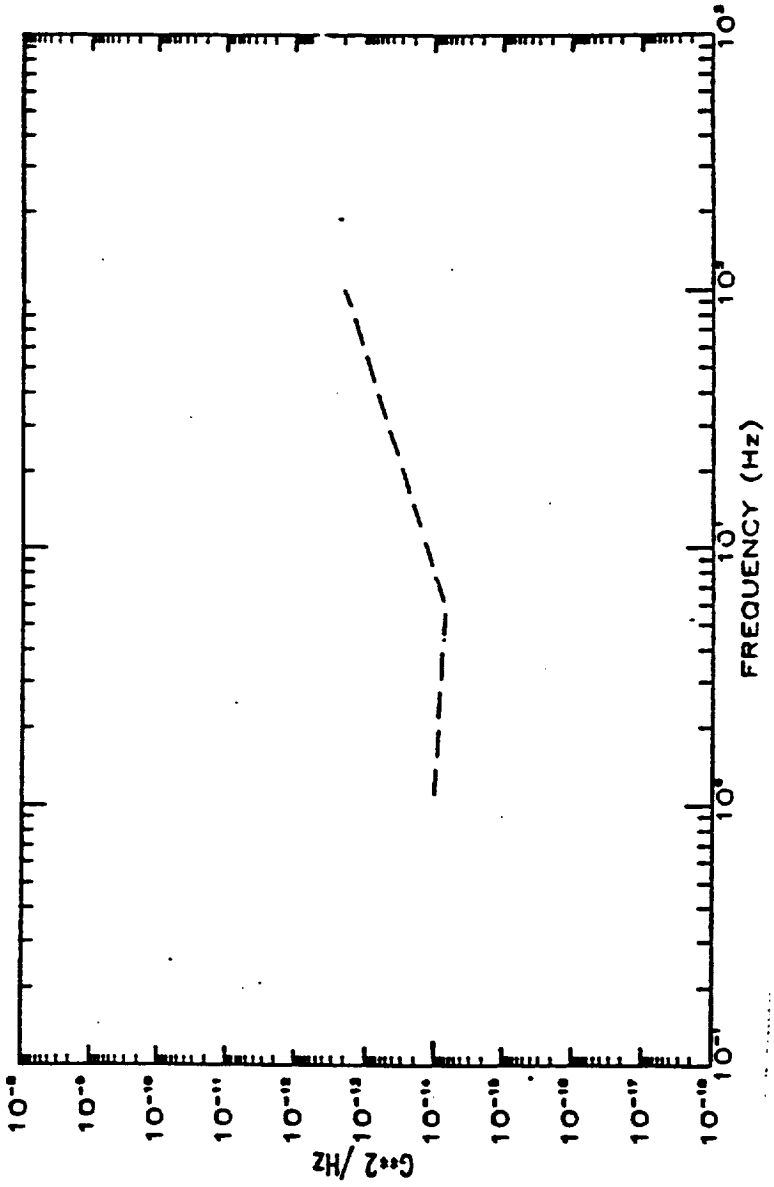

Figure 3.9: Noise floor of the Sunstrand QA-2000 accelerometer.

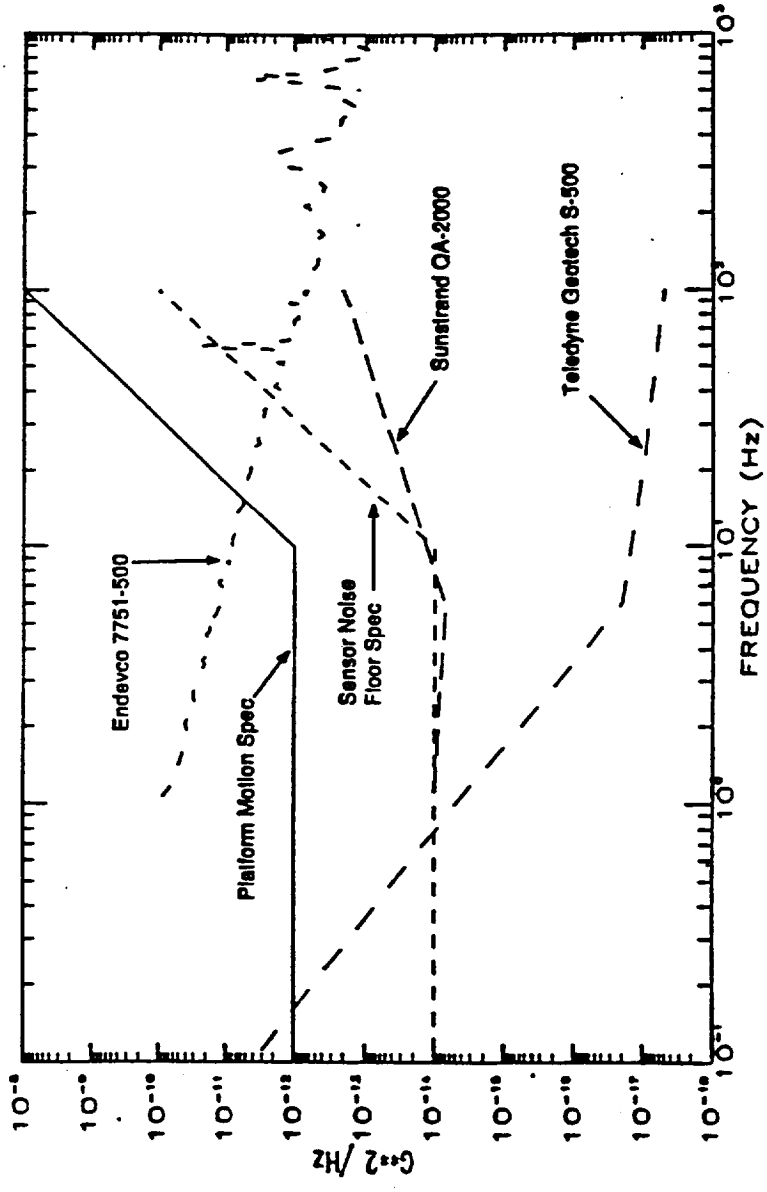

Figure 3.10: Comparison of sensor noise floors with system specification.

The Bently proximity probe is a non-inertial transducer which functions on an eddy current principle. The proximitor, powered by a -18 Vdc to -24Vdc supply voltage, generates a radio frequency (rf) output voltage which is applied through the extension cable and probe lead to the probe tip coil. The coil radiates rf energy in the form of an alternating magnetic field that induces eddy currents in an observed conductive specimen. The eddy currents increase in amplitude as the observed surface approaches the probe tip, thus causing a power loss because of a back electro-motive force (emf) in the probe/proximitor system and a corresponding decrease in the rf voltage of the probe coil. As the conductive material moves closer to the probe tip, the voltage decreases proportionally to the displacement. The proximitor measures the peak amplitude of the rf voltage to provide a proportional dc output voltage that is applied to associated instrumentation. If the gap remains constant, the output voltage remains constant; if the gap varies as a function of time, the output voltage changes accordingly. Therefore, the eddy current proximitor device is a dc transducer whose frequency response is flat limited only by the demodulation electronics. The device is not electromechanical in nature as the inertial transducer mentioned previously which has a specific bandwidth due to its physical response to the motion of its housing. This proximity sensor measures the change in rf amplitude due to the generated eddy currents in a conductive material so the frequency response is only limited by the flow of electrons in the material and therefore, is not a limiting factor.

The scale factor or proportionality constant for this proximitor is generated by calibrating the probe voltage with a known displacement from the probe/proximitor thereby giving a voltage output per unit displacement. This proximitor probe has a calibrated range from 50 to 550 mils and the sensitivity of the transducer is approximately 20 mV/mil. Since the active magnetic systems equilibrium position and "dead band" is defined by the relative position sensors, a scale factor or sensitivity had to be measured for each transducer in order to normalize the state control vectors and

a noise floor measurement had to be made for performance predictions and system noise floor performance requirements.

Unlike the QA-2000 proof-mass accelerometers, the relative probes had to be calibrated and normalized to each other since individual sensitivities were not available from the manufacturer. The probes were fastened on a fixed mounting and a conductive target was placed on a micrometer stand. Measurements were taken from 0 mm (probe just touching target) to 20 mm in increments of 0.5 mm. These measurements consisted of measuring the output voltage of the transducer and calibrating each transducer with the known sensor target position. These conversion factors for a particular probe-proximitor-cable set were used to normalize the relative sensors to one another. Some different combinations of sets were also measured in order to determine if one part of the proximity sensor system was a primary source of variance in the conversion factors. The results of these calibrations are given in Table 3.1. As seen in Table 3.1, the largest variance between measurements for set 1 through 6 was 0.1 V/in. From remaining measurements establishing a variance with changes in the probe-proximitor-cable sets it was demonstrated that a change in proximitor electronics could give a scale factor variance of 0.18 V/in.

Set	Probe	Proximitor	Cable	Sen. (V/in.)
1	JUNR409117 (1)	APRR112981 (1)	1	19.57
2	JUNR409115 (2)	FEBR104309 (2)	2	19.27
3	JUNR409119 (3)	FEBR104310 (3)	3	19.07
4	JUNR409116 (4)	APRR112983 (4)	4	19.09
5	JUNR409118 (5)	FEBR104311 (5)	5	19.31
6	JUNR409114 (6)	FEBR104302 (6)	6	19.17

Table 3.1

As in the inertial transducer case, the frequency response and noise floor performance must be measured or known for the relative transducers in order to predict the impact on system performance, and to insure that the performance goals of the actively controlled platform are met. A

frequency response of 0 to 600,000 rpm (0 to 36 MHz) is quoted from the proximity probes specifications and some frequency response curves are given in Figure 3.11 giving a number of curves as functions of different capacitive loads resulting from various cable lengths. The curves are plotted from 360 kHz in dB's showing this sensors flat response. As shown from these curves the frequency response is more than adequate for this application.

The noise floor performance is important for the relative sensor because it will give a performance limit for the active control system on the resolution of the displacement and equilibrium position of the platform. This transducer's theory of operation is dictated by the amplitude modulation of an rf signal, due to the magnitude of the generated eddy currents proportionality to a conductive specimens distance from this rf source. Hence, the noise floor performance is limited by the voltage source generating the carrier coils rf signal. Therefore, the voltage sources stability dictates the amplitude stability of the probe which is independent of the conductive specimen's position or displacement. Since all six relative displacement probes were powered by the same -18 Vdc supply this voltage source's power spectral density was measured. The power spectral density function as defined in section 3.1.1.1, for a stationary record (stationary in time), represents the rate of change of the mean square value with frequency giving a measure of the noise floor amplitude as a function of frequency. This power spectrum shown in Figure 3.12 was plotted as the rms voltage verses frequency for a bandwidth from 0.1 to 100 Hz. This measurement gives the noise floor for each probe, in displacement units, from each probe-proximitor-cable sensitivity factor listed in Table 3.1. A discussion of this noise floors propagation into acceleration performance will be discussed in section 3.1.6.

3.1.4 Signal Conditioning

3.1.4.1 Inertial Signal Conditioning Circuits

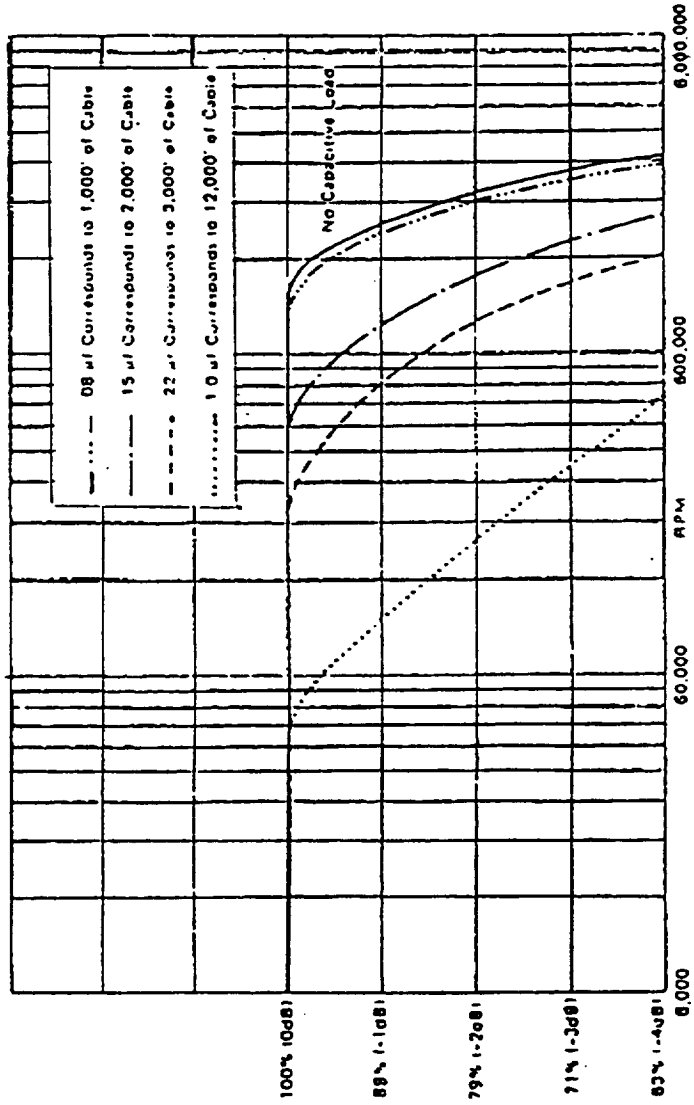

Figure 3.11: Frequency response of Bently relative sensor.

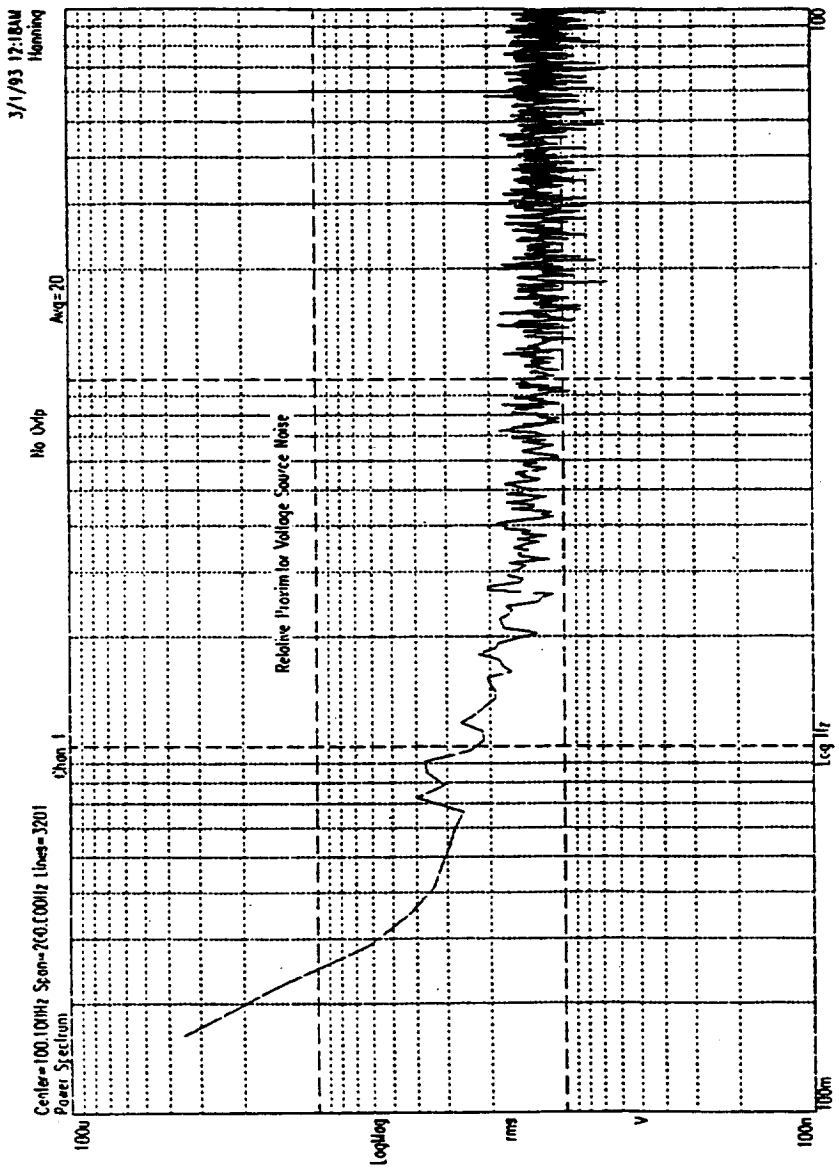

Figure 3.12: Eddy current probes voltage source noise floor measurement.

In the interest of optimizing sensor range and linearity, only a relatively small portion of the full scale range of the accelerometer will be utilized. The closed-loop operation provides this capability from the QA-2000 since the torquer coil, which applies the control force to the proof mass, maintains the proof mass at the reference position while in the presence of an input force. Therefore, the measure of the torquer current provides a measure of the input force. Thus, a load resistor inserted between the current output and ground allows for the selection of the sensor's full scale range and provides an output voltage proportional to input force.

This output load resistor (connection between the signal out and return pins) can range from a short, giving the current proportional to g, to over 10 megaohms without affecting performance of the transducer. Referencing the signal to ground through a smaller load resistor permits wider g ranges, while larger resistance loads permit sensing of smaller input forces over narrower ranges (higher voltage scale factors). In practice, the selection of the load resistor can be calculated assuming the largest dynamic acceleration range to be sensed and multiplying this range by the accelerometer current scale factor, $K_{I(A)}$. This product will be in units of milli-amperes and if one calls this result I, the maximum allowable load resistance R_{max} (torquer resistance plus reference load resistance to ground) can be calculated by the following relationship:

$$R_{max} = \frac{(V_{ref} - 2.5)}{I} - R_{torq}, \tag{3.13}$$

where V_{ref} is the voltage source for the transducer, and R_{torq} is the sensors torquer coil resistance, 0.146 kΩ. From this relationship, equation (3.13) and from a desired scale factor in volts/g, $K_{(V)}$, one can compare the desired load resistance for the transducer circuit with the maximum load value for an assumed dynamic acceleration range.

The six accelerometers used for the determination of the six inertial degrees of freedom of the support structure exhibited approximately the same current scale factor, so the above calculations only had to be completed once. The value, $K_{I(A)} = 1.33$ mA/g, along with the desired design g range

of ±1 g provides the needed values for determining the load resistance for a voltage scale factor used in the inertial signal conditioning circuits. The following calculations support the value of a 7.5 kΩ resistor chosen for the inertial bandpass circuit design giving an approximate 10 V/g sensitivity.

(1) $$I = K_{I(A)} \bullet g(range)$$

$$I = 1.33mA / g \bullet 1g$$

$$I = 1.33mA$$

(2) $$R_{max} = \frac{(V_{ref} - 2.5)}{I} - R_{torq}$$

$$R_{max} = \frac{(15 - 2.5)V}{1.33mA} - 146\Omega$$

$$R_{max} = 9.25k\Omega$$

(3) Selected $K_{(V)}$ = 10 V/g

(4) $$R_l = K_{(v)} / K_{I(A)}$$

$$R_l = \frac{10V / g}{1.33mA / g}$$

$$R_l = 7.692k\Omega \cong 7.5k\Omega$$

Therefore, selecting the load resistor as R_l = 7.5kΩ, for all six accelerometers, a range of ±1.0 g was obtained resulting in a 10 V/g voltage scale factor.

Unlike most quartz-based accelerometers, the QA-2000 provides a dc measure of input force. Thus, in the presence of a gravity field or a large residual acceleration, the sensor responds to the force opposing gravity, e.g., the force resulting from the surface upon which the sensor is mounted.

Here, this force acts on the accelerometer case and not on the proof mass, thereby causing the proof mass to deflect from the reference position. As described previously, the output voltage required to null the displacement of the proof-mass will be a direct measure of the input acceleration. Therefore, large bias voltages are inherent in the signals generated by this sensor and a high-pass filter is needed for the closed loop inertial stabilization of the isolation system as well as the low-pass filter needed to roll off the accelerometer signals because of phase loss and electrical noise. Therefore, a bandpass filter is dictated which must be designed with the closed-loop performance requirements.

This bandpass filter was designed by cascading a four pole active high and low pass filter with a programmable low noise operational amplifier giving a gain adjustment capability to the inertial signal conditioning circuit. These active filters were designed as four pole Bessel filters. Bessel filters give good phase characteristics, i.e., constant signal delay in the passband. Which is very desirable where performance in the time domain is important as in this application which is for a near real time active control system. The amplitude response of a filter, though important, is not the critical issue for the design of this inertial signal conditioning circuit. A filter which is characterized by a flat amplitude response may have large phase shifts. The result is that a signal in the passband will suffer distortion of its waveform. Since in this application the shape of the waveform is very important, a linear-phase filter (or constant-time-delay filter) is extremely desirable. A filter whose phase shift varies linearly with frequency is equivalent to a constant time delay for signals within the passband, i.e., the waveform is not distorted. Therefore, the Bessel filter was chosen having maximally flat-time delay within its passband [18].

The specific bandpass filter design which is used for all six inertial feedforward channels is illustrated in Figure 3.13. The bandpass filter was designed with a "flat" transmissibility or frequency response with the high pass part of the bandpass having a cut off frequency of about 0.03 Hz and the low pass cut off set at about 30 Hz. The 30 Hz cut off frequency for the bandpass filter was set because the active isolation system, being designed as a dynamically soft system, will act as a low

pass filter and attenuate the higher frequencies. In addition, the payload did not need to be inertially controlled at higher frequencies to meet acceleration requirements.

The inertial signal conditioning circuit has three sections. The first being a four-pole high-pass Bessel filter with the high-pass cut-off frequency set at 0.03 Hz, as mentioned earlier. The second stage having an instrumentation amplifier using a digitally controlled programmable gain Burr-Brown PGA-2000 (Programmable Gain Amplifier). The programmable gain was dip switch selectable from 1, 10, 100, and 1000 times gain on the circuit board for each of the six accelerometer channels. The third stage was a four-pole low-pass Bessel filter with a cut-off frequency of 30 Hz. From Figure 3.13 the inertial circuit configuration also allowed for a jumper selectable by-pass around the active four-pole high-pass filter. This by-pass was included as an option because of the very slow response of the front-end high-pass active filter. If a large shock acceleration was introduced into the system it would take seconds to decay, causing the inertial control to react with excessive displacement drift. The by-pass included a simple RC network (R = 1 MΩ, C = 4.7 μF). With this by-pass selected, the front-end of the inertial circuit has the high-pass characteristic as follows:

$$\left|\frac{V_{out}}{V_{in}}\right| = \frac{2\pi fRC}{\sqrt{1+(2\pi fRC)^2}}. \tag{3.14}$$

The dc gain for this circuit assuming the instrumentation amplifier stage had a gain selection of one, is calculated to be 3.8. Appendix E has the detailed design and a list of the circuit component values and parameters.

Following the completion of the design and assembly of the inertial circuits, a validation of the circuit performance and the individual circuit gains had to be measured in order to normalize the inertial control states to include the sensitivity factors for each inertial transducer/signal conditioning channel set. The individual inertial circuits and a Hewlet Packard 3566A signal analyzer were configured for taking data for transfer function determination. As shown in Figure 3.14, ± 15V were

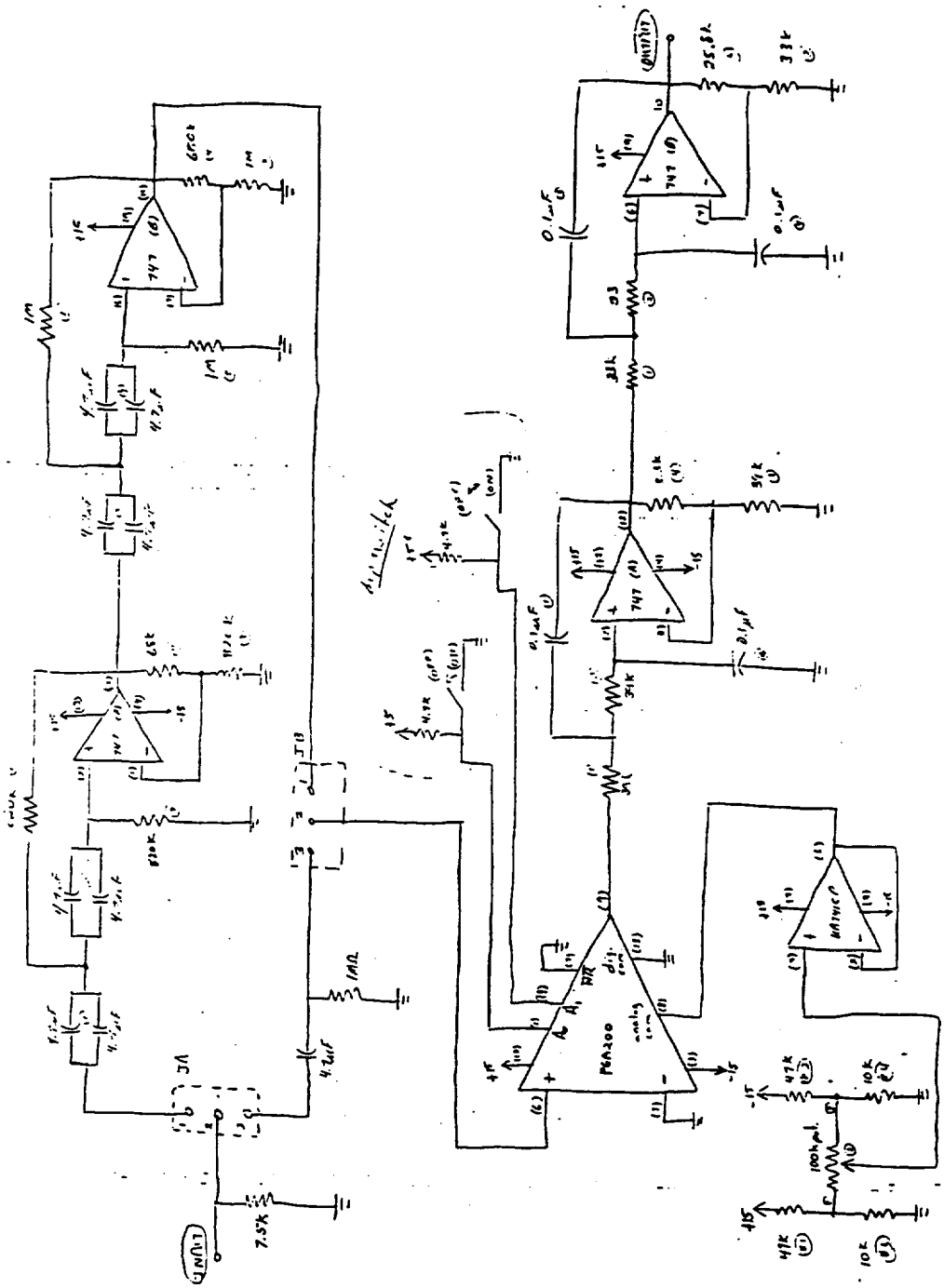

Figure 3.13: Inertial sensors signal conditioning circuit.

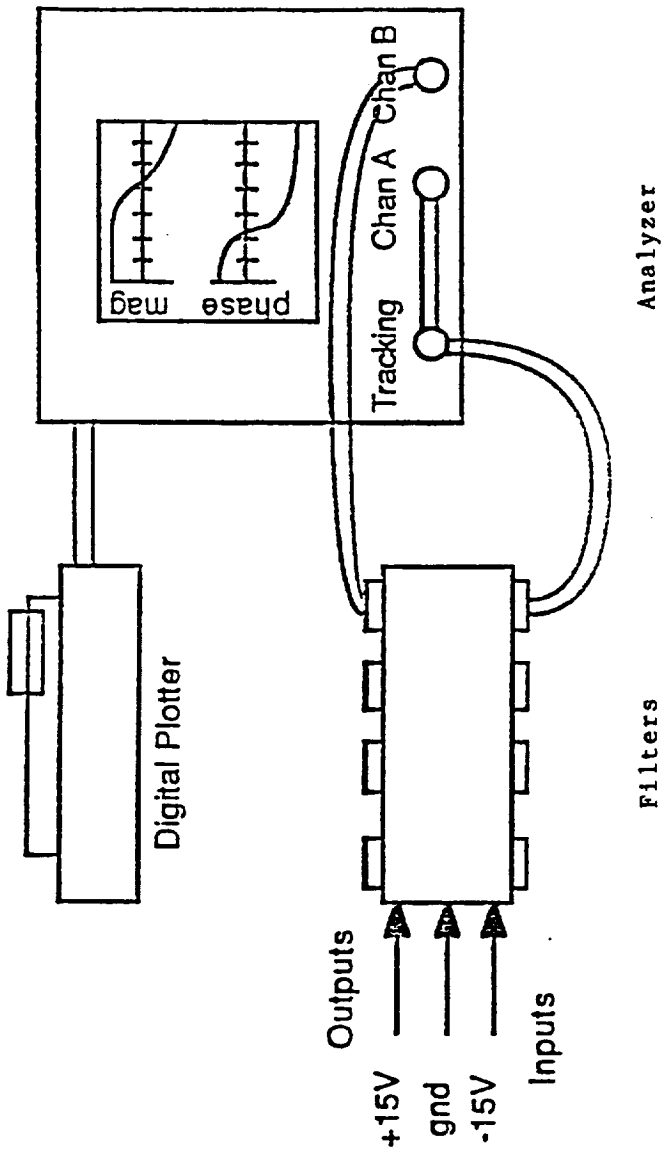

Figure 3.14: Filter transfer function determination.

applied to the individual filters and the filter output was connected to a channel of the analyzer. The tracking signal of the analyzer, which generates random noise, was connected to the filter input and connected to an input channel of the analyzer. The high-pass filter was not analyzed using the spectrum analyzer due to the long measurement time required for enough averages to determine a smooth transfer function. The AC coupling high-pass circuit was tested using an oscilloscope to determine the AC coupling ability of the circuit, as well as the instrumentation amplifiers trimming capability of any dc voltage offsets from internal electronics as well as the transducers bias signal measurement. The transfer function was taken with ten averages in the frequency band from 0.1 to 100 Hz. Table 3.2 gives the gain settings for a ten times gain select on the instrumentation amplifiers for each inertial channel. These values with the individual inertial transducers sensitivities were used to normalize the inertial control states for the digital control algorithm.

Inertial Conditioning Circuit	10 Times Gain Setting	1 Times Gain Setting
Vertical Location 1 Channel 1	33.4309	3.35722
Vertical Location 2 Channel 2	33.9174	3.47602
Vertical Location 3 Channel 3	33.4180	3.45865
Horiz. Location 1 Channel 4	31.8346	3.27049
Horiz. Location 2 Channel 5	32.9180	3.60637
Horiz. Location 3 Channel 6	34.8583	3.34386

Table 3.2

3.1.4.2 Relative Signal Conditioning Circuits

The Bently proximitor probes used for the stable closed-loop control of the suspended mass have a linear range from 1.27 mm to 13.97 mm (0.05 to 0.55 in). The calibrated probes gave a scale factor for each probe for control channel normalization of each probe-proximitor-cable set as described in section 3.1.3. These relative transducers give a voltage output proportional to displacement from a conductive target where the maximum voltage is equal to the proximitor supply

voltage source and a minimum at zero gap distance (probe touching conductive target). Since the platform controller is designed to suspend the mass, i.e., the experimental payload, around some defined equilibrium condition, the relative displacement output voltage needs to be referenced to a relative motion around this equilibrium position.

In order to arrive at such an equilibrium state the relative controller functions as an error signal around the equilibrium condition defined by a relative displacement output of zero, i.e., no deviation from a prescribed nominal equilibrium gap distance. This requirement dictates the relative conditioning circuits to have bucking voltage front-ends forcing the transducer outputs to have control voltages about zero. The relative control signals were also filtered at the higher frequencies to roll-off the control of the magnetic circuits.

The relative displacement conditioning circuits consisted of two parts. The first was a summing circuit which acted as the bucking voltage stage to set the equilibrium position of the platform. The second part of the circuit was a two pole low-pass Bessel filter with a cut off frequency set at 35 Hz. The output was configured to be jumper selectable between the filter output or the summer output, (bypassing the filter). This allowed the relative control signals to have a much higher bandwidth, i.e., limited only by the digital loop speed, and allowing the control signals to be rolled off and therefore limiting the noise influencing the controllable power supplies which control the magnetic actuators incremental control current.

The two pole low-pass Bessel filter was chosen because of its phase characteristics: a linear phase response, i.e., a constant time delay in the passband, as discussed in the inertial signal conditioning section. Figure 3.15 is the circuit layout for the relative displacement transducers showing the front-end summing circuit followed by a two pole low-pass active Bessel filter. As was done for the inertial conditioning circuits, a validation of the circuit performance and the individual circuit gains were determined in order to normalize the transducer-conditioning circuit pairs to each

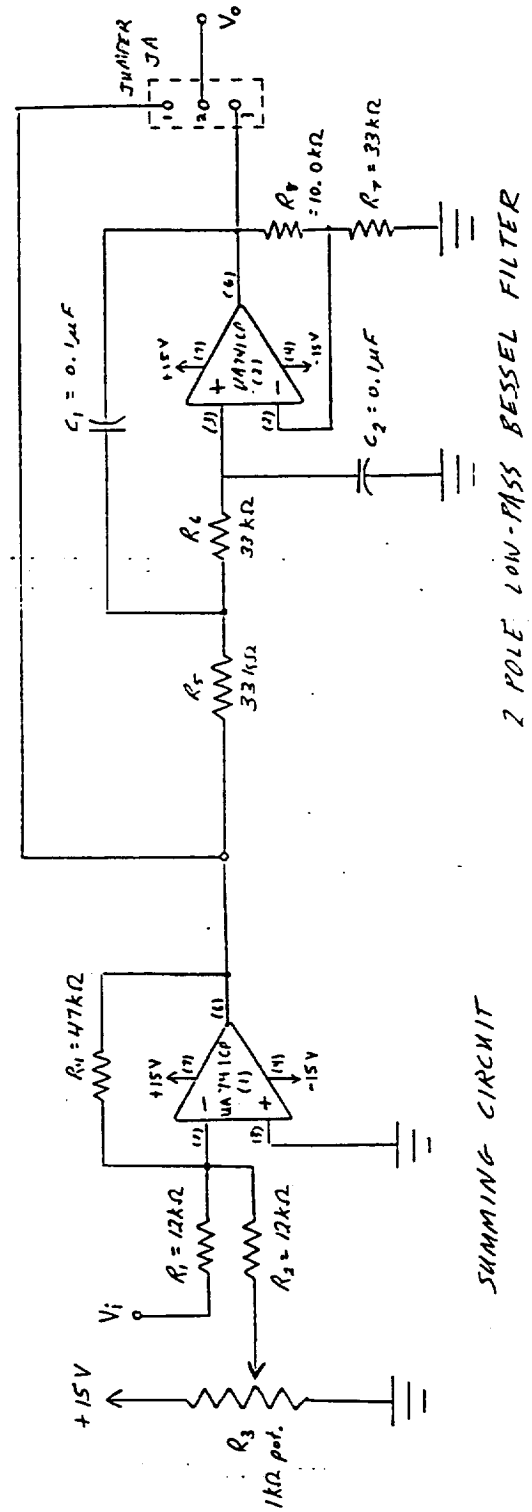

Figure 3.15: Relative sensor conditioning circuit.

other. Transfer functions were taken for each circuit as described in section 3.1.4.1. Table 3.3 gives the gain values for the six relative conditioning circuit channels.

Relative Conditioning Circuits	Circuit Channel Gains
Vertical Pos. Sensor Location 1 (Sen. 1)	5.14348
Vertical Pos. Sensor Location 2 (Sen. 2)	5.48857
Vertical Pos. Sensor Location 3 (Sen. 3)	5.20922
Horizontal Pos. Sensor Location 1 (Sen. 6)	5.21621
Horizontal Pos. Sensor Location 2 (Sen. 4)	5.22146
Horizontal Pos. Sensor Location 3 (Sen. 5)	5.18666

Table 3.3

3.1.5 Sensor Placement

The number of degrees of freedom to be controlled, or control states, of the isolated platform were three translational and three rotational motions. These degrees of freedom were defined previously as the three dimensional rigid body motions of the controlled platform. As discussed previously inertial and non-inertial measurements were utilized to demonstrate the active relative feedback and inertial feedforward cancellation of base induced disturbances. The accelerometer transducers were placed to sense the inertial rigid body motion of the support structure while the relative proximity sensors were placed to sense the relative motion between the controlled platform and the support structure.

As dictated by the need to resolve the six rigid body motions, six equations can be written describing the control input channels. Therefore, six relative and inertial sensors must be poled in order to derive the six control states. Once a generic set of algebraic equations are solved these equations can be used for both the relative and inertial sensors since the placement of these transducers were geometrically equivalent.

The geometric placement of the control sensors were the same in function for both the prototype and demonstration hardware configurations. The exact geometrical placement for the relative sensors for both sets of hardware are shown in Figure 3.16 (a) and (b). The inertial transducer placements were located under each actuator pod, for the prototype hardware, and housed above each actuator pod in the Learjet configuration. Figure 3.17 (a) and (b) show the placement of the inertial sensors for both hardware configurations.

In order to derive the control degrees of freedom a generic three dimensional representation of the relative displacement transducers is given in Figure 3.18. This figure shows the proximity sensors output relation to the target displacement with respect to a global or structure fixed x, y, and z coordinate system. The proximitors will be generically numbered therefore, the same equations will be applied to a generic set of inertial sensors.

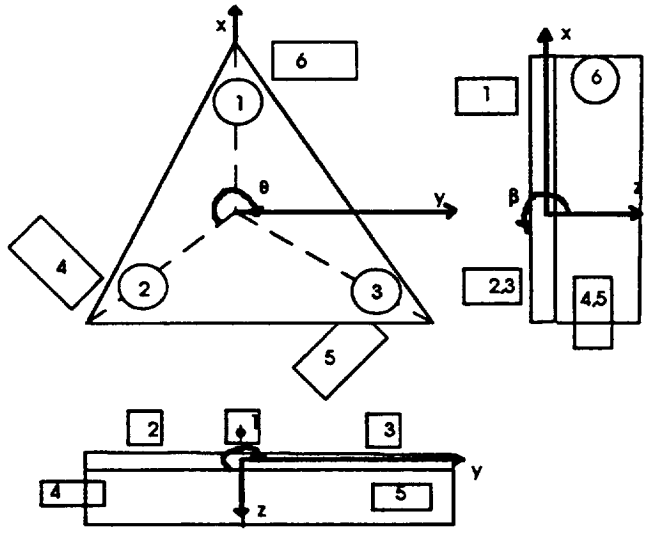

Figure 3.18

From this pictorial representation of the transducer placements the following equations can be resolved for the three translational and rotational displacements of the target body from the global x,

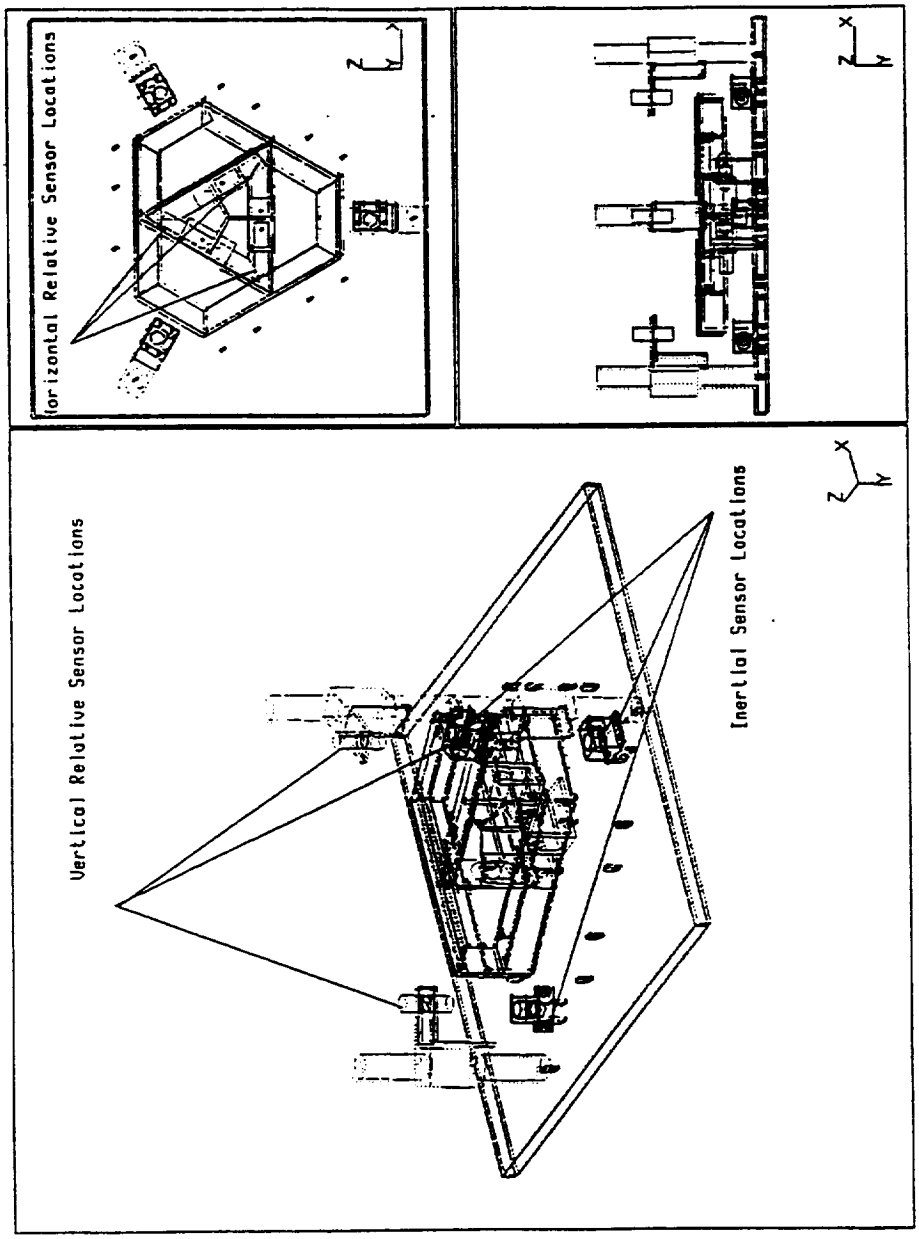

(a) Prototype System Configuration

Figure 3.16: Relative sensor placement locations.

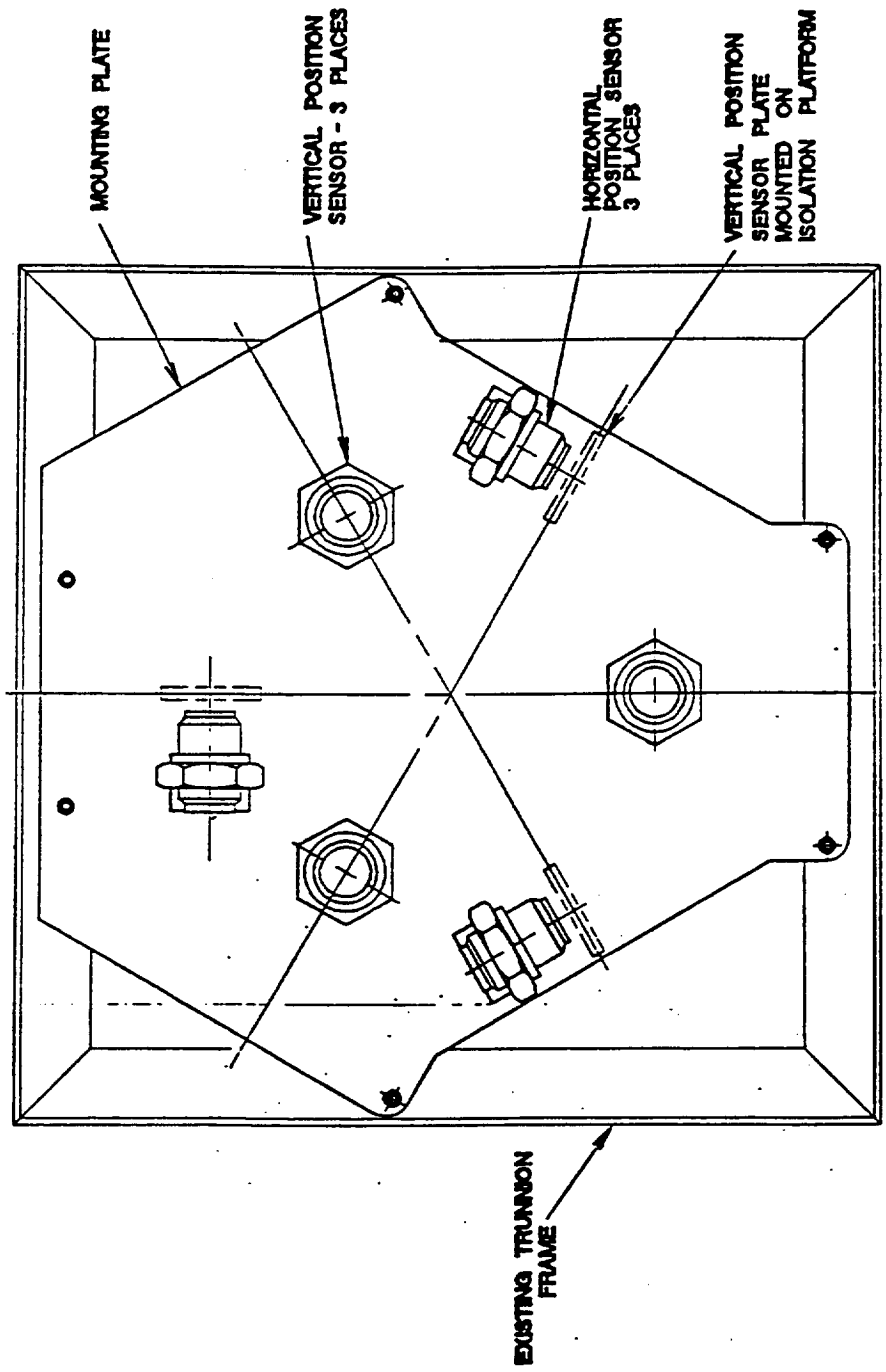

(b) Learjet System Configuration
Figure 3.16: Relative sensor placement locations.

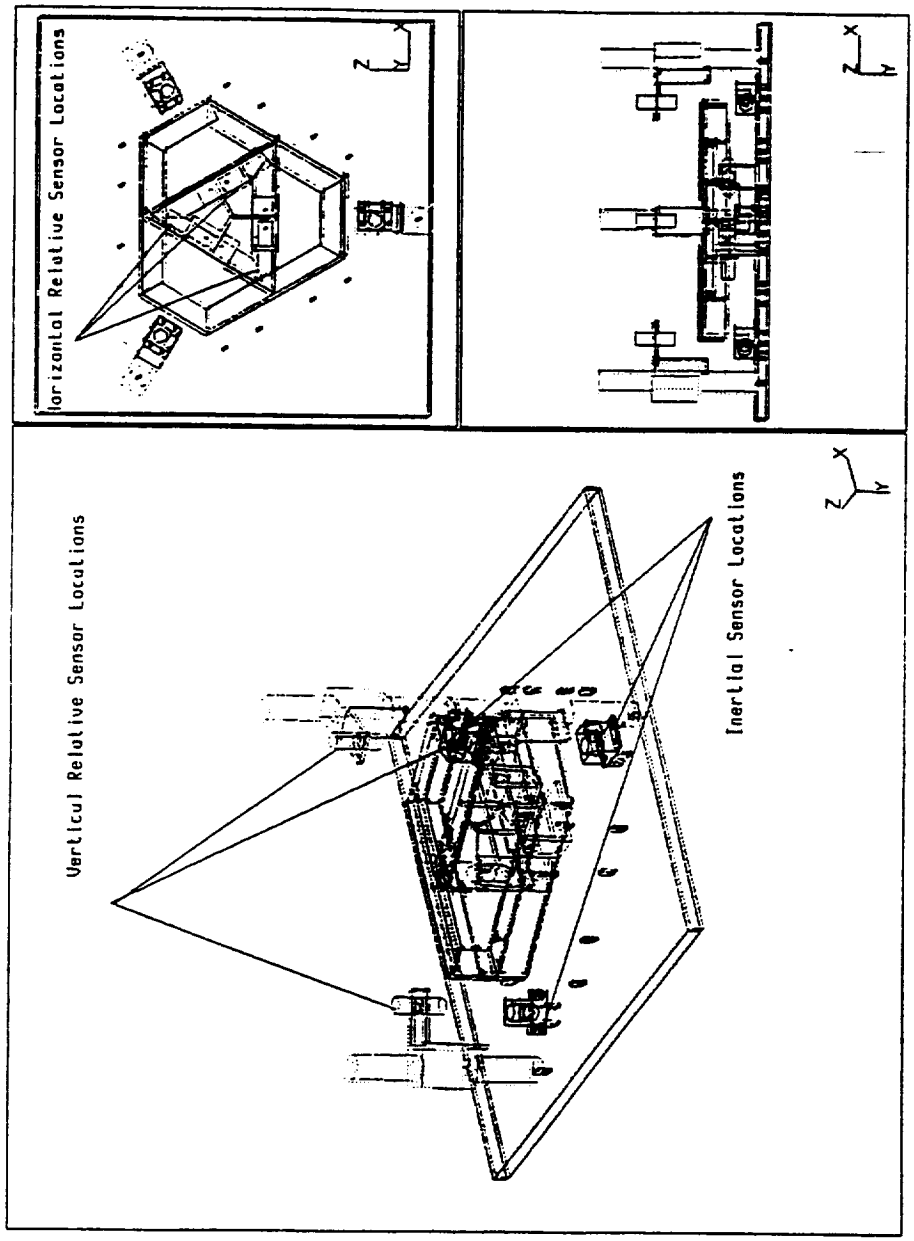

(a) Prototype System Configuration

Figure 3.17: Inertial sensor placement locations.

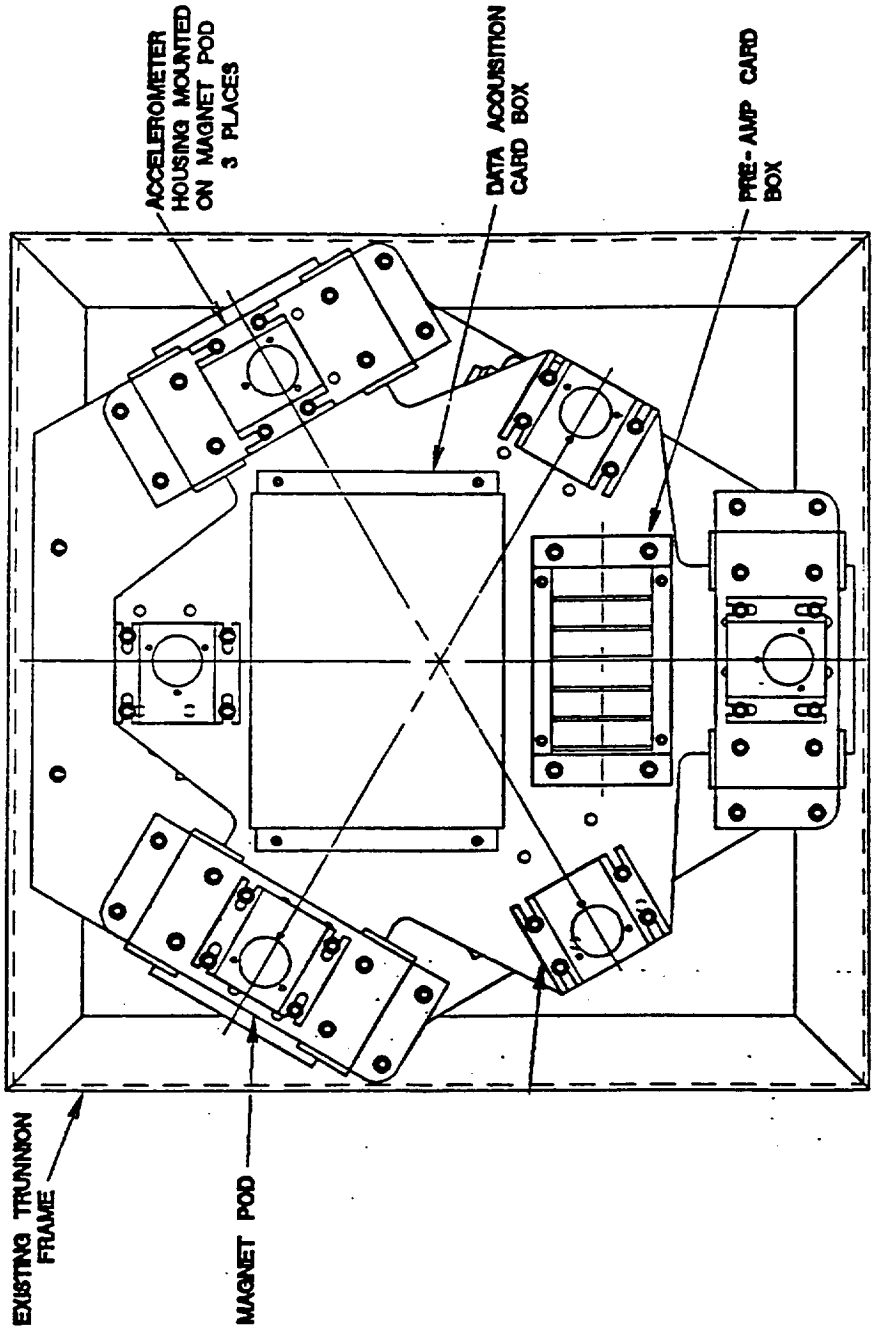

(b) Learjet System Configuration
Figure 3.17: Inertial sensor placement locations.

y, and z coordinate directions. The following equations are the global relative control states for the feedback/feedforward control algorithm:

$$x = \frac{Sensor5 - Sensor4}{2l_h \cos 30^\circ} \tag{3.15}$$

$$y = \left[\frac{Sensor4 + Sensor5}{2} - Sensor6\right]\frac{1}{(1+\cos 60^\circ)l_h} \tag{3.16}$$

$$z = [Sensor1 + Sensor2 + Sensor3]\frac{1}{3l_v} \tag{3.17}$$

$$\theta = [Sensor4 + Sensor5 + Sensor6]\frac{1}{3l_h} \tag{3.18}$$

$$\beta = \left[\frac{2}{3}(Sensor2 + Sensor3) - \frac{4}{3}(Sensor1)\right]\frac{1}{2l_v} \tag{3.19}$$

$$\phi = [Sensor3 - Sensor2]\frac{1}{2l_v \sin 60^\circ}. \tag{3.20}$$

The constants l_v, and l_h represent the distance of the horizontal and vertical transducers centerline to a parallel line through the center of the global vertical and horizontal coordinates. These specific constants are not extremely important in the implementation of the control in that the controller gains will be representative of the constants associated with geometric positioning of the transducers as well as those gains for the respective proportional, derivative, and integral terms in the control equations.

Coupling between the control degrees of freedom was assumed to be negligible for the theoretical development discussion of an active feedforward/feedback control algorithm. However, the placement of the vertical verses horizontal relative transducers will result in cross-axis stiffness and damping terms as well as the inertial transducers cross-axis sensitivity not being representative of input disturbances. The most important of these coupling effects is the relative transducers output caused by coupling between vertical and horizontal motions due to the proximitor sensors target center not being in the same plane. For instance, if their is an angular motion about an x or y axis

and the horizontal proximity sensor targets are not centered on this xy plane the relative transducers would have sensed a net translational motion in the horizontal sensors control plane defined by the target center points. However, this displacement was in actuality a rotation about the x or y axis and should not effect the horizontal control signals. This coupling can be minimized by placing the vertical and horizontal proximitor target center points in the same plane since this will define the controllers global degrees of freedom. In practice it is difficult to realize this. However, if the distance between the horizontally defined center point plane and the vertically defined center point plane is kept at a minimum the coupling between vertical and horizontal degrees of freedom is minimized. The prototype was an active six degree of freedom system however, since the vertical control outputs were significantly greater in magnitude due to the bias currents needed to support the weight of the platform, the horizontal and vertical control was accomplished independently. Data was acquired with an attempt to decouple the horizontal and vertical degrees of freedom which of course posses serious limitations in testing a fully functional six degree of freedom controller. Therefore, if there were significant rotational vertical inputs, the horizontal sensors would have sensed motion due to this vertical/horizontal coupling.

In order to demonstrate the possible coupling due to this effect, assume that there is an angular displacement of the support structure around the x axis, such that the control algorithm inertially cancels this disturbance and the relative motion of the platform verses the support structure causes the platform to go to its geometric extremes, defined by the volumetric constraints on the system, which in the prototype hardware was about 6.35×10^{-3} m (0.25 in.). This would be equivalent to an angular motion of about 2.5×10^{-2} radians. This motion would be detected by the horizontal sensors as a net translational displacement in the y axis of approximately 1.905×10^{-3} m (7.5×10^{-2} in.) because the plane defined by the horizontal sensors center targets was approximately 7.62×10^{-2} m (3 in.) from the vertical sensor defined plane. Therefore, in order to avoid solving the six equations in their coupled form, the relative transducers center targets were placed in the same plane

for the Learjet demonstration hardware, and thus, the horizontal and vertical displacement sensors could be assumed independent.

3.2 Noise Floor Measurements and Performance Limitations

In order to estimate the performance limitations on the closed-loop active isolation system one must appropriately connect the control input channels from the sensor outputs to their respective signal conditioning circuits. The control output signal resolution was one to one with the input digital resolution and the noise floor of the actuator power amplifiers were found to be an order of magnitude lower than the digital resolution. Therefore, the noise floor performance of the system was dominated by the relative control inputs. The inertial feedforward cancellation approach would be limited by the inertial noise floor however, assuming no disturbance in the passband of the controller, the system acceleration performance is dominated by the equilibrium or steady state performance which is defined by the relative displacement control input and digital resolution.

For a prediction of the performance limits for the relative control signals an infinite digital resolution, is assumed so the noise floor is defined by the proximitor/relative signal conditioning channel noise. Using Figure 3.12, where the proximitor voltage source stability was given as a function of frequency, and taking the first probe-proximitor-cable set sensitivity scale factor from Table 3.1 of 19.57 V/in, one arrives at a performance limit as a function of frequency which is shown in Figure 3.19. The noise floor of the relative conditioning circuits was an order of magnitude below that of the probe-proximitor-cable noise, therefore, it does not enter into the controller performance prediction. The transfer function and gain of the signal conditioning circuits do affect the analog noise spectrum, and therefore, must be accounted for. Figure 3.20 shows the sensor channel 1 signal conditioning circuits transfer function illustrating the passband of this low pass filter up to the cut off frequency or -3 dB point at 35 Hz. The gain for this filter in the passband was measured at 1 Hz with

a magnitude of 5.14348. The designed gain setting was calculated to be 4 from the largest allowable displacement of ± 0.25 in. giving a maximum voltage output of ± 5 V from the probe-proximitor. Therefore, in order to utilize the ± 10 V full scale range of the digital converters the bucking part of the circuits had a gain setting of 4. However, the low pass Bessel filter has some dc gain associated with it. This dc gain value was 1.268 giving a designed value of 5.072. The discrepancy from the measured value of 5.14348 at 1 Hz arises from component resistance values in the circuits being no better than 1%. This is why each signal conditioning channel must be analyzed and the actual gain values measured to normalize the control input channels. From Figures 3.19 and 3.20, one can estimate the analog noise floor of the relative measurements to be on the order of 1.0×10^{-8} in. in the passband of the conditioning filter. The noise floor performance is a function of frequency and an estimate of the performance for an infinite resolution digitizer in non-dimensional acceleration units verses frequency can be calculated by taking Figure 3.19 and dividing it by a gain of 5.14, taking the second derivative in the frequency domain of this curve, and dividing by 386.4 in/s^2, thus non-dimensionalizing the curve. This non-dimensional noise floor performance is given in Figure 3.21. This prediction was estimated assuming that the digitizer had an infinite resolution. Of course this is not the case and, in addition to the digital resolution or "dead band" of the digital controller (which will effect the system depending on the proportional, integral, and derivative (PID) terms in the control algorithms and the digital loop speed of the control program), the analog-to-digital (AD) and digital-to-analog (DA) also have some noise floor performance associated with them. Since these boards are tied to the same power bus, the DA card was given a command for a zero output and the DA was connected to a signal analyzer measuring the voltage output noise floor performance of the converter. This noise floor tracked that of the proximitor voltage source, therefore, the noise floor predicted in g's from the proximitor estimate will be representative.

The "dead band" of a control system typically refers to the digital resolution of the control system. One can calculate from a unit scale factor, for some digitized transducer, the resolution of the

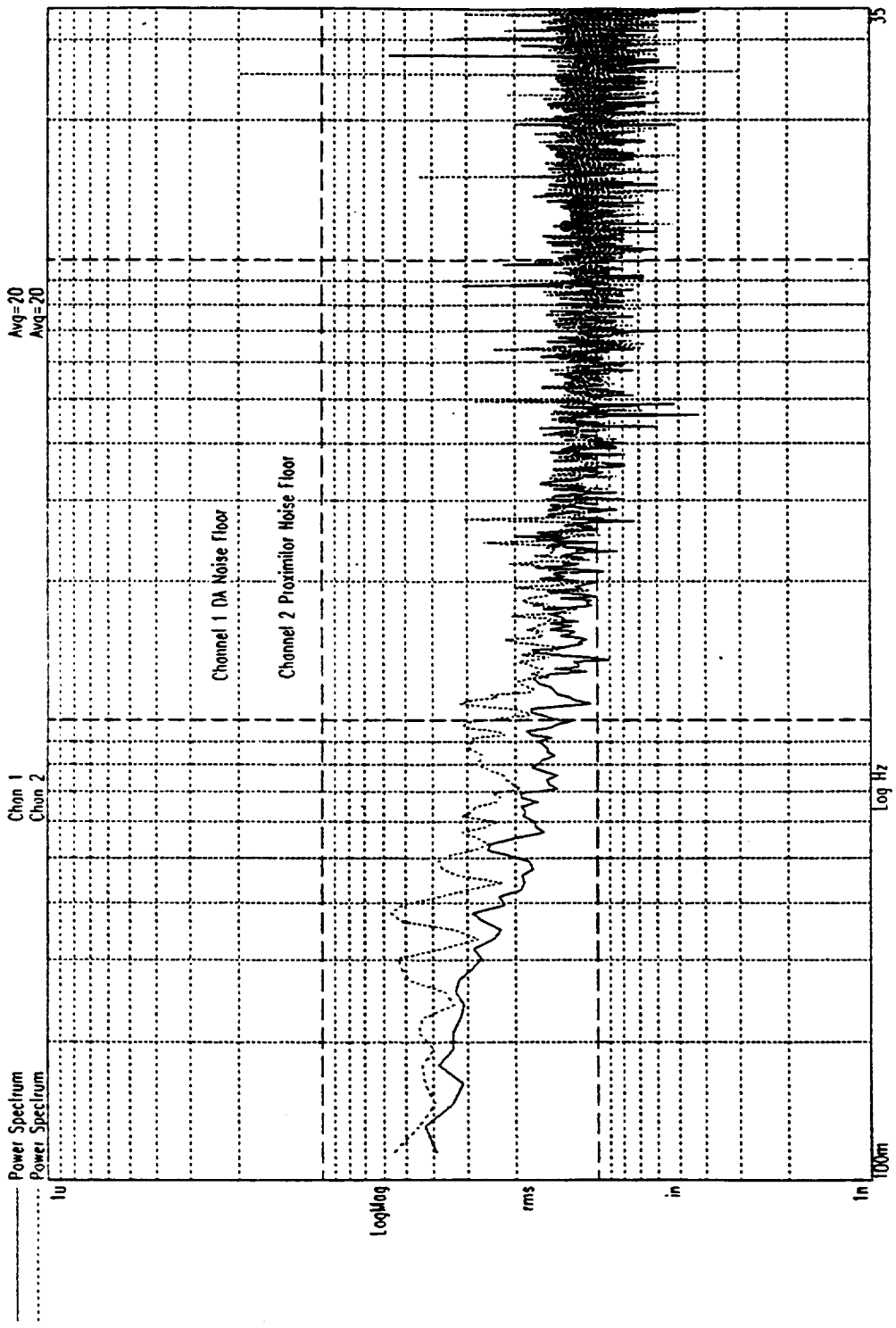

Figure 3.19: Proximitor noise floor due to voltage source stability.

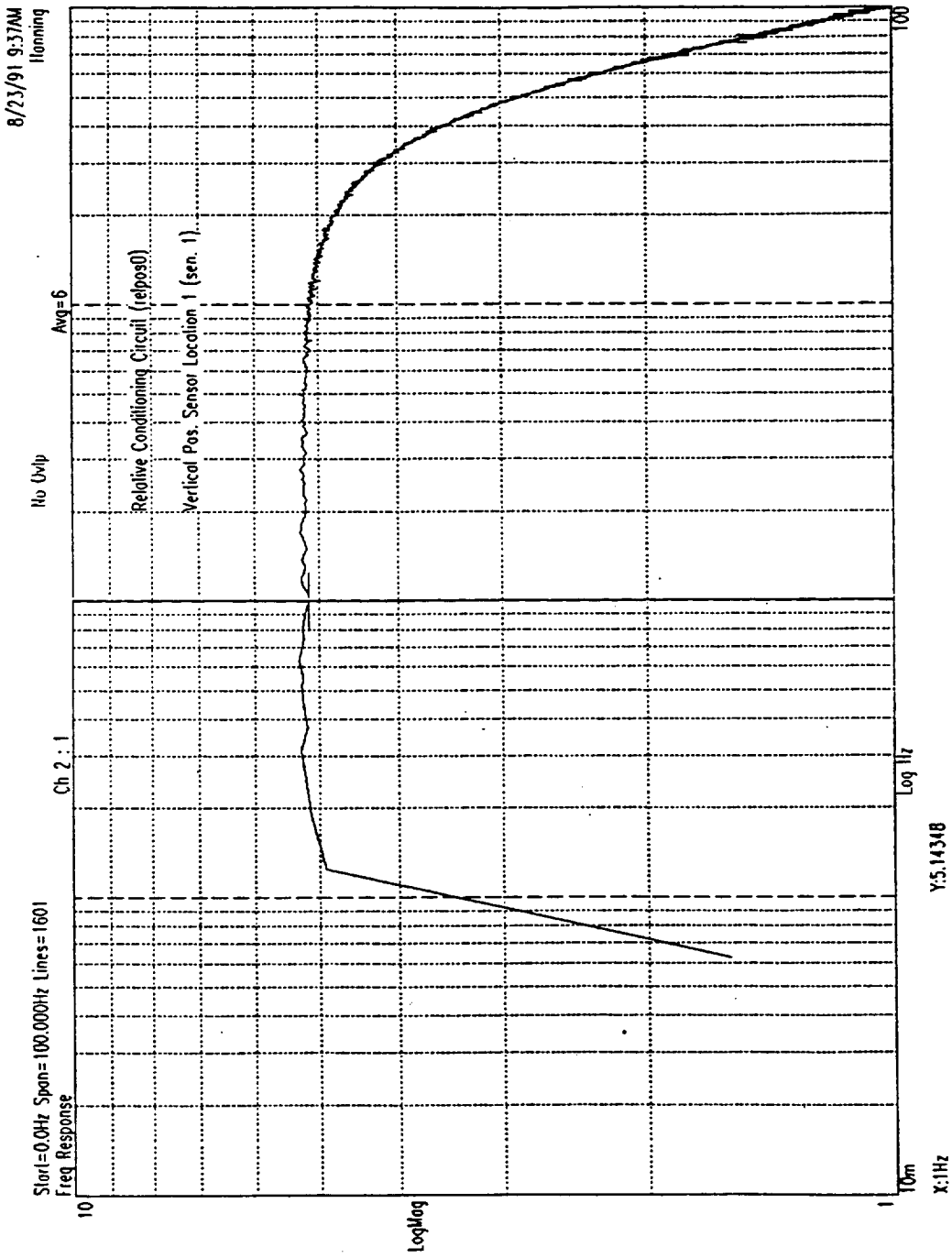

Figure 3.20: Relative signal conditioning circuit frequency response.

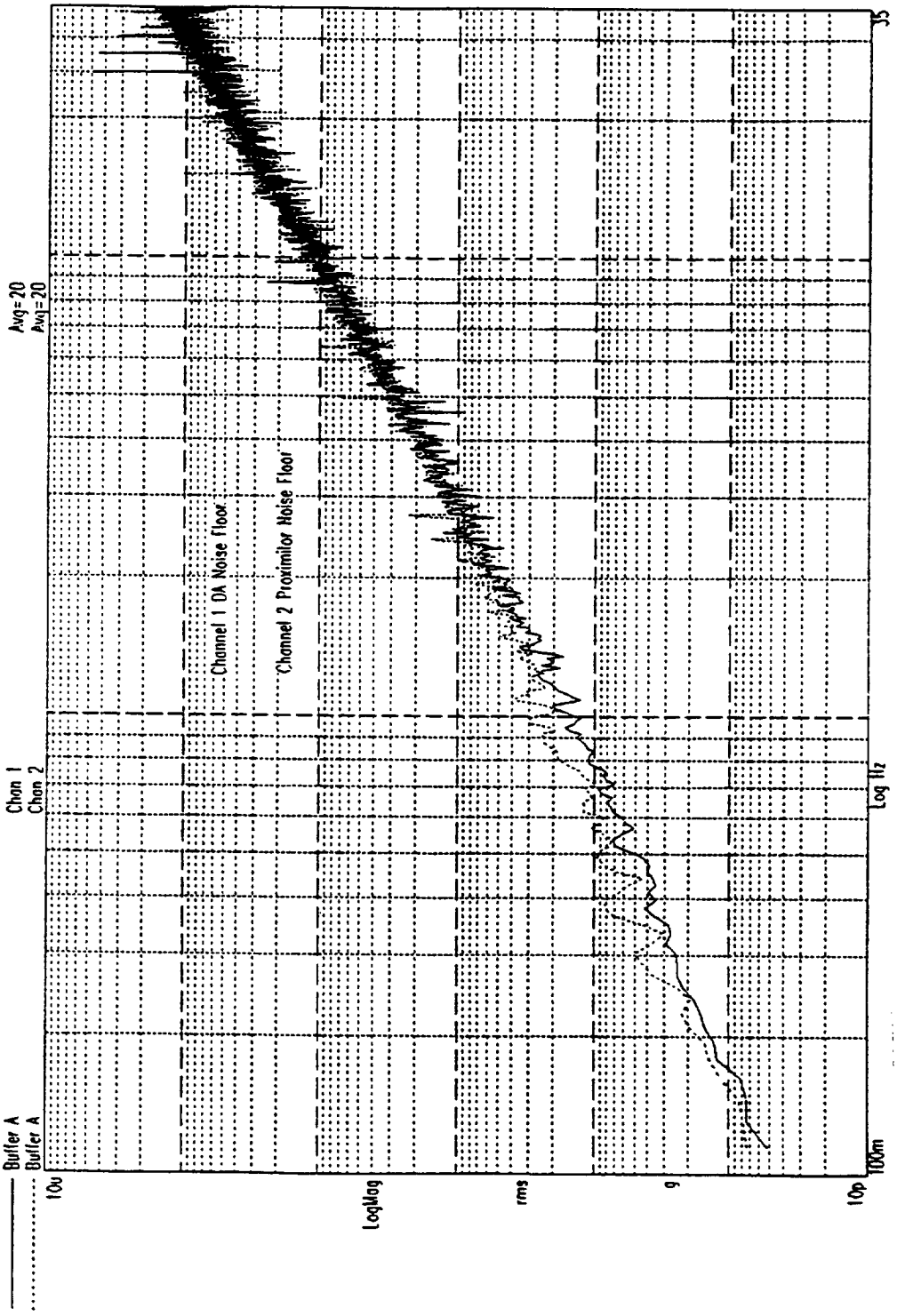

Figure 3.21: Proximitor acceleration noise estimate.

digitized signal depending on the converter and the full scale maximum range of the converted signal. The relative displacement control is realized by six displacement transducers where these sensors are electronically conditioned, as discussed earlier, and digitized by a 12 bit converter and a 16 bit converter for the laboratory and Learjet hardware, respectively. Therefore, for the Learjet hardware, since the scale factor for channel 1 was computed at 19.57 V/in and the conditioning circuit had a gain of 5.14 in the passband, a nominal sensitivity of 100.59 V/in is used to determine the controller with a full scale range of $\pm$ 10 V. Thus, the unit displacement resolution or controller "dead band" is calculated as follows:

$$\varepsilon = \left(\frac{\text{Full Scale Range}}{2^{16} \text{ bit resolution}} \right) \frac{1}{\text{Transducer Sensitivity}}, \tag{3.21}$$

where for this case the system "dead band" was 3.034×10^{-6} in, while for the 12 bit laboratory system the horizontal degrees of freedom had a system sensitivity of 1.526×10^{-5} in.

3.3 Actuator Design and Current Control

The attractive magnetic actuator force is controlled by the introduction of a fluctuating current through the magnetic circuits conductive coil, based on the platforms relative position, velocity, and the inertial states of the support structure. This control current must be commanded by the digital controller output signals produced by the digital-to-analog converters. The control voltage signal controls the current to the magnetic circuits thus, producing control forces on the ferromagnetic platform.

The maximum current requirement and voltage to current sensitivity must be specified based on the operational range of the actuator magnetic circuits. These current ranges are based on the operational environment for the isolation system. Since the high fidelity 16 bit Learjet demonstration hardware was to be tested in an off-loaded condition, the dynamic environment of the low gravity

maneuver dictated the control current range needed for the current power amplifiers. The maximum current output per actuator and the current amplifier control sensitivity were also based on the actuator magnetic circuit design.

The actuator designs for the laboratory and Learjet hardware were different due to their different operating environments. The laboratory system had to contend with a large 1 g bias field in the vertical direction, and therefore, the vertical control magnets were sized accordingly where as the horizontal actuators did not support a large bias force. These actuators were sized to control the horizontal degrees of freedom in the microacceleration range. This section will be dedicated to the design and control of the Learjet demonstration system and will be kept as a general discussion. Therefore, the approach can be utilized for any attractive magnetic system based on the systems operational environment.

Volume constraints will dictate a certain design envelope for an attractive magnetic actuator. However, the most critical design specification for any magnetic actuation device is the peak force requirement for a specific situation or operating environment. Specific to the Learjet, a dynamic and non-stationary loading occurs during a low gravity maneuver imposing strict limitations on system requirements which are not limited on Earth or orbitally based platforms. The maneuver is characterized by three phases, an entry phase, low gravity phase, and an exit phase. These three phases can be characterized primarily by the pitch axis accelerations imposed on any equipment attached to the aircraft structure. The first phase of the trajectory is defined by a high g maneuver pitching the nose of the aircraft to a desired 45^{o} nose high condition prior to the push-over, which begins the low gravity portion of the trajectory. The nominal loading of the aircraft and its contents at this point is typically from 2 to 3 g's. This condition lasts a few seconds where the nose is then pitched forward and the free-fall begins with an initial negative acceleration followed by a 2 to 4 second oscillatory condition while the pilots are stabilizing the control point of the trajectory, "zero g", after which the 10 to 15 second low gravity stabilized portion of the trajectory follows. This

portion of the trajectory is the so called operating environment of the platform. However, since this condition does not simply present itself and has a prior and future history the operational environment for the whole trajectory must be taken into account [22,23].

The maximum force of the pitch or vertical actuators was dictated by the 3 g maximum pull up condition. The volumetric constraints on the actuators forced the designs to be constrained by a magnetic pole face area of $(0.75\ \text{in})^2$ and $(0.5\ \text{in})^2$, for the vertical and horizontal magnets respectively. By determining the maximum force needed, a maximum bias current for each vertical magnet can be calculated from the following magnetic force equation (3.12). (See Appendix B for a detailed discussion of magnetic circuit equations.)

$$F_{max} = \frac{\mu_0 A N^2 i_{max}^2}{h_o^2} \tag{3.22}$$

Using this equation, the magnetic cores pole face area A, and the number of coil turns N available around the magnetic circuit, the maximum bias current was calculated. From the dimension of the vertical actuators a packing area of $0.352\ \text{in}^2$ was calculated where the conductor used for this application had a crossectional area of $0.347 \times 10^{-3}\ \text{in}^2$. Therefore, the total number of coil turns possible, with a 100% packing efficiency, would be the ratio of these two areas. However, since a 100% packing efficiency is not possible the number of maximum coil turns was 750 per magnetic pole giving a respectable 74% packing efficiency from a jumble coil winding process. Therefore, the maximum coil current for one actuator was calculated with a nominal magnetic gap of 0.25 inches from equation (3.22) as $i_{max} = 3.24$ amps. The maximum force per actuator was calculated from the total platform and support electronics mass of 13.61 kg.

Another secondary issue concerning the maximum residual control current which will effect the overall design of the magnetic actuator coil design and its interface to the overall system configuration is the heating of the conductor coil. In a space based application this residual current will be dictated by the bias current linearization and will not be a limiting factor. However, the

laboratory based system needs to account for the heating of the vertical coils due to the large bias currents needed to support the weight of the system as well as the maximum force needed to control the dynamic and steady state operational conditions of the platform. The criteria for the heating of the coil is to insure the coils can reject enough heat so the temperature does not exceed the maximum allowable for the conductor insulation. For the Learjet application the maximum current condition would only last a few seconds therefore, even though this maximum current would overheat the coils the temperature would not exceed specified limits in such a short time.

The power operational amplifier used to command the actuator currents was an APEX PA10. This power amplifier is a high output current operational amplifier designed to drive resistive, inductive and capacitive loads. The features of this power amplifier gave a wide supply range of ± 10 V to ± 50 V with a peak current output of ± 5 amps. Figure 3.22 shows the APEX PA10 power operational amplifier control circuit which was designed to give a full scale range of 4 amps for a 10 volt input range giving the current to voltage sensitivity of 0.4 amps/Volt. The dc supply voltage for the APEX power operational amplifiers was given by two Power-One Model SPM3 ± 24 V @ 5 amp supplies wired in parallel giving a maximum current draw of 10 amps at ±25 volts.

As was done for the signal conditioning circuits and control sensors, the control power amplifiers and the magnetic actuators needed to be tested in order to normalize each control output channel for discrepancies in power amplifier sensitivities and actuator-current-to-force sensitivities between channels to minimize coupling due to non-symmetric actuation of the platform. The actuator power amplifiers were individually tested to determine each channel's current to voltage sensitivity. The individual magnetic circuits were tested by connecting each magnetic pole coil in series and in parallel, the configuration flown on the Learjet was with parallel wired coils, a current source was then provided to the magnetic coil circuits and a Hall effect probe was placed in the center of the pole face with the nominal 0.25 inch gap between the magnetic pole face and the ferromagnetic platform. The sensitivity of the force producing magnetic field in each magnetic circuit was measured verses

the magnetic circuit's current source. The sensitivity of each magnetic actuator was used as the normalization for the control force magnets. Table 3.4 gives the power amplifier circuits sensitivity and the attractive magnetic actuators sensitivity for the three actuation pod locations for the vertical and horizontal magnetic pairs.

Magnetic Circuit Location	Actuator Sensitivity (G/A)	Power Amplifier Sens. (A/V)
Location 1 V1	Series: 1030 Parallel: 500	0.4326
Location 1 V2	Series: 1060 Parallel: 529	0.4486
Location 1 H1	Series: 903 Parallel: 443	0.2874
Location 1 H2	Series: 917 Parallel: 459	0.3382
Location 2 V3	Series: 852 Parallel: 422	0.4375
Location 2 V4	Series: 1000 Parallel: 500	0.4345
Location 2 H3	Series: 944 Parallel: 458	0.3249
Location 2 H4	Series: 879 Parallel: 432	0.3319
Location 3 V5	Series: 943 Parallel: 462	0.4900
Location 3 V6	Series: 1020 Parallel: 494	0.4631
Location 3 H5	Series: 952 Parallel: 467	0.3261
Location 3 H6	Series: 903 Parallel: 447	0.3317

Table 3.4

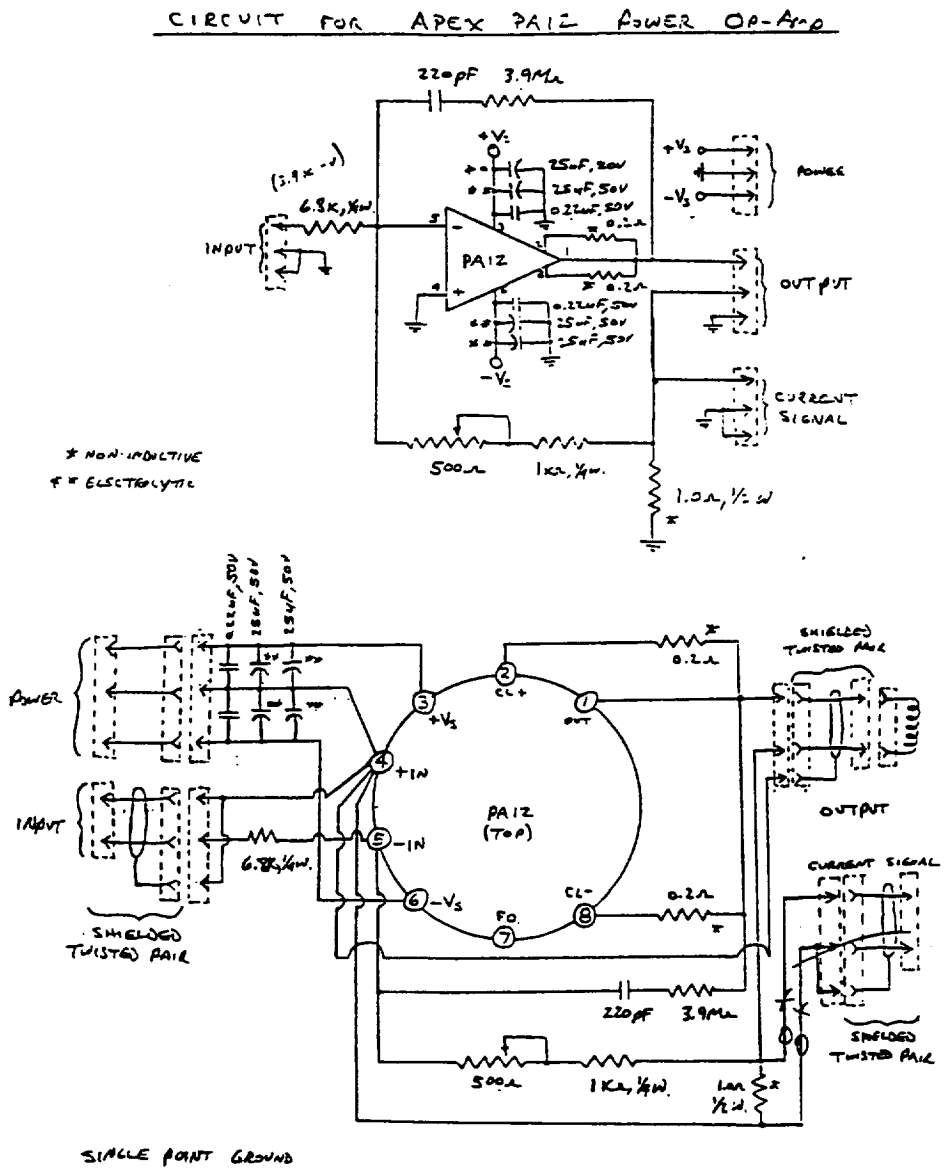

Figure 3.22: Circuit for APEX PA12 power operational amplifier.

IV. Experimental Results

4.1 Laboratory Experimental Results

The development and proof-of-concept or feasibility of active inertial isolation was accomplished using an active magnetically suspended platform. The isolation goal of a generic payload was to develop the capability for the attenuation of sub-Hertz frequency disturbances to microgravity acceleration levels. The ground based testing of six degree of freedom systems, in all dimensions, poses severe limitations in bandwidth and acceleration magnitude limits. The large 1 g bias acceleration in the vertical direction limited the prototype hardware testing to the horizontal plane. However, the prototype system was actively controlled in all dimensions where the vertical control signals were acting primarily as an off-loading device for the performance testing of the horizontal degrees of freedom. The first section in this chapter will describe the experimental setup used to acquire the laboratory performance data for the horizontal three degrees of freedom, two translations and one rotation about a vertical dimension.

4.1.1 Laboratory Experimental Environment

The laboratory hardware was structurally mounted to a large aluminum plate which was bolted to the corner of a pneumatic isolation table. This isolation table was simply used as a support device and the pneumatic legs were not pressurized during the testing of the suspended platform. Initially the pneumatic table was pressurized in order to actuate the support structure of the active platform with a minimum amount of force. However, the table would undergo large vertical rocking motions at 0.6 Hz because the horizontal degrees of freedom would couple to the vertical motions of the pneumatic table. Hence, the legs could not be pressurized during the experiments. However, the

voice coil shaker was sufficiently powerful to introduce enough accelerations into the support system for calculating the desired transfer functions in the horizontal degrees of freedom. The pneumatic table with the prototype active isolation hardware is shown in Figure 4.1. As depicted in the photograph the magnetically levitated platform was attached to an aluminum interface plate which was fastened to the pneumatic table. Not shown in the photograph, a voice coil was attached to the pneumatic table actuating against a laboratory wall. This actuator was powered by a controllable current source where the control input was introduced by the spectrum analyzer. A triaxial accelerometer head was placed on the actuated table and the horizontal axes of the triaxial head were aligned with the x and y axes of the levitated platform on which a second triaxial accelerometer was mounted. These sensors were used to give the noise floor performance of the isolated platform as well as the transfer function performance of the forced support structure in the x and y axes. The full six degree of freedom performance of such isolation systems will be covered under the demonstration hardware results since the full six degree of freedom control was representative of an off-loaded system, although for a limited amount of time.

The laboratory experimental environment was dominated by the bias acceleration in the vertical direction. However, the prototype system could be tested in the sub-Hz frequency domain to the noise floor regime of the sensitive accelerometers by exciting only the horizontal plane and testing the control functions of the horizontal degrees of freedom independently of the vertical degrees of freedom. The non-forced horizontal accelerations of the isolation system support structure gave the testing resolution of the laboratory environment where the disturbances to this support were structure born due to its attachment to the building. It is assumed that the direct disturbances to the pneumatic table were minimal. Figures 4.2 and 4.3 show frequency spectrums of an x and y axis acceleration time history for the pneumatic table where their directions where defined by the platform fixed coordinates. Referring to Figure 3.8, the laboratory acceleration environment is in the noise of the

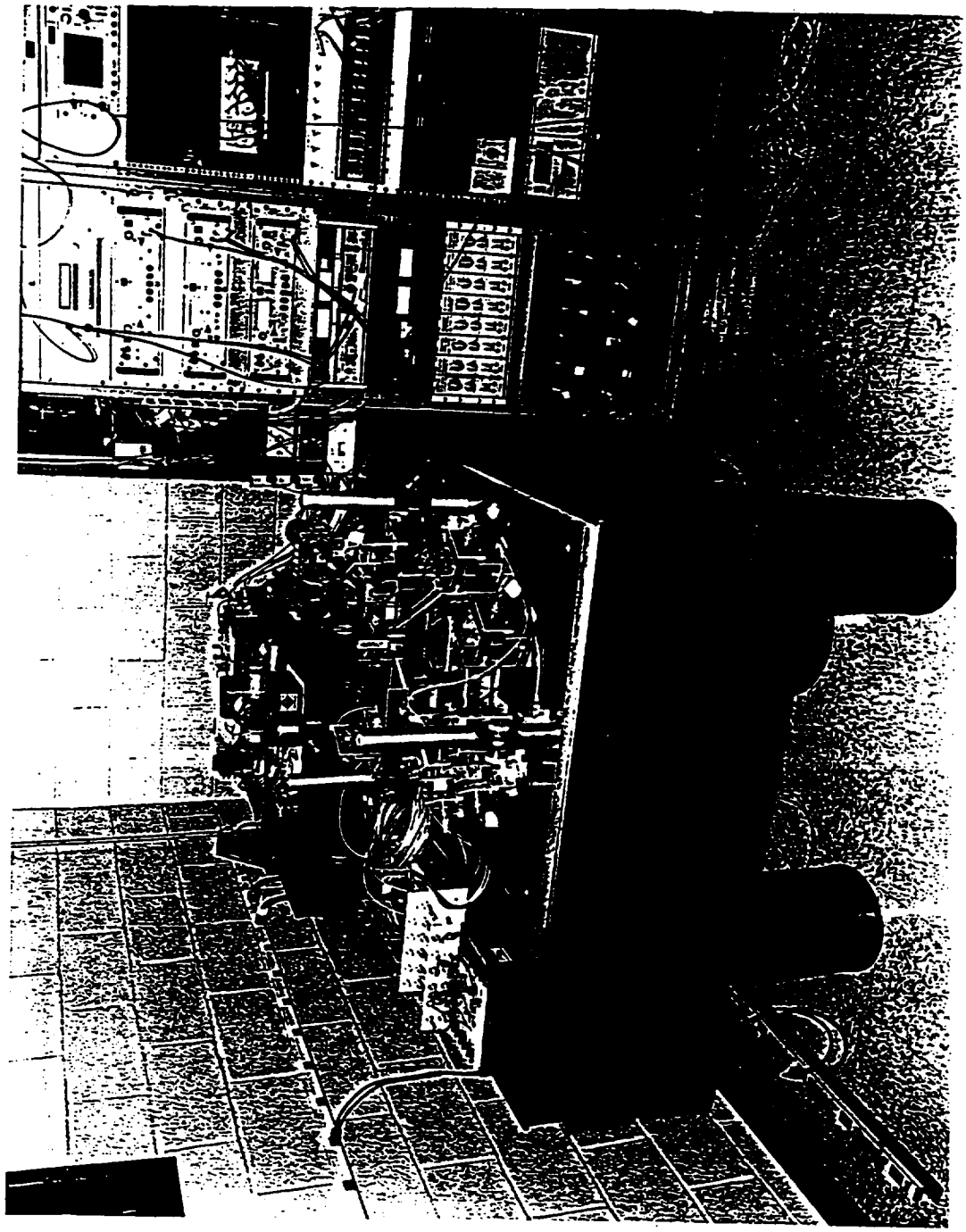

Figure 4.1: Laboratory view of active isolation hardware.

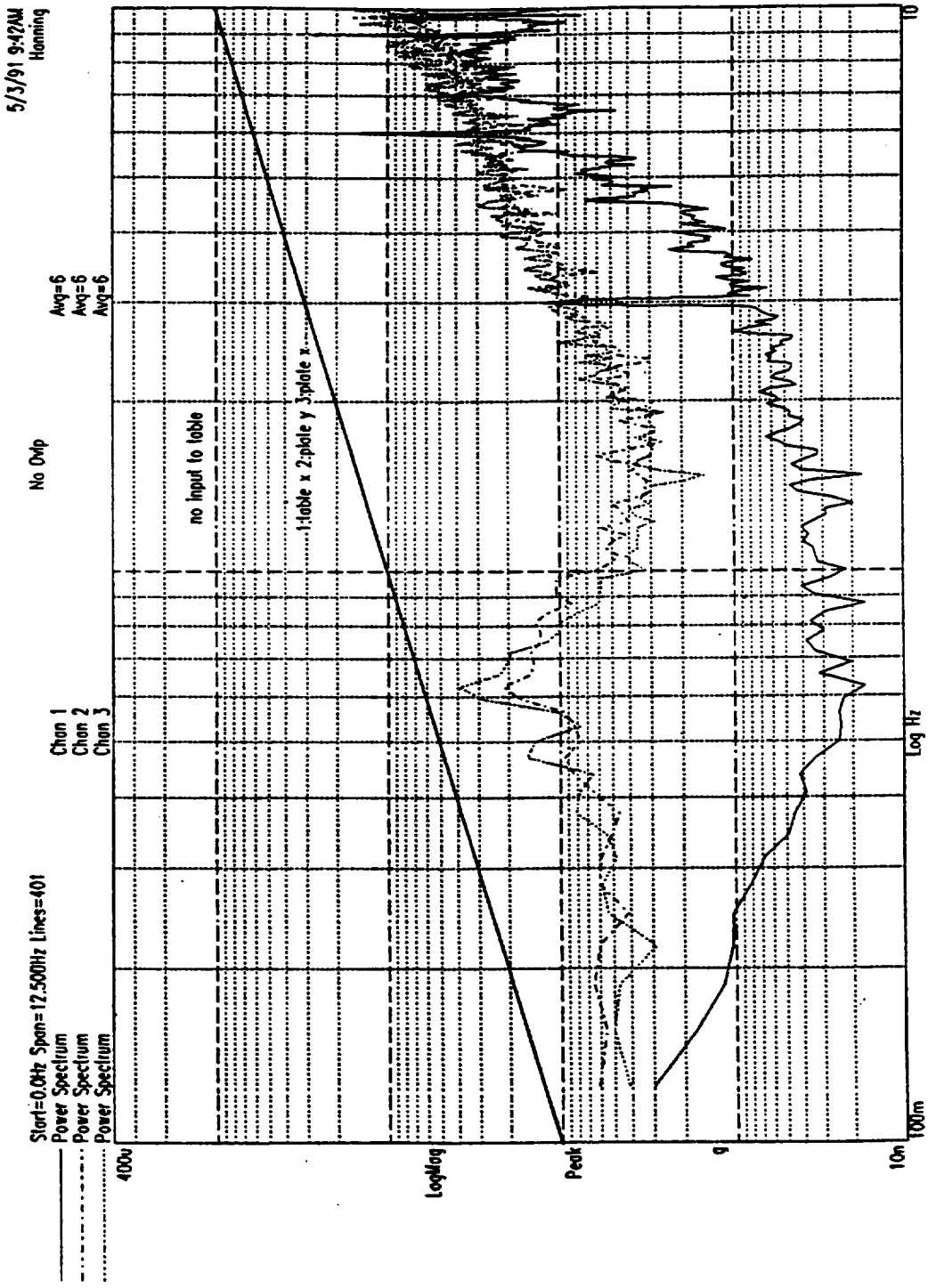

Figure 4.2: Acceleration spectrums of table x, and platform x and y directions.

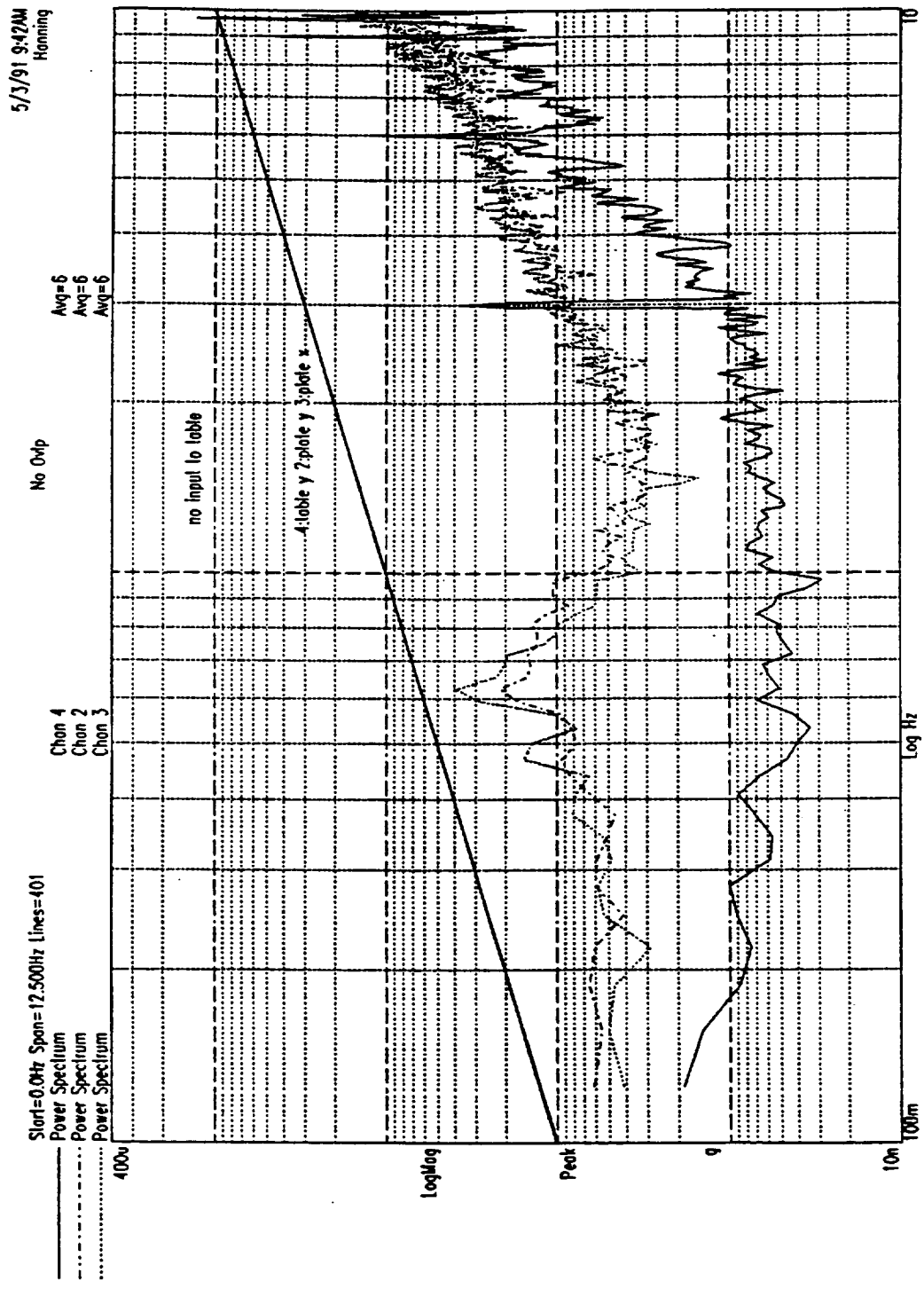

Figure 4.3: Acceleration spectrums of table y, and platform x and y directions.

QA-2000 accelerometer signal. From Figures 4.2 and 4.3, a pneumatic table support structure mode is evident at 3 Hz where multiples of 3 Hz are also present in both the x and y sensors, respectively.

4.1.2 Laboratory Data Collection and Transfer Function Measurements

The acceleration noise floor performance of the laboratory system is formed by measuring the accelerations of the levitated system in the horizontal dimensions. The acceleration data was taken with Sunstrand QA-2000 proof mass linear accelerometers housed in a triaxial sensor head with two of the orthogonal sensors aligned with the platform defined x and y axes, respectively. These accelerometer outputs were digitized using an HP analyzer where the power spectral density functions were calculated. These power spectral densities of the levitated platform's horizontal accelerations gave the acceleration noise floor performance of the system as a function of frequency while the support structure was not being disturbed. These measurements were taken in an open laboratory so their was no attempt at shielding the experimental platform from direct disturbances. Therefore, these measurements assumed that the accelerations introduced to the payload were dominated by the control current noise in the electromagnets, due to the total control system noise. The many contributors to this overall noise in the control magnets were discussed in the previous chapter, and will be compared to the measured values in the experimental results discussion section.

Figures 4.2 and 4.3, showing the acceleration spectrum of the table x and y axes, also show the corresponding accelerations of the x and y sensors attached to the isolated payload. For comparison the microgravity acceleration requirement for the space station is superimposed on these plots, in the bandwidth from 0.1 to 10 Hz. As shown in these plots the support structure modes are not disturbing the isolated payload and the system acceleration noise floor performance is simply dictated by the closed loop performance of the magnetic actuators feedback loops. Again the direct disturbances are assumed to be negligible and the noise floor is dictated by the control resolution of

the total system. These power spectral density functions were calculated with 401 frequency lines of resolution for the frequency band of 0 to 12.5 Hz. Therefore, the spectral resolution for the bandwidth shown from 0.1 to 10 Hz was 0.03 Hz. Six averages were used for these plots with a non-overlapped Hanning window. The control was strictly relative feedback since the support structure was not being disturbed and therefore these plots represent the system equilibrium or steady state noise floor performance for the 12 bit laboratory hardware configuration. The relative position feedback for the x, y and ϕ degrees of freedom were set to give a damped natural frequency of 0.6 Hz.

The transfer function determination of the laboratory hardware was accomplished using both the support structure and platform mounted accelerometers. The support structure was actuated by a Lorentz actuator attached between a corner of the pneumatic table and a laboratory wall. This actuator was controlled by taking an input voltage signal generated by the HP analyzer and driving a bi-directional current controlled source provided by a laboratory controllable power supply. This current drove the voice coil giving an excitation force proportional to the current controlled signal. Since the support structure for the levitated platform was actuated by one servo-force mechanism, the actuator was judiciously positioned to introduce a torque into the support table in the horizontal plane. This input force caused the pneumatic table to pivot about its support legs since the actuator was positioned with a moment arm to a leg attachment point. This multi-dimensional excitation at the isolation systems attachment points gave an approximately equal acceleration spectrum in the x and y axis aligned accelerometers attached to the support. The angular accelerations introduced by the torquing of the pneumatic table were not measured since only two triaxial acceleration heads were available, one for the isolated platform and the other for the support structure, an angular acceleration measurement was not possible for the laboratory hardware.

The spectrum analyzer assumes that the transfer function calculations or frequency response functions are referenced to a single channel of the analyzer. In order that multiple tests need not be run during the proof of concept phase of development for each control parameter settings, the support

structures acceleration spectrums were checked to see if the acceleration input power spectral densities were truly similar in their spectral content. The two table-fixed accelerometers were connected to the spectrum analyzer to calculate the input power spectral densities commanded by the excitation source. Figures 4.4 and 4.5 show the input power spectral density functions for the corresponding table-fixed x and y axis accelerometers. Included for comparison on Figures 4.4 and 4.5 the x and y platform accelerometers are also plotted and the space station requirement is superimposed for reference. The x and y axis support accelerometers demonstrate very similar spectral response. These commanded excitations were introduced by controlling the servo-force mechanism with a white noise disturbance signal. However, since the white noise introduces a voltage signal across all frequencies the current source could not drive the voice coil actuator to excite the support structure as strongly as if a single frequency excitation was introduced as the drive signal. The low frequency range was of most interest and a large force was required to drive the large mass of the table in the testing bandwidth from 0.1 to 10 Hz. Figure 4.6 gives the input power spectrum of the table-fixed accelerometers for a swept sine wave excitation input with the superimposed space station requirement as a reference. As shown the table accelerations are of larger magnitude than in the white noise excitation disturbance.

Transfer functions give a measure of the attenuation and amplification profile of an isolation system. These transfer functions and their associated input and output power spectral densities are given in the 0.1 to 10 Hz bandwidth. This bandwidth was chosen because the goal was the sub-Hertz isolation of a package by active inertial means. A space born payload will most likely have a cut off frequency set at about 0.01 Hz. However, performing a multi-dimensional test on a ground based system in this frequency range would be cost prohibitive. Their have been single-axis active tests in the 0.01 Hz frequency range however, the active system tested was constrained to this same axis. In addition, these tests did not demonstrate inertial isolation, but a simple lead-lag compensator approach was tested. The strokes required for a multi-dimensional test would dictate a very

complicated and costly test apparatus. However, testing in the 0.1 to 10 Hz frequency range for ground based systems is a valid demonstration for active low frequency inertial isolation concepts. The approaches and active control techniques are readily extendible to the lower frequencies and should pose no limitations on controller designs. A second levitated system with the appropriate noise levels and strokes could be built to test a ground based system at the lower frequencies in the horizontal plane, but would be unnecessary and increase costs.

To demonstrate the advantage of active inertial isolation the transfer functions were calculated for an inertially referenced and a relative feedback controller. These transfer functions were calculated using the table x axis accelerometer as the spectrum analyzers input power reference. Again, referring to Figures 4.4, 4.5, and 4.6 the support structure had very similar spectral densities in both the x and y dimensions however, the x axis consistently had greater acceleration magnitudes and, therefore, was used as the input power reference for the transfer function calculations in order to give conservative results. Figure 4.7 gives the transfer function calculations for the x and y axis platform accelerometers referenced to the input power spectrum from the support structure. These four curves demonstrate the advantages of inertially referencing the payload through the feedforward cancellation of the support structure excitations as opposed to a simple relative feedback isolation control approach. The natural frequency for both sets of curves was set at 0.65 Hz. As shown, the inertial controller is attempting to cancel the coupling of the levitated mass through the spring and viscous damper connections, due to the active relative position and velocity feedback of the closed loop relative control. The relative controller demonstrates a nominal 50 dB/decade roll off while the inertial controller is rolling off at approximately 100 dB/decade. The theoretical prediction for the inertial feedforward approach for an infinite resolution controller would show the attenuation continuing however, the 12 bit system reaches its resolution or deadband limits and the transfer function goes to the limiting case as demonstrated by the inertial curves in Figure 4.7. In addition, the phase and linearity of the accelerometers and relative proximitors will effect the roll off and

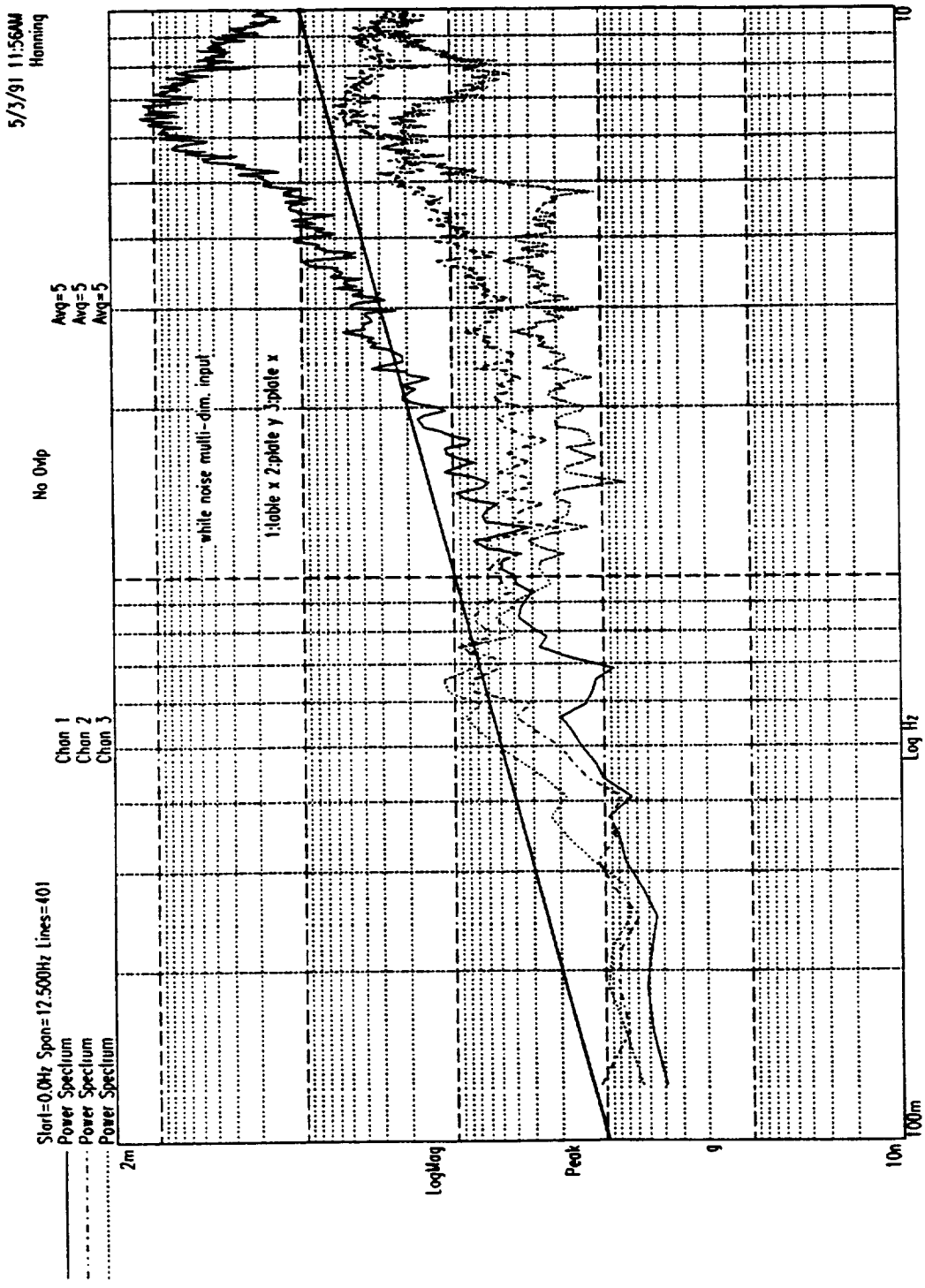

Figure 4.4: Forced acceleration spectrums for table x, and platform x and y directions.

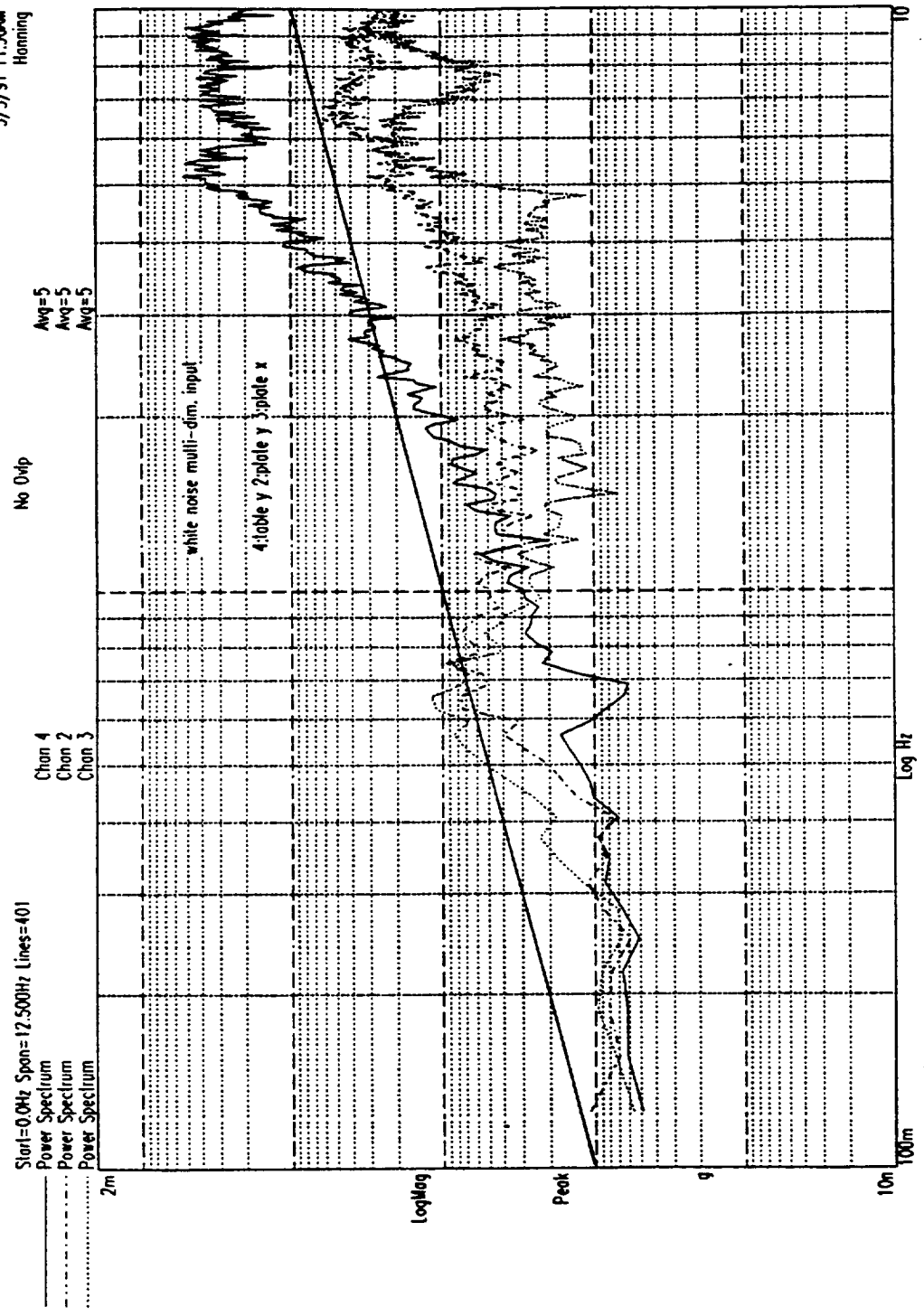

Figure 4.5: Forced acceleration spectrums for table y, and platform x and y directions.

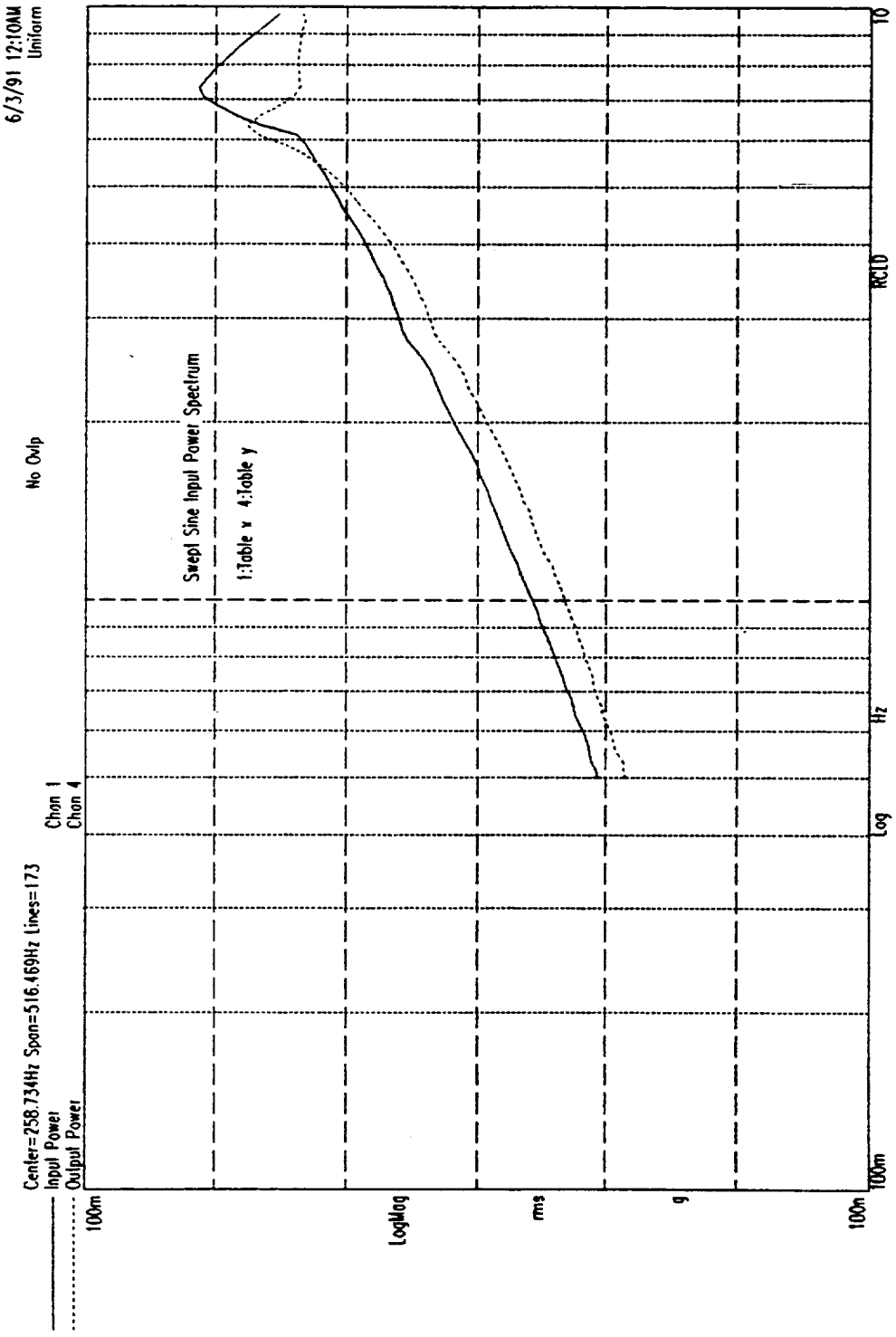

Figure 4.6: Swept sine wave acceleration spectrum for table fixed x, and y directions.

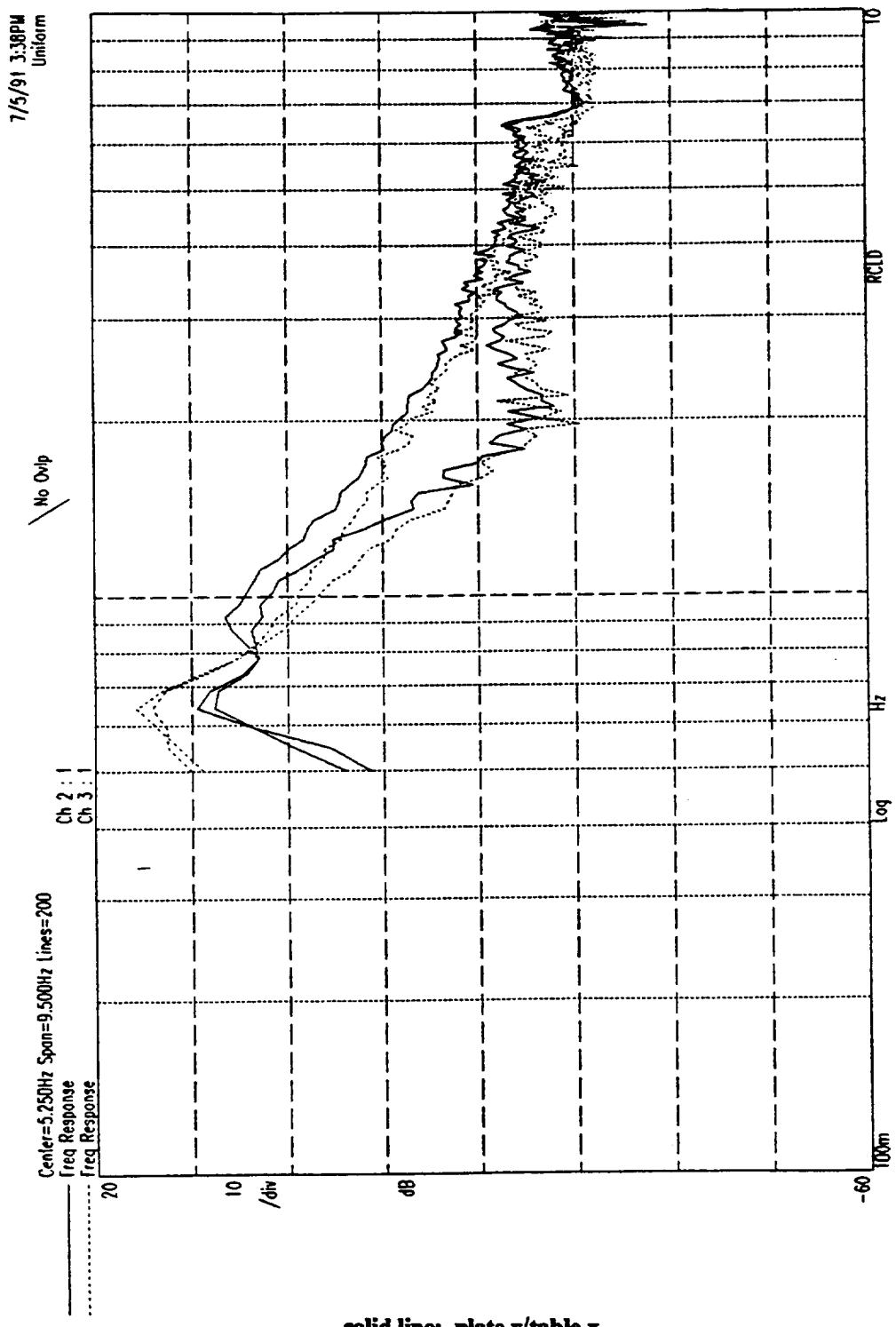

solid line: plate y/table x
dashed line: plate x/table x

Figure 4.7: Transfer function calculations for relative and inertial control.

attenuation profiles. This can be shown by plotting the input and output power spectrums of the transfer functions and analyzing the physical parameters of the controller from the acceleration spectrums. The results discussion will give a comparison of the predicted deadband and noise floor limits with the measured experimental results.

4.2 Learjet Demonstration Hardware Experimental Results

The six degree of freedom demonstration hardware was flown through low gravity Keplarien trajectories to acquire performance data in an off-loaded environment. Although the low gravity environment is limited in time and the non-stationary aspects of the maneuver cause limitations in bandwidth and system control parameter testing, this environment allowed the testing of the full six degrees of freedom with comparable control and equilibrium states for both vertical and horizontal motions. This then allowed the analysis of the data in the full three dimensional configuration where comparisons could be made in the multi-axis performance of the hardware. This chapter will describe the Learjet flight experimental environment and the acceleration performance of the isolated payload with respect to its dynamic inputs while attached to the aircraft during the low gravity maneuver.

4.2.1 Aircraft Experimental Environment

The Learjet demonstration hardware was housed in a standard Learjet rack. These racks have standard instrumentation interfaces with T-rail mountings to attach to the aircraft fuselage. The Learjet hardware consisted of two instrumentation racks, one for the levitated test section and the second housing the control computer, dc power supplies, and support electronics. The levitated test section was interfaced with a trunnion support package housed internal to a standard rack allowing

the experimental package to pivot about a trunnion support shaft. Figure 4.8 is a photograph of the two Learjet mounted experimental racks where the trunnioned support is shown pivoted about its support shaft. The electronics rack shows the control computer with the proximitor, accelerometer, and magnet dc power supplies. A master data acquisition computer was also housed in this rack which poled fourteen Learjet referenced data channels. In addition, a monitor and two current meters were attached to the electronics rack, where the current meters gave the total magnetic actuators ± current draw. The trunnion attached hardware consisted of the levitated platform, three actuation pods, the control sensors, and the magnetic actuators current control power amplifiers. Figure 4.9 is a photograph showing an end view of the trunnioned payload. The top part of the trunnioned cube housed the twelve power amplifiers and the proximitor drive signal conditioning circuits. The bottom of the trunnioned volume housed the actual isolation system. The isolated payload consisted of a ferromagnetic structure where an autonomous six channel data acquisition system (DAS) was housed and slaved to the master DAS. The autonomous slaved system was time synchronized with the master DAS to take the acceleration time histories by triggering the two data acquisition systems using a physical trigger which was pressed prior to entering the low gravity portion of the Keplarien trajectories.

In order to describe the experimental acceleration environment for the Learjet tests, the dynamic rigid body control of the aircraft will be discussed. The Learjet low gravity guidance system, provides low frequency acceleration data for the aircraft's X, Y, and Z axes as shown in Figure 4.10 [23]. Acceleration levels are displayed in the cockpit for crew guidance and are recorded for research data correlation. However, attached experiments are subjected to higher frequency vibratory accelerations emanating from structure-borne noise and direct acoustic energy. Additionally, since the reference accelerometers used for guidance are usually located near the aircraft's center of gravity (C.G.), experiments located at other locations experience different rigid body accelerations, especially in the Z axis, due to the rotation of the fuselage about the Y axis.

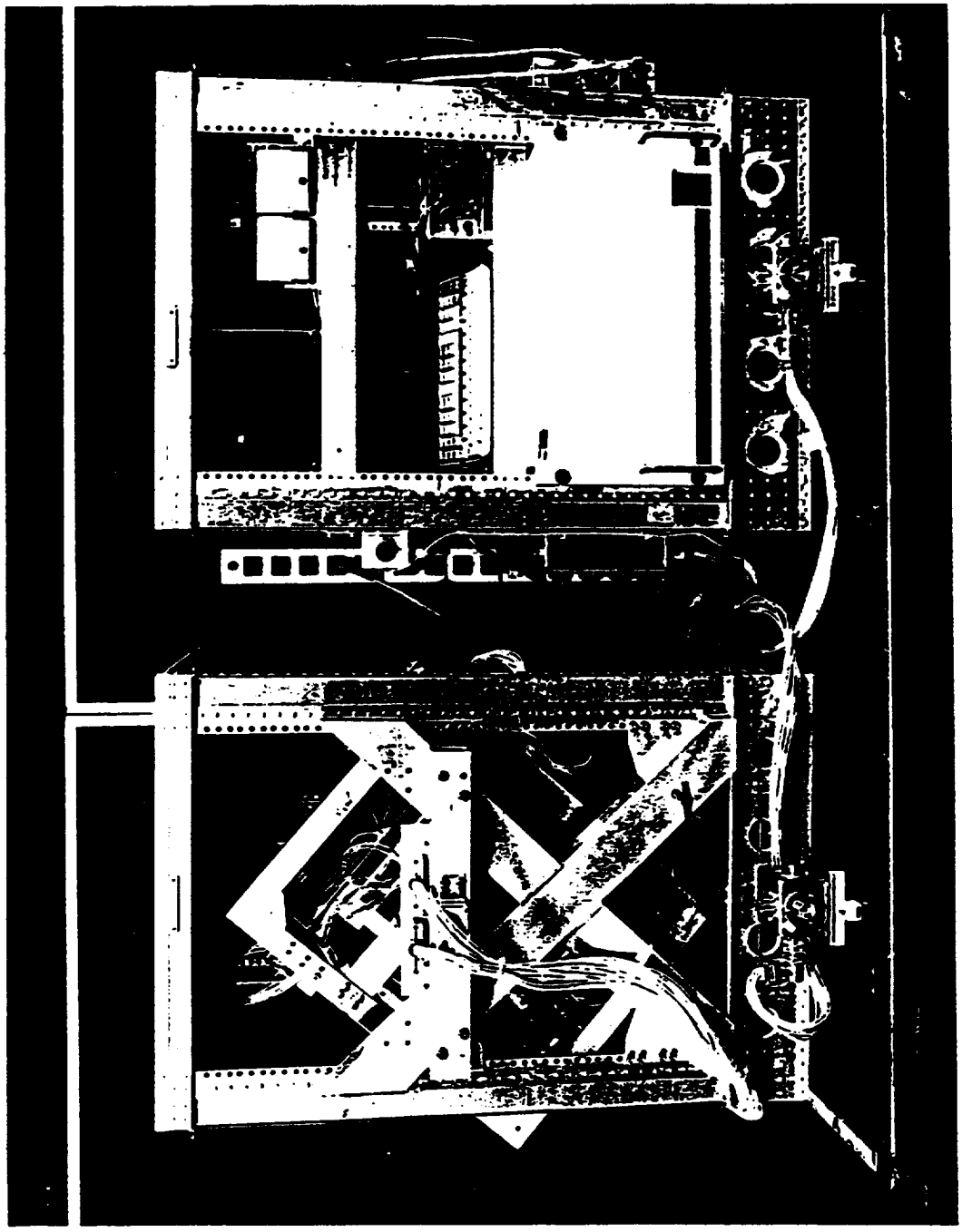

Figure 4.8: Learjet demonstration hardware.

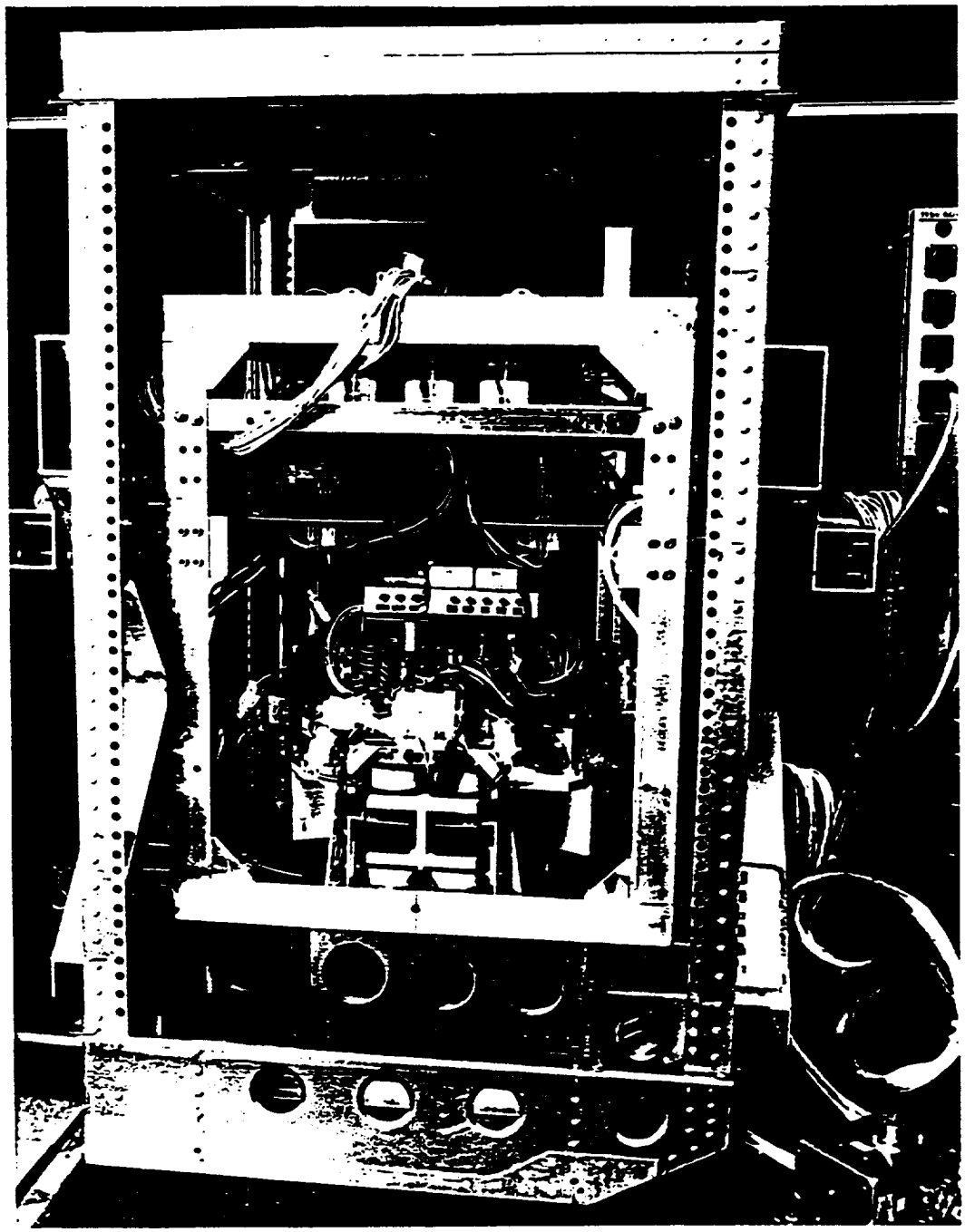

Figure 4.9: Learjet trunnioned rack support structure and isolated platform.

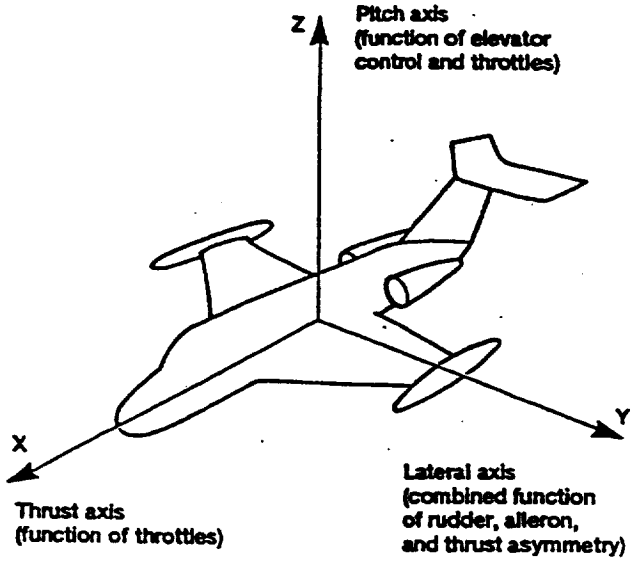

Figure 4.10: Aircraft coordinate system.

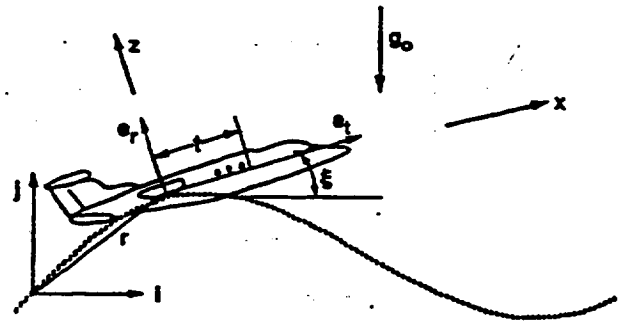

Figure 4.11: Aircraft rigid body dynamics coordinate systems definition.

The system by which these trajectories are flown may best be described by theoretically deriving the equation of motion for the flight maneuver in two dimensions, or assuming simple planar motion. A typical trajectory is illustrated in Figure 4.11 where the low gravity portion of this trajectory begins after a high g maneuver, as indicated in the figure. The coordinates for the trajectory and body fixed axes will be defined as shown in Figure 4.11. The vector r is defined as the vector tracking the position of the trajectory reference sensor to an inertial coordinate system. In the body fixed frame, the distance from an accelerometer to this coordinate system is defined by a vector length t in the e_t direction. Summarizing, the two acceleration equations for the body fixed coordinate system can be written as [24]:

$$\vec{r}_t = \left(v\dot{\xi} - g_o \cos\xi\right)\hat{e}_r + \left(\dot{v} - g_o \sin\xi\right)\hat{e}_t \tag{4.1}$$

and,

$$\vec{r}_t = \left(v\dot{\xi} - t\ddot{\xi} - g_o \cos\xi\right)\hat{e}_r + \left(\dot{v} - t\dot{\xi}^2 - g_o \sin\xi\right)\hat{e}_t. \tag{4.2}$$

The rotational velocity or pitch rate and forward thrust of the aircraft is being controlled in order to cancel the acceleration due to gravity in the body fixed axes. This flight control is accomplished by viewing a Light Emitting Diode (LED) display where one axis of the display is proportional to acceleration in the radial direction and the other axis is proportional to tangential acceleration. Both of these accelerations are measured at the remotely mounted reference sensor. The maneuver "control loop" is closed by the pilots controlling the pitch rate and thrust of the aircraft.

Controlling the aircraft trajectory in this manner, the reference sensor, in effect, becomes the electronic center of gravity of the aircraft. As seen in equation (4.2), there is an additional acceleration term due to the pitch rate and the pitch rate as a function of time in the radial and tangential coordinate directions, respectively. These acceleration components are linearly related to the distance from a point to the electronic C.G.. This simplified planar equation of motion shows that the residual acceleration of an experiment can be substantially different from that of the control sensor accelerations.

In order to adequately describe the dynamics of a low gravity maneuver, and thus the experimental environment for the Learjet hardware, it is advantageous to give the filtered time trace of the accelerations throughout the aircraft as well as the acceleration spectrum during the off loaded phase of the trajectory. The filtered acceleration traces give the residual trends of a typical low gravity flight maneuver as well as the sensors acceleration history based on its attachment to the aircraft. In addition, these filtered time histories are used to defined the three phases of a low gravity trajectory. Figure 4.12, shows the filtered time history traces of three vertically positioned accelerometers whose relative distance, 2Z to 4Z and 3Z to 4Z, were approximately 0.838 m (33 in.) and 0.94 m (37 in.), respectively. The average mean acceleration in non-dimensional units for accelerometers 2Z, 3Z, and 4Z, were -0.0025, -0.0027, and -0,0021 g's, respectively. The residual relative offsets shown in Figure 4.12 can be attributed to two sources, one being rigid body angular accelerations of the aircraft and the second due to non-calibrated bias voltages inherent to the signal conditioning circuits. A correction for the later was attempted by zeroing the signal conditioning boards and taking an offset reading in addition to the bias calibration factors used for the QA-2000 proof mass accelerometers. The increased negative residual acceleration offset with increasing distance from the control sensor location for sensors 2Z, 3Z, and 4Z, is consistent with the expected magnitude increase in residual average accelerations because of their location relative to the control sensor. To attempt a quantitative check of the measured observation, the second derivative of a pitch gyroscope time history was taken for the same time history giving a peak value of 0.3 (deg/s^2). This calculated angular acceleration compared well with observed measurements of 0.27 and 0.36 (deg/s^2). These measured values are calculated from the difference in mean acceleration values of sensors 2Z to 4Z, and 3Z to 4Z, respectively. The calculations using the gyroscopic data assume only planar motion. Out-of-plane dynamics due to roll and yaw were not accounted for. These residual accelerations were on the order of 10 to 20 percent of the residual g experienced at the control sensor for a typical accelerometer position of 2.54 m (100 in.) from the aircraft trajectory control point.

A typical acceleration environment for the Learjet tests will be defined by the filtered time trace as shown in Figure 4.12. As shown on this figure, the aircraft accelerations are shown having transitioned from the high g maneuver into the entry phase of the trajectory. This entry phase is defined by a push over maneuver by the pilots, to zero out the pitch axis accelerometer. The aircraft typically overshoots the target "zero g" and an oscillatory residual acceleration condition follows until the pilot controlling the pitch axis of the aircraft stabilizes the control point. Subsequently, a 10 to 15 second stable, low gravity, residual acceleration environment is established. At the end of the stable low gravity time the aircraft is pitched approximately 45 to 50 degrees nose down, at which time the pilots pull out of the trajectory and prepare for the next maneuver. The low gravity trajectories can be dissected into three major phases, entry, low gravity, and exit. The low gravity trajectory phase, which defines the testing environment, typically lasts 10 to 15 seconds. This stationary part of the trajectory therefore, limits the low frequency bandwidth of any isolation system as well as the testing bandwidth to approximately a 0.1 to 0.3 Hz low frequency boundary.

The methodology used to produce the power spectral densities for each accelerometer during the low gravity trajectory first involved determining the times at which the stable low gravity period began and ended, determining how many ensembles (time samples) could be processed into a spectrum average for that duration, and then processing the autospectra. A basic check of random process stationarity was conducted. It was demonstrated that there was minimal variation of the resultant power spectral densities if three or more low gravity ensembles were used. It was also noted that there was significant variation in the power spectral densities if the entire low gravity maneuver acceleration data set were processed as a set of ensembles. This demonstrated the nonstationarity of the entry/low gravity/exit time domain process. An example of a longitudinal (X axis) accelerometer's time domain response, can be seen in Figure 4.13. Figure 4.13 clearly shows the drop in response level occurring during the low gravity period compared to the entry and exit maneuvers.

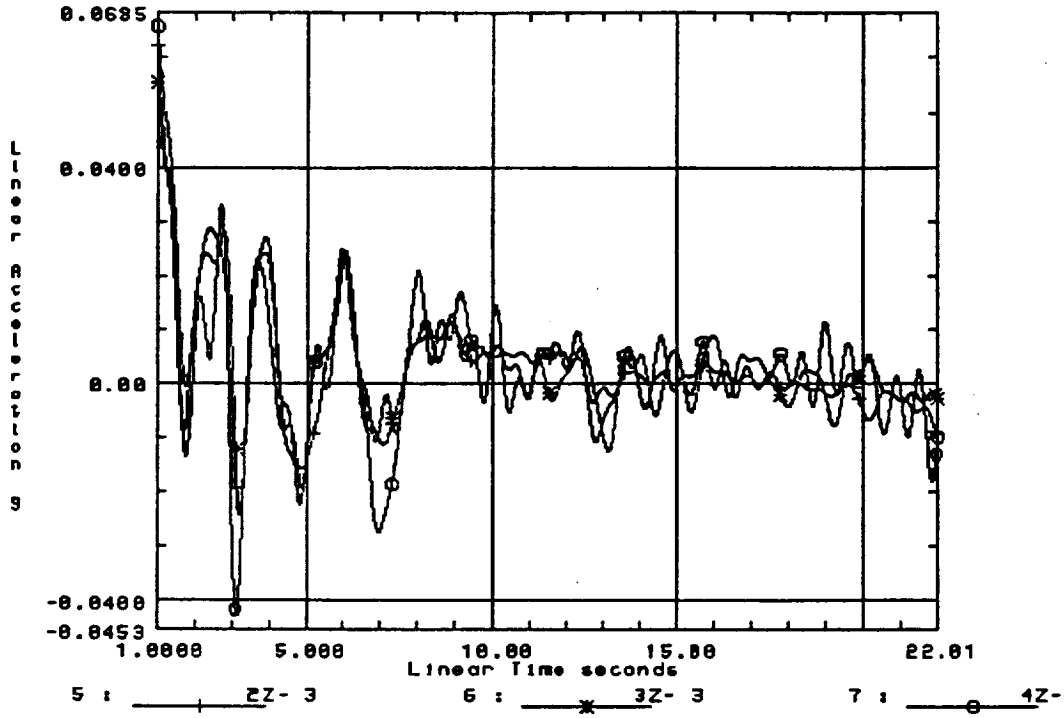

Figure 4.12: Filtered Learjet Z acceleration traces.

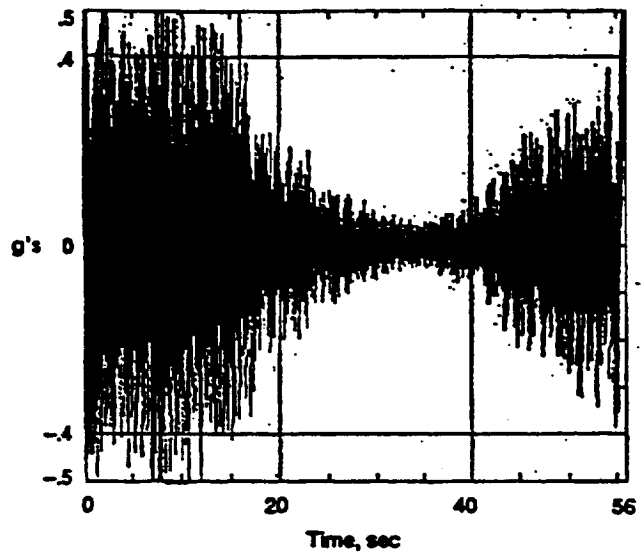

Figure 4.13: X axis acceleration time trace of full trajectory.

The frequency spectrum magnitudes seen by the accelerometers of attached payloads are dependent upon the payload structural dynamics, as well as the aircraft's dynamic response during the low gravity maneuver. As demonstrated in Figure 4.13, the aircraft's response during the low gravity phase of the trajectory is representative of an off-loaded structure. Figure 4.14, shows the power spectrum of an accelerometer on the trunnioned experimental rack and one mounted on the actively isolated payload, calculated for the same flight as the residual traces shown in Figure 4.12, for a 22 and 12 second time history. The 22 second time history included both initial transient acceleration oscillations, and the low gravity portion of the trajectory, once the transient entry dynamics stabilized. The 12 second time history only captured the quiet low gravity portion of the flight with the entry level accelerations removed. The time points per ensemble were set with a 50 percent Hanning window giving a minimum of three averages per power spectrum. This resulted in a frequency resolution of 0.14 and 0.17 Hz for the 22 and 12 second time histories, respectively.

As seen in Figure 4.14, the accelerometers attached to the experiment rack demonstrated responses both broadband in nature with indications of modal response specific to the trunnioned rack. As can be seen for the 22 second data set processed, the entry transient dynamics of the initial entry phase dominates the low frequency spectral response, while the 12 second data set shows a more broadband response with rack resonance's, for the rack mounted accelerometer. The isolation performance spectrums will be calculated and used for the transfer function calculations during the stable low gravity phase of the trajectories since the control system was not activated until the aircraft was into the off loaded environment.

Inconsistencies in the flight regime and flight conditions such as aircraft weight caused differing structural responses, the altitude effects on engine output performance (RPM variations), and even the variability on the entry technique levels and styles from pilot to pilot will tend to affect the frequency vibro-acoustic response of the aircraft. Even so, the individual channel responses demonstrated a degree of consistency from one trajectory to the next and allowed the testing of the

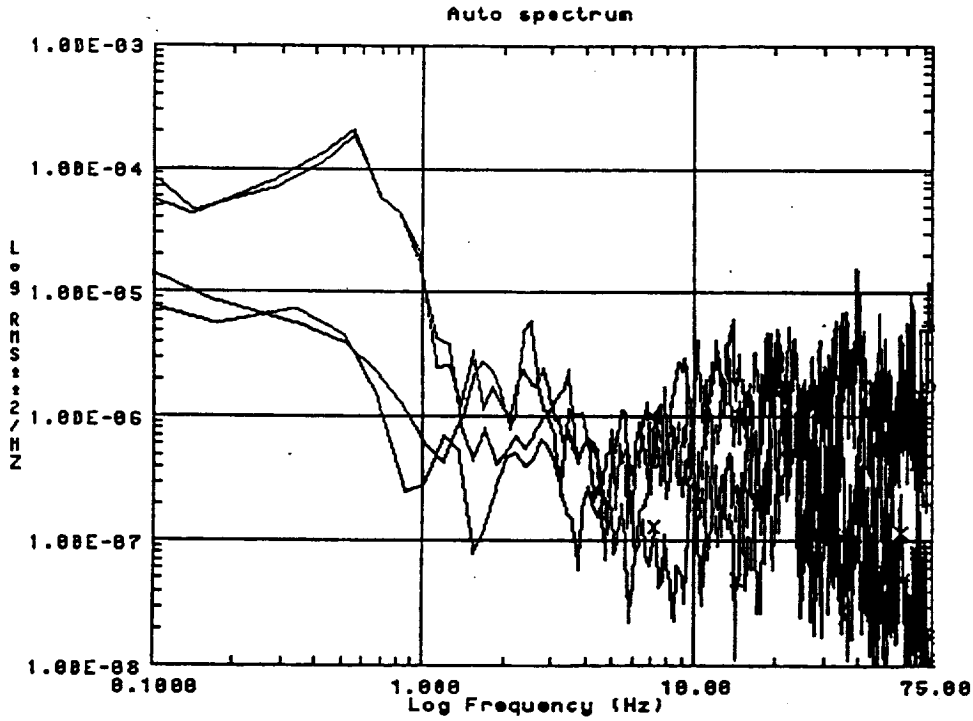

Figure 4.14: Power spectral density functions of aircraft mounted accelerometers.

active isolation hardware in the full six degrees of freedom for the off loaded condition. Even though the low frequency bandwidth was limited due to the duration of the low gravity phase of the trajectories there was enough time to take statistically representative acceleration data in the sub-Hertz frequency regime.

4.2.2 Aircraft Data Collection and Transfer Function Measurements

The experimental data acquired during the active Learjet demonstration tests were obtained during a series of low gravity flight tests. These data sets represent a wide range of dynamic conditions which posed a unique challenge in acquiring low frequency acceleration data from a fully active six degree of freedom inertially controlled payload. These flights were successful in demonstrating the sub-Hertz control of a payload in a uniquely dynamic non-stationary acceleration environment. The goal of isolating a payload in an orbital flight environment will be a much smaller task than the gathering of data during low gravity aircraft trajectories.

The Learjet aircraft, trunnion frame, and the active isolation platform were instrumented with Sunstrand QA-2000 accelerometers. In addition, a Humphrey V624-0825-1 two axis vertical displacement gyroscope was installed on the trunnion system to measure the rotation and pitch angles of the trunnion support structure with respect to the vertical, based on a ground coordinate system. The gyroscope had a resolution of $\pm$ 3 degrees (0.0524 radians). The data collection instrumentation is shown in Figure 4.15. Figure 4.15 illustrates the input acceleration sensor locations for the transfer function calculations where the output data channels acceleration sensors were mounted on the isolation platform in the configuration shown in Figure 4.16. Each accelerometer block in Figure 4.15 consisted of three accelerometers oriented othogonally and aligned with the three aircraft-fixed coordinates X, Y, and Z. As previously stated, a total of 20 channels of data were acquired during each trajectory. The data was stored with 14 bit digital resolution and a sampling frequency of 142

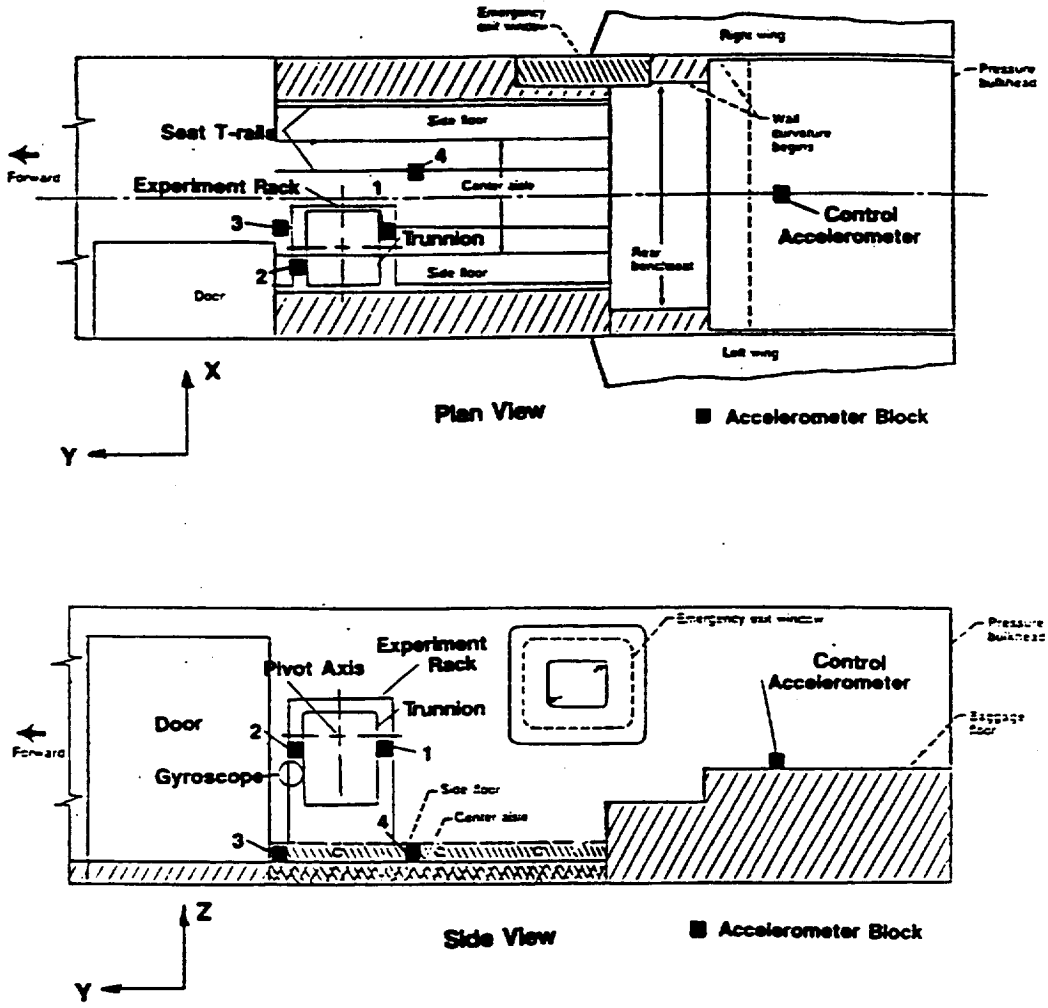

Figure 4.15: Input power spectrum accelerometer locations.

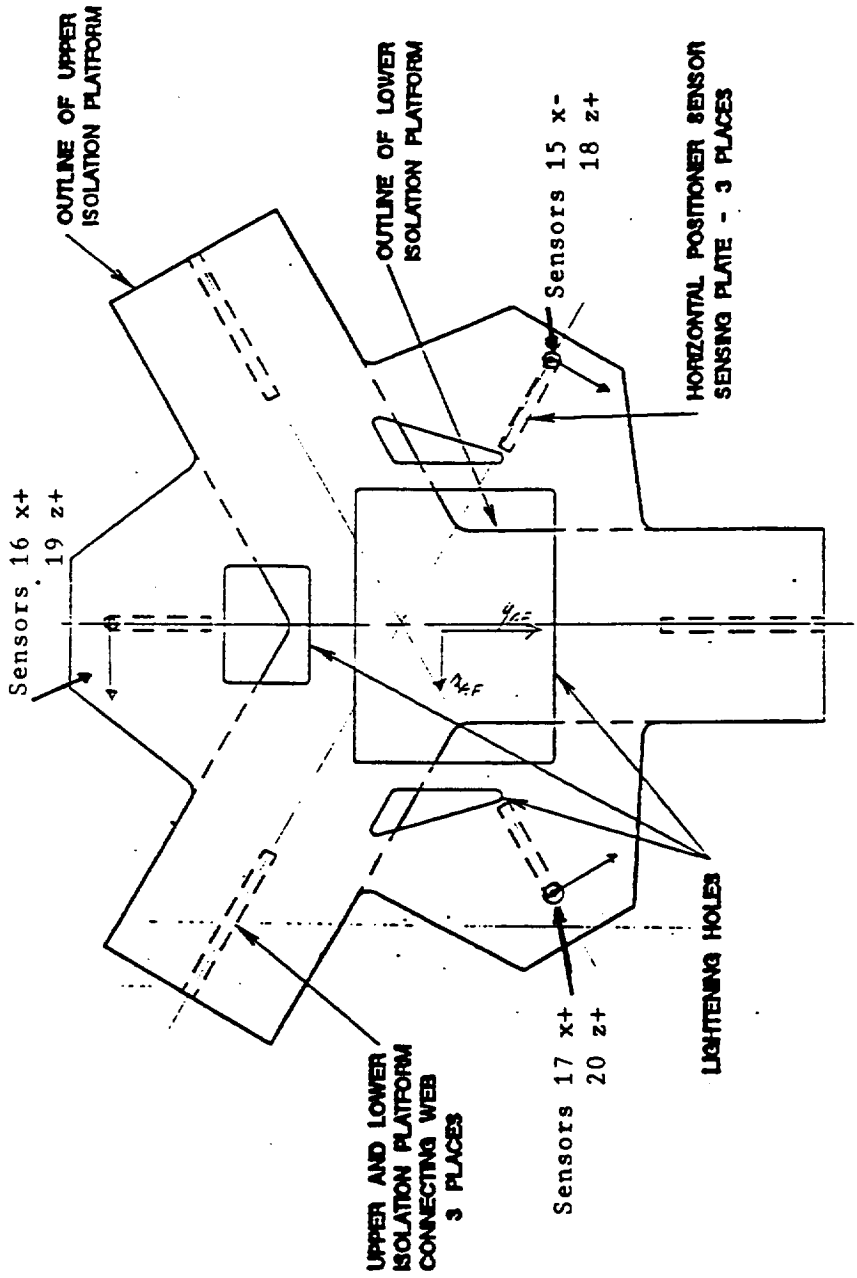

Figure 4.16: Output power spectrum accelerometer locations on platform.

Hz per channel. The acceleration measurement system had a ± 5 Volt dynamic range with a typical sensor sensitivity of 5 Volts/.5 g. Each accelerometers sensitivity was used in calculating the per channel sensitivity values in Volts per g. The resolution of this data acquisition system was 61 μg per bit using a typical accelerometer sensitivity of 5 Volts per g. As previously mentioned, the data acquisition system was manually triggered during the on-set of the low gravity portion of each trajectory. The manual trigger was pressed when the operator felt the transition from the 2.5 g pull-up into the low gravity portion of the trajectory, at which time the data acquisition system was initiated and data was taken for 27.6 seconds. Manual triggering, the non-stationary trajectory, and trajectory acceleration histories, all make comparisons between trajectories difficult. Therefore, comparisons must be made with reference to specific phases of a maneuver such as the stabilized low gravity portion in which the active system was activated.

The low gravity parabolic maneuver is depicted in Figure 4.17, where each phase of the trajectory is shown, entry/ low gravity/ exit. Referring to this figure, the active demonstration hardware was activated during the low gravity phase of the trajectory, stabilized, and data was acquired to calculate the frequency response of the payload. In order to best recreate the dynamics of both the actively controlled payload and its support structure, two data acquisition systems were flown. A slaved autonomous six channel data acquisition system (DAS) was attached to the suspended platform, while a master 14 channel DAS was flown for the Learjet acceleration and rotational environment histories. A total of 18 acceleration and two gyroscopic data channels where digitized by the 14 bit converter.

The natural frequency of the demonstration hardware was set at about 0.6 Hz for the following pitch axis transfer function comparisons. However, the demonstration flights posed considerable environmental challenges. Therefore, the system was intentionally over damped in order to insure the stabilization of the platform after the initial conditions during the push over phase of the low gravity trajectories. Figure 4.18 shows the frequency response curves for two typical

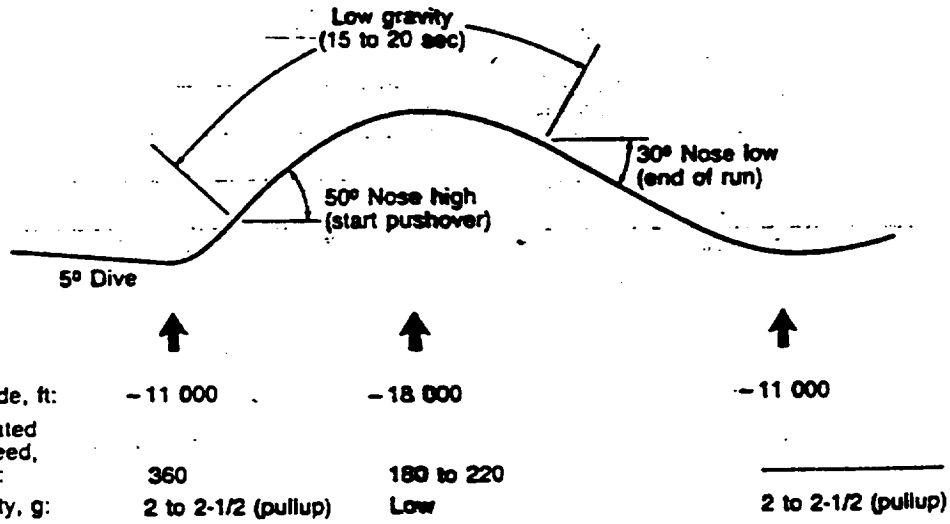

Figure 4.17: Low gravity parabolic trajectory maneuver.

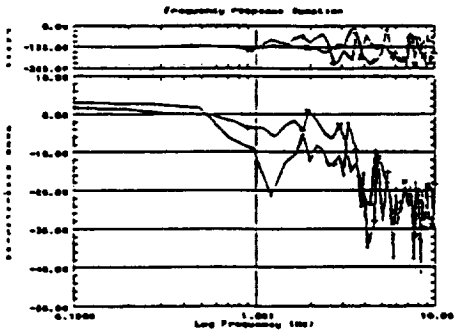

Location 6 on platform vs.
location 1 on trunnion.

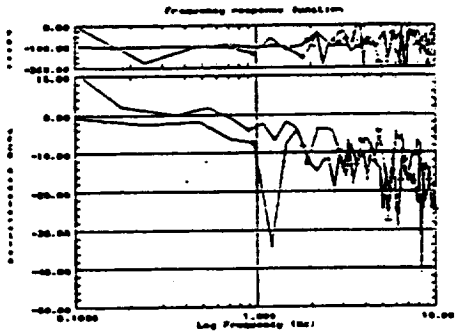

Location 6 on platform vs.
location 2 on trunnion.

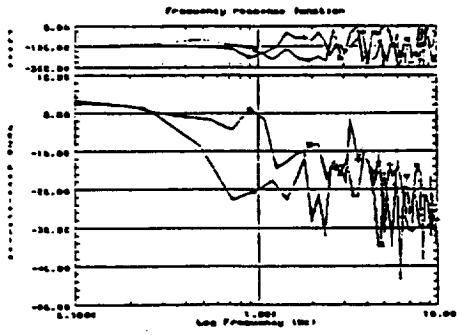

Location 6 on platform vs.
location 3 on aircraft fuselage.

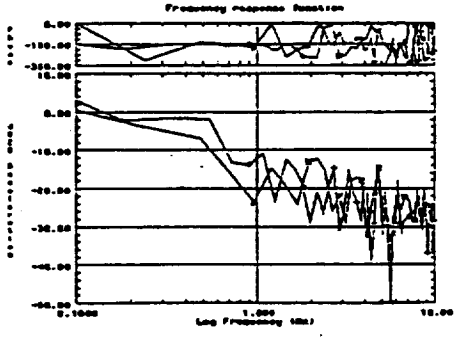

Location 6 on platform vs.
location 4 on aircraft fuselage.

Figure 4.18: Frequency response of demonstration hardware in vertical dimension for inertial and relative control.

trajectories where the active system is under a closed loop, relative feedback and relative/inertial feedback/feedforward control, respectively. These frequency response curves are given for the vertical direction where the acceleration spectrum of the payload is compared to that of the support structure.

The relative and inertial frequency response curves were calculated from 17 and 14 second low gravity time histories. In order to get fairly representative frequency response functions for both cases, the elements per ensemble, with a 50 percent Hanning window, were set to generate the plotted curves with stable results. This gave a frequency resolution of 0.2 and 0.24 Hz for the relative and inertial cases, respectively. Figure 4.18 (a) through (d), show the response functions of a soft well damped system with a natural frequency of about 0.6 Hz. The inertially referenced curves as compared to the relative feedback curves show the system's increased roll off and attenuation as a function of frequency. The expected increase in attenuation of inertial feedforward compared to relative control was masked in the bandwidth from 2 to 10 Hz for these sensor to sensor comparisons.

The multi-dimensional transfer function calculations for an inertially referenced case and a relative feedback case will be given. The cross-axis calculations are not presented in that the input power spectrums for two aircraft fixed locations were used, where each location consisted of two triaxial acceleration measurements giving the three translational components in the aircraft fixed X, Y, and Z axes, respectively. Two rotational input power spectrums were estimated for the trunnion and aircraft fuselage fixed locations by differencing the two accelerometers sensitive to the pitch and yaw motions of the aircraft. The third rotational component was estimated by cross differencing the two locations, trunnion fixed and aircraft fixed, since the roll sensitive accelerometers for each individual location were aligned along the same accelerometer defined axis. Referring to Figure 4.15, the input power spectrums in the aircraft fixed translational axes were simply used directly as input power spectral reference channels for the X, Y, and Z axis frequency response calculations. This allowed the comparison between attenuation responses of the isolated payload with respect to each axis at the four locations, where two locations are paired as aircraft fixed and the other as trunnion

fixed accelerometers. This gave a good estimate of the overall attenuation from the aircraft attachment input acceleration power spectrum to the payload response as well as the trunnion support structure to payload attenuation. Therefore, locations 1 through 4 X, Y, and Z accelerometers were used as a single axis reference to the X, Y, and Z axis output power spectrums of the payload. These payload output power spectral densities were calculated by taking the six inertial data sensors on the payload, and from their geometrical placements, resolving the appropriate six inertial degrees of freedom of the platform. Referring to Figure 4.16, the following equations represent the accelerations that the individual platform accelerometers sense along their sensitive axes.

$$a_{15} = \frac{1}{g_o}\left(-\ddot{X}\cos 30 + \ddot{Y}\sin 30 + \ddot{\beta}_z R\right) \tag{4.3}$$

$$a_{16} = \frac{1}{g_o}\left(-\ddot{X} - \ddot{\beta}_z R\right) \tag{4.4}$$

$$a_{17} = \frac{1}{g_o}\left(\ddot{X}\cos 30 + \ddot{Y}\sin 30 - \ddot{\beta}_z R\right) \tag{4.5}$$

$$a_{18} = \frac{1}{g_o}\left(\ddot{Z} + \ddot{\theta}_x R\cos 30 - \ddot{\phi}_y R\sin 30\right) \tag{4.6}$$

$$a_{19} = \frac{1}{g_o}\left(\ddot{Z} - \ddot{\theta}_x R\right) \tag{4.7}$$

$$a_{20} = \frac{1}{g_o}\left(\ddot{Z} + \ddot{\theta}_x R\cos 30 + \ddot{\phi}_y R\sin 30\right) \tag{4.8}$$

Using these equations the following non-dimensional translational accelerations can be resolved for the platform inertial accelerations in the X, Y, and Z directions as well as the rotational accelerations of the platform, where these rotational accelerations are in units of radians/sec^2. (Note: g_O is the acceleration of gravity and R is the radial distance from the center of the platform, R=5 inches.)

$$\frac{\ddot{X}}{g_o} = \left[\frac{a_{17}}{2} - a_{15}\left(1 - \frac{1}{2}\right) - a_{16}\right]\frac{1}{1+\cos 30} \tag{4.9}$$

$$\frac{\ddot{Y}}{g_o} = \frac{(a_{15} + a_{17})}{2\sin 30} \tag{4.10}$$

$$\frac{\ddot{Z}}{g_o} = a_{19}\left[1 - \frac{1}{(1+\cos 30))}\right] + \frac{a_{18}}{(1+\cos 30)} \tag{4.11}$$

$$\ddot{\theta}_x = \frac{g_o(a_{18} - a_{19})}{R(1+\cos 30)} \tag{4.12}$$

$$\ddot{\phi}_y = \frac{g_o(a_{20} - a_{19})}{2R\sin 30} \tag{4.13}$$

$$\ddot{\beta}_z = \frac{g_o \cos 30}{R(1+\cos 30)}\left[\frac{a_{17}}{2} - \frac{a_{15}}{2} - a_{16}\right] + \frac{g_0(a_{15} - a_{17})}{2R} \tag{4.14}$$

Therefore, by using equations (4.9) through (4.14) the inertial six degrees of freedom were calculated from the respective acceleration channels a_{15} through a_{20}. Referring to Figure 4.15, the rotational input power spectrums were calculated by using difference relations between the aircraft and trunnion fixed accelerometers as follows:

$$\ddot{\theta}_{xtrunnion} = \frac{g_o}{20.149''}(a_3 - a_6), \tag{4.15}$$

$$\ddot{\theta}_{xaircraft} = \frac{g_o}{35.5''}(a_7 - a_{10}), \tag{4.16}$$

$$\ddot{\phi}_{y2-3} = \frac{g_o}{6.5''}(a_6 - a_7), \tag{4.17}$$

$$\ddot{\phi}_{y1-4} = \frac{g_o}{6.5''}(a_3 - a_{10}), \tag{4.18}$$

$$\ddot{\beta}_{ztrunnion} = \frac{g_o}{20.149''}(a_2 - a_5), \tag{4.19}$$

$$\ddot{\beta}_{zaircraft} = \frac{g_o}{35.5''}(a_8 - a_{11}). \tag{4.20}$$

Once these acceleration time histories were calculated from the respective individual acceleration sensor channels the stable low gravity time was determined from the individual time histories. This low gravity time slice of the trajectory is the acceleration time history which must be processed in order to calculate the individual autospectra and the respective single axis frequency response curves for the inertial and relative control data sets.

The following two data sets were taken from the same flight test. The first data set processed was under relative control where the second data set was processed with the same relative parameters as the first but the inertial control loops closed during the low gravity trajectory. Again, since each trajectory can have substantially different initial conditions, the data was processed by determining the stable low gravity portion of each trajectory, and at which time the active feedback and or feedback/feedforward loops were closed, during these trajectories. This was accomplished by using the acceleration time histories of the isolated payload and determining when the initial acceleration spike occurred, giving the time reference of the controlled isolation period. In addition to the beginning of the processible acceleration time history, the duration of this acceleration data set must be determined because each trajectory is subject to different operating environments which therefore, determine the overall time of each trajectory as well as the controllability of each maneuver by the pilots. The termination of each acceleration time history was determined by reviewing the total acceleration time trace and viewing a second acceleration spike on the isolation system which noted a wall-to-wall contact. Each acceleration channel for the respective trajectory was reviewed and the time slice with no acceleration spikes for all six acceleration output channels was used to process the frequency response curves and their respective autospectra. This of course ment that the overall spectral resolution would not be the same for the two trajectories compared. However, if three or more averages were available the frequency response functions were stable. Since the frequency domain is used for these calculations the trajectories can be compared to one another in the bandwidth defined by the total time history processed and the sampling frequency of the data

acquisition system. Figure 4.19 (a) and (b) gives the overall acceleration time trace for a vertically mounted accelerometer on the trunnion support frame, where the entry/ low gravity/ exit phases can be seen for the relative control and the inertial control trajectories, respectively. Figure 4.20 (a) and (b) show the acceleration time trace of a vertically mounted accelerometer attached to the isolated system showing the period of control as well as the end of the process time history to be used for both trajectories, respectively. These two time slices for the relative and inertial control were used to generate the following frequency response curves for the X, Y, and Z dimensions and their respective rotations. For brevity, only the frequency response curves for the locations and the rotational definitions, as defined previously, will be given in this chapter. The associated autospectral densities of each frequency response curve is given in Appendix F.

The time history processed for the relative case had a total time window of 16 seconds where 760 points per ensemble average were used giving a spectral resolution of 381 lines for a frequency window from 0.01 to 75 Hz. The inertial time history had a total window time of 9.5 seconds where 600 points per ensemble average was used giving a spectral resolution of 301 lines for the same frequency window. Each frequency response curve was calculated with a 50 percent Hanning window and the relative data set used five spectral averages where the inertial data set had three spectral averages. This caused the inertial frequency curves to be slightly more choppy however, comparisons in the frequency response curves could be made over the operational bandwidth of 0.1 to 75 Hz. From the total time history of 16 and 9.5 seconds for the relative and inertial control trajectories, respectively, a sampling rate per channel of 142 Hz gives a total of 2272 and 1349 points available for a spectral average. Therefore, for the relative case with a 760 point per ensemble average, the frequency resolution limit is 0.19 Hz while for the inertial trajectory a 600 point per ensemble average gives a frequency resolution limit of 0.24 Hz. Figures 4.21 through 4.24 (a) and (b), give the frequency response curves for the X direction for the single input reference locations one through four for both trajectories, respectively. Figures 4.25 through 4.28 (a) and (b) give the frequency response

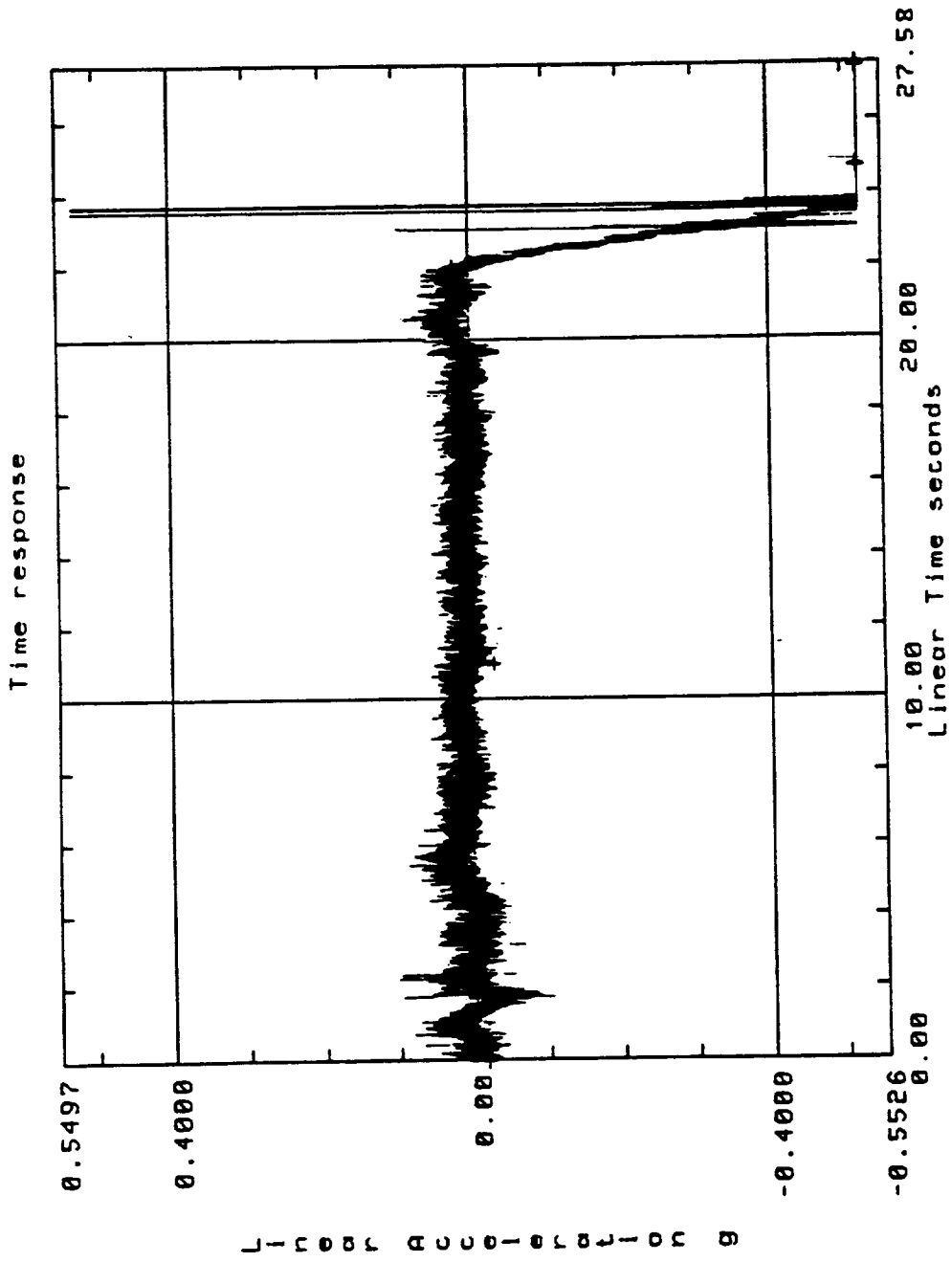

(a) Payload under relative control.

Figure 4.19: Acceleration time trace of full trajectory for aircraft mounted accelerometer.

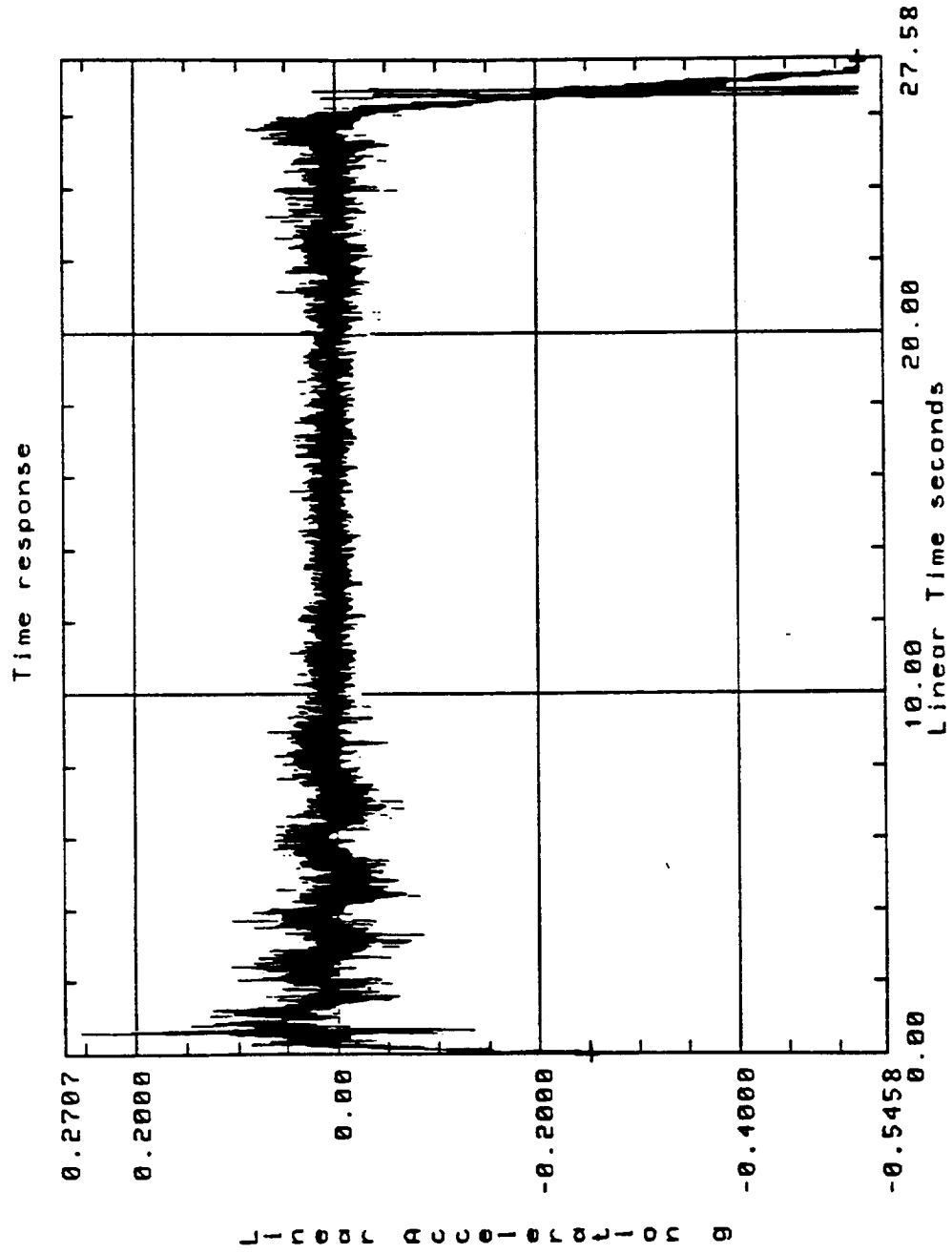

(b) Payload under inertial control.

Figure 4.19: Acceleration time trace of full trajectory for aircraft mounted accelerometer.

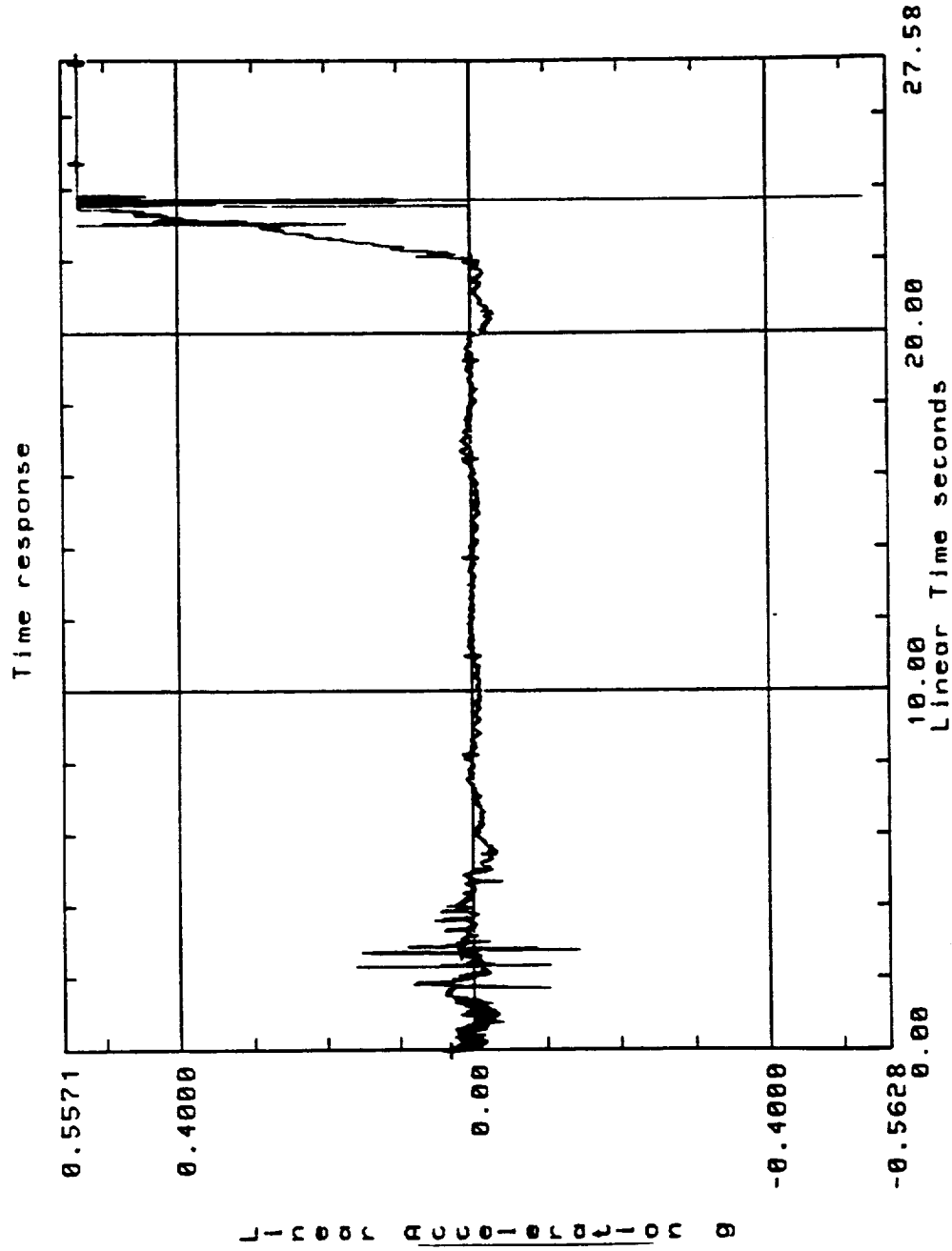

(a) Payload under relative control.

Figure 4.20: Acceleration time trace of full trajectory for platform mounted accelerometer.

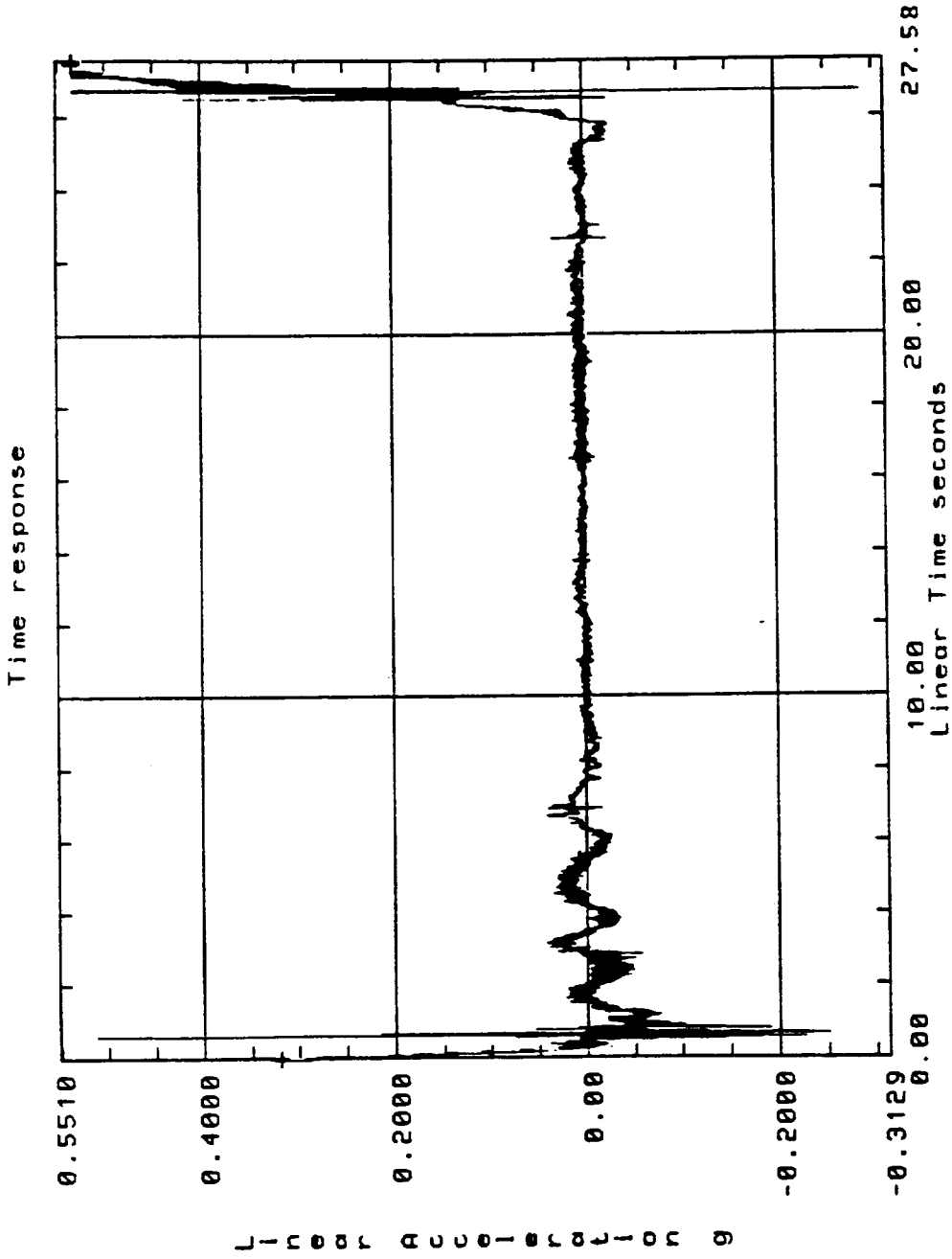

(b) Payload under inertial control.

Figure 4.20: Acceleration time trace of full trajectory for platform mounted accelerometer.

curves for the Y direction, and Figures 4.29 through 4.32 (a) and (b) give the frequency response curves for the Z direction, for the single input reference locations one through four for both trajectories. Figures 4.33 and 4.34 (a) and (b) give the frequency response curves for the θ_X rotation for the trunnion location and the aircraft location, respectively. Figures 4.35 and 4.36 (a) and (b) give the frequency response curves for the ϕ_Y rotations as defined in equations (4.17) and (4.18), and Figures 4.37 and 4.38 (a) and (b) are the frequency response curves for the β_Z rotation as defined in equations (4.19) and (4.20). The response functions have been plotted with the same minimum and maximum values for both trajectories. This data will be discussed in the next chapter under data analysis and discussions.

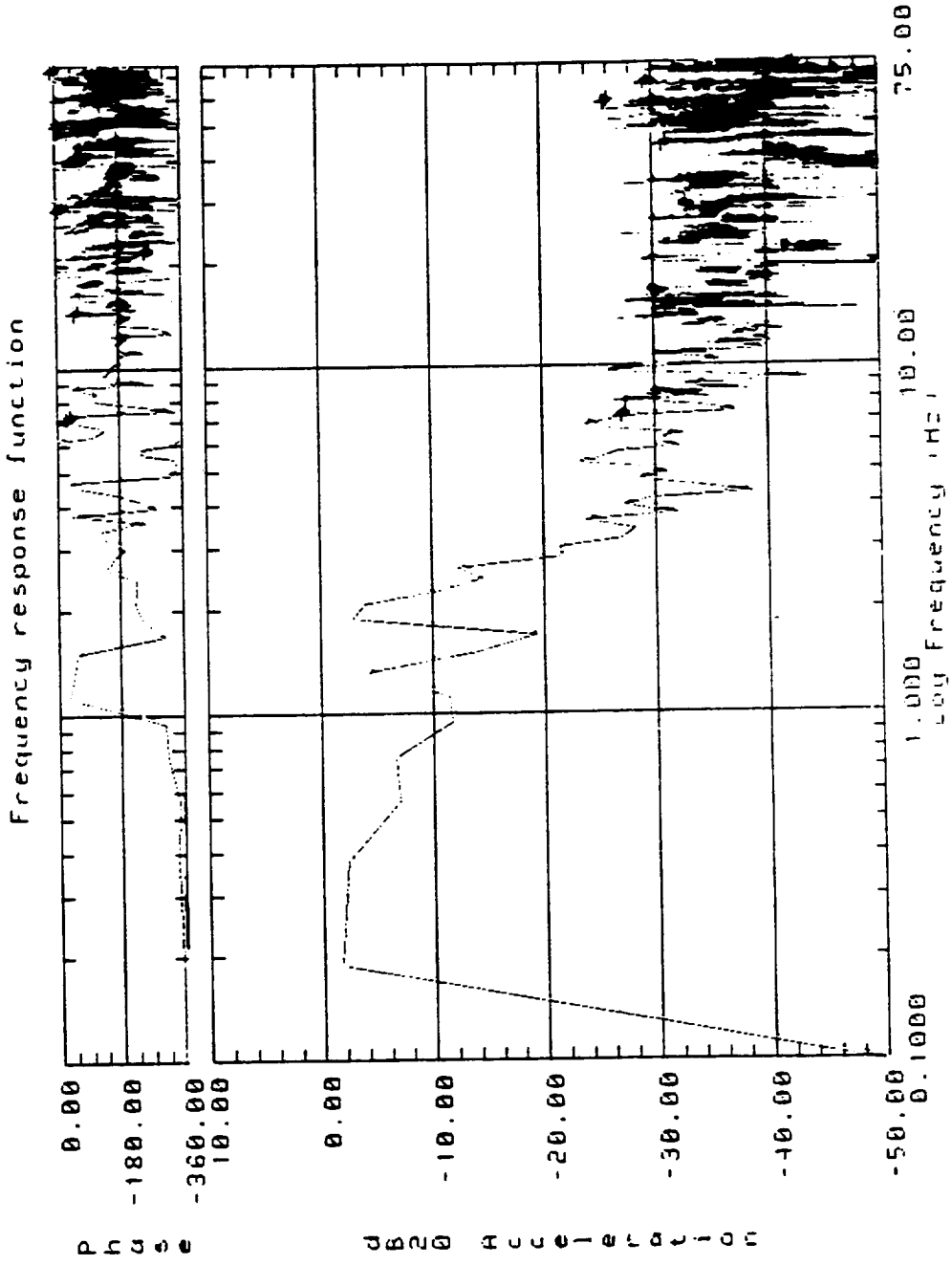

(a) Relative control of platform.

Figure 4.21: Transfer function calculation for platform x vs. aircraft location 1 x.

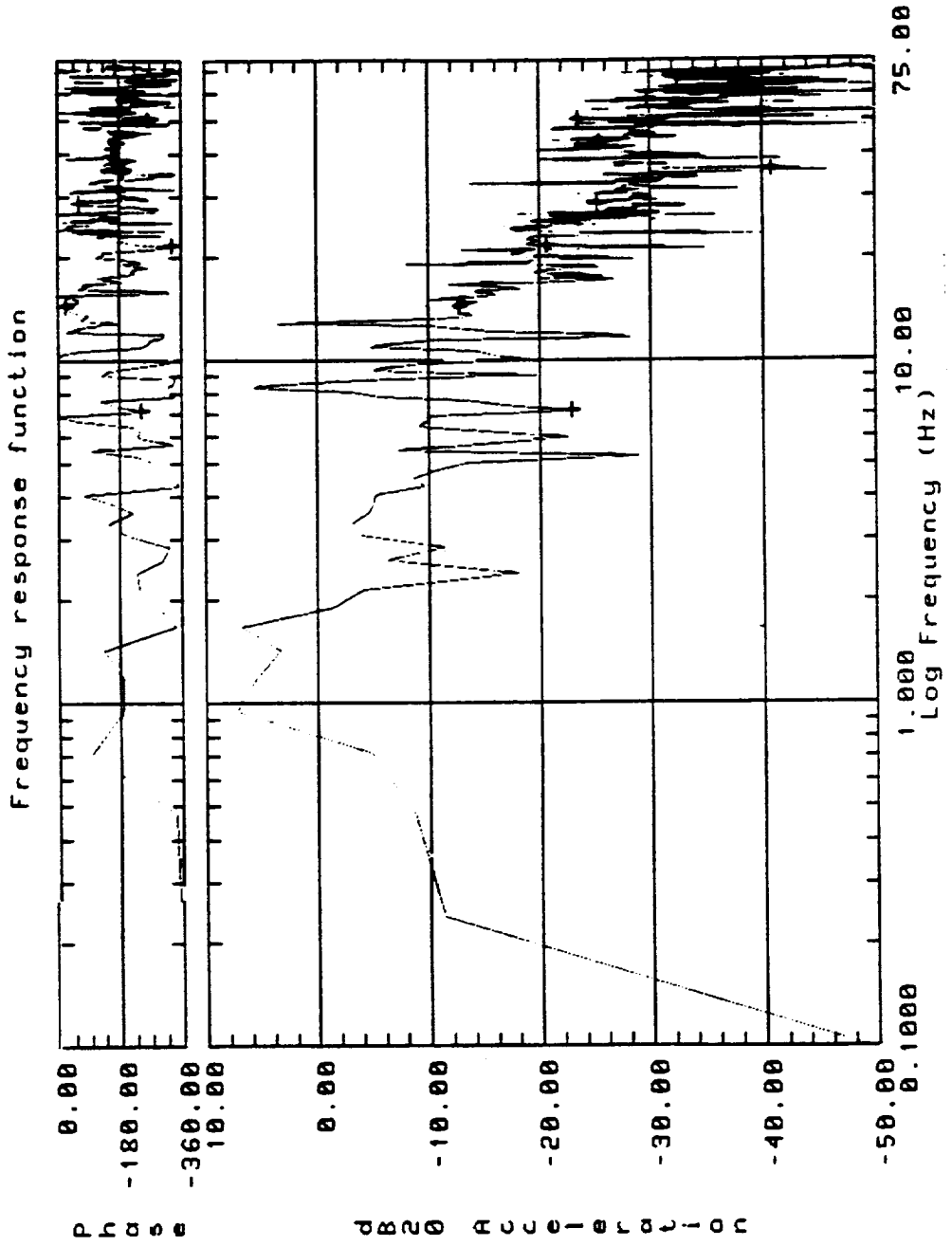

(b) Inertial control of platform.

Figure 4.21: Transfer function calculation for platform x vs. aircraft location 1 x.

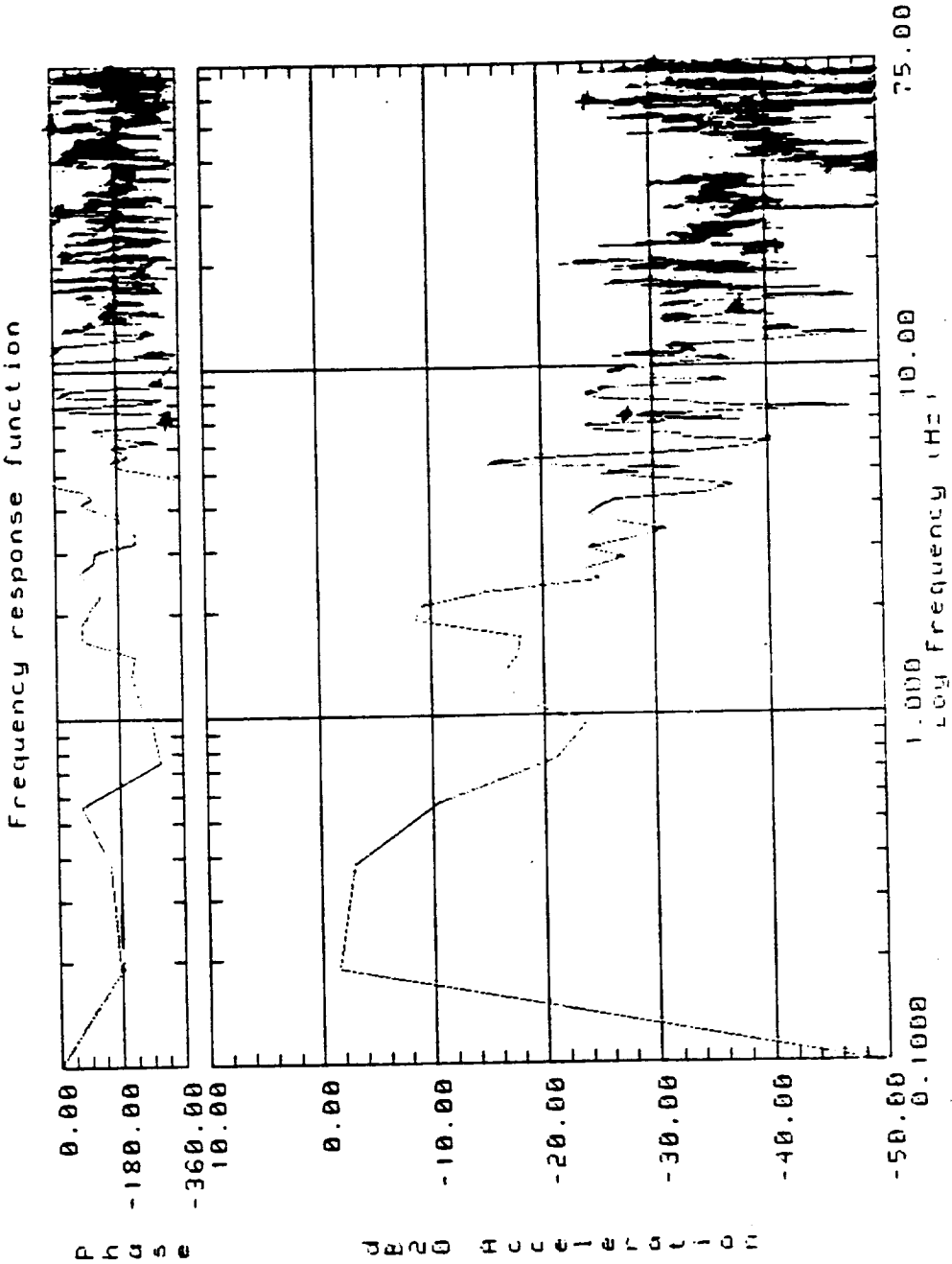

(a) Relative control of platform.

Figure 4.22: Transfer function calculation for platform x vs. aircraft location 2 x.

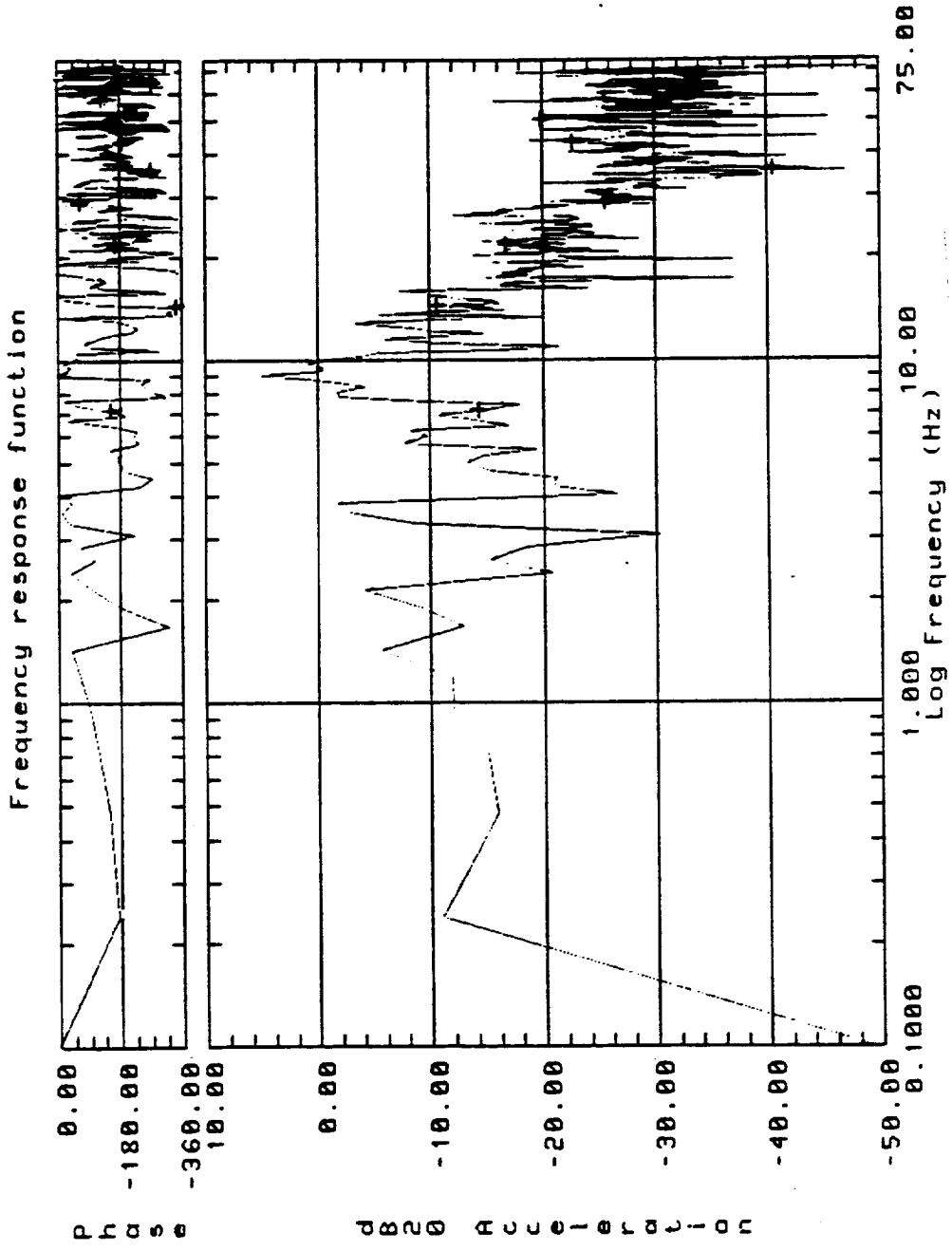

(b) Inertial control of platform.

Figure 4.22: Transfer function calculation for platform x vs. aircraft location 2 x.

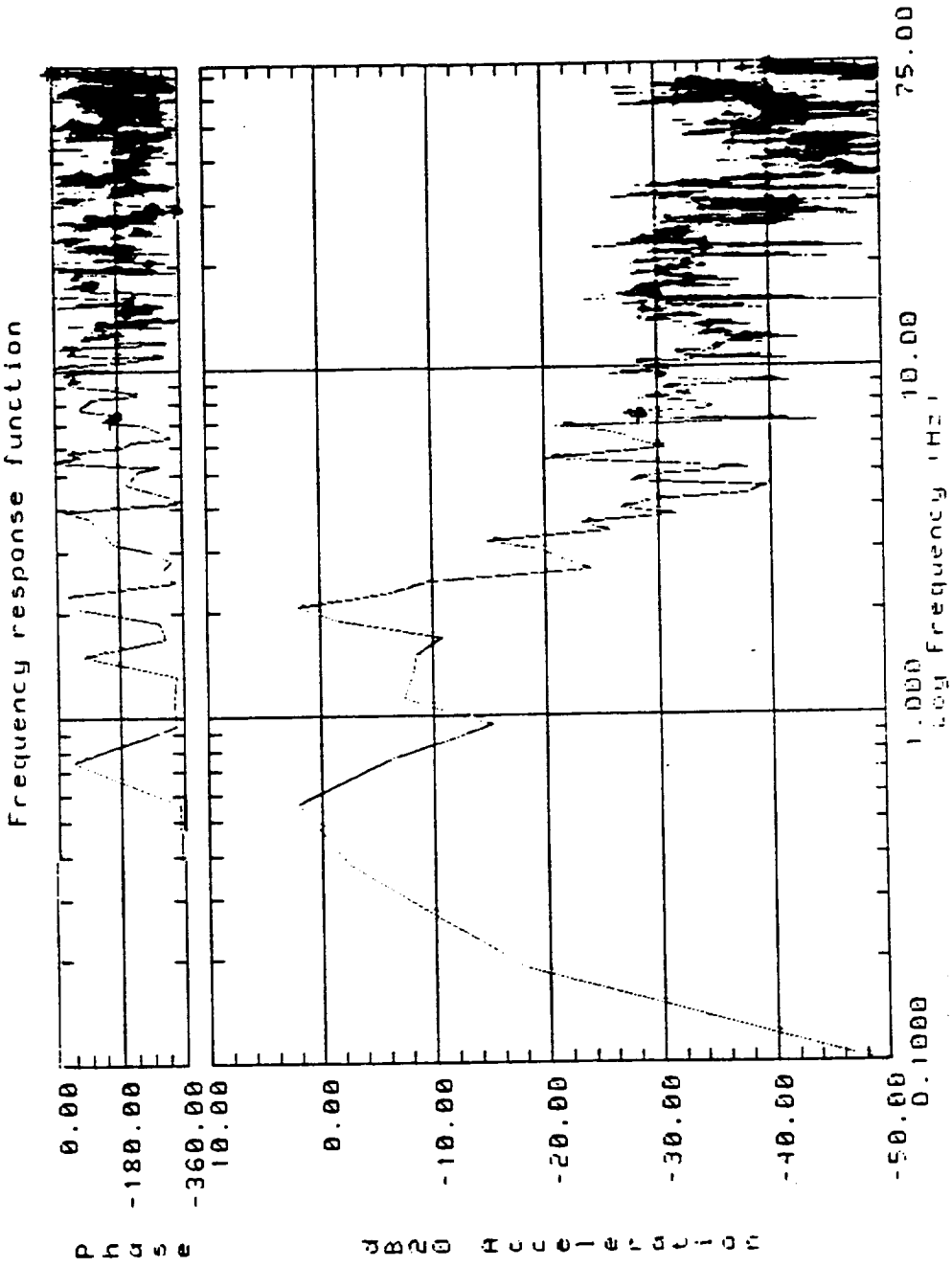

(a) Relative control of platform.

Figure 4.23: Transfer function calculation for platform x vs. aircraft location 3 x.

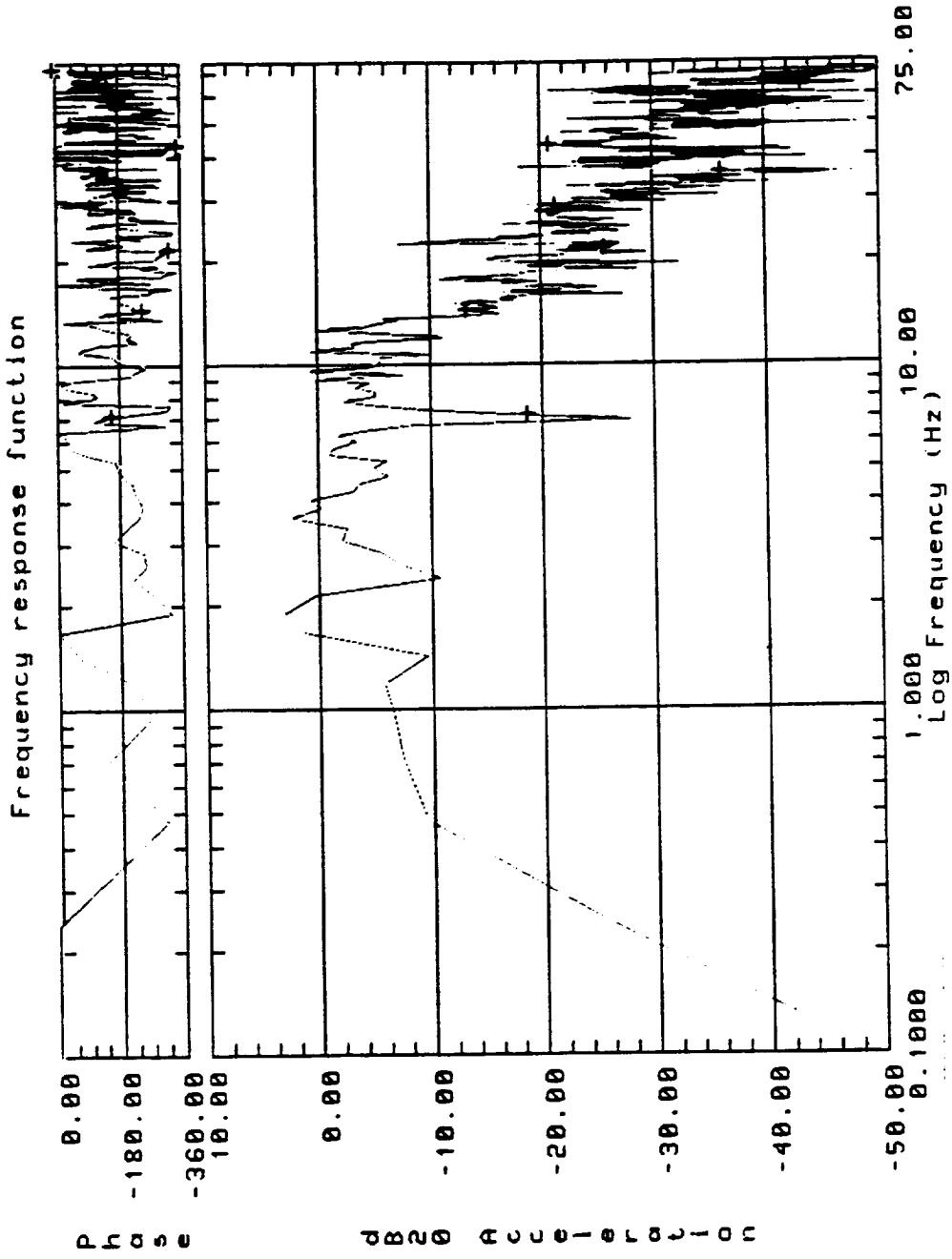

(b) Inertial control of platform.

Figure 4.23: Transfer function calculation for platform x vs. aircraft location 3 x.

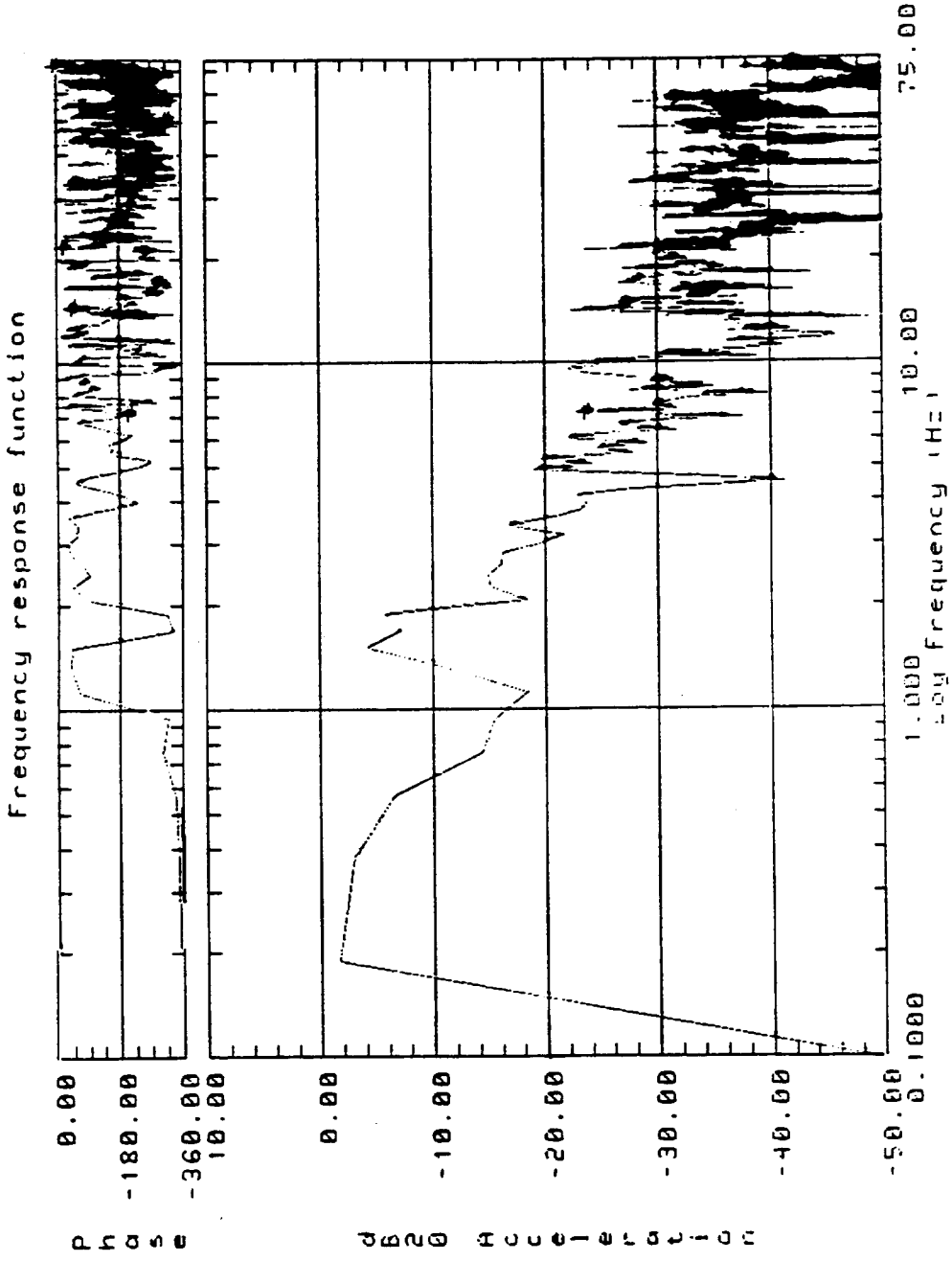

(a) Relative control of platform.

Figure 4.24: Transfer function calculation for platform x vs. aircraft location 4 x.

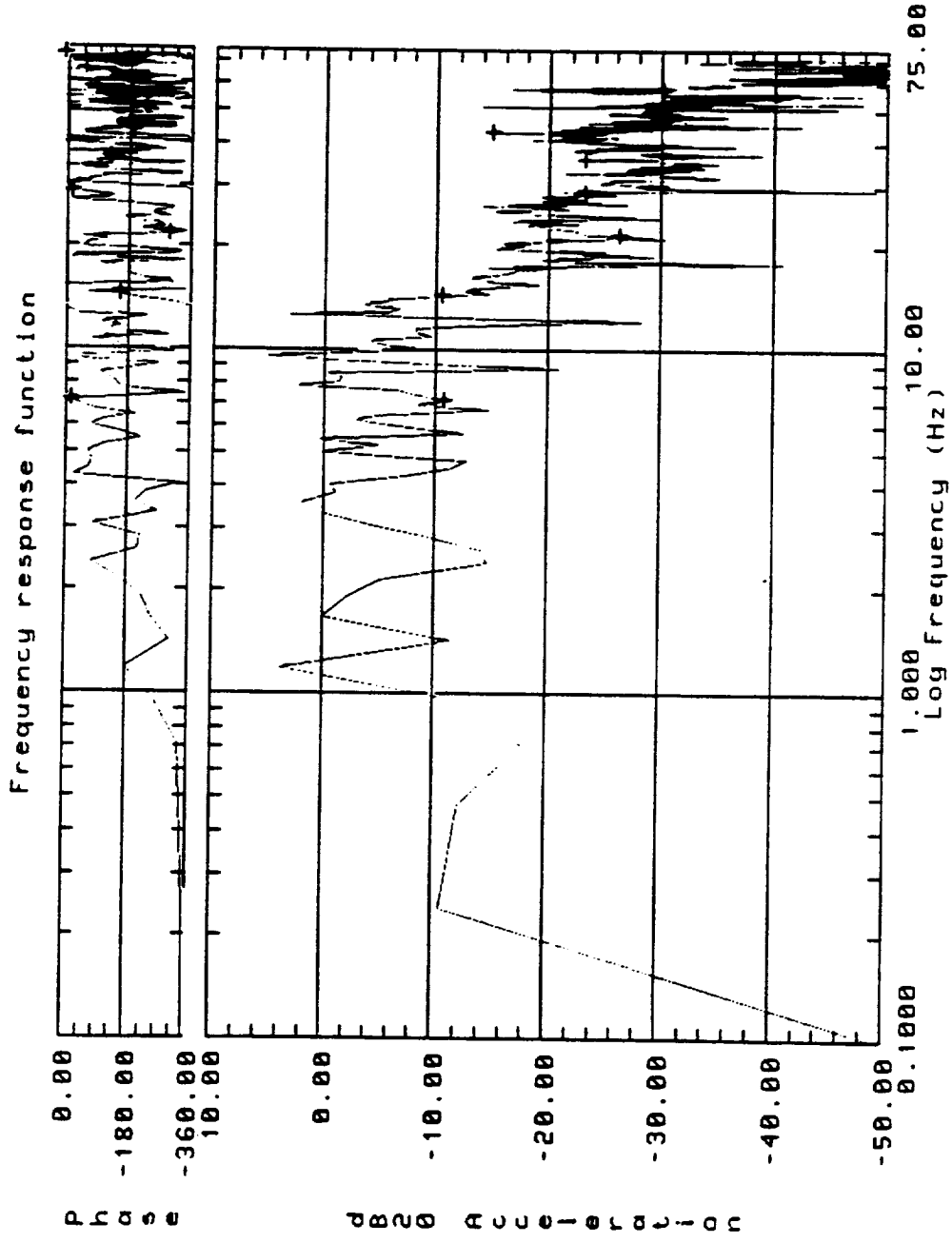

(b) Inertial control of platform.

Figure 4.24: Transfer function calculation for platform x vs. aircraft location 4 x.

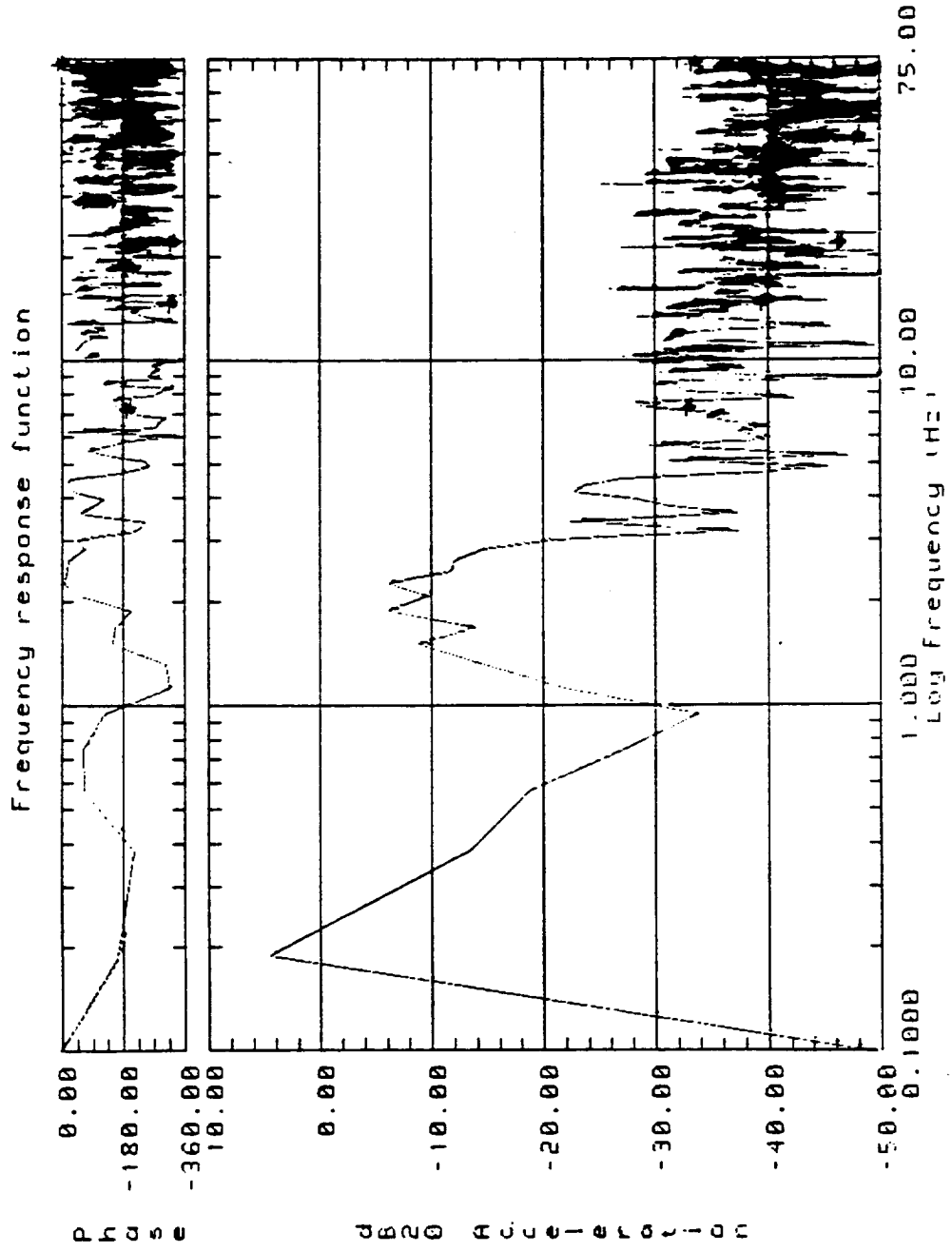

(a) Relative control of platform.

Figure 4.25: Transfer function calculation for platform y vs. aircraft location 1 y.

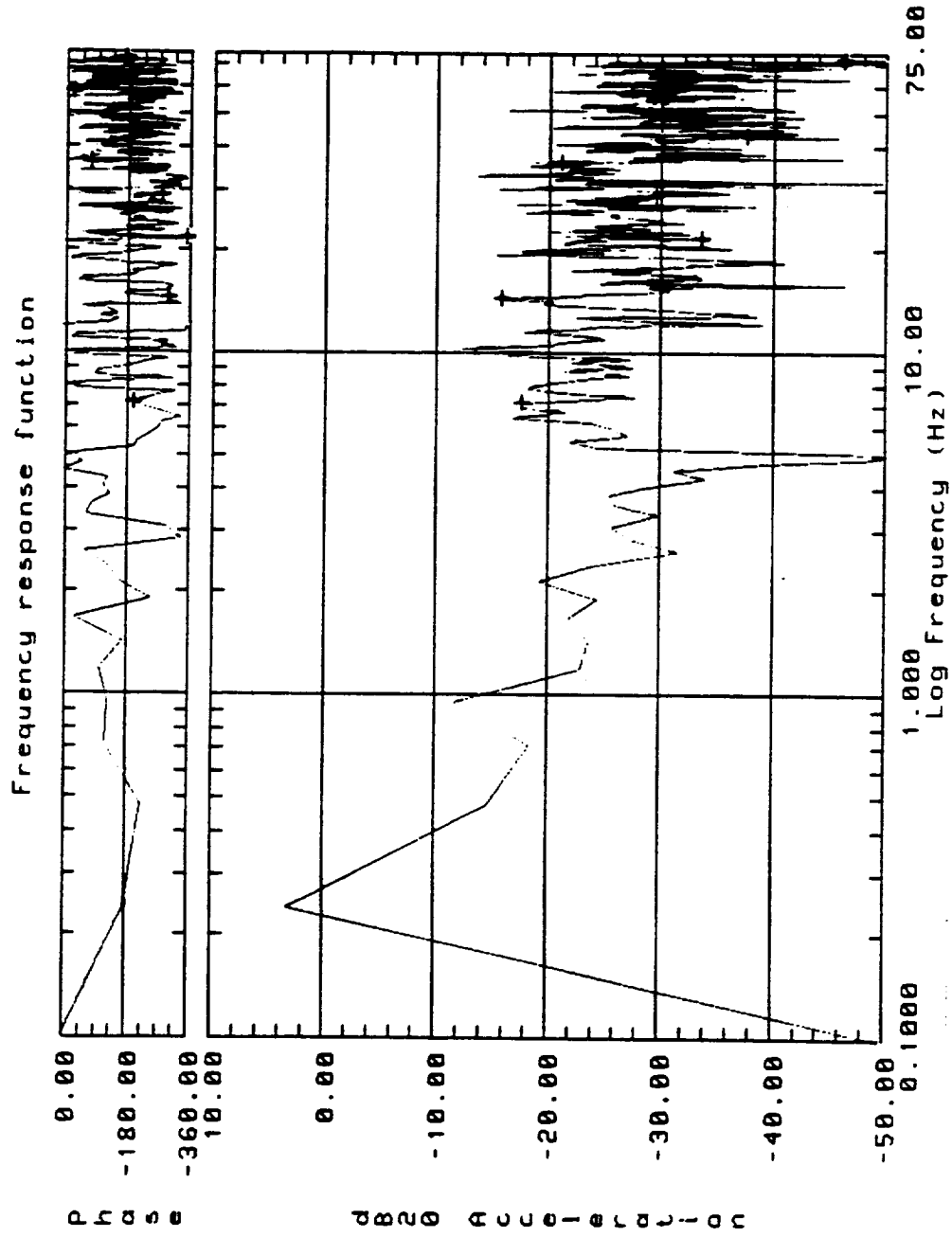

(b) Inertial control of platform.

Figure 4.25: Transfer function calculation for platform y vs. aircraft location 1 y.

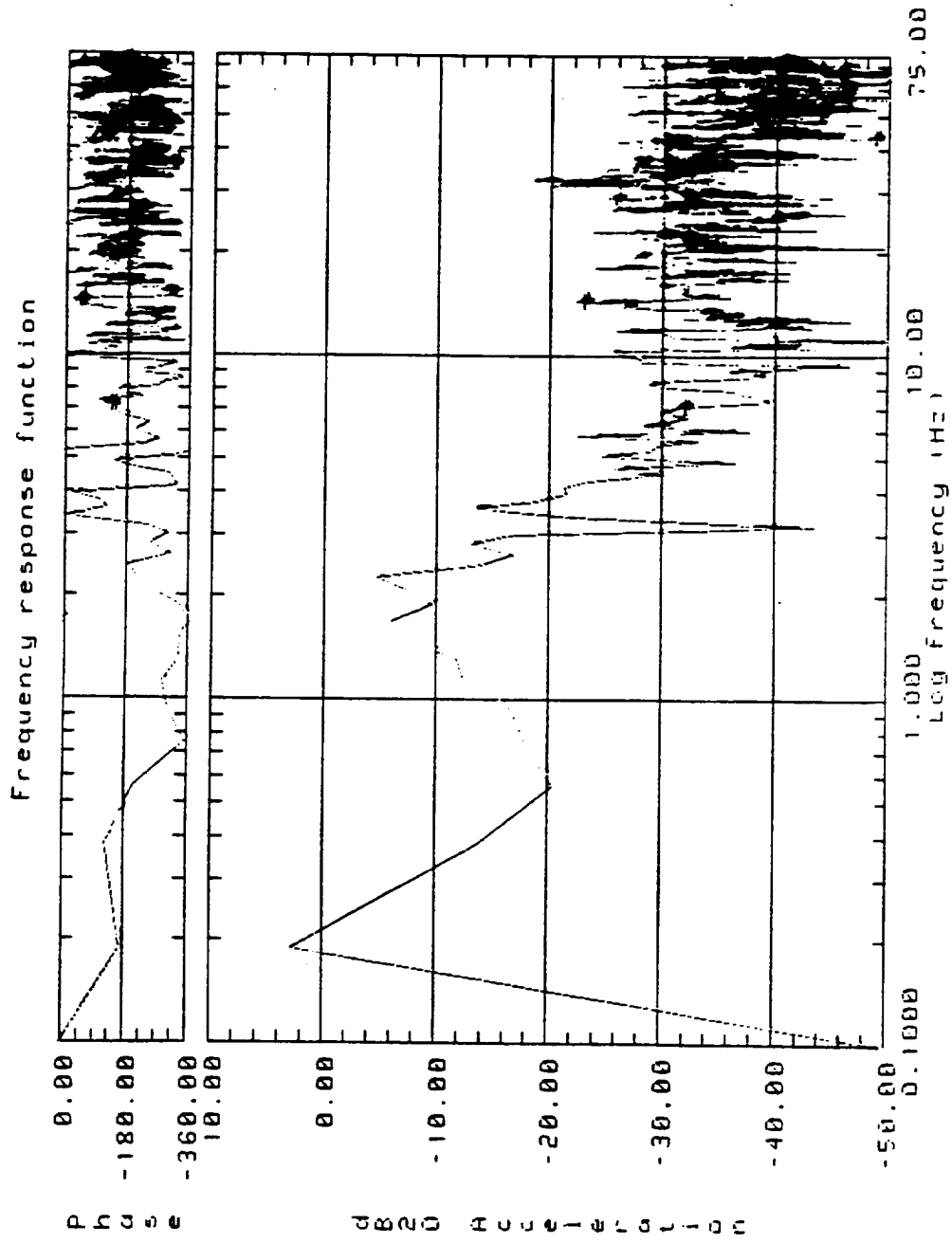

(a) Relative control of platform.

Figure 4.26: Transfer function calculation for platform y vs. aircraft location 2 y.

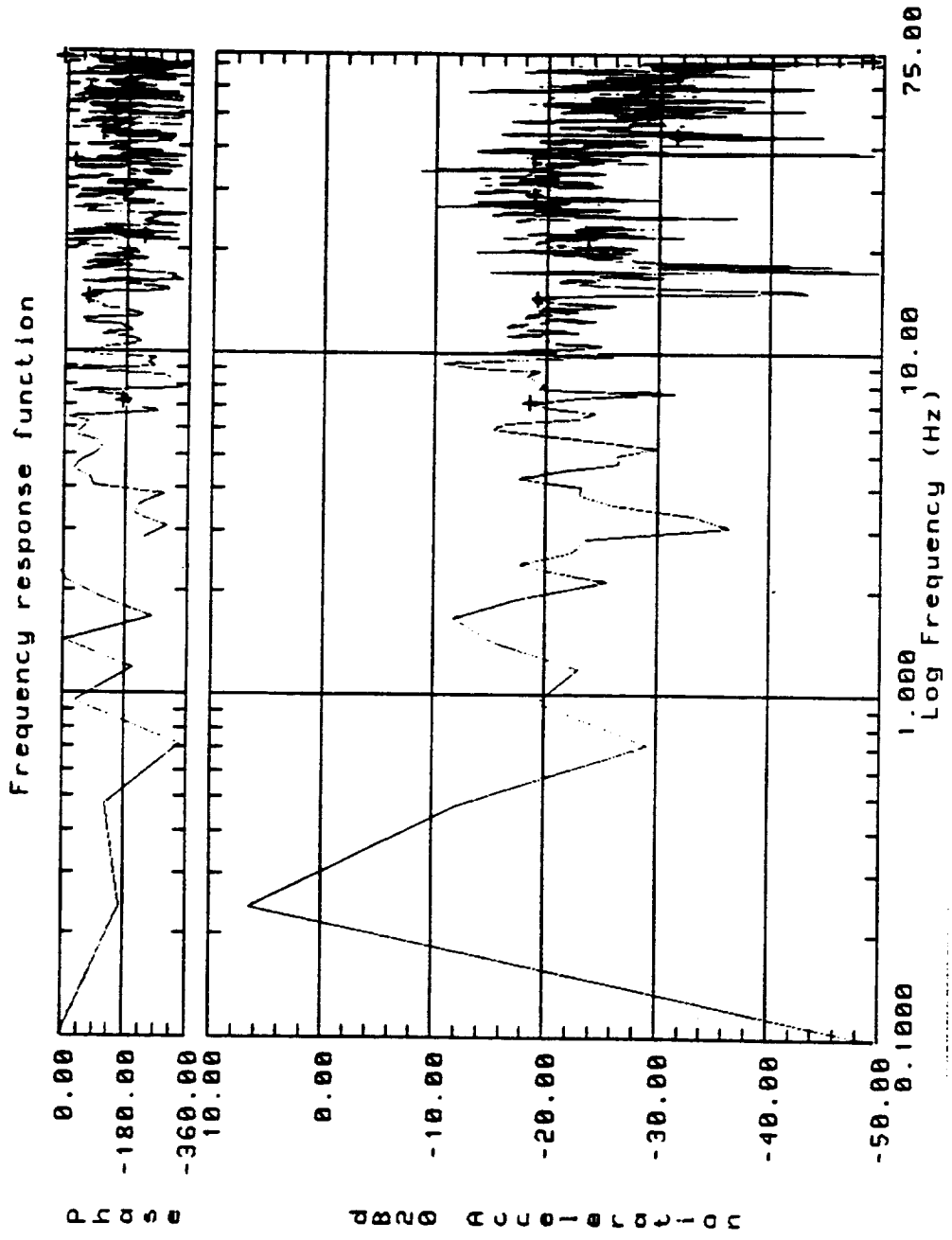

(b) Inertial control of platform.

Figure 4.26: Transfer function calculation for platform y vs. aircraft location 2 y.

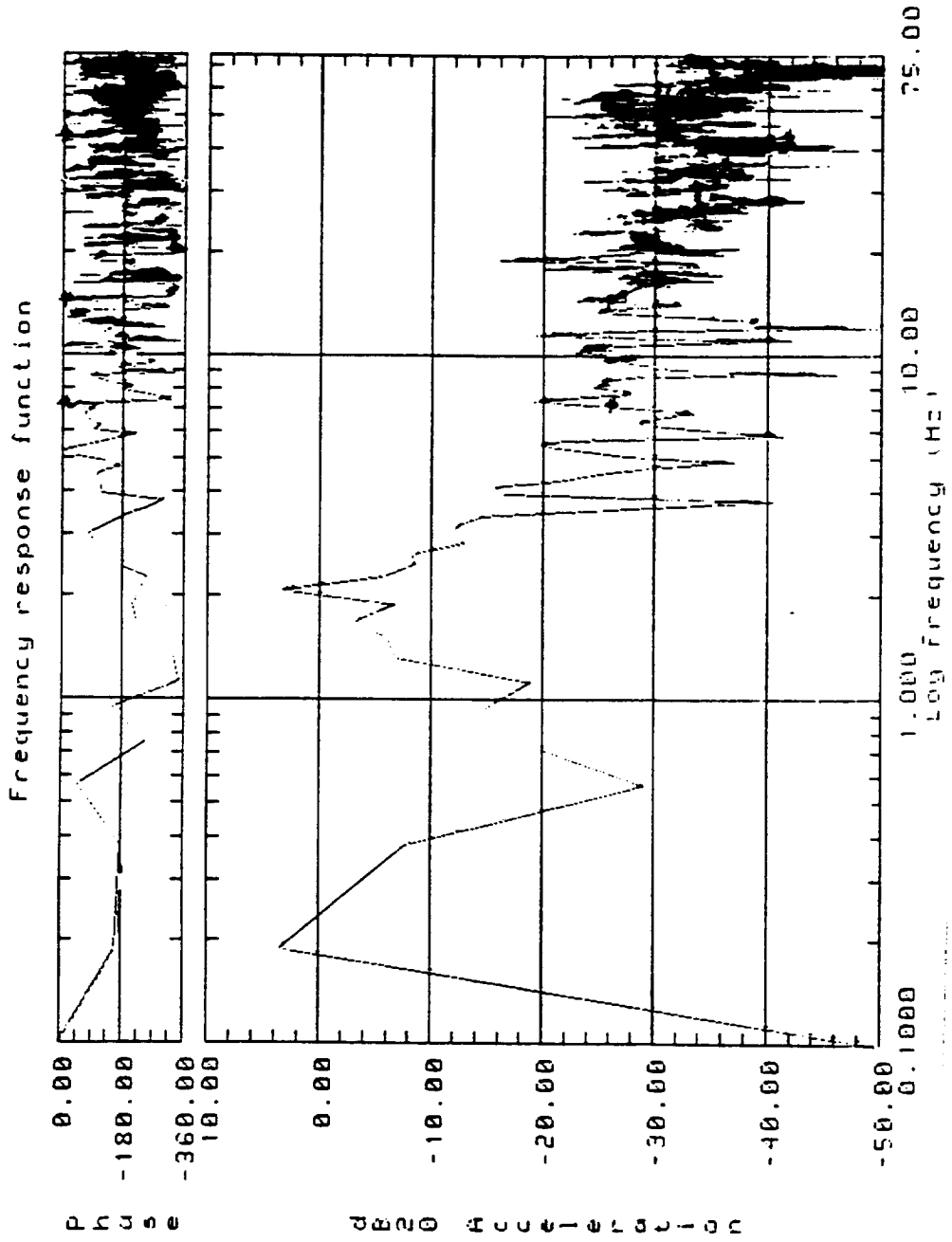

(a) Relative control of platform.

Figure 4.27: Transfer function calculation for platform y vs. aircraft location 3 y.

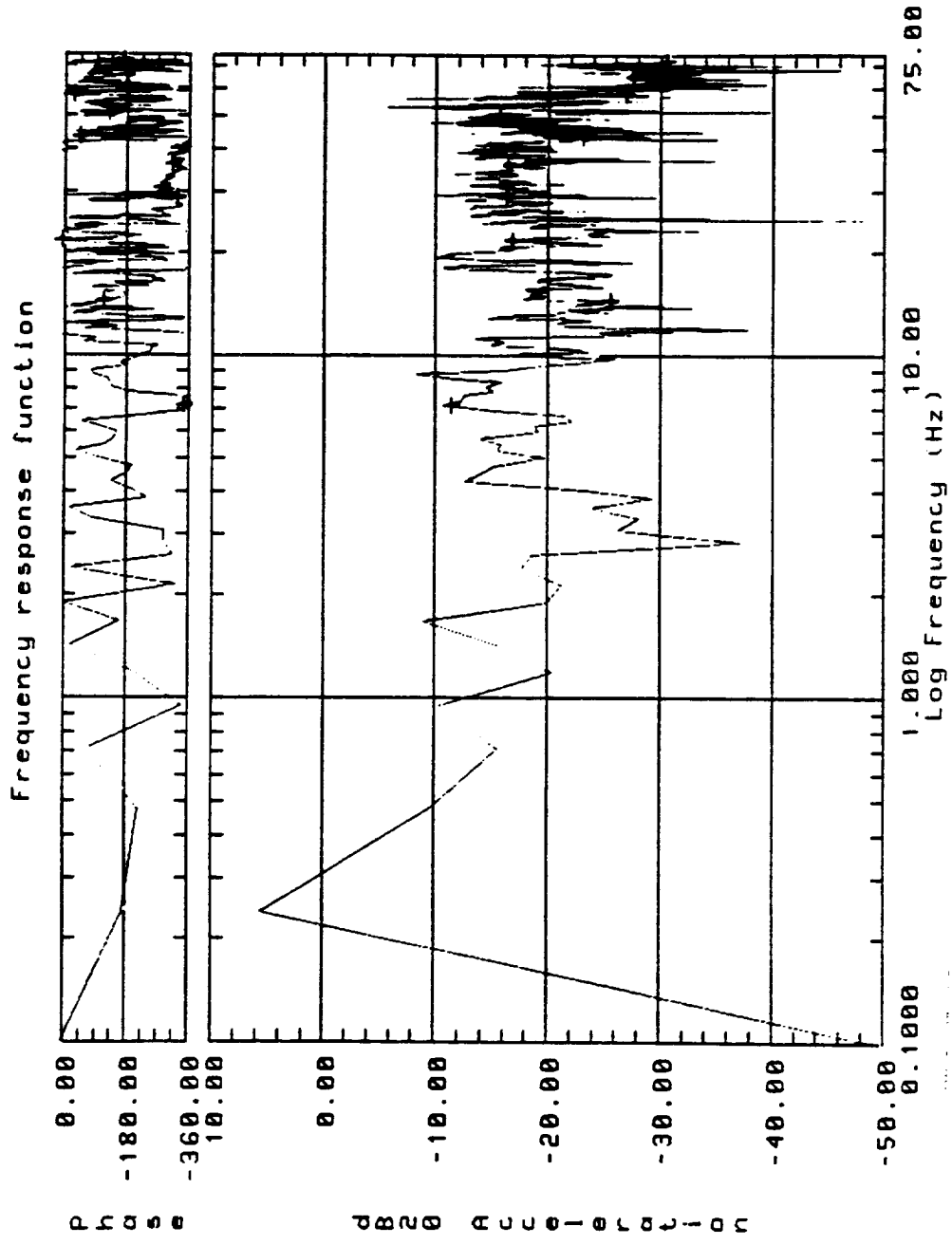

(b) Inertial control of platform.

Figure 4.27: Transfer function calculation for platform y vs. aircraft location 3 y.

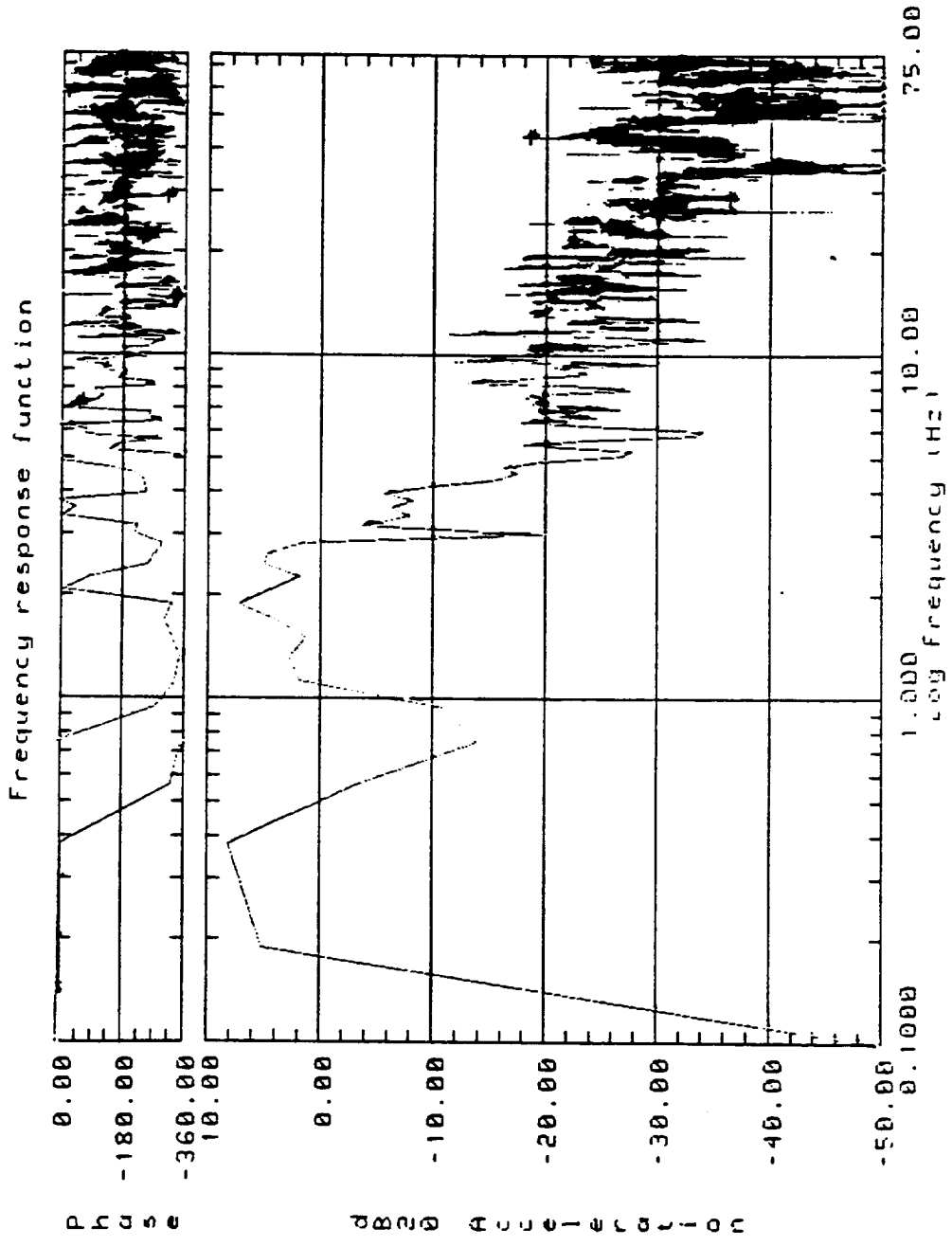

(a) Relative control of platform.

Figure 4.28: Transfer function calculation for platform y vs. aircraft location 4 y.

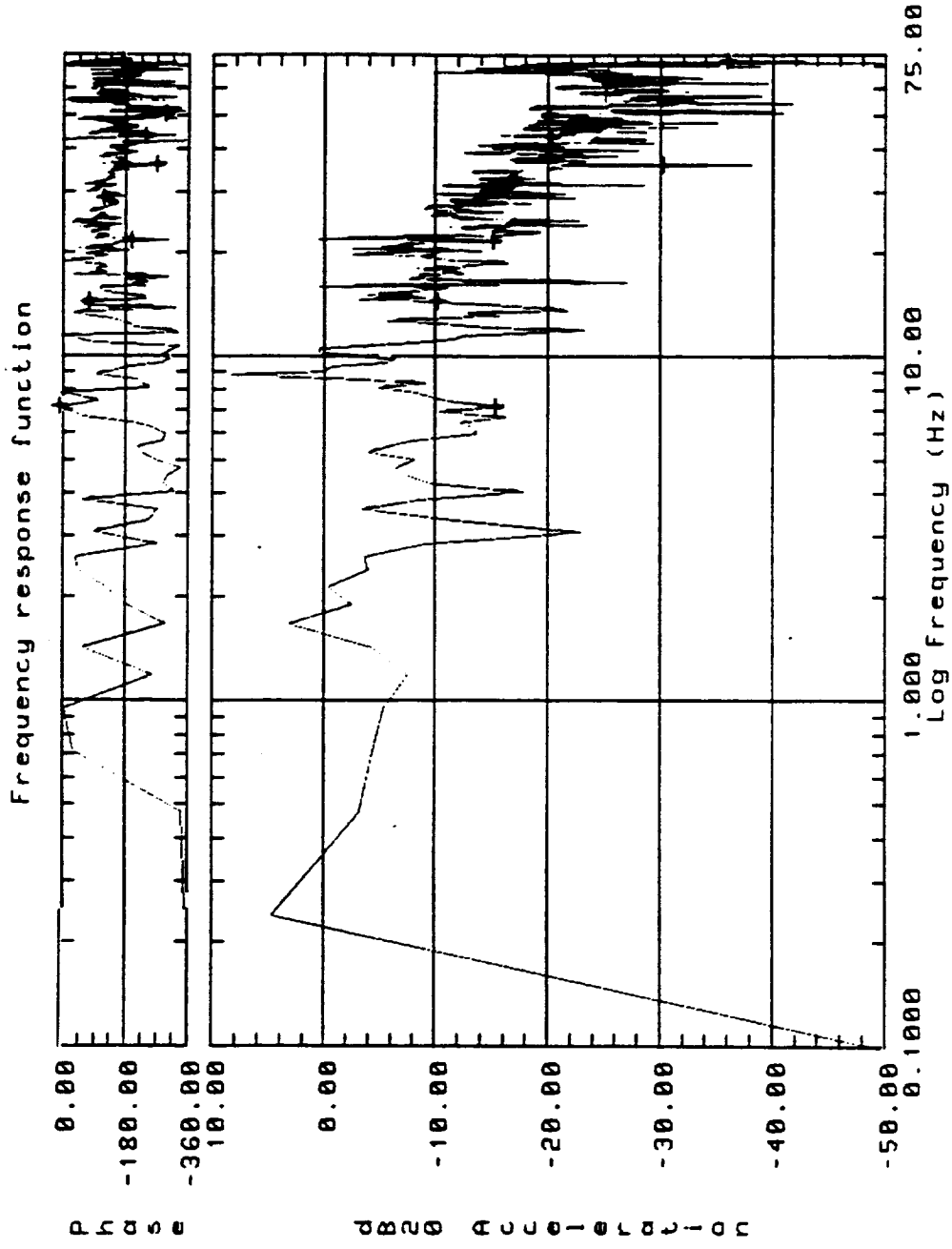

(b) Inertial control of platform.

Figure 4.28: Transfer function calculation for platform y vs. aircraft location 4 y.

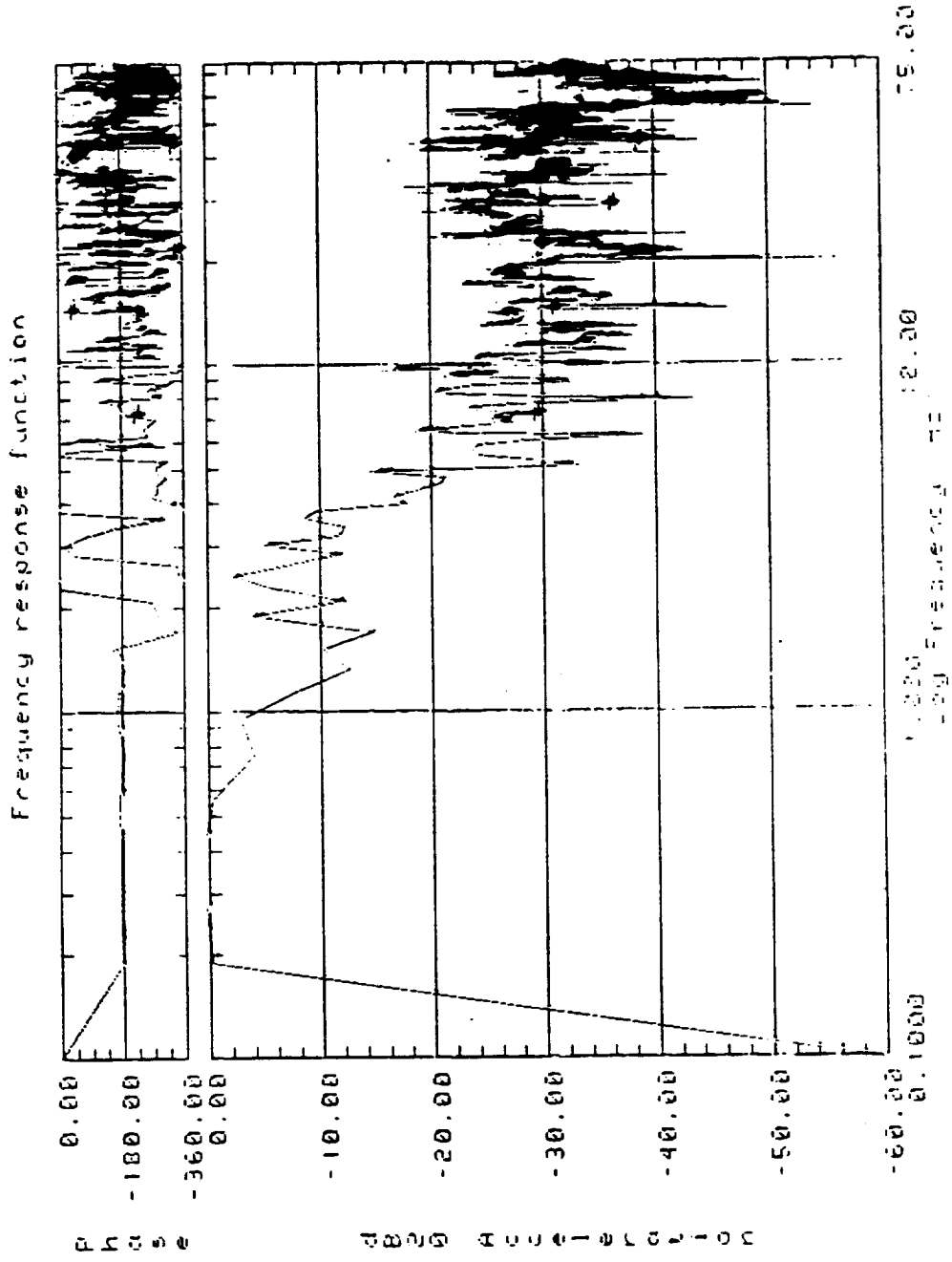

(a) Relative control of platform.

Figure 4.29: Transfer function calculation for platform z vs. aircraft location 1 z.

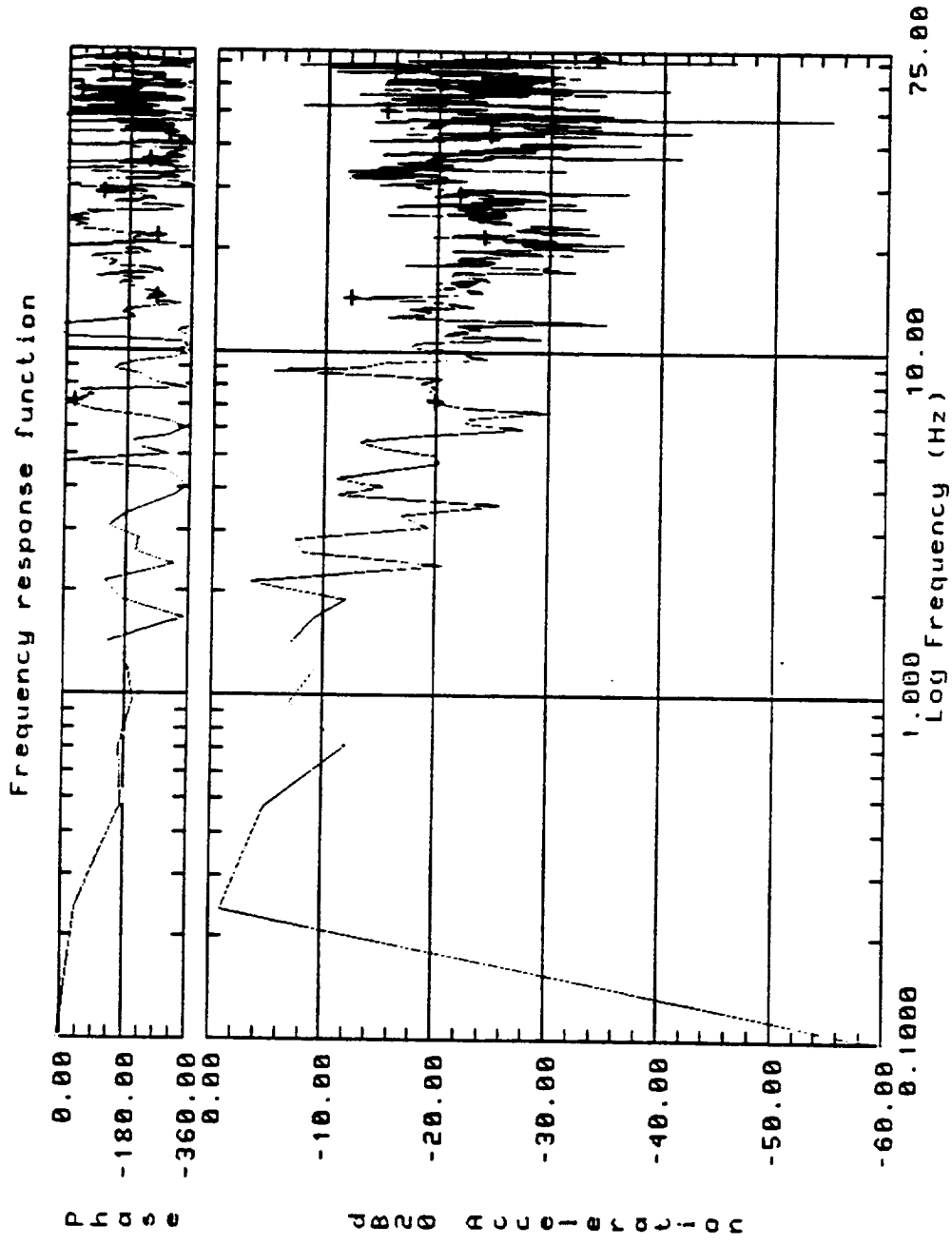

(b) Inertial control of platform.

Figure 4.29: Transfer function calculation for platform z vs. aircraft location 1 z.

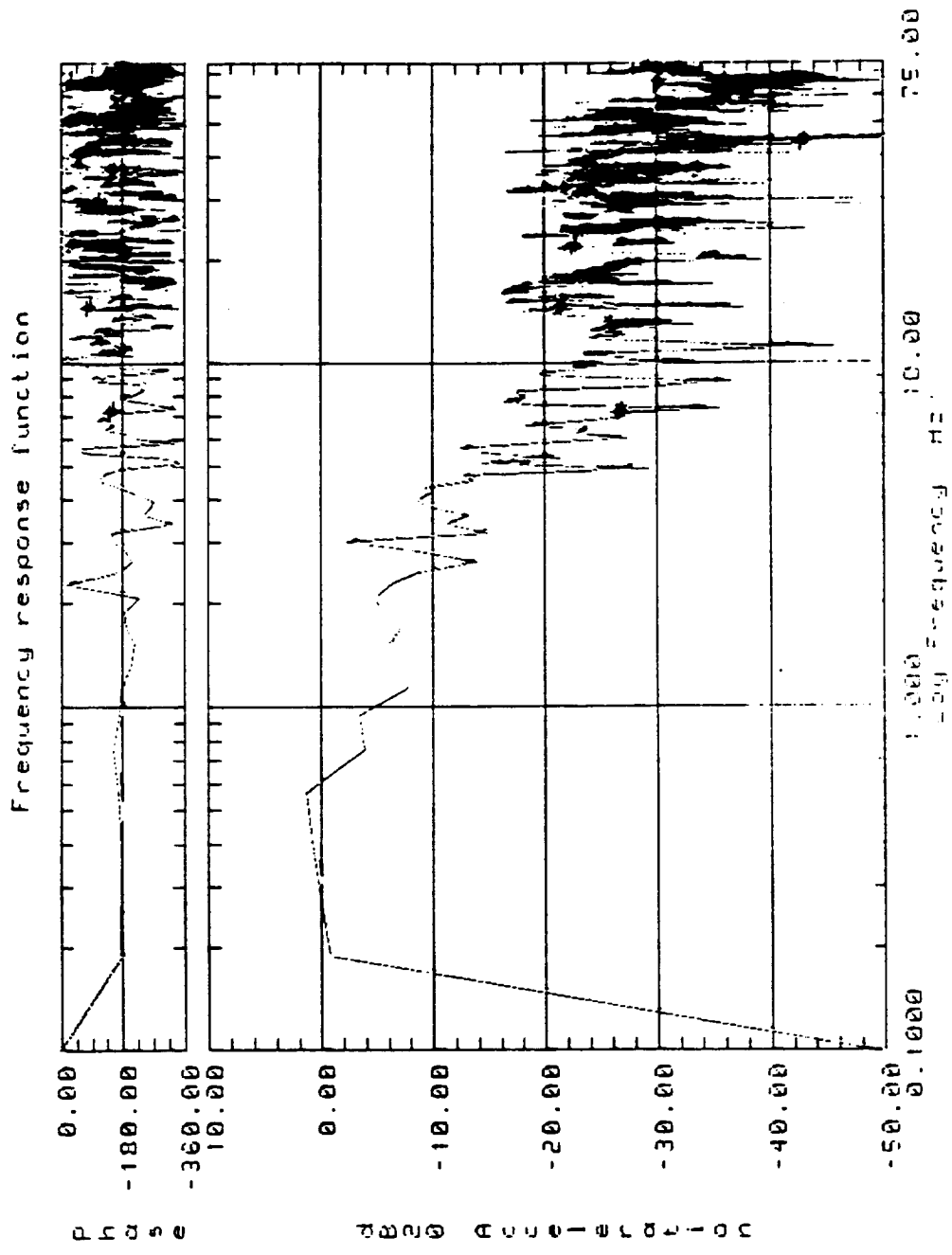

(a) Relative control of platform.

Figure 4.30: Transfer function calculation for platform z vs. aircraft location 2 z.

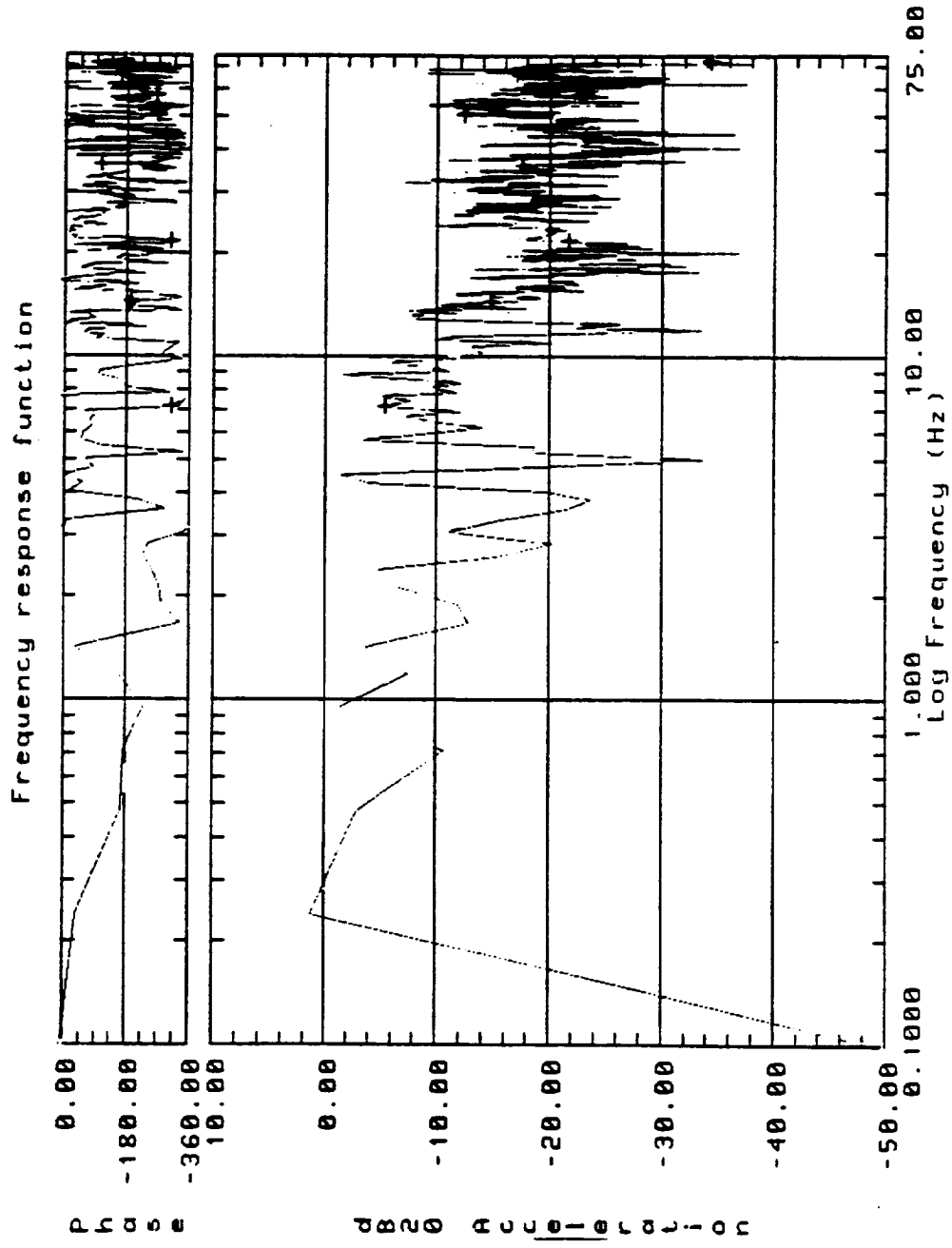

(b) Inertial control of platform.

Figure 4.30: Transfer function calculation for platform z vs. aircraft location 2 z.

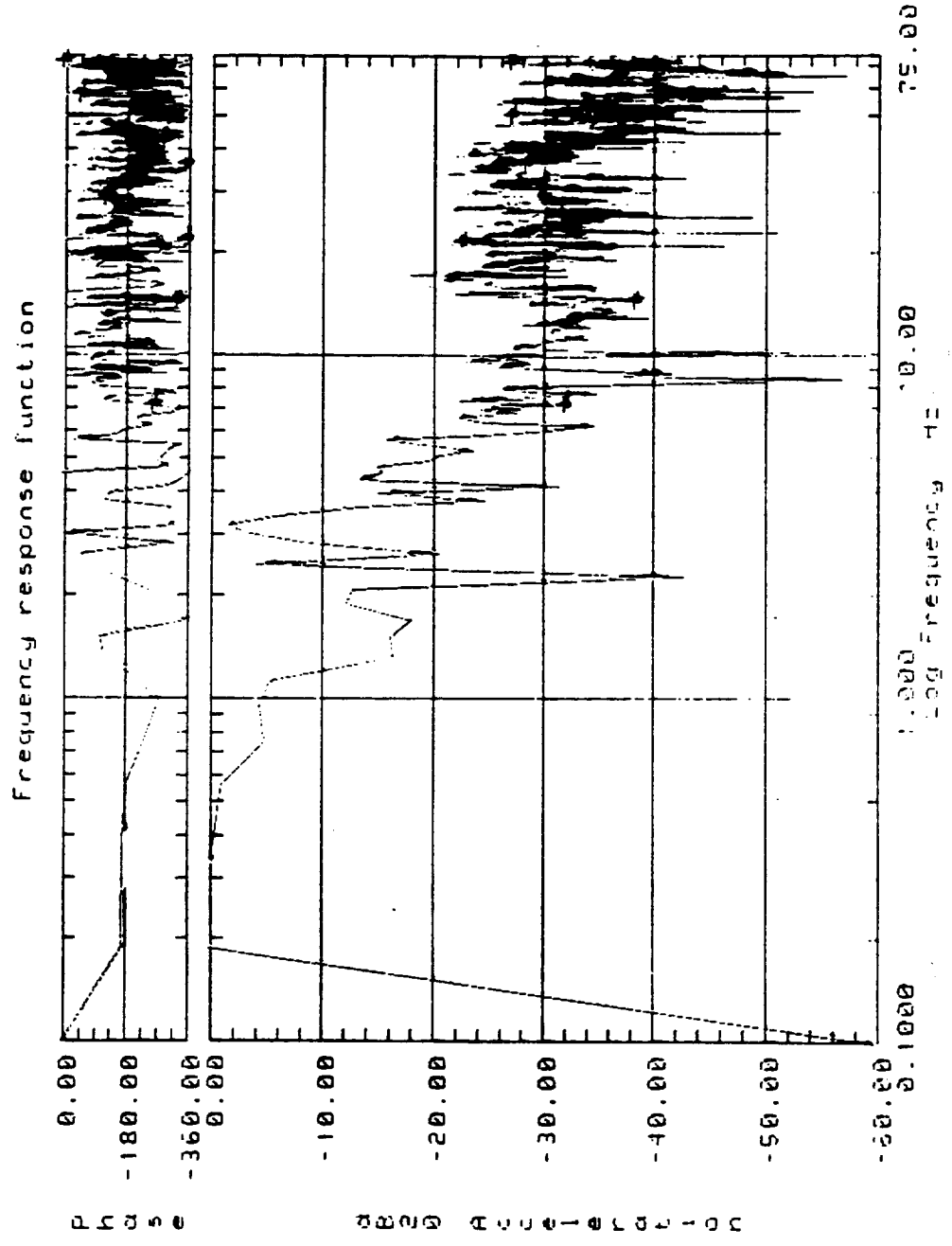

(a) Relative control of platform.

Figure 4.31: Transfer function calculation for platform z vs. aircraft location 3 z.

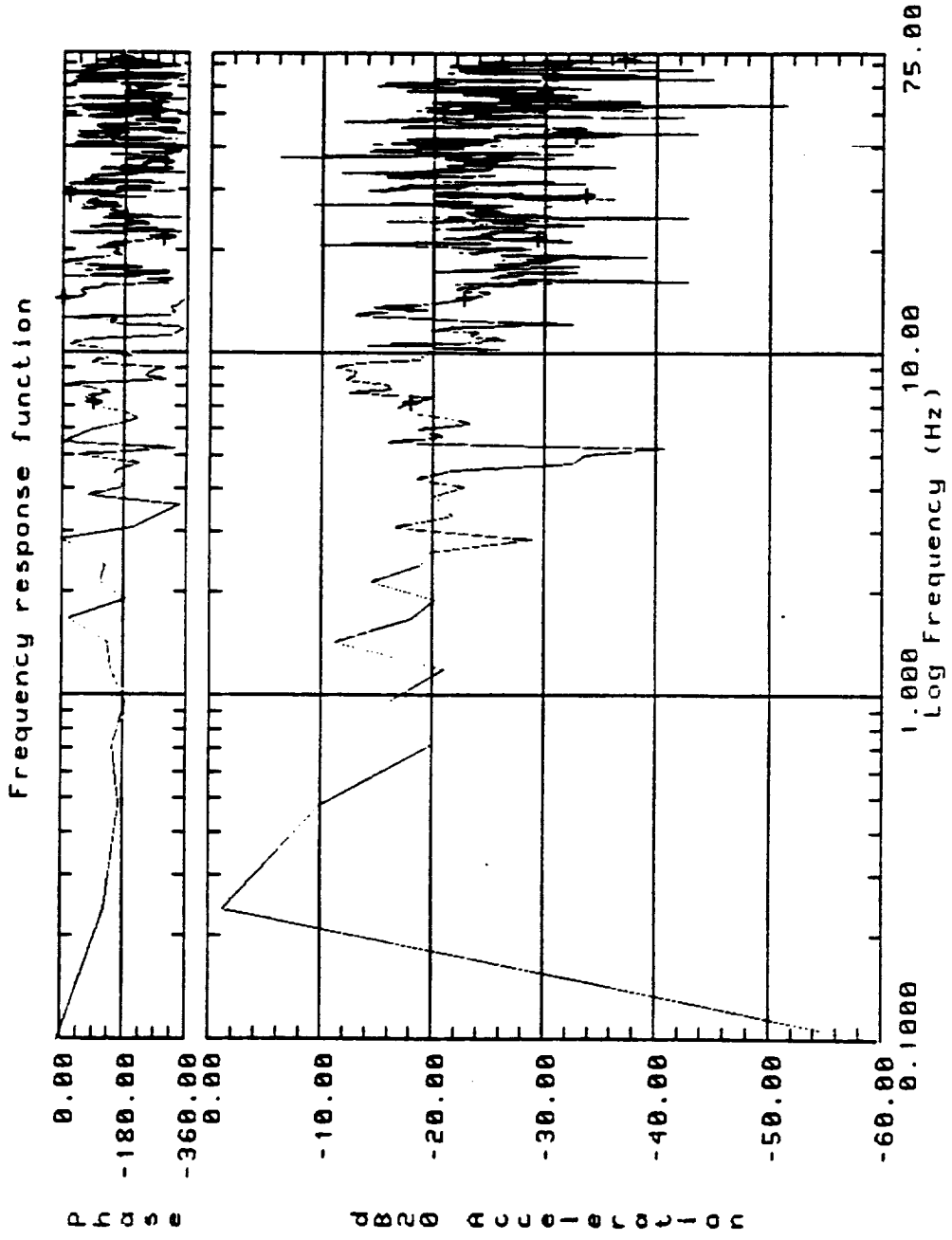

(b) Inertial control of platform.

Figure 4.31: Transfer function calculation for platform z vs. aircraft location 3 z.

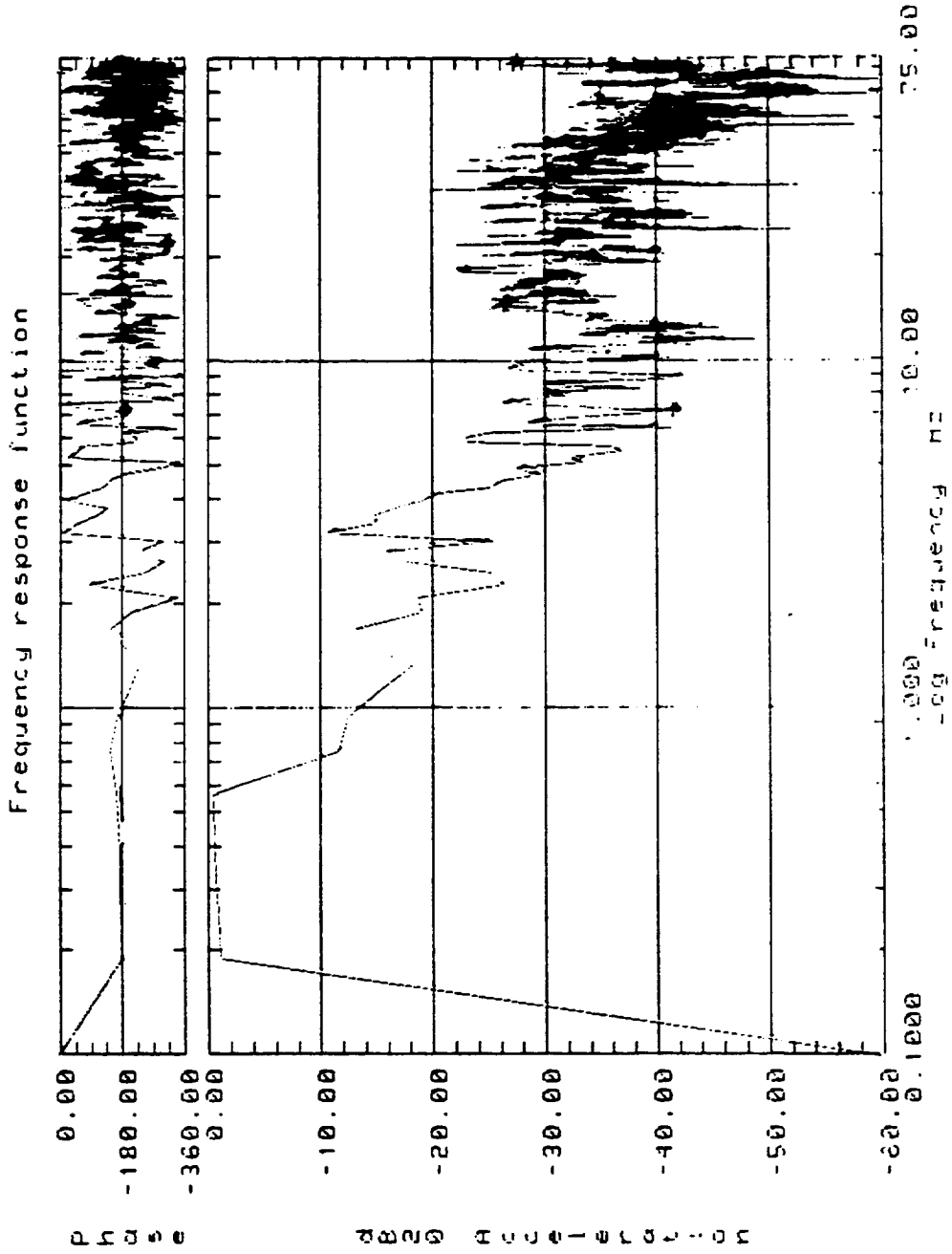

(a) Relative control of platform.

Figure 4.32: Transfer function calculation for platform z vs. aircraft location 4 z.

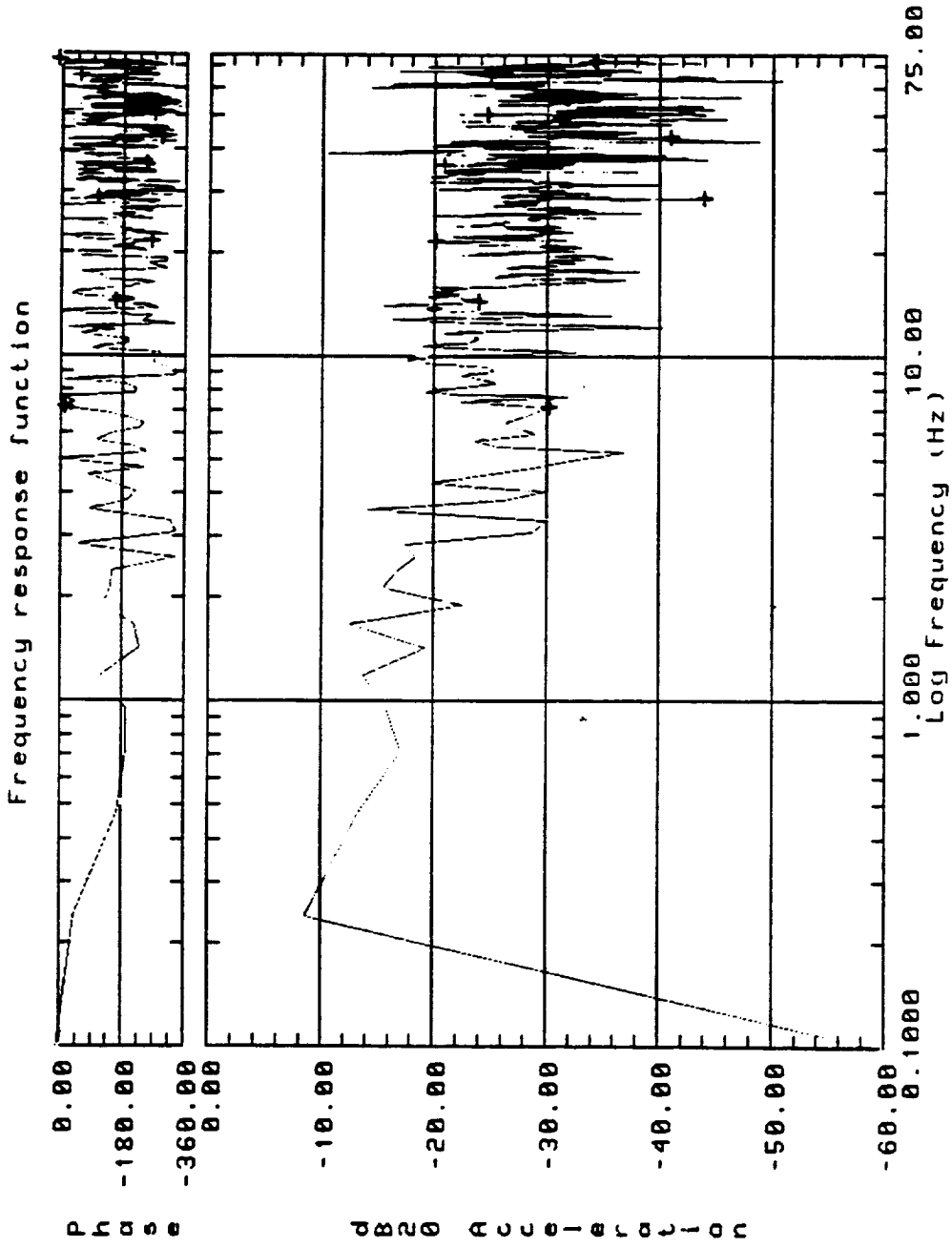

(b) Inertial control of platform.

Figure 4.32: Transfer function calculation for platform z vs. aircraft location 4 z.

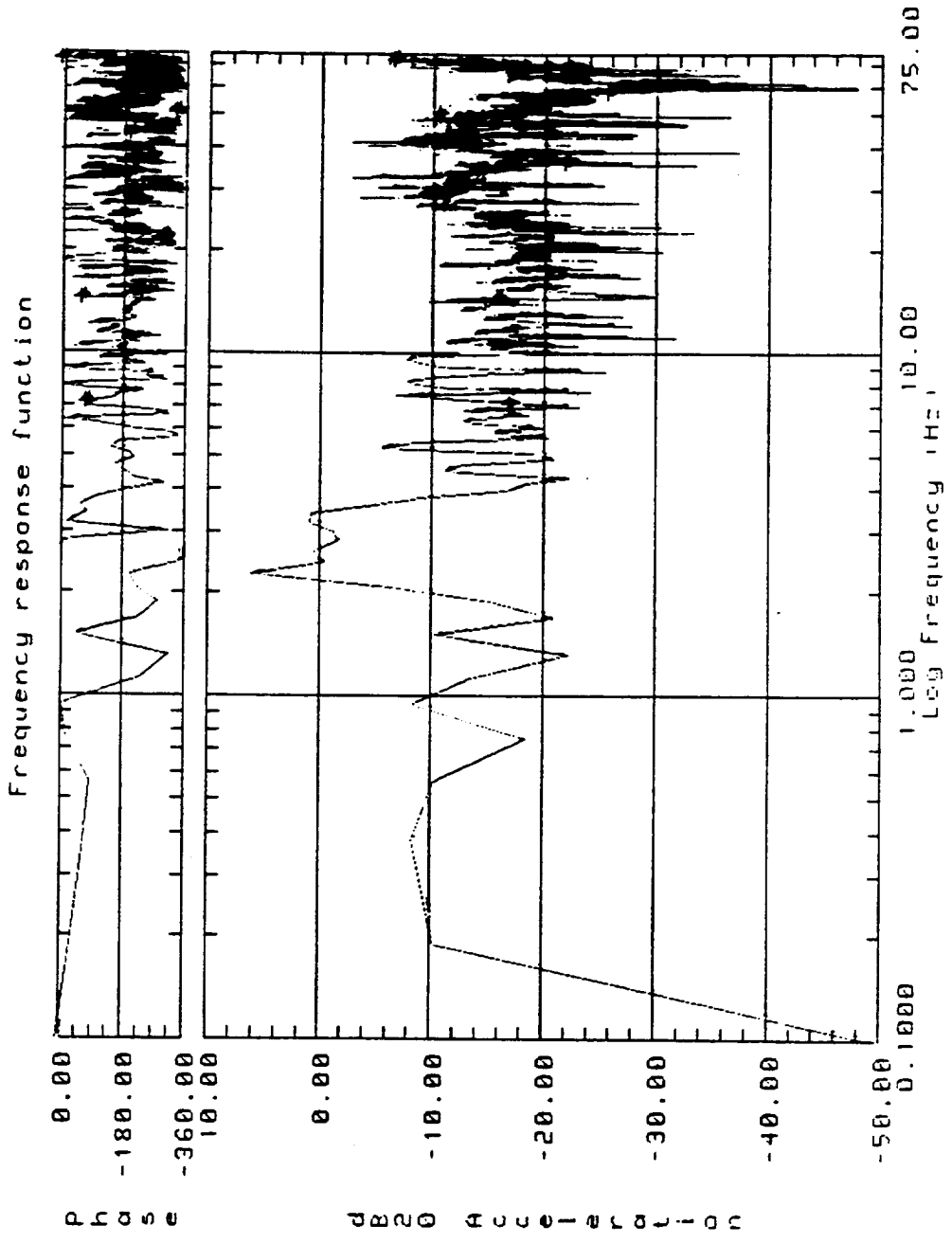

(a) Relative control of platform.

Figure 4.33: Transfer function calculation for platform θ_X vs. trunnion θ_Y.

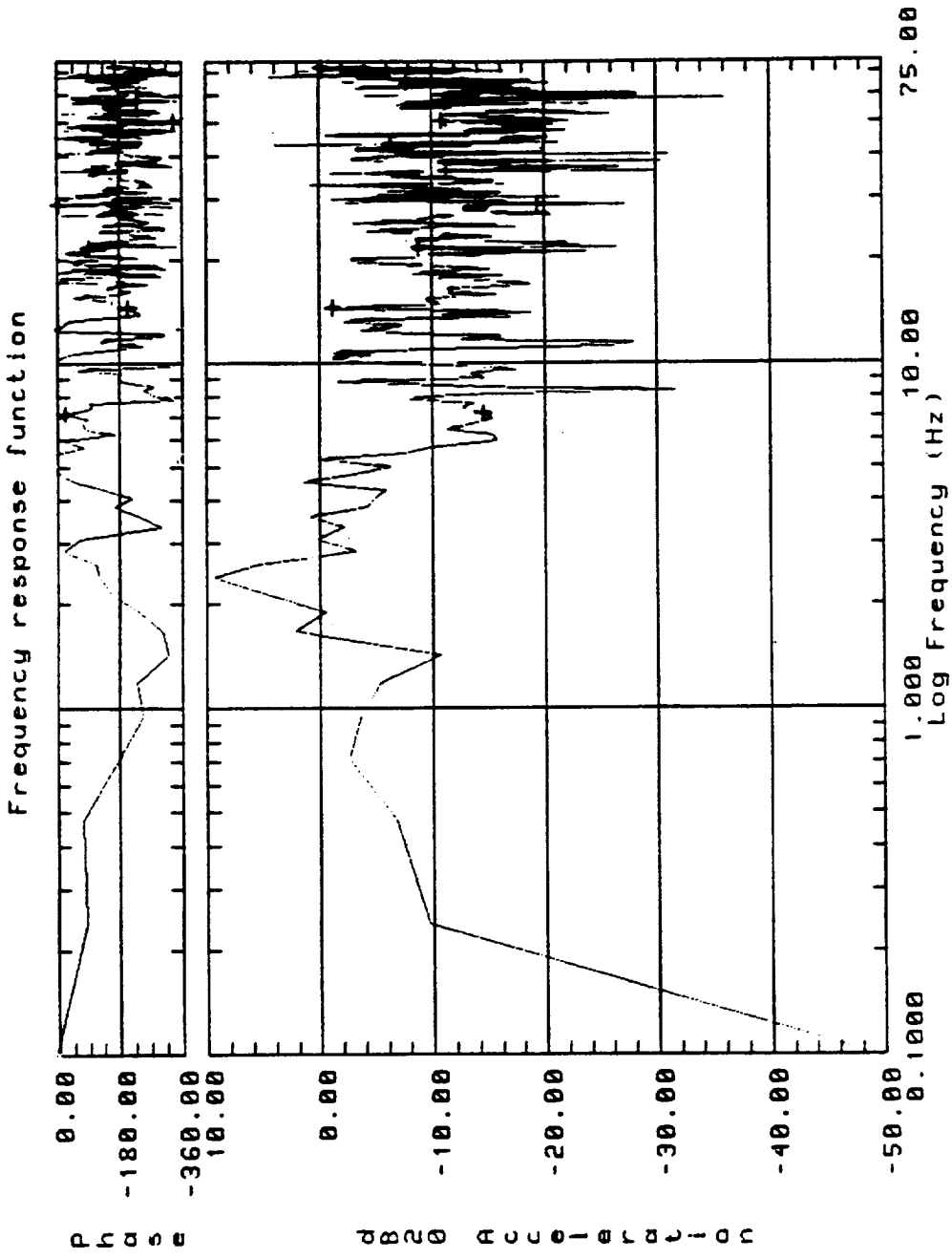

(b) Inertial control of platform.

Figure 4.33: Transfer function calculation for platform θ_x vs. trunnion θ_x.

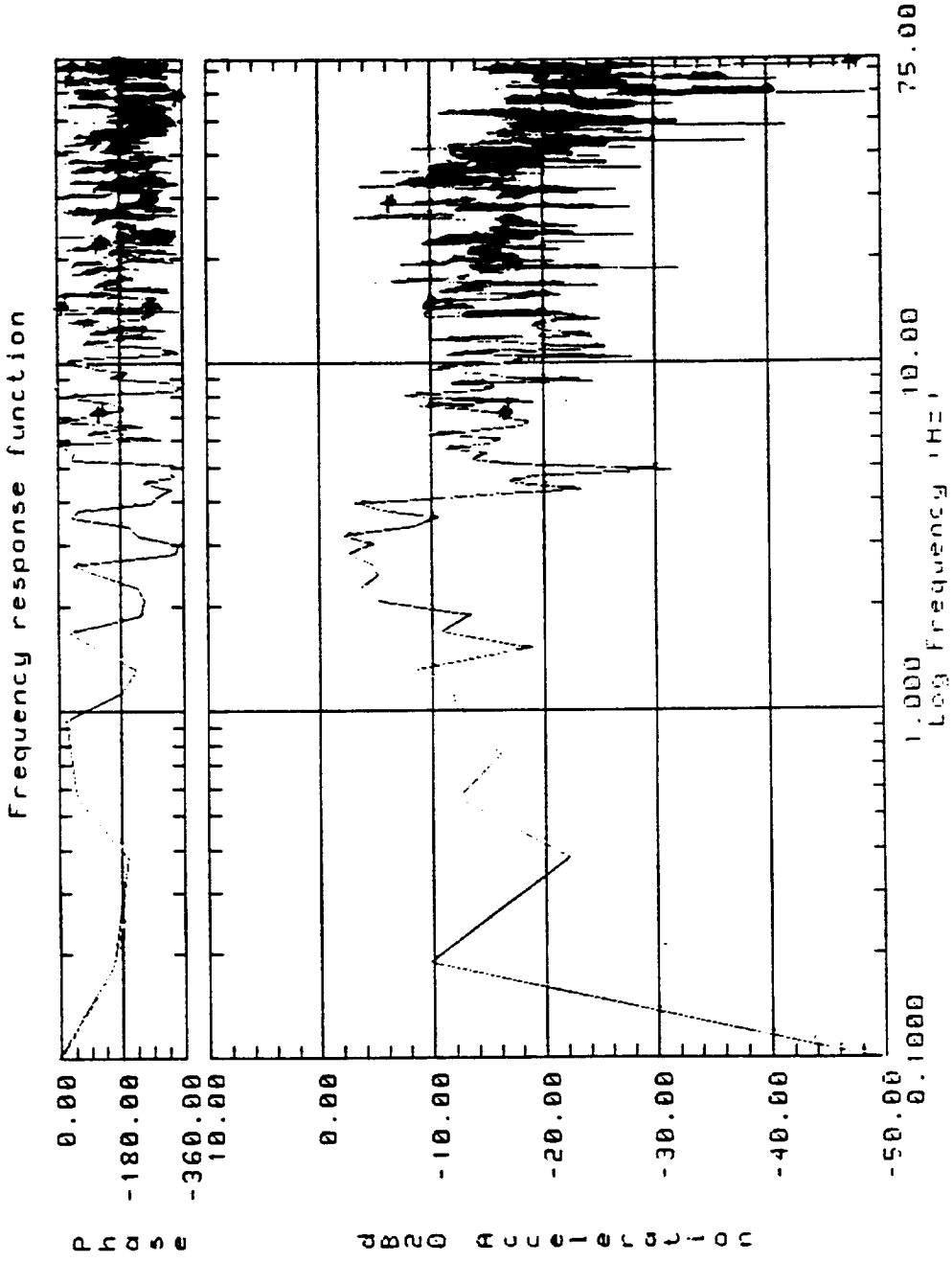

(a) Relative control of platform.

Figure 4.34: Transfer function calculation for platform θ_x vs. aircraft θ_x

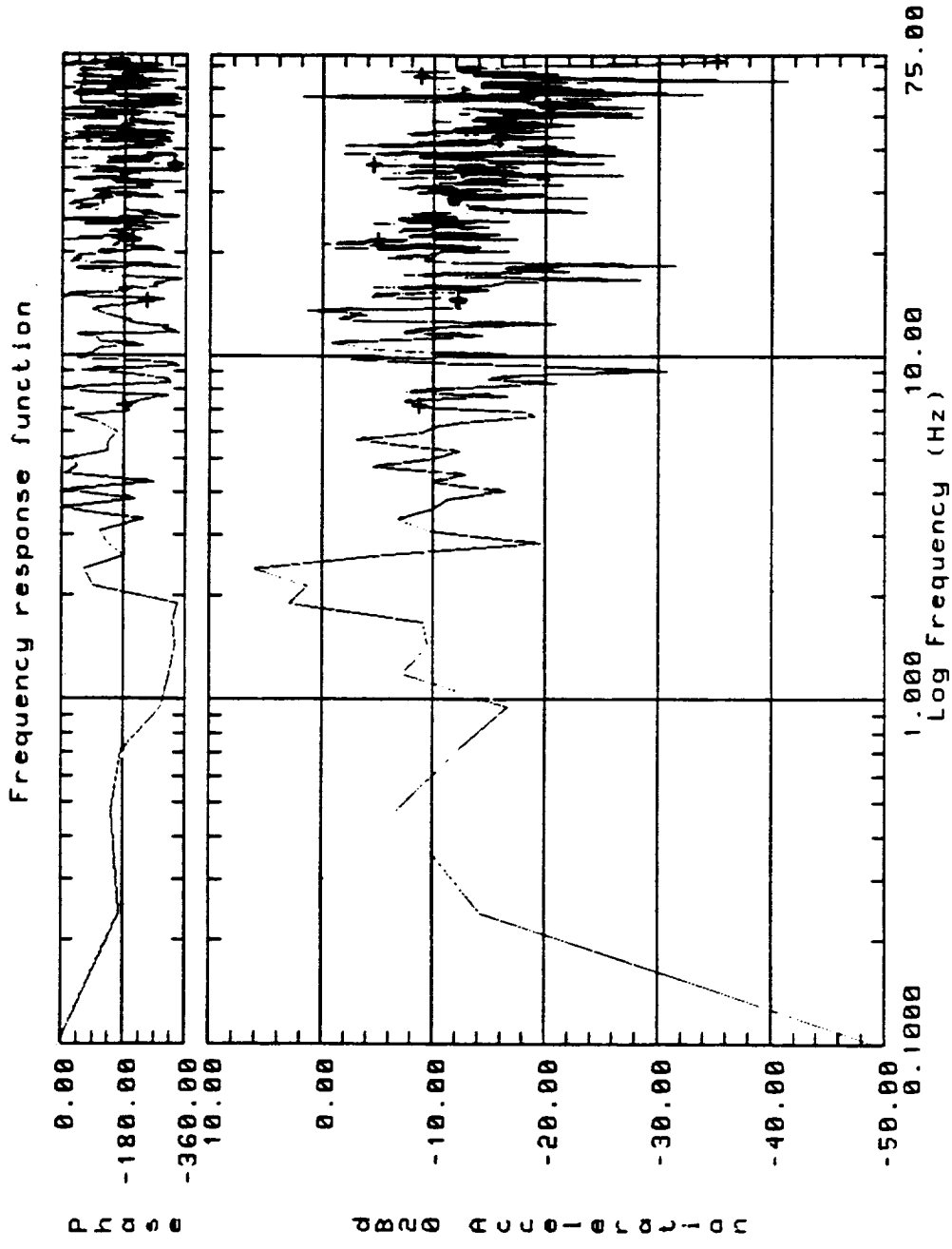

(b) Inertial control of platform.

Figure 4.34: Transfer function calculation for platform θ_x vs. aircraft θ_x.

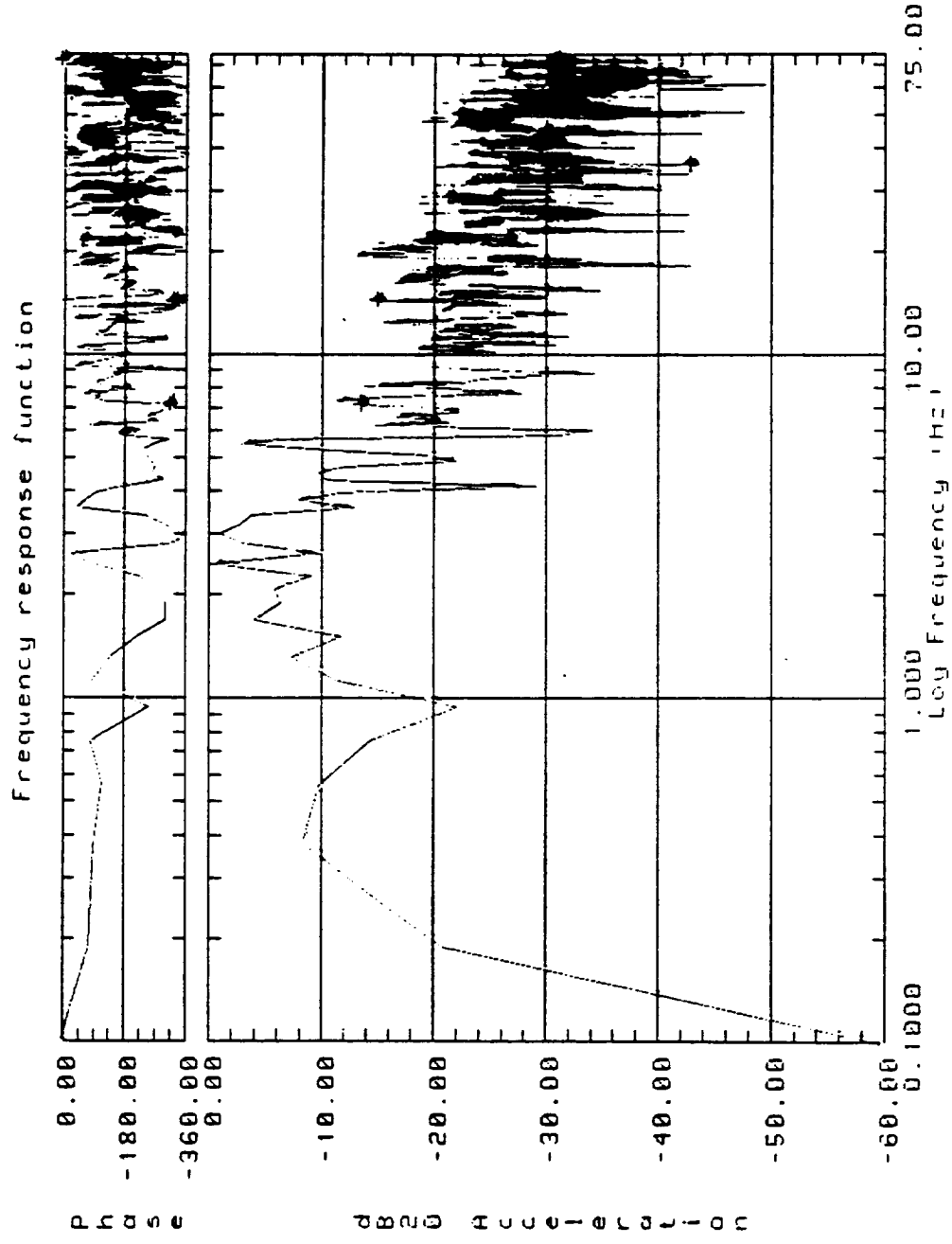

(a) Relative control of platform.

Figure 4.35: Transfer function calculation for platform ϕ_y vs. ϕ_{y2-3}.

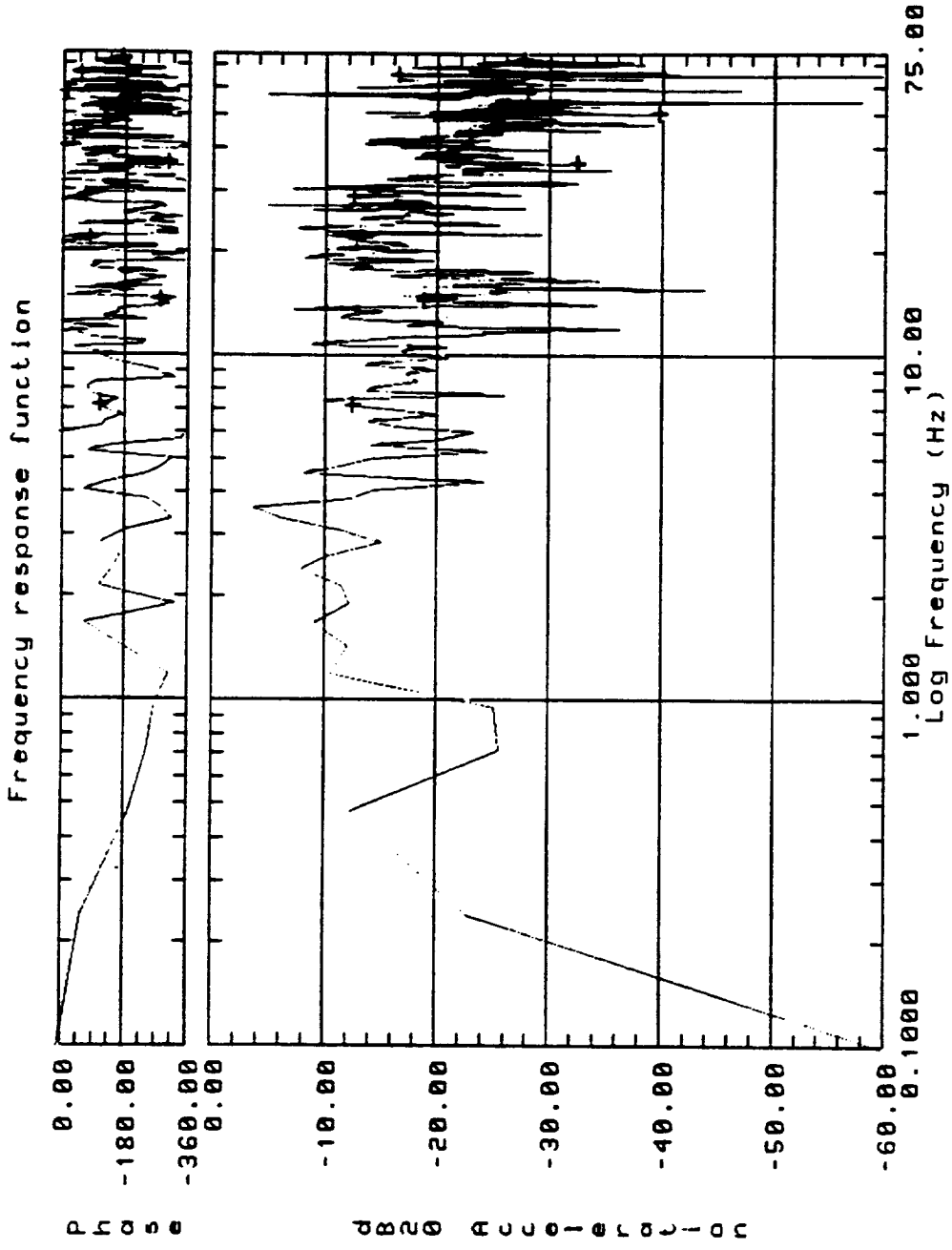

(b) Inertial control of platform.

Figure 4.35: Transfer function calculation for platform ϕ_y vs. $\phi_{y2\text{-}3}$.

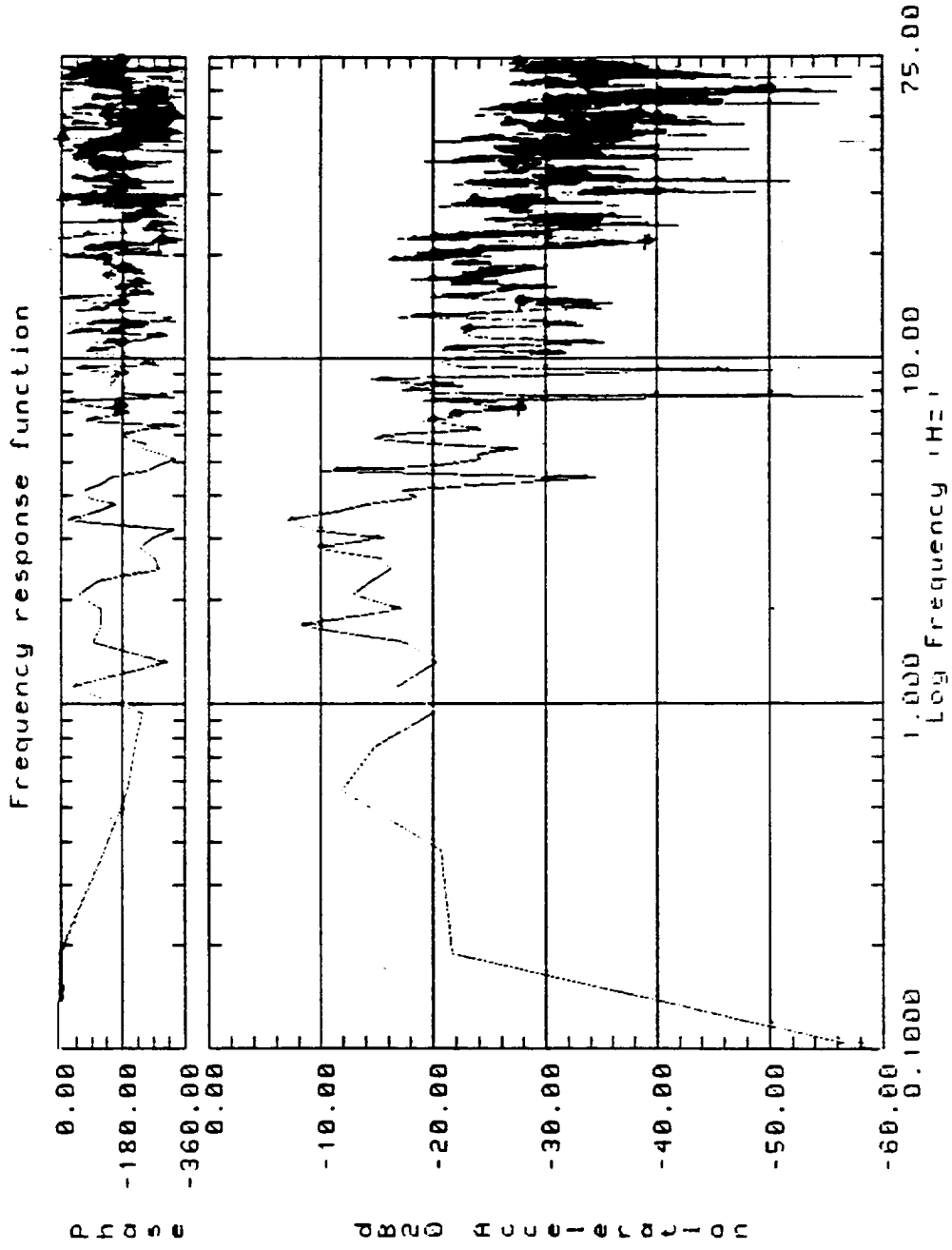

(a) Relative control of platform.

Figure 4.36: Transfer function calculation for platform ϕ_y vs. ϕ_{y1-4}.

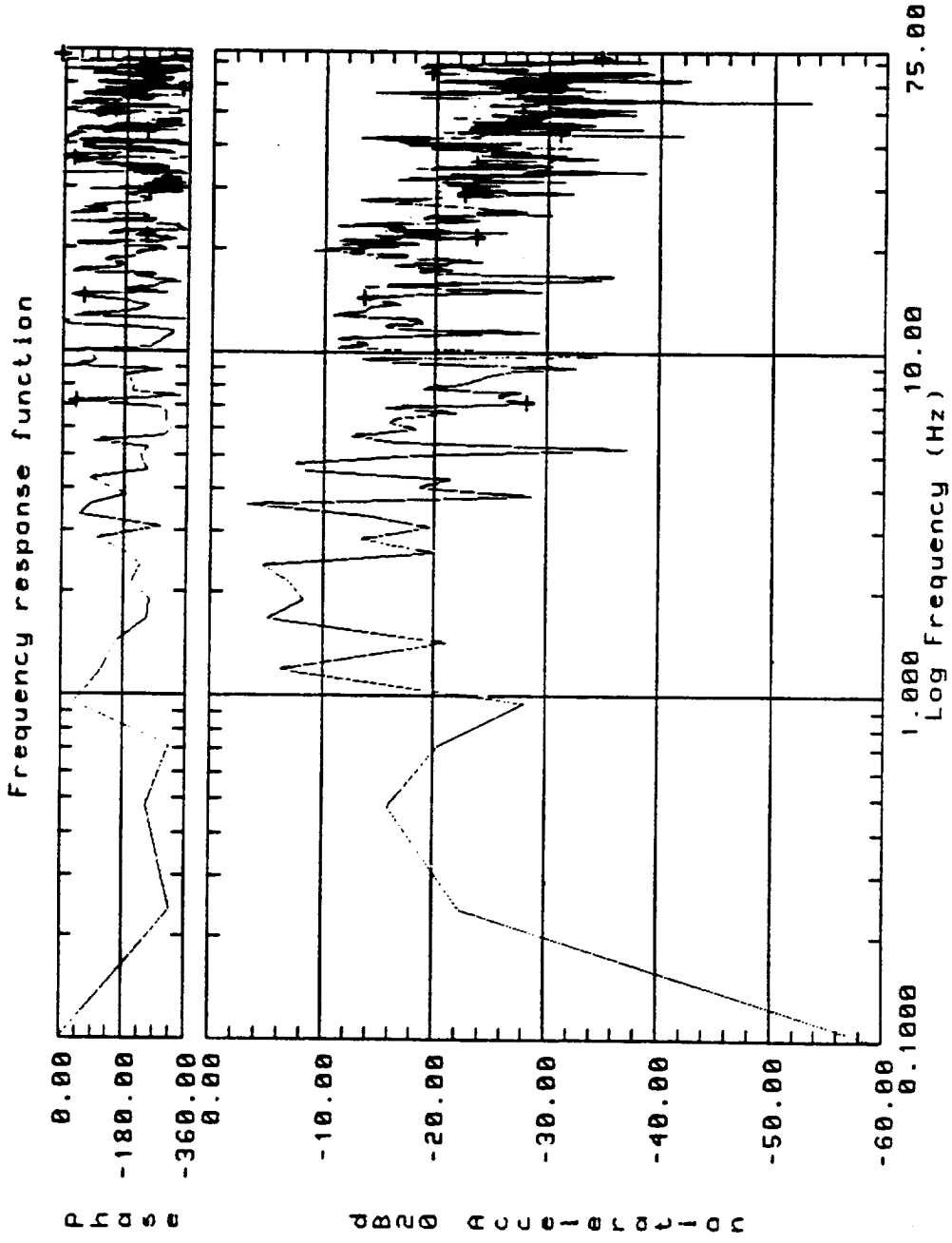

(b) Inertial control of platform.

Figure 4.36: Transfer function calculation for platform ϕ_y vs. $\phi_{y1\text{-}4}$.

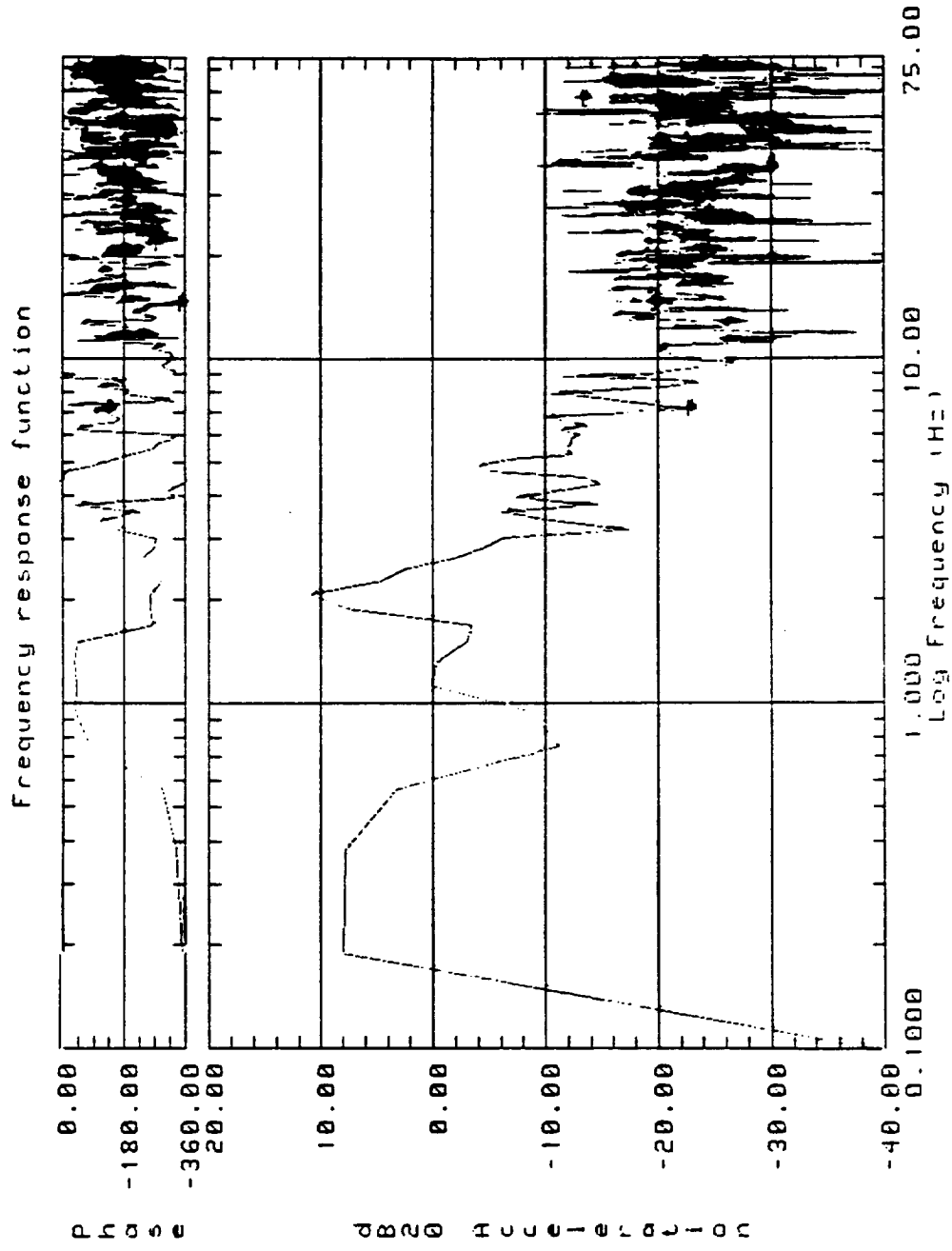

(a) Relative control of platform.

Figure 4.37: Transfer function calculation for platform β_z vs. trunnion β_z.

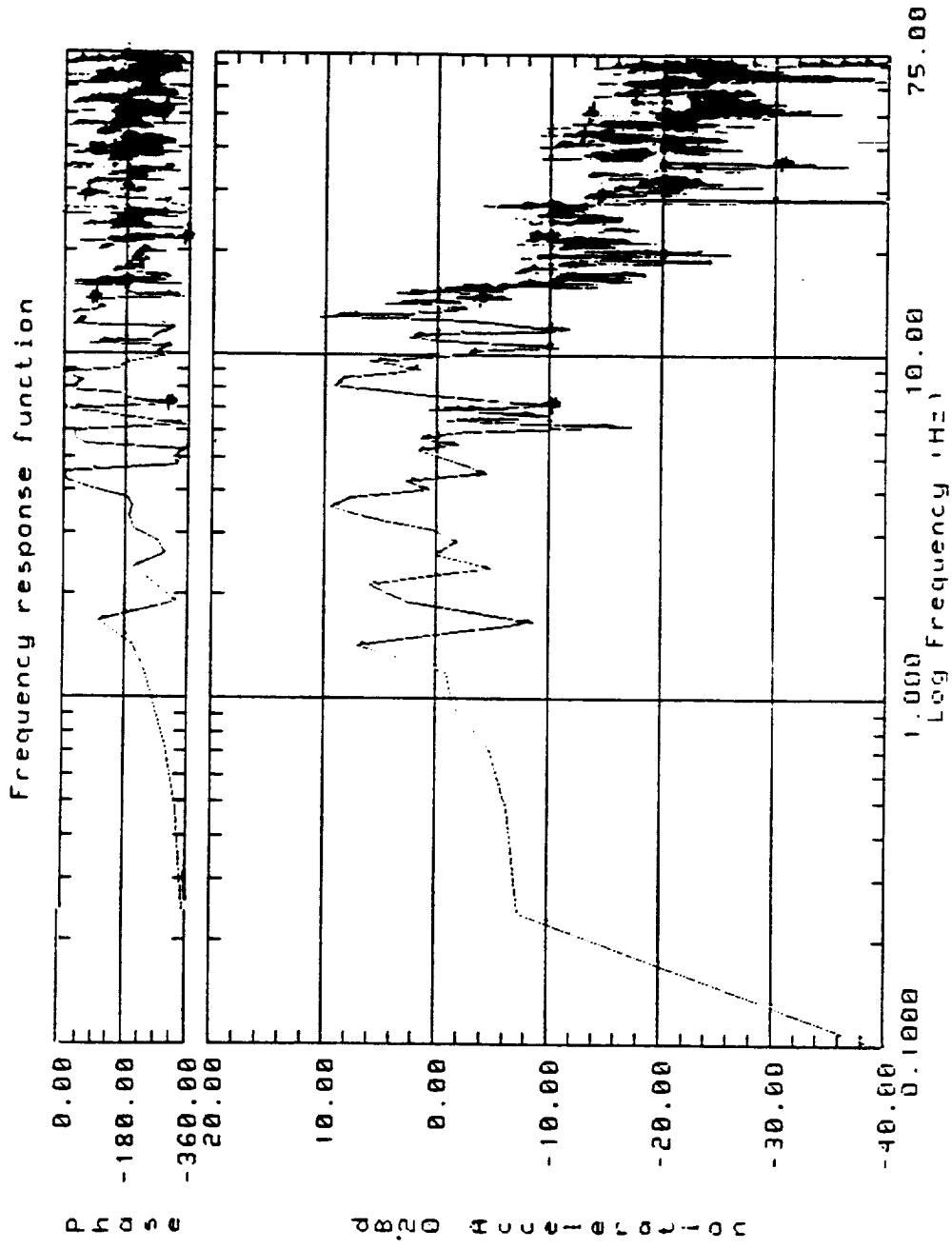

(b) Inertial control of platform.

Figure 4.37: Transfer function calculation for platform β_z vs. trunnion β_z.

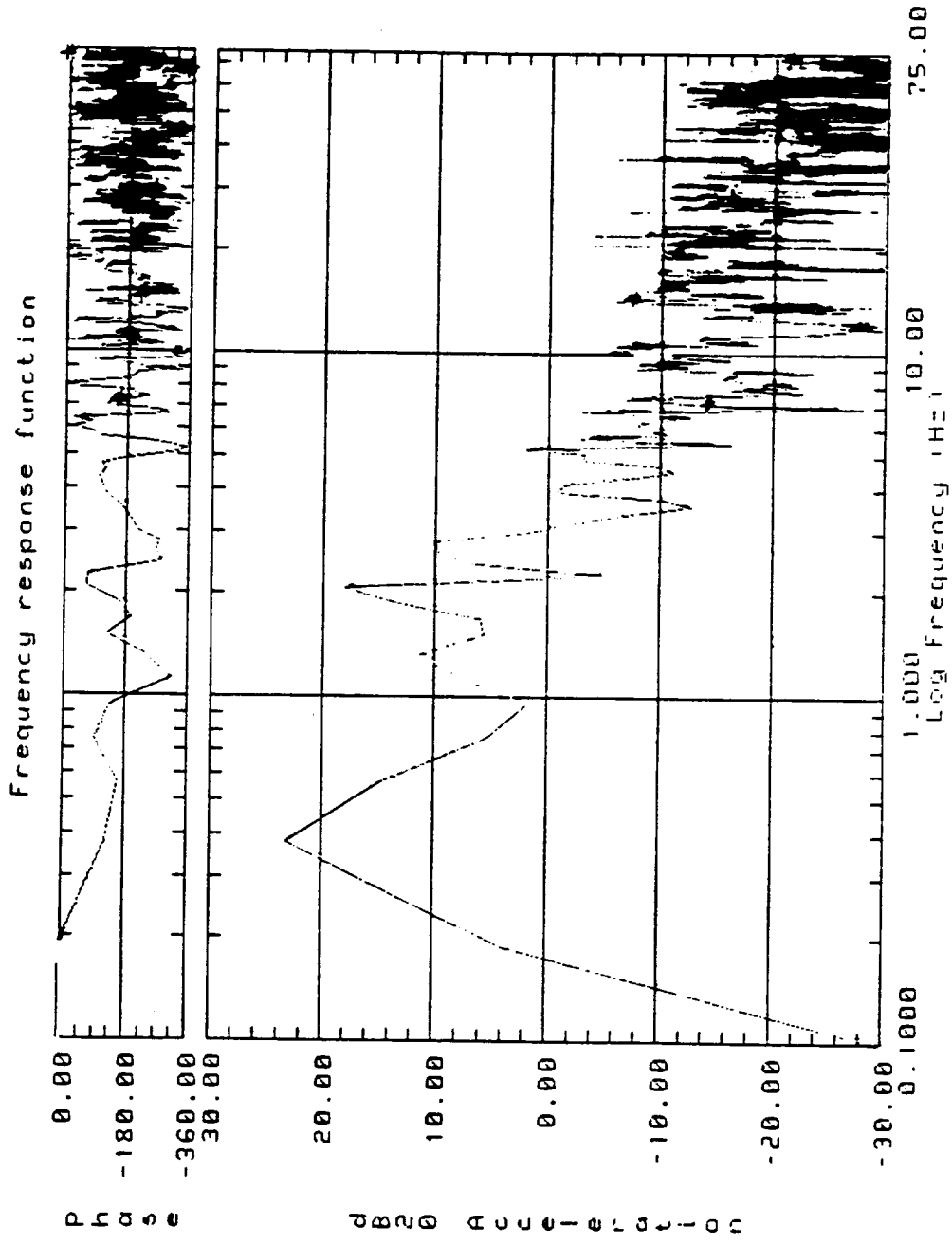

(a) Relative control of platform.

Figure 4.38: Transfer function calculation for platform β_z vs. aircraft β_z.

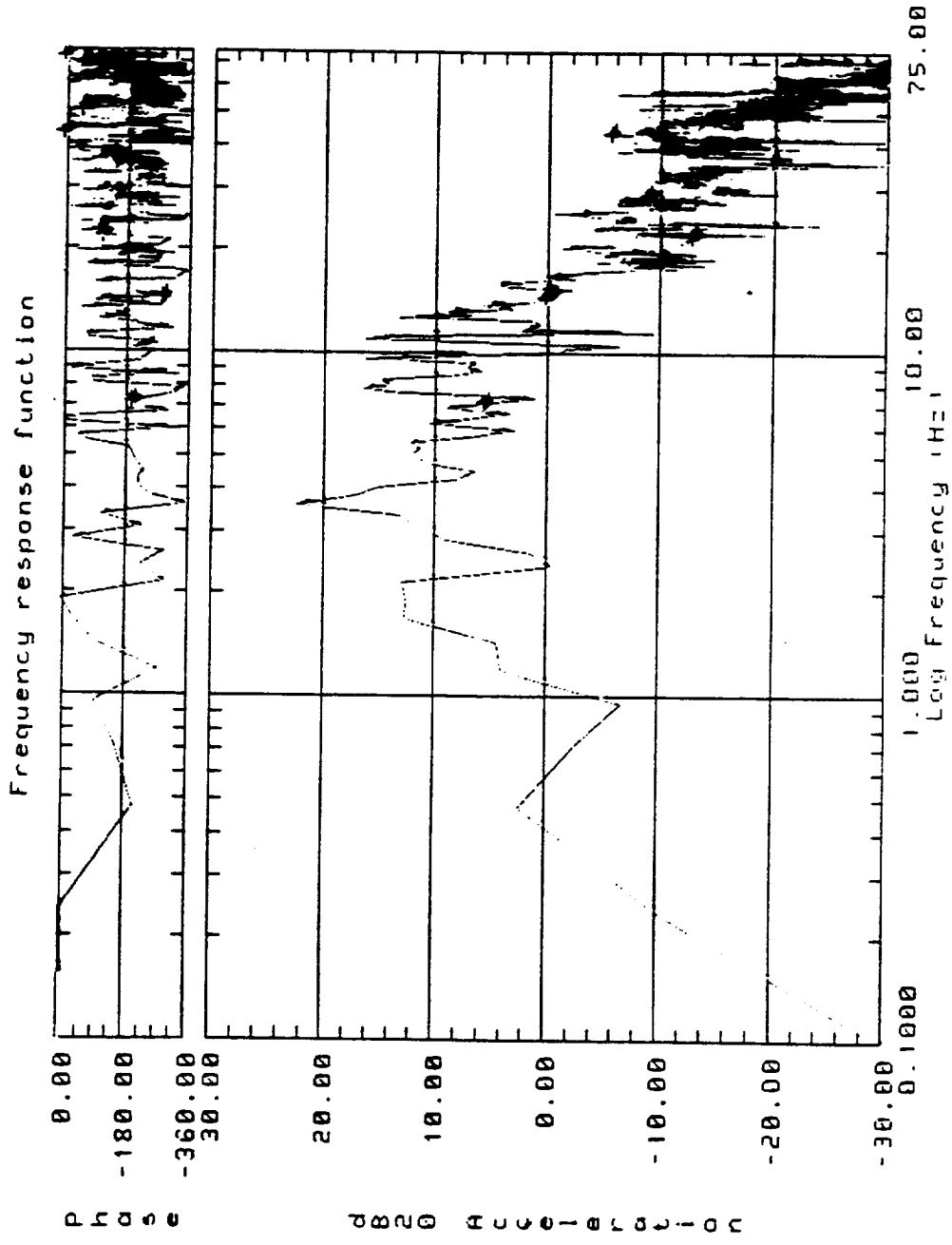

(b) Inertial control of platform.

Figure 4.38: Transfer function calculation for platform β_z vs. aircraft β_z.

V. Development and Demonstration Systems Experimental Measurements Analysis

Two six degree of freedom active magnetic isolation systems were designed and developed for the demonstration of inertial sub-Hertz isolation. The laboratory hardware was designed to have a configurable system where multiple control algorithms and inertial isolation techniques could be tested in a ground based environment. The proto-type hardware was tested in the horizontal plane due to constraints associated with the ground based 1 g environment. The Learjet demonstration hardware was designed as a functional equivalent to the laboratory system demonstrating multi-axis control and testing in an off loaded environment during low gravity Keplarien trajectories. The following sections will cover the experimental performance measurements data analysis, and discussions of frequency response trends, and system acceleration and attenuation performance limits.

5.1 Laboratory Hardware Acceleration Measurements and Transfer Function Analyses

The noise floor acceleration measurements for the payload fixed laboratory accelerometers were shown in Figures 3.2 and 3.3. These curves show the horizontal x and y accelerations of the payload where the space station "micorgravity" requirement was plotted for reference. Estimates of system noise for the laboratory hardware predictions of the total system noise performance in g's verses frequency can be made. Referring to Chapter 3 section 3.1.3, the noise floor for relative position control was given, where the eddy-current probes signal conditioning circuits had a noise floor performance of approximately 10^{-5} to 10^{-6} volts rms over the bandwidth from 0.1 to 100 Hz. Since the frequency response of the eddy-current probes over the control bandwidth is flat, with the signal conditioning filters having a gain of approximately 4.0, the sensitivity is estimated at 80 V/in from a nominal transducer sensitivity of 20 V/in. The horizontal 12 bit digital converters with a ± 5

Volt dynamic range gave a voltage per count sensitivity of $10/2^{12}$ V/count. Therefore, the eddy-current and control system deadband can be estimated at 3.05×10^{-5} inches. This is equivalent to a voltage noise of the controller of 2.4×10^{-3} Volts peak-to-peak. In comparison to the eddy-current probes voltage, noise becomes the limiting factor for the steady state case. Using this dimensional resolution of 3.05×10^{-5} inches, one can estimate an acceleration performance for steady state operation. Taking the deadband of the controller both steady state and in the controller bandwidth, a deadband resolution of 3.05×10^{-5} inches is an estimate of the amplitude peak to peak resolution across the controller bandwidth. If the control loop was to command the dimensional position of the payload across its bandwidth to the deadband resolution of the digital system, a non-dimensional acceleration verses frequency curve can be calculated using the deadband resolution estimate, where $a_{limit}(\omega) = (3.05 \times 10^{-5} \text{ inches})(2\pi f_{bandwidth})^2/g_o$. Figure 5.1 gives this curve with the acceleration measurements of the platforms x and y dimensions. The estimated noise limit only predicts the sub-Hertz response of the acceleration noise floor measurements. This acceleration limit estimate assumes there is a count change at the frequencies in the control bandwidth and leads to a conservative estimate for the deadband response, with no input excitation, as demonstrated by the support acceleration measurements in Figure 5.1. If one assumes the signal conditioning circuits and the analog-to-digital converters are stable, then the digital-to-analog converters output will dictate the dimensional stability of the active system with no feedback signal. Using the displacement probes sensitivity of 80 V/in and the voltage noise from the digital-to-analog converters, a dimensional stability can be estimated as shown in Figure 3.18. Using this spectrum and taking the second derivative in the frequency domain, one arrives at the acceleration noise spectrum shown in Figure 5.2. This noise measurement was done on the 16 bit hardware, therefore, if an adjustment of 2^4 were made on this curve there is good agreement with the acceleration measurements shown in Figure 5.1 for the frequency range from 2 to 10 Hz. The noise floor estimate using the input dimensional

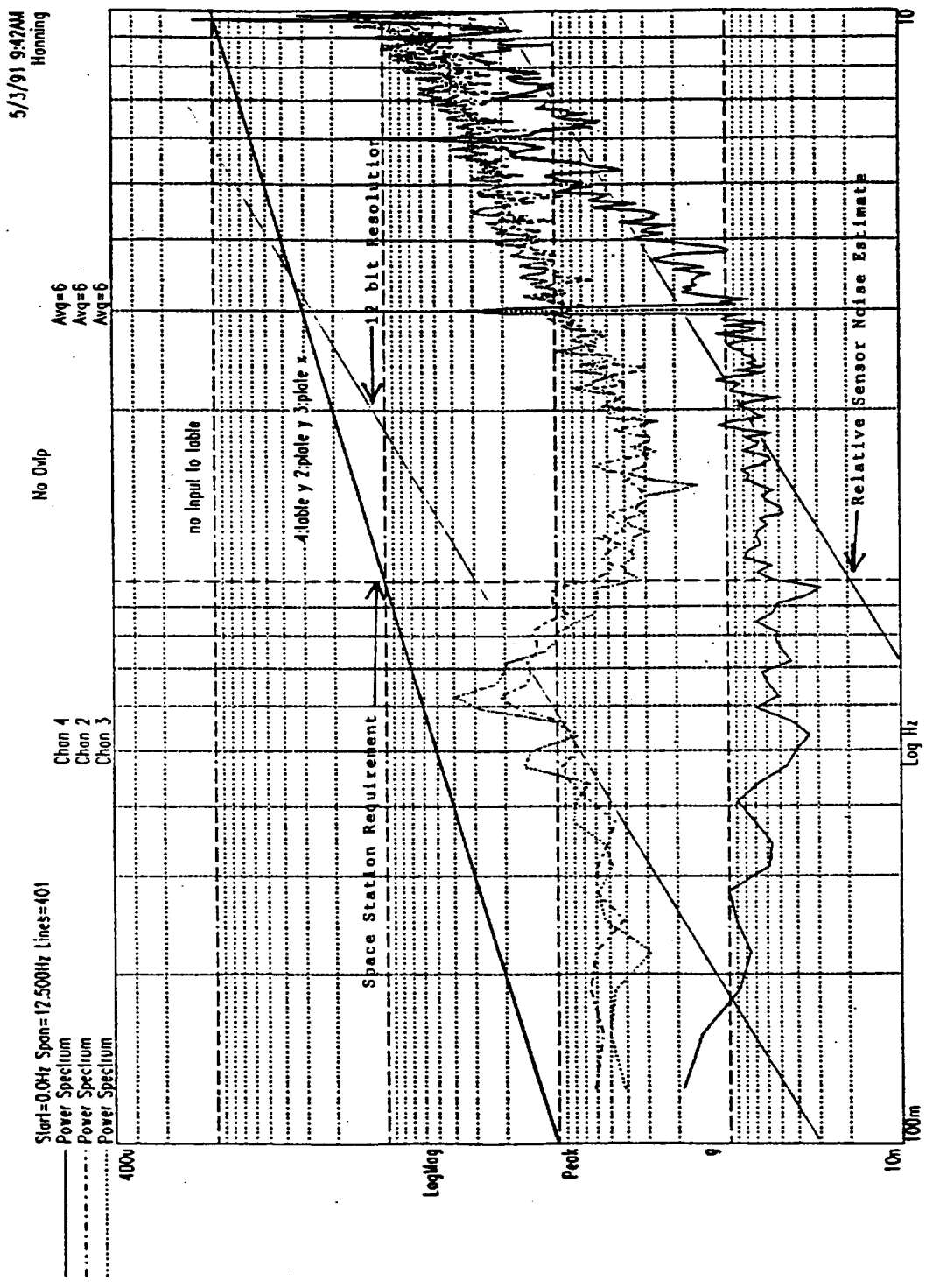

Figure 5.1: **Acceleration noise performance spectra for laboratory system with performance boundary estimates.**

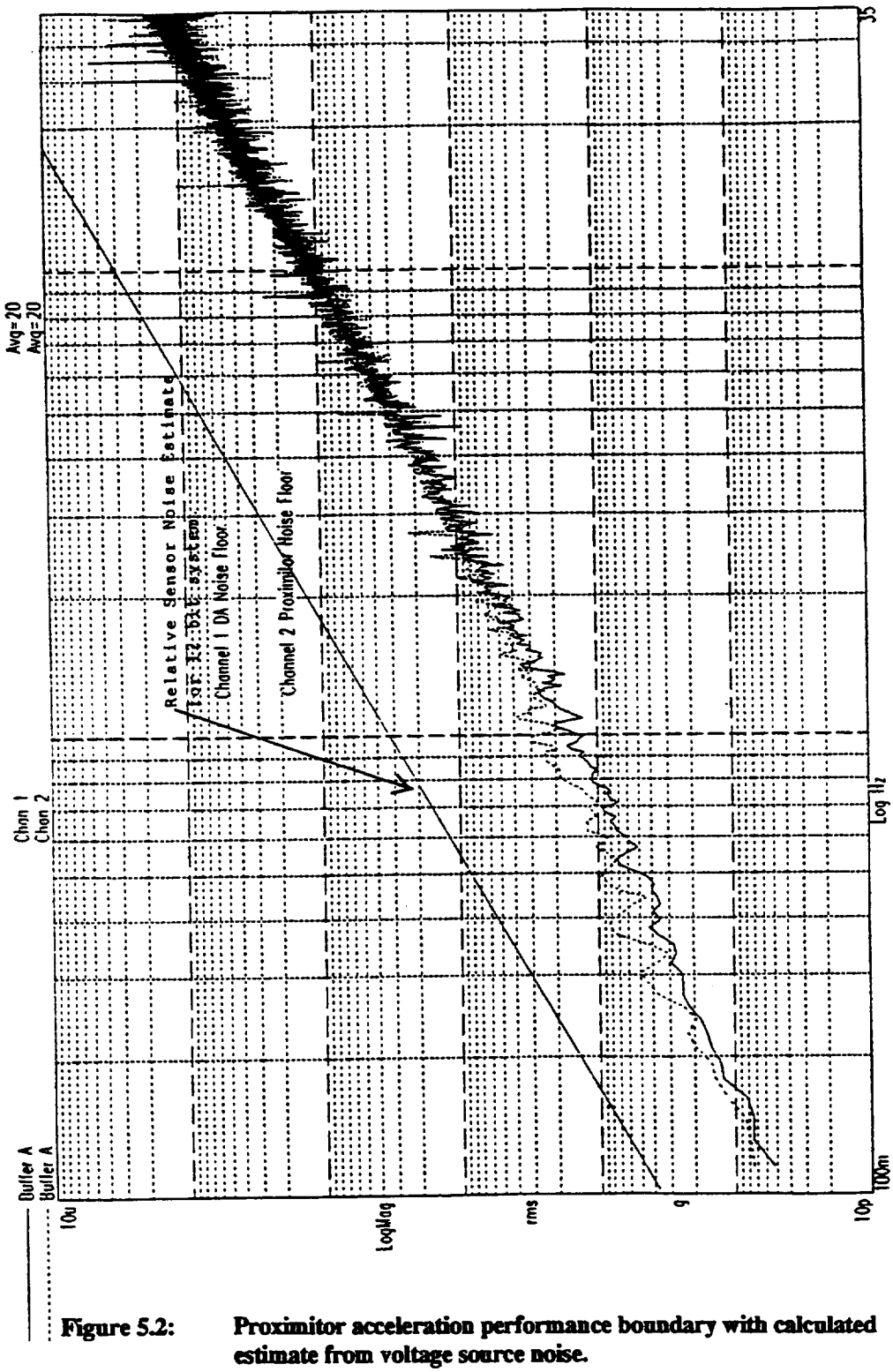

Figure 5.2: **Proximitor acceleration performance boundary with calculated estimate from voltage source noise.**

resolution is an estimate of the limiting case at the control systems set natural frequency or the controller steady state resolution. The systems proportional feedback term controls the system at its set natural frequency to the displacement resolution of the feedback sensors. The peak-to-peak response of the 12 bit system with a natural frequency of 0.65 Hz can be estimated as follows:

$$a_{\omega_n} = \frac{A_{deadband}}{g_o}(2\pi\omega_n)^2. \tag{5.1}$$

Using the 12 bit dimensional deadband and the systems natural frequency an estimated one count change in the controller gives an acceleration peak-to-peak stability of 1.317×10^{-6} g's. However, the controller must see a few count changes for control of the platform giving a value of 2.633×10^{-6} g's where this estimated acceleration stability is in good agreement with the amplitude response of the measured values in Figure 5.1 at the systems natural frequency.

The transfer function results for the prototype hardware are dictated by the digital resolution of the input converters. Referring to the transfer function calculations from the input power and output power spectral densities for the horizontal plane, shown in Figure 4.7, the attenuation profiles for the inertial control of the platform demonstrated a 100 dB/decade roll-off with a stop frequency of about 2 Hz. The attenuation bottomed out at approximately -30 dB where the transfer functions leveled out. This leveling out of the transfer function can be explained using the dimensional resolution of the control system by analyzing the input and output power spectrums used in the transfer function calculations of Figure 4.7. The input and output spectral densities from the inertial transfer function calculations are plotted in Figure 5.3. This figure shows the output spectrums being attenuated where they bottom out and follow the dimensional resolution of the controller plotted on the same figure. The acceleration feedforward resolution for the laboratory hardware was approximately 6.563×10^{-5} g's. Figure 5.3 shows the input spectrum crossing this feedforward resolution at approximately 0.9 to 1 Hz where the inertial cancellation begins to take effect and the

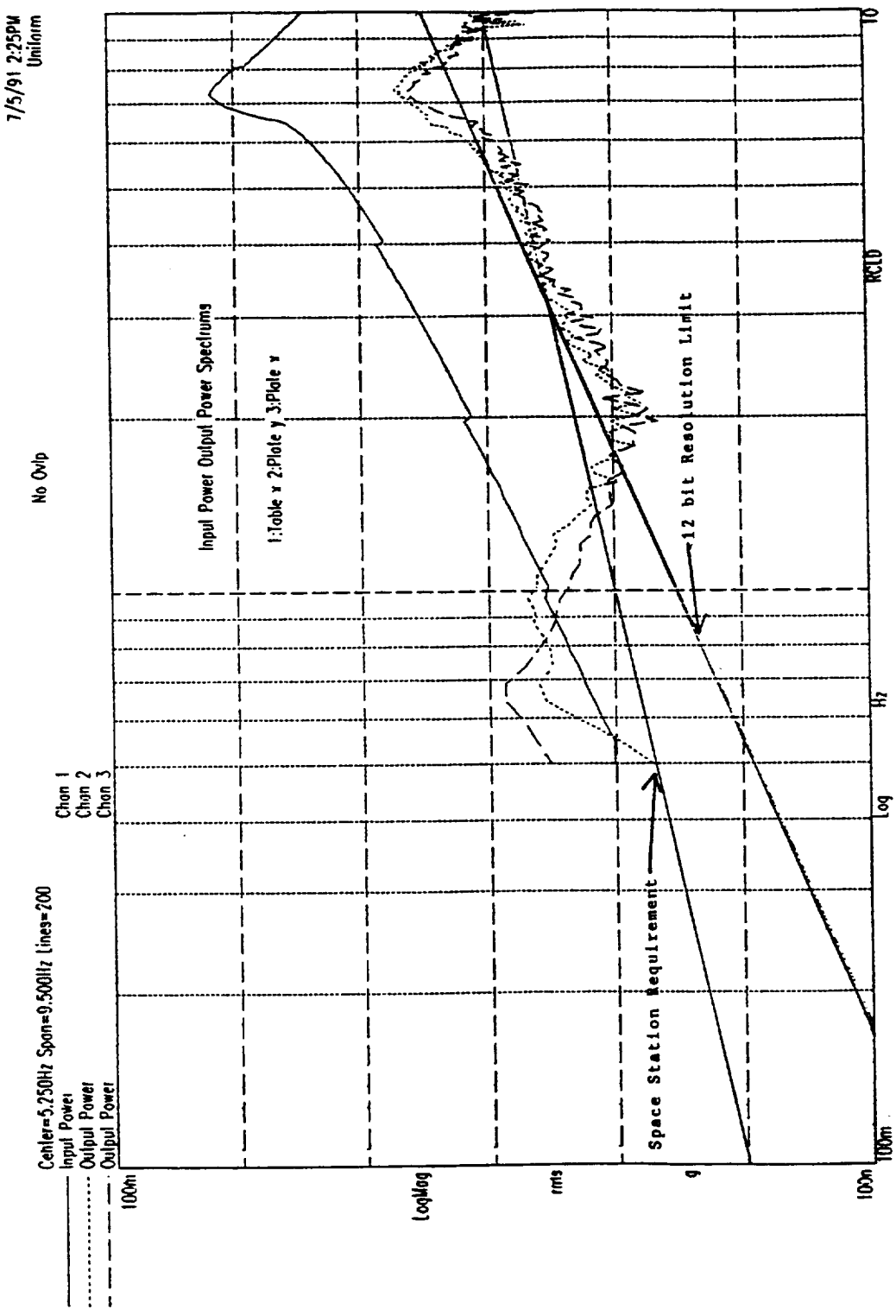

Figure 5.3: Input and output power spectra for inertial transfer function calculations.

output power spectrums begin to attenuate the input accelerations of the support structure within the dimensional resolution of the feedback sensors. This control approach, as mentioned in the theoretical developments, commands the payload to be inertially still where an observer on the support structure would find the payload in motion equal to the resolution of the feedback control. Therefore, the steady state and controller bandwidth noise performance is bounded by the digital resolution of the control loops and by the output resolution of the digital-to-analog converters, assuming no input feedback signals. The transfer function is also bounded by the digital resolution where, theoretically, for an infinite resolution system and no sensor to sensor phase shifts, the control system should command an infinite attenuation or to the sensor noise floors in the feedback/feedforward control system.

Figure 5.4 depicts the relative case with the input and output power spectrums plotted. The dimensional resolution is superimposed showing the output power spectrums following this curve as in Figure 5.3. The space station requirement is also plotted in Figures 5.3 and 5.4 as a reference. These sets of data show the advantages of inertial and active isolation in general for low frequency requirements. Specific to "microgravity" levels, it is quite apparent that although laboratory digital equipment was successfully utilized for the developments of these state of the art isolation techniques, at least 16 bit high resolution control is dictated by the stringent "microgravity" requirements for orbital platforms.

5.2 Learjet Hardware Acceleration Measurements and Transfer Function Analyses

The Learjet demonstration hardware was designed as a functional equivalent to the laboratory prototype system. Both systems were actively controlled in six degrees of freedom where the demonstration hardware was built to investigate the off loaded response by testing during Keplarien low gravity trajectories. This environment posed unique limitations in testing however, it

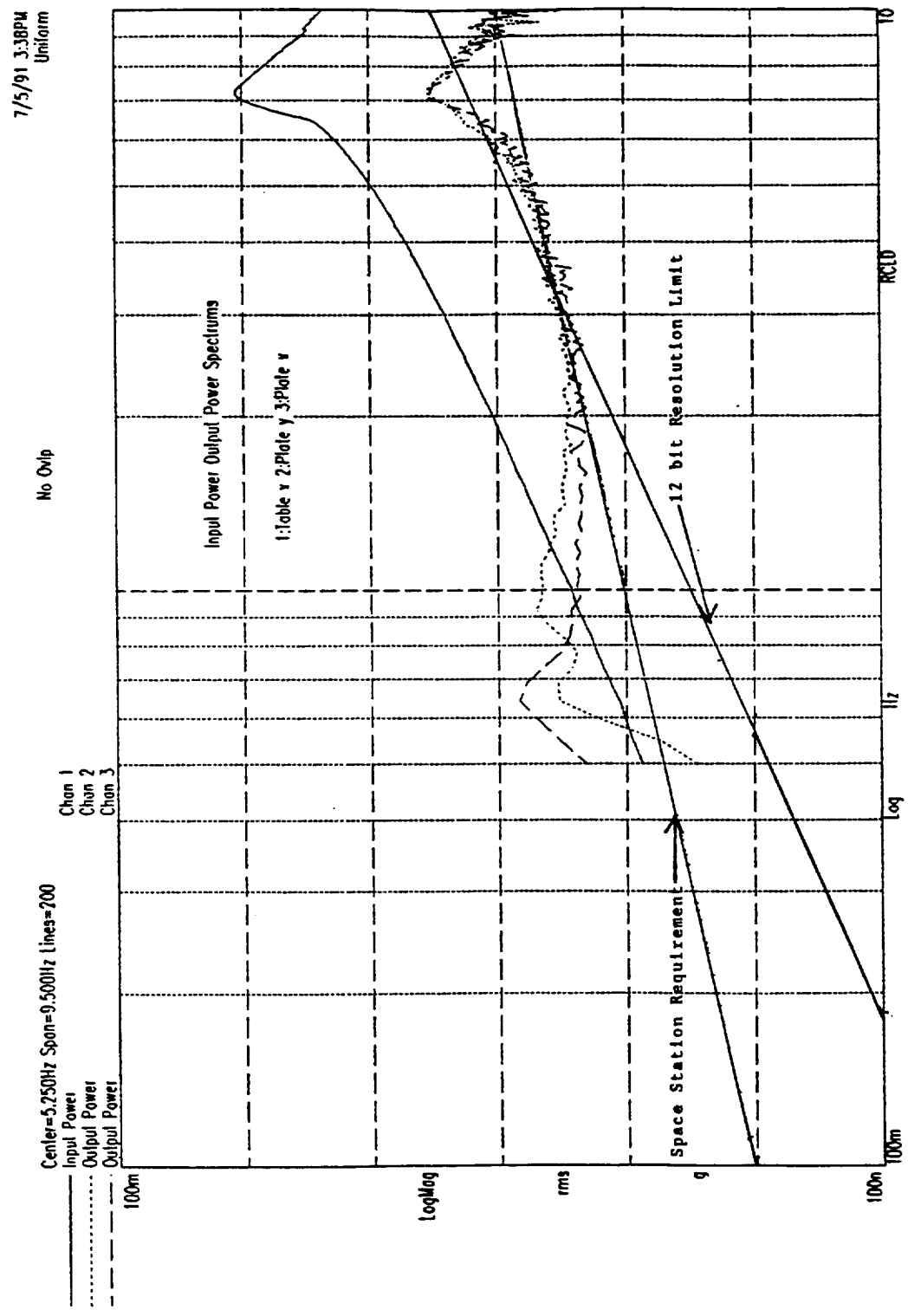

Figure 5.4: Input and output power spectra for relative transfer function calculations.

was adequate for demonstrating the sub-Hertz inertial control of a package, where the final validation of such technology to the 0.01 Hz range will be accomplished during orbital flight.

The experimental data taken during the low gravity trajectories encompassed the full trajectory acceleration phases, entry/low gravity/exit, where the actively controlled payload was activated during the oscillatory part of the entry phase as depicted in the full acceleration trace of Figures 4.19 (a) and (b). The total current draw for the twelve magnets during the high-g portion of the trajectories was calculated at approximately 14 amps for a 2.5 g pull-up maneuver. However, the g's pulled during each trajectory vary from 2 to 3 g's and therefore, the current draw to maintain the equilibrium gap in many instances was substantially greater than 14 amps which tripped the experimental power circuit breakers, where the max current draw allowed was 15 amps. Therefore, the control computer was constantly active with all input sensors powered. However, the power amplifiers were not activated until the pull-up portion of the entry phase was complete and the trajectory was into the free-fall condition thus, off loading the reference frame of the aircraft. This of course gave an initial shock to the payload. Therefore, the control parameters were set to apply substantial damping to the system to maintain control and stabilize the platform in one to two seconds after power was applied. This then typically allowed a window of 10 to 15 seconds to acquire good actively controlled payload acceleration data for the calculation of the transfer functions plotted in Chapter 4.

In order to acquire a quick estimate of the attenuation achieved, there were four transfer functions calculated for an inertial control case and a relative case. These four transfer functions were calculated by referring an isolated payload pitch axis accelerometer to the four aircraft fixed pitch axis locations. The four locations were defined in Figures 4.15 (a) and (b). The pitch axis or Z axis accelerometers were used as a quick performance check. This axis was chosen due to the largely non-stationary acceleration environment caused by the dynamics of the trajectory maneuver. The curves plotted do not demonstrate the rapid roll off achieved during the laboratory horizontal

measurements because of the large relative damping required to provide a stable entry phase and therefore, giving a long enough window of time to acquire data for calculating the sub-Hertz power spectral densities and their associated transfer functions. However, in demonstrating active inertial verses relative control the Learjet aircraft provided an adequate means for a quantitative evaluation of these active techniques in an off loaded case. Figures 18 (a) and (b) depict the attenuation of the platform pitch axis accelerations with respect to the direct support structure provided by the trumnioned frame. These two plots show the platform attenuating the support structure input power by approximately -20 to -30 dB at 10 Hz. The inertial control curves demonstrate the inertial cancellation approach where at the lower frequencies the payload does not want to follow its support. Therefore, the attenuation of the active system is dropping off well before the relatively referenced payload. The frequency range from 3 to 10 Hz is masked by direct vibro-acoustic disturbances where the payload will react similarly in the feedforward or feedback control cases. Figures 4.18 (c) and (d) are the transfer functions calculated for the pitch axis accelerometer referenced to locations three and four directly mounted to the aircraft fuselage. The same response for the inertial and non-inertial control cases are seen as in Figures 4.18 (a) and (b).

The purpose of the Learjet demonstrations was to quantify the attenuation performance of the active magnetic system in multi-dimensions for an off loaded case. This was performed by resolving the six inertial degrees of freedom of the isolated platform and calculating the transfer functions for these six spectrums referenced to the trunnion and aircraft fixed accelerometers. The translational accelerations for the aircraft and trunnion fixed locations were used for the XYZ transfer functions while the rotational accelerations were estimated by the geometrical differencing of the appropriate input power acceleration sensors as defined in section 4.2.2. Figures 4.19 and 4.20 (a) and (b) show the full time traces of the relative and inertial acceleration traces for locations one and six, as defined in Figures 4.15 and 4.16, which were used to compute the multi-dimensional transfer functions.

Performing the inertial control during the parabolic flight posed considerable difficulty since the total trajectory could not be controlled due to the large current draw needed during the high-g maneuver. The inertial circuits were set with a bandpass beginning at 0.03 Hz, where for the Learjet environment was a liability. This liability was found once the control actuators were powered and the inertial feedforward sensors sensed this large acceleration. The long time constant associated with the 0.03 Hz high pass filter required a few seconds to reach the steady state condition, limiting the isolation window. Therefore, the inertial loops were not closed for a few seconds in order to allow this transient condition to subside. Therefore, the controller would not command the isolation system to react to this large input which was self induced by the Learjet operational procedure. Although this caused problems in the ultimate performance for the inertial control, comparisons could be made in the low frequency decoupling of the isolated payload with its support environment while the inertial loops were closed. The relative time histories processed had a 21% greater frequency resolution and allowed the transfer functions to be calculated with five averages while the inertial data permitted only three averages.

Comparing the X axis response from Figures 4.21 through 4.24 (a) and (b), where the relative control cases are shown in Figures 4.21 through 4.24 (a), the inertial cancellation may be seen to command the platform to be decoupled to its support at low frequencies. However, the lack of averages and the direct disturbances caused by airborne noise and the initial conditions mask the performance in the 2 to 10 Hz range because a data acquisition card cage exhibited a strong resonance at approximately nine Hz. In this case the relative loops are more effective at damping out this direct excitation source. This response, however, is specific to the testing environment of the aircraft. The roll off of the inertial control is quantifiably greater as shown in the plots. The relative loops show a well damped low frequency system with an approximate -10 dB/decade slope past 3 Hz while the inertial control with the same relative parameters exhibits a 30 to 40 dB/decade roll off past 10 Hz with the low frequency response being attenuated at -10 to -20 dB.

The Y axis response of the relative and inertial transfer functions from Figures 4.25 to 4.28 shows the relative curves demonstrating a damped 2 Hz frequency filtering into the payload, whereas the inertial loops are canceling this response with a fairly flat -20 dB attenuation from 0.5 to 75 Hz. This 2 Hz spectrum is believed to be caused by the pilots reaction time of approximately 0.5 to 1 second while controlling the pitch axis of the airplane.

The Z axis transfer function calculations for both cases plotted in Figures 4.29 and 4.32 (a) and (b) for the relative and inertial control , respectively, exhibit the same overall response as the X and Y axes, where the low frequency attenuation is increased by the inertial loops. The broadband attenuation of the inertial response shows the direct energy forcing the acceleration response of the payload where the relative control does a better job of damping the energy input to the payload. This of course was expected since only inertial feedforward control is effective for base disturbance cancellation.

The rotational transfer functions for the θ_X, ϕ_Y, and β_Z, degrees of freedom showed approximately the same response for both control cases. The differencing of the accelerometers to estimate the rotational accelerations is not highly accurate. However, for the β_Z and ϕ_Y transfer functions the inertial control plots did demonstrate the low frequency decoupling of the payload whereas the 2 to 10 Hz frequency band was masked by the direct disturbances.

It was very difficult to predict and estimate the dynamic environment of the aircraft due to the non-stationary aspects of the maneuver as well as the non controlled inputs to this environment as was mentioned previously. However, quantitative comparisons were made assuming a fairly representative low gravity environment for both trajectories used in each comparison during the stable low gravity phase. Of course, initial conditions and exit conditions effect the power spectrums and with a limited window of active data a limited number of averages for the spectral densities makes the low frequency regime difficult to compare trajectories.

VI. Conclusions

In order to utilize the low gravity environment of space a well characterized and reproducible acceleration environment will dictate the isolation of many true "microgravity" sensitive payloads. It has been found that many fundamental materials and fluids experiments are limited in their potential success due to excessive dynamic excitations present on the Shuttle orbiter and on any future or existing orbital carriers. Though the frequency content will be vehicle specific, all orbital vehicles are fairly soft structures and will be excited by manned presence as well as various dynamic pieces of support equipment such as pumps, motors and orbit keeping thrusters. The most difficult portion of the dynamic disturbances present on the various orbital vehicles are the sub-Hertz to 10 Hz range where, for the Shuttle, the crew accounts for many of these excitations while the future larger space structures may have many structural resonances below 1 Hz as well.

The need for active verses passive isolation has been discussed thoroughly for the past several years for the orbital environment. Although, for certain specific cases a passive system may be sufficient for a certain bandwidth of interest, this work has been focused on the sub-Hertz or low frequency isolation problem where an active system is dictated. This work has focused on two phases of the "microgravity" vibration isolation research to date, development of theoretical approaches and demonstration of a fully active six degree of freedom system which illustrates the advantages of active inertial and relative control of a package. The inertial referencing of a payload has many advantages over relative feedback soft suspension systems. Therefore, an active six degree of freedom prototype development system was designed and built to verify theoretical predictions, as well as to provide an experimental testbed for the study of different controllers. This development system was then transitioned into a higher fidelity demonstration package for the testing of a feedback/feedforward fully suspended system during a reduced gravity environment. The successful demonstration of such devices in a fully off loaded case was a good test of robustness, given the severe limitations posed by

the testing environment during low gravity parabolic flights. The full verification and technology demonstration of these devices will have to occur during orbital flights, since this is the intended environment for these isolation platforms. Testing in the low frequency regime of 0.01 to 0.1 Hz is not practical in a ground based program which is another limitation that can only be overcome by space based testing. The prototype hardware successfully demonstrated the advantages of inertial feedforward cancellation where a 100 dB/decade roll off was achieved. The relative system was also successfully demonstrated with it's inherent advantages over passive systems through the low stiffnesses achievable by decoupling of the static and dynamic stiffness of a system. The Learjet tests successfully demonstrated a fully active feedback and feedforward system in a low gravity environment and successfully reduced the excitation environment by at least one decade. The inertial loops closed during the Learjet testing demonstrated the low frequency decoupling of the active system from its support environment. However, in the Learjet vibro-acoustic environment an inertially damped system by inertial feedback would have been more effective in attenuating this specific environment.

6.2 Future Research

Within the international space community there is a considerable amount of research and development on going relative to vibration isolation technology for microgravity payloads. NASA's Microgravity Sciences and Applications Division of OSSA sponsored a workshop to bring the various organizations involved in this area together. An International Workshop on Vibration Isolation Technology for Microgravity Science Applications was held in April 1991, which included the international SSF partners, to review current technology status and assess future technology needs. All of the SSF international partners have active programs in this technology area. The European Space Agency (ESA) is currently developing hardware concepts through two contracts. The

hardware being developed is a Columbus facility for improving the microgravity environment quality for payloads. The facility is called the Microgravity Isolation Mount (MGIM) and uses current state of the art vibration isolation technology as a baseline. Validation in only one degree of freedom has been completed. ESA's work in this area has been published in the open literature.

The Japanese Space Agency (NASDA) is also involved in vibration isolation technology development. The NASDA program is similar to existing NASA programs consisting of ground based testing and use of low gravity aircraft flights. NASDA however has not published much data on their efforts. The Canadian Space Agency (CSA) effort has been principally directed toward improving the low gravity environment aboard the KC-135 or any other aircraft with a Large Motion Isolation Mount (LMIM). There is merit in doing this since use of low gravity aircraft flights is a cost effective way to conduct noteworthy low gravity research. None of the on-going international programs are presently addressing the issue of flight evaluation and validation of vibration isolation technology and advanced concepts such as inertial referencing through feedforward and feedback means. At the International Workshop this issue was discussed with the conclusion that until this is done there will always be doubt about the suitability of orbital flight for science experiments and commercial processing sensitive to the vibration environment. An experiment has been submitted under an announcement of opportunity through the Office of Advanced Concepts and Technology OACT in the vibration isolation area and is focused on addressing this need. The ground based work that has been conducted in this area is extensive and the results obtained indicate that the state of the art for vibration isolation can be extended into the sub-Hertz regime. The ability to do so in a microgravity environment must be evaluated and verified in orbit. Successful verification and documentation of this capability will give users confidence to use orbital flight opportunities to attempt sensitive science endeavors and will give to commercial space initiatives the technology to provide a stable, well-characterized, affordable and reproducible microgravity environment critical to commercialize a reproducible product. The technology being evaluated will provide a data base

enabling flight hardware developers to include in their hardware the specific components and control systems best suited for their requirements with confidence of success.

References

1. Nelson, Emily S., "An Examination of Anticipated g-Jitter on Space Station and Its Effects on Materials Processes," NASA TM-103775, April 1991.

2. Hamacher, H., "Simulation of Weightlessness," Materials Sciences in Space, B. Feuerbacher, H. Hamacher and R. J. Naumann, eds., Springer-Verlag, New York, 1986, pp. 31-51.

3. Mitchell, R. A. K., et al., eds, "Measurements and Characterization of the Acceleration Environment on Board the Space Station," Guntersville, AL, Aug. 11-14, 1986, Teledyne Brown Engineering, Huntsville, AL.

4. Jones, D. I., et al., "Microgravity Isolation Mount," ESA-CR(P)-2480, European Space Agency, Paris, France, 1987.

5. Hamacher, H., et al., "Analysis of Microgravity Measurements in Spacelab," Fifteenth International Symposium on Space Technology and Science, Vol. 2, H. Matsuo, ed., AGNE Publishing Inc., Tokyo, Japan, 1986, pp. 2087-2097.

6. Ramachandran, N., "Numerical Studies of Convective Transport Associated with Crystal Growth in Microgravity," International Workshop on Vibration Isolation Technology, NASA Lewis Research Center, Cleveland, OH, April 23-25, 1991.

7. "Minutes of the Eighth Meeting of the Microgravity Measurements Group," Chairman: Charles R. Baugher, MSFC, Nov. 6&7, 1991.

8. Grodsinsky, C. M., et al., "Low Frequency Vibration Isolation Technology for Microgravity Space Experiments," NASA TM-101448, 12th Biennial Conference on Mechanical Vibration and Noise , ASME, Montreal, Canada, Sept. 17-20, 1989.

9. Grodsinsky, C., "Development and Approach to Low Frequency Microgravity Isolation Systems," NASA TP-2984, Aug., 1990

10. Knospe, C., and Allaire, P., "Limitations on Vibration Isolation for Microgravity Space Experiments," Journal of Spacecraft and Rockets, Vol. 27, No. 6, Nov.-Dec. 1990, pp. 642-646.

11. Ruzicka, J. E., "Active Vibration and Shock Isolation," SAE Paper 680747, Oct. 1968.

12. "International Workshop on Vibration Isolation Technology for Microgravity Science Applications," Lubomski, J. F., ed., NASA Conference Publication 10094, NASA Lewis Research Center, Cleveland, OH., April 23-25, 1991.

13. Wolke, P. J., "Advanced Technology for Active and Passive Vibration Isolation of Spaceborne payloads," Glendale, Arizona: Honeywell Inc., Satellite Systems Division, presented at the workshop on Vibration Isolation Technology for Microgravity Science Applications, NASA Lewis Research Center, Cleveland, OH., Sept. 28-29, 1988.

14. Stampleman, D. S., and von Flotow A. H., "Microgravity Isolation Mounts Based Upon piezoelectric Film," Active Noise and Vibration Control Conference, ASME 1990, NCA Vol. 8, pp. 57-65.

15. Meirovith, L., "Analytical Methods in Vibrations," The Macmillan Co., New York, 1967.

16. Sinha, A., Kao, C. K., and Grodsinsky, C. G., "A New Approach to Active Vibration Isolation for Microgravity Space Experiments," NASA TM-102470, Feb., 1990.

17. Tedeschi, F. P., "The Active Filter Handbook," TAB Books, 1st Edition, 1979, pp. 11-41.

18. Horowitz, P., and Hill W., "The Art of Electronics," Cambridge University Press, 1980, pp. 148-162.

19. Dally, J. W., Riley, W. F., and McConnell, K. G., "Instrumentation for Engineering Measurements," John Wiley and Sons, 1984, pp. 23-26 and 329-340.

20. Bendat, J. S., and Piersol, A. G., "Random Data," 2nd Edition, 1986, John Wiley and Sons, pp. 111-113, 136-137, 178-179, and 278-286.

21. Meirovitch, L., "Methods of Analytical Dynamics," McGraw Hill Book Co., 1970.

22. Grodsinsky, C. G., and Sutliff, T. J., "The Vibro-Acoustic Mapping of Low Gravity Trajectories on a Learjet Aircraft," Second Workshop on Microgravity Experimentation, Ottawa, Canada, May 8-9, 1990.

23. Boyer, E. O., Rieke, W. J., and Grodsinsky, C. G., " Microgravity Research on the NASA Lewis Learjet Test Facility," 31st Aerospace Sciences Meeting & Exhibit, AIAA-93-0573, Reno, NV., Jan. 11-14, 1993.

24. Humphris, R. R., et al., "Effect of Control Algorithms on Magnetic Journal Bearing Properties," Eng. Gas Turbines Power, Vol. 108, No. 4, Oct. 1986, pp. 624-632.

Appendix A

Nomenclature

A	cross-sectional area of magnetic pole face
a	average acceleration of gravity on the Earth's surface, 9.81 m/s^2
B	peak amplitude
b_2	servo force per payload mass
c	inertial electromagnetic damping coefficient, Nsec/m
c_{eq}	relative electromagnetic damping coefficient, Nsec/m
E_{avv}	accelerometer voltage output, V
F	direct disturbance, N
F_s	isolator force, N
F_o	force due to gravity on a system of mass m
F_p	force exerted by magnetic pole face
f_o	accelerometer's natural frequency
G_a	acceleration feedback gain term in Appendix B
G_{aifb}	acceleration feedback in text gain term
G_{piff}	inertial position feedforward gain term
G_v	inertial velocity feedback gain term in Appendix B
G_{vifb}	inertial velocity feedback gain term in text
G_{viff}	inertial velocity feedforward gain term in text
$G_{1h\text{-}3h}$	electro-magnetic actuator constant for horizontal actuators
$G_{1v\text{-}3v}$	electro-magnetic actuator constant for vertical actuators
g	non-dimensional acceleration
g_o	acceleration due to Earth's gravitational field
h	air gap between pole face and armature
h_o	static equilibrium gap length
$h_{1r\text{-}3r}$	relative horizontal displacement of horizontal actuation points one through three
I_{avv}	electromagnet current, α velocity
i	current through a coil
i_b	magnetic circuit current bias
K	passive stiffness coefficient, N/m
k_a	magnetic circuit current amplifier stiffness
k_{eq}	magnetic circuit isolator stiffness, N/m
k_g	magnetic circuit position gain
k_i	magnetic circuit current stiffness
k_p	magnetic circuit sensor amplifier gain
k_r	magnetic circuit velocity feedback gain
k_θ	magnetic circuit position stiffness
l	length of pivoted beam
l_1	actuator location from pivot point
m	mass, kg
N	number of ampere turns
R	resistance, Ω
T	transmissibility

t	time, sec
u	position of base
v_{1r-3r}	relative vertical displacements at vertical actuation points one through three
$X_f(s)$	mobility effectiveness
x	position of payload
x_r	relative displacement of payload in x direction
y_r	relative displacement of payload in y direction
z_r	relative displacement of payload in z direction
β_r	relative angular displacement of payload about y axis
θ	angular displacement
θ_r	relative angular displacement of payload about x axis
μ_o	permeability of free space, $4\pi x10^{-7}$ H/m
υ_c	control voltage
υ_p	proportional feedback voltage
ξ	active damping coefficient
ξ_1	passive damping coefficient
τ_1	time constant of sensing circuit
τ_2	time constant of differentiator
Φ	magnetic flux
ϕ_r	relative angular displacement of payload about z axis
Ψ	magnetic field strength
ω	excitation frequency
ω_n	system natural frequency
ω_{na}	active system resonance frequency

Appendix B

Theoretical Evaluation of Several Active Feedback and Feedforward Methods

The following analysis supports the background summary of the inertial isolation techniques which, with the needed relative support information, lead to the prototype design. The approach taken for the response analysis on these one degree of freedom inertially based isolation systems were based on work by D. Schubert, Barry Controls Eastern Operation, Barry Wright Corporation, Watertown, Massachusetts. Three physical models, Figure B.1, will be analyzed to characterize isolation using acceleration, velocity, and both acceleration and velocity as the control feedback signals.

For the physical systems described in Figure B.1 two system disturbances exist. The first is the base motion or a structural excitation, u. The second is an applied force, F, to the payload mass, m. Both terms u and F are considered to be functions for which Laplace transformations can be realized. The servo force, F_S, on the active control configurations is generated by sensing velocity, acceleration, or both and driving an actuator out of phase with the control signal.

The sensor function is to convert the velocity, dx/dt (or acceleration, d^2x/dt^2), of the payload into an electrical voltage proportional to the excitation. The sensor output voltage, E_v, is proportional to velocity dx/dt (or acceleration, d^2x/dt^2) such that $E_{vv}=A_v dx/dt$ (or $E_{va}=A_a d^2x/dt$). The voltage E_v is amplified with gain B_v (or B_a), such that the output voltage from the amplifier E_{avv} (or E_{ava}) will be $E_{avv}=A_v B_v dx/dt$ (or $E_{ava}=A_a B_a d^2x/dt^2$), respectively. The voltage is then applied to a Lorentz force actuator coil of resistance R(Ω) having negligible inductance. This coil is immersed in a magnetic field having a field strength, ψ. Application of the voltage to the coil produces a current having magnitude $I_{avv}=E_{avv}/R$ (or $I_{ava}=E_{ava}/R$). The effect of the current flowing through a coil of N turns of wire results in a force, F_S, where $F_{sv}= \psi N I_{avv}$ (or $F_{sa}= \psi N I_{ava}$). To simplify all of the

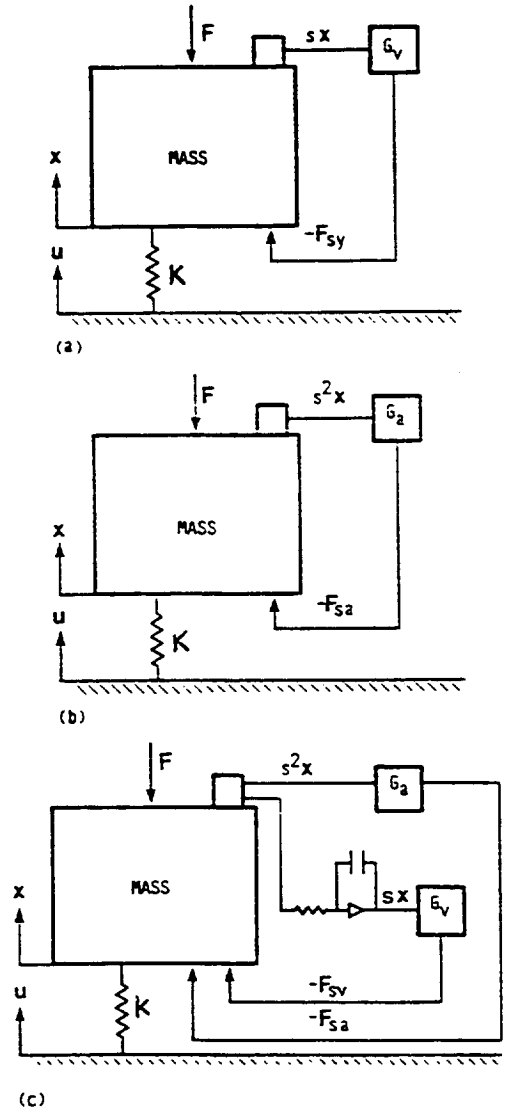

(a) Velocity feedback.
(b) Acceleration feedback.
(c) Acceleration and velocity feedback.

Figure B.1: **Physical description of three one degree of freedom inertial feedback configurations.**

above, a gain term G_v (or G_a) is applied to the feedback signal. This gain term relates the velocity dx/dt (or acceleration, (d^2x/dt^2) to the force F_{sv} (or F_{sa}) such that $F_{sv}=G_v dx/dt$ (or $F_{sa}=G\, d^2x/dt^2$). Now $F_{sv}=-G_v dx/dt$ and $F_{sa}= -G_a d^2x/dt^2$, where the negative sign denotes negative feedback. The sign applied to the servo force term, F_s, is governed by the direction the servo current flows through the coil of wire.

The equations to model the three isolation systems are as follows. The active isolation system(s) differential equation of motion is obtained from the force balance method using Newton's first and second laws. Here the base motion, u, is actually a time function, so u=u(t), with the same implied for the applied force, F, such that in actuality F=F(t). Thus, for velocity feedback,

$$m\frac{d^2x}{dt^2} = F + F_{sv} + K(u-x) \tag{B.1}$$

Substituting and rearranging give the following equations:

$$m\frac{d^2x}{dt^2} = F - G_v\frac{dx}{dt} + K(u-x) \tag{B.2}$$

$$m\frac{d^2x}{dt^2} + G_v\frac{dx}{dt} + Kx = F + Ku\,. \tag{B.3}$$

For acceleration feedback,

$$m\frac{d^2x}{dt^2} = F + F_{sa} + K(u-x) \tag{B.4}$$

Substituting and rearranging give the following equations:

$$m\frac{d^2x}{dt^2} = F - G_a\frac{d^2x}{dt^2} + K(u-x) \tag{B.5}$$

$$m\frac{d^2x}{dt^2} + G_a\frac{d^2x}{dt^2} + Kx = F + Ku \tag{B.6}$$

For acceleration and velocity feedback,

$$m\frac{d^2x}{dt^2} = F + F_{sa} + F_{sv} + K(u-x) \tag{B.7}$$

Substituting and rearranging give the following equations:

$$m\frac{d^2x}{dt^2} = F - G_a\frac{d^2x}{dt^2} - G_v\frac{dx}{dt} + K(u-x) \tag{B.8}$$

$$m\frac{d^2x}{dt^2} + G_a\frac{d^2x}{dt^2} + G_v\frac{dx}{dt} + Kx = F + Ku \tag{B.9}$$

B.1 Base-Excited Vibration Response

To determine the base-excited response for the three vibration isolation systems, the force term F(t) is set to zero. The base displacement term u(t) is assumed to be a sine wave having a peak amplitude of B. Thus, u(t) = Bsin(t) where is a frequency term. The three equations of motion become, for velocity feedback,

$$m\frac{d^2x}{dt^2} + G_v\frac{dx}{dt} + Kx = KB\sin(\omega t) \tag{B.10}$$

for acceleration feedback,

$$m\frac{d^2x}{dt^2} + G_a\frac{d^2x}{dt^2} + Kx = KB\sin(\omega t) \tag{B.11}$$

and for both acceleration and velocity feedback,

$$m\frac{d^2x}{dt^2} + G_a\frac{d^2x}{dt^2} + G_v\frac{dx}{dt} + Kx = KB\sin(\omega t) \tag{B.12}$$

The equations are then transformed into the frequency domain using the Laplace transformation:

$$F(s) = \int_{-\infty}^{\infty} F(t)e^{-st}dt \tag{B.13}$$

The velocity system equation becomes

$$ms^2X(s) + G_v sX(s) + KX(s) = KU(s) \tag{B.14}$$

the acceleration system equation becomes

$$ms^2X(s)+G_as^2X(s)+KX(s)=KU(s) \tag{B.15}$$

and the acceleration and velocity system equation becomes

$$ms^2X(s)+G_as^2X(s)+G_vsX(s)+KX(s)=KU(s) \tag{B.16}$$

The base-excited system transfer function is defined as X(s)/U(s) = T(s). Thus, the transfer functions for the three isolation systems are, for velocity feedback,

$$\frac{X(s)}{U(s)}=\frac{K}{ms^2+G_vs+K} \tag{B.17}$$

for acceleration feedback,

$$\frac{X(s)}{U(s)}=\frac{K}{ms^2+G_as^2+K} \tag{B.18}$$

for both acceleration and velocity feedback,

$$\frac{X(s)}{U(s)}=\frac{K}{ms^2+G_as^2+G_vs+K} \tag{B.19}$$

Transforming these transfer functions into a standard vibration notation gives, for velocity feedback,

$$\frac{X}{U}(s)=\frac{\omega_n^2}{s^2+2\xi\omega_ns+\omega_n^2} \tag{B.20}$$

for acceleration feedback,

$$\frac{X}{U}(s)=\frac{\omega_n^2}{s^2+\frac{b_2}{s\pi f_o^2}s^2+\omega_n^2} \tag{B.21}$$

and for acceleration and velocity feedback,

$$\frac{X}{U}(s)=\frac{\omega_n^2}{s^2+\frac{b_2}{s\pi f_o^2}s^2+2\xi\omega_n+\omega_n^2} \tag{B.22}$$

where $G_a/m = b_2/2\pi f^2_o$, $G_v/m = 2\xi\omega_n$, $\xi = 1/2G_v(1/Km)^{1/2}$.

In this form the denominator of each transfer function is called the characteristic equation. If the characteristic equation has real negative roots, then the vibration isolation system will not oscillate; if it has complex roots, it will oscillate. If the base motion displacement time function u(t) is a "pure sinusoid", the steady state frequency response in complex form is given by letting $s = j\omega$.

Thus, the frequency response is obtained by the function

$$\frac{X}{U}(j\omega)=\lim_{t\to\infty}\left[\frac{X}{U}(s)\right] \tag{B.23}$$

where $s = j\omega$ and $j = \sqrt{-1}$. This frequency response, which is a vector, becomes, for velocity feedback,

$$\frac{X}{U}(j\omega)=\frac{\omega_n^2}{\left(\omega_n^2-\omega^2\right)+2\xi\omega_n j\omega} \tag{B.23}$$

for acceleration feedback,

$$\frac{X}{U}(j\omega)=\frac{\omega_n^2}{\omega_n^2-\left(1+\frac{b^2}{2\pi f_o^2}\right)\omega^2} \tag{B.24}$$

and for both velocity and acceleration feedback,

$$\frac{X}{U}(j\omega)=\frac{\omega_n^2}{\left[\omega_n^2-\left(1+\frac{b^2}{2\pi f_o^2}\right)\omega^2\right]+2\xi\omega_n j\omega} \tag{B.25}$$

The magnitudes of vibration measured on the isolated payload resulting from the sinusoidal excitation Bsin(ωt) is the vector of length $\left|X(j\omega)/U(j\omega)\right|$. This value is a scalar since the phase angle is not used and it is called the transmissibility. It is generally written as T(jω) = $\left|X(j\omega)/U(j\omega)\right|$. Thus, the transmissibility function for the systems of interest become, for velocity feedback,

$$T_{av}=\left|\frac{X}{U_{av}}(j\omega)\right|=\left\{\frac{1}{\left[1-\left(\frac{\omega}{\omega_n}\right)^2\right]^2}\right\}T_{av}=\left|\frac{X}{U_{av}}(j\omega)\right|=\left\{\frac{1}{\left[1-\left(\frac{\omega}{\omega_n}\right)^2\right]^2+\left(2\xi\frac{\omega}{\omega_n}\right)^2}\right\}^{1/2} \tag{B.27}$$

for acceleration feedback,

$$T_{aa}=\left|\frac{X}{U_{aa}}(j\omega)\right|=\left\{\frac{1}{\left[1-\left(1+\frac{b_2}{2\pi f_o^2}\right)\left(\frac{\omega}{\omega_n}\right)^2\right]^2}\right\}^{1/2} \tag{B.28}$$

and for both acceleration and velocity feedback,

$$T_{aav}=\left|\frac{X}{U_{aav}}(j\omega)\right|=\left\{\frac{1}{\left[1-\left(\frac{b_2}{2\pi f_o^2}\right)\left(\frac{\omega}{\omega_n}\right)^2\right]^2+\left(2\xi\frac{\omega}{\omega_n}\right)^2}\right\}^{1/2} \tag{B.29}$$

The data shown in Figures B.2-B.4 present transmissibility vs non-dimensional frequency as functions of the damping term, ξ, and the acceleration term $b_2/2\pi f^2_o$.

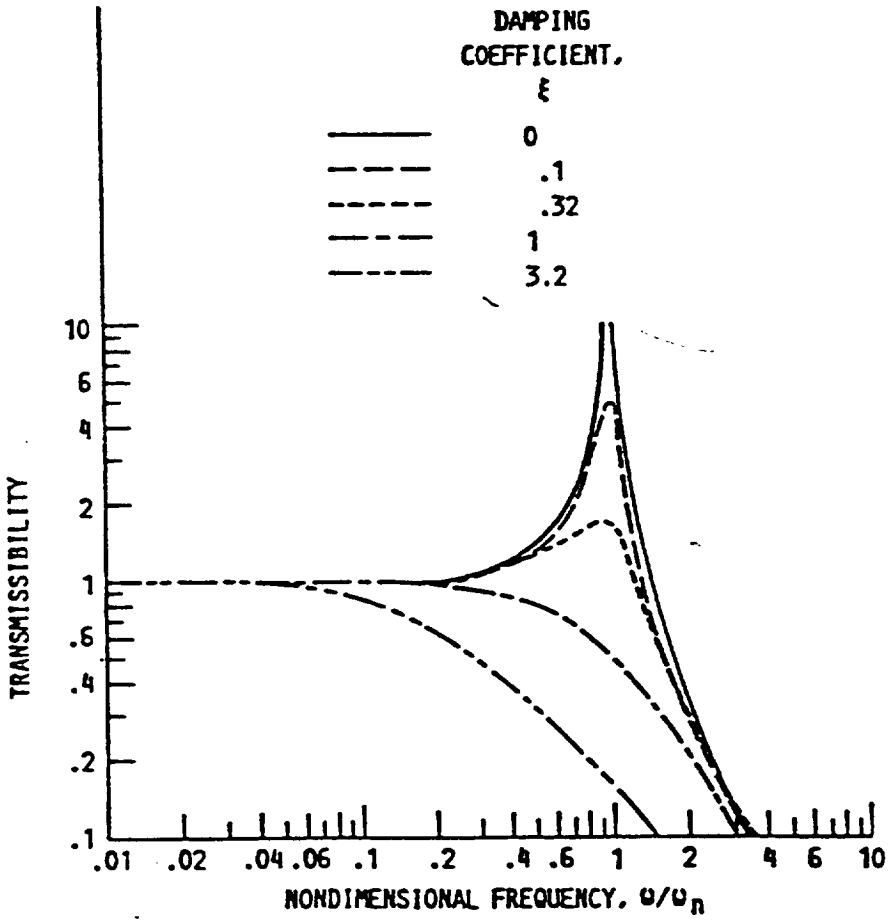

Figure B.2: Inertial velocity feedback transmissibility curves.

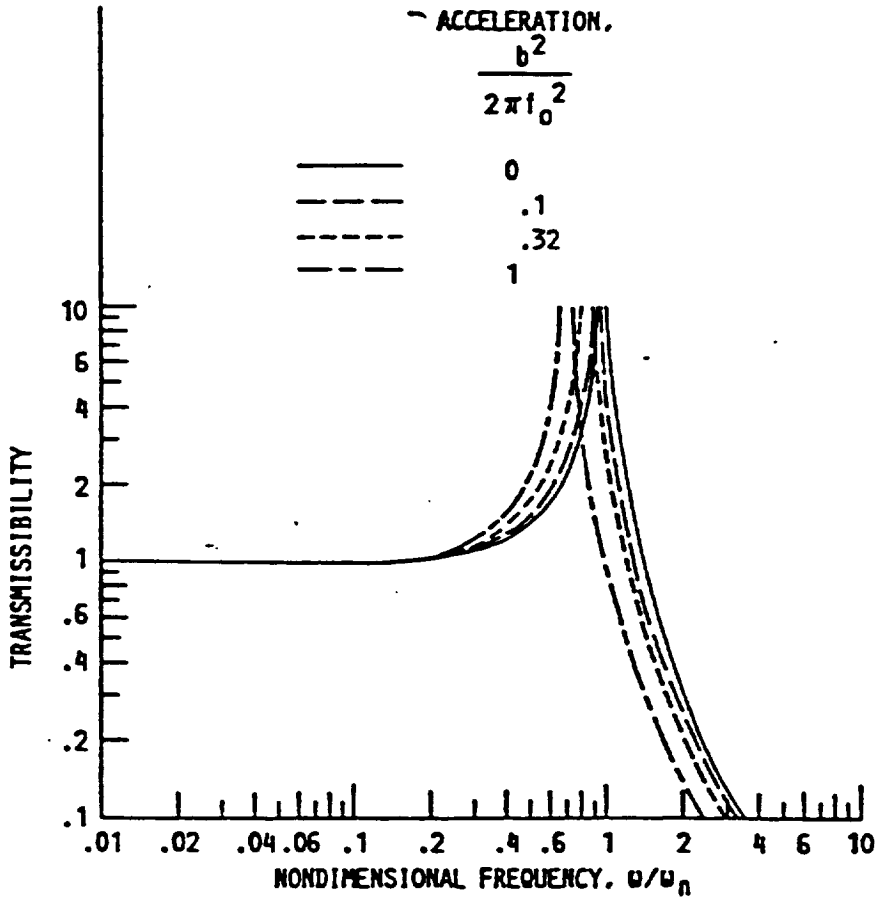

Figure B.3: Inertial acceleration feedback transmissibility curves.

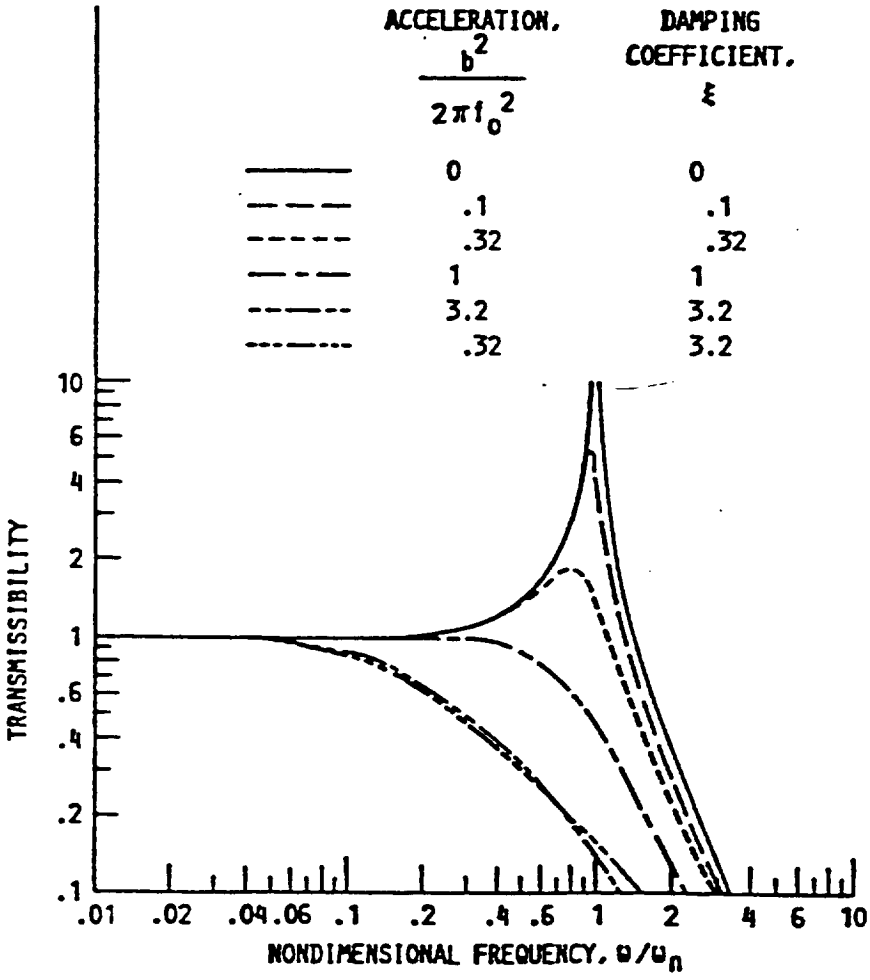

Figure B.4: Inertial acceleration and velocity feedback transmissibility curves.

B.2 Force-Excited Vibration Response

Motion of the isolated payload can result from two excitation sources. The first is base motion. The second results from external forces applied directly to the isolated payload. Referring back to the first differential equations of motion (B.3), (B.6), and (B.9), and setting the base excitation term u(t) to zero, the external force, F(t), is allowed to excite the payload. The equations of motion are, for velocity feedback,

$$m\frac{d^2x}{dt^2} = F(t) - F_{sv} - Kx \tag{B.30}$$

for acceleration feedback,

$$m\frac{d^2x}{dt^2} = F(t) - F_{sa} - Kx \tag{B.31}$$

and for both velocity and acceleration feedback,

$$m\frac{d^2x}{dt^2} = F(t) - F_{sa} - F_{sv} - Kx \tag{B.32}$$

These equations can be placed in the Laplace operation format, for velocity feedback,

$$ms^2X(s) + G_v sX(s) + KX(s) = F(s) \tag{B.33}$$

for acceleration feedback,

$$ms^2X(s) + G_a s^2X(s) + KX(s) = F(s) \tag{B.34}$$

and for both velocity and acceleration feedback,

$$ms^2X(s) + G_a s^2X(s) + G_v sX(s) + KX(s) = F(s) \tag{B.35}$$

The sensitivity of the isolated payload to the disturbing force, F(s), is characterized by a term called the isolated payload mobility. Mobility is the vector magnitude of X(s)/F(s). Mobility measures the amount by which the payload is deflected per unit of externally applied force. In Laplace notation form, the equations for mobility become, for velocity feedback,

$$\frac{X}{F}(s)_v = \frac{1}{ms^2 + G_v s + K} \tag{B.36}$$

for acceleration feedback,

$$\frac{X}{F}(s)_a = \frac{1}{ms^2 + G_a s^2 + K} \tag{B.37}$$

and for both acceleration and velocity feedback;

$$\frac{X}{F}(s)_{av} = \frac{1}{ms^2 + G_a s^2 + G_v s + K} \tag{B.38}$$

These equations are made non-dimensional, as was done for the transmissibility functions, by dividing by the mass m of the isolated payload and defining the following: $\omega_n = (K/m)^{1/2}$, $\xi = 1/2G_v(1/Km)^{1/2}$, and $G_a/m = b_2/2\pi f_o^2$. Making the above substitutions gives, for velocity feedback,

$$\frac{X}{F}(s)_v = \frac{1}{s^2 + 2\xi\omega_n s + \omega_n^2} \tag{B.39}$$

for acceleration feedback,

$$\frac{X}{F}(s)_v = \frac{1}{s^2 + \frac{b_2}{2\pi f_o^2}s^2 + \omega_n^2} \tag{B.40}$$

and for both acceleration and velocity feedback,

$$\frac{X}{F}(s)_v = \frac{1}{s^2 + \frac{b_2}{2\pi f_o^2}s^2 + 2\xi\omega_n s + \omega_n^2} \tag{B.41}$$

To show the effectiveness of the active systems, the ratio of X(s)/F(s) for an active system to X(s)/F(s) for the passive part of the system will be used. This ratio will be called the mobility effectiveness, $X_f(s)$. Thus, if X_f is unity, the effectiveness of the active vibration isolation system in reducing force induced payload motion is zero, or the active portion of the system does nothing. If X_f

is zero, the effectiveness of the active portion of the system is complete and there is no motion of the isolated payload resulting from a finite applied force. If X_f is greater than unity, then the active portion of the vibration isolation system amplifies the effect of the applied force, giving rise to more payload motion with active feedback than without it. The equations for the effectiveness function for the different systems are, for velocity feedback,

$$X_f(s)_v = \frac{s^2 + 2\xi_1\omega_n s + \omega_n^2}{s^2 + 2\xi\omega_n s + \omega_n^2} \tag{B.42}$$

for acceleration feedback,

$$X_f(s)_a = \frac{s^2 + 2\xi_1\omega_n s + \omega_n^2}{s^2 + \frac{b_2}{2\pi f_o^2}s^2 + \omega_n^2} \tag{B.43}$$

where $\xi_1 = 1/2c(1/Km)^{1/2}$, and for both acceleration and velocity feedback,

$$X_f(s)_a = \frac{s^2 + 2\xi_1\omega_n s + \omega_n^2}{s^2 + \frac{b_2}{2\pi f_o^2}s^2 + 2\xi\omega_n s + \omega_n^2} \tag{B.44}$$

In terms of frequency response, the vector length $X_f(s)$ is $\left|X_f(j\omega)\right|$. This value is obtained in the same manner as was done for transmissibility. The equations for the effectiveness of the systems become, for velocity feedback,

$$\left|X_f\left(\frac{j\omega}{\omega_n}\right)_v\right| = \left\{\frac{\left[1-\left(\frac{\omega}{\omega_n}\right)^2\right]^2 + \left(2\xi_1\frac{\omega}{\omega_n}\right)^2}{\left[1-\left(\frac{\omega}{\omega_n}\right)^2\right]^2 + \left(2\xi\frac{\omega}{\omega_n}\right)^2}\right\}^{1/2} \tag{B.45}$$

for acceleration feedback,

$$\left|X_f\left(\frac{j\omega}{\omega_n}\right)_a\right| = \left\{\frac{\left[1-\left(\frac{\omega}{\omega_n}\right)^2\right]^2 + \left(2\xi_1\frac{\omega}{\omega_n}\right)^2}{\left[1-\left(1+\frac{b_2}{2\pi f_o^2}\right)\left(\frac{\omega}{\omega_n}\right)^2\right]^2}\right\}^{1/2} \tag{B.46}$$

and for both acceleration and velocity feedback,

$$\left|X_f\left(\frac{j\omega}{\omega_n}\right)_{av}\right| = \left\{\frac{\left[1-\left(\frac{\omega}{\omega_n}\right)^2\right]^2 + \left(2\xi_1\frac{\omega}{\omega_n}\right)^2}{\left[1-\left(1+\frac{b_2}{2\pi f_o^2}\right)\left(\frac{\omega}{\omega_n}\right)^2\right]^2 + \left(2\xi\frac{\omega}{\omega_n}\right)^2}\right\}^{1/2} \tag{B.47}$$

Figures B.5-B.7 represent the effectiveness of the force actuated vibration isolation systems for a passive damping ratio of 0.05, which is typical of spring elements made of steel. The figures show the effectiveness term $\left|X_f(j\omega)\right|$ as a function of the non-dimensional gain terms.

B.3 Transmissibility Evaluation of Inertial Feedforward Controller

In order to demonstrate the advantages of isolating a payload by the proposed feedforward inertial controller design, a simple one degree of freedom spring mass damper system, shown in Figure B.8, is solved were F_S is a servo force proportional to the inertial position and velocity of the support structure, specifically F_S is defined as; $F_s = ku' + c\dot{u}'$. This force is achieved by referencing an actuator to the appropriate integrals of an accelerometer, attached to the support structure of the mass. The equation of motion for this system is:

$$m\ddot{x} + c(\dot{x}-\dot{u}) + k(x-u) + F_s = 0 \tag{B.48}$$

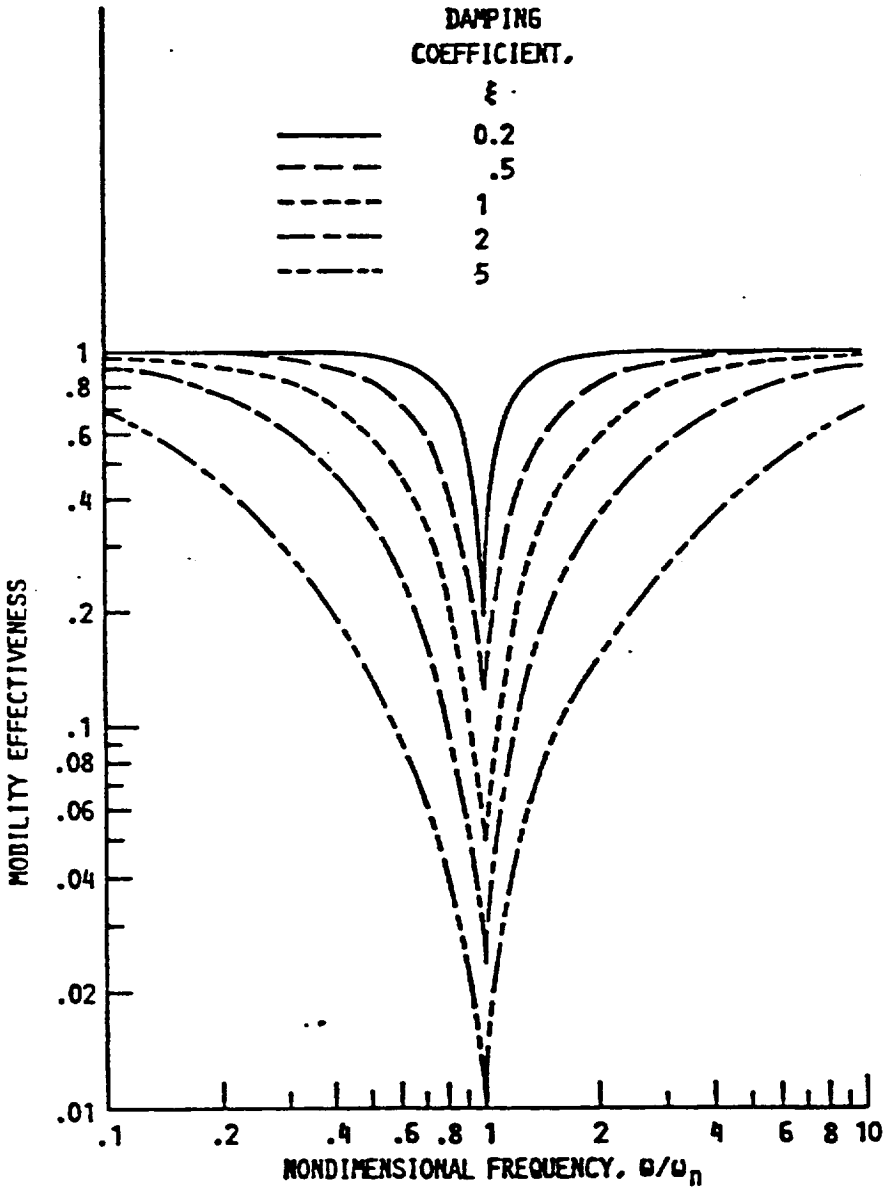

Figure B.5: Inertial velocity feedback mobility curves.

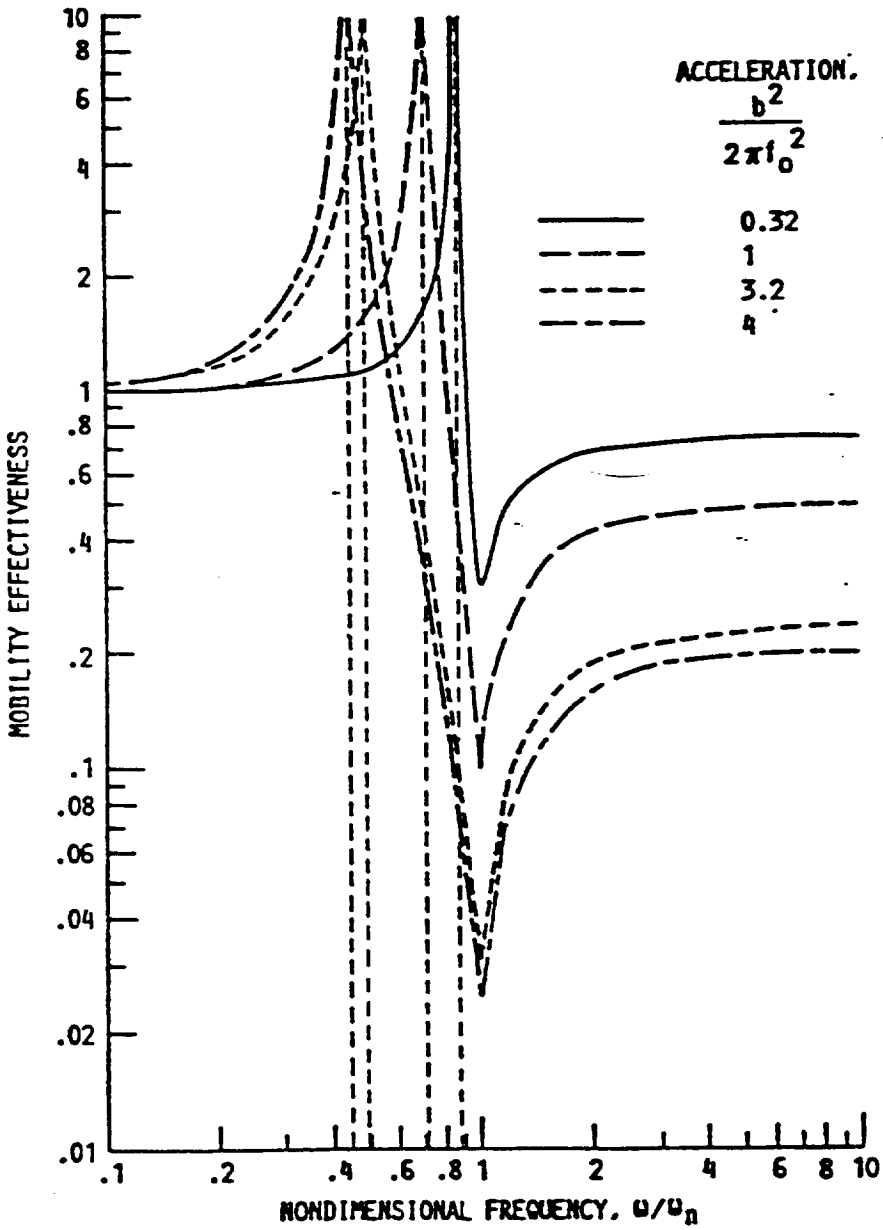

Figure B.6: Inertial acceleration feedback mobility curves.

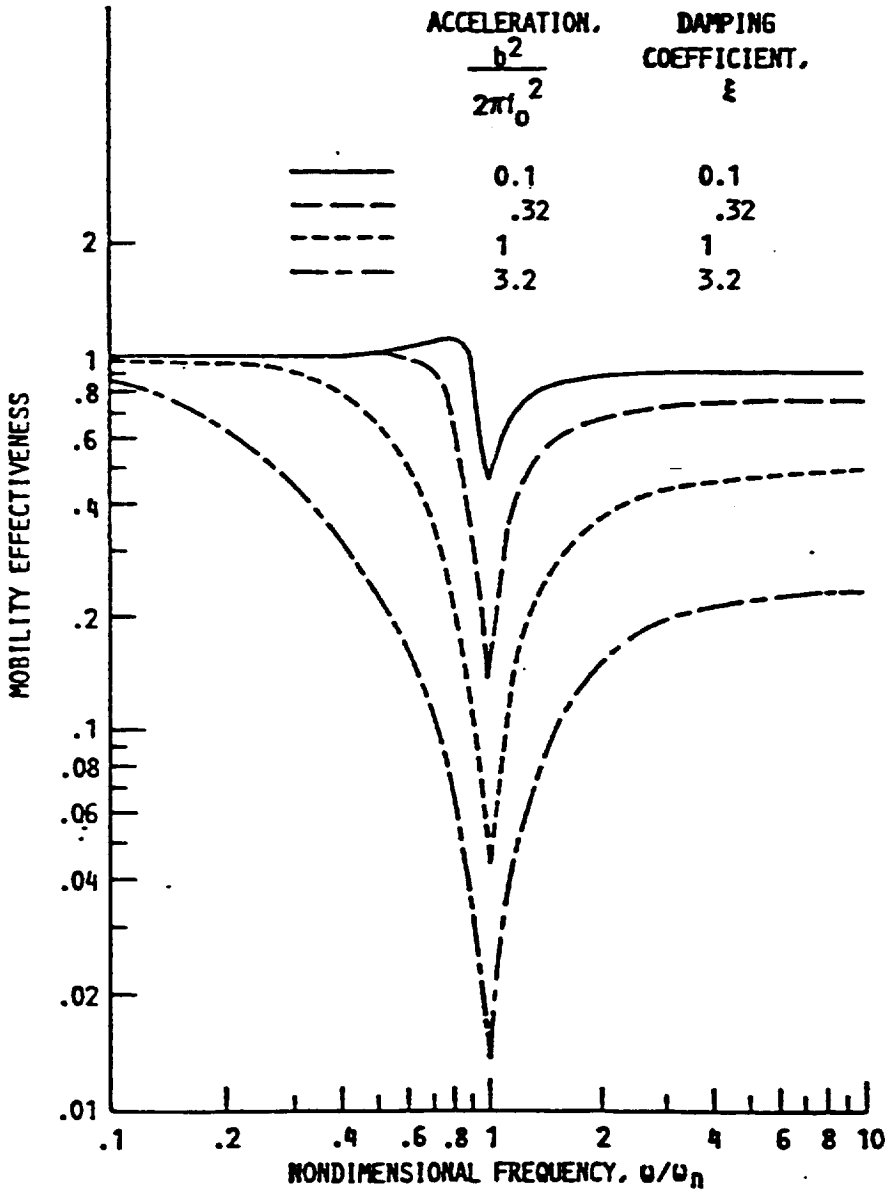

Figure B.7: Inertial acceleration and velocity feedback mobility curves.

and substituting the defined servo force into (B.48),

$$m\ddot{x}+c(\dot{x}-\dot{u}+\dot{u}')+k(x-u+u')=0. \tag{B.49}$$

Using the following definitions, the viscous damping factor $\xi = c/2m\omega_n$, where ω_n is the natural frequency of vibration for the system, $\omega^2_n = k/m$. Equation (B.49) can be put into vibration notation using the above definitions and the equation of motion becomes:

$$\ddot{x}+2\xi\omega_n\dot{x}+\omega_n^2 x=u\omega_n^2\left(1-\frac{u'}{u}\right)+2\xi\omega_n\dot{u}\left(1-\frac{\dot{u}'}{\dot{u}}\right). \tag{B.50}$$

If one assumes monochromatic motion of the base structure and that the inertial sensor has some phase and amplitude error, one can write the displacement, u, as Asin(ωt), where A is the displacement amplitude. Therefore, the inertial sensor, not including constants of integration, would give an inertial displacement of the support structure equivalent to u' as A'sin(ωt + ϕ), where A' is the displacement amplitude detected by the accelerometer. If we take the Laplace transforms of x, u, and u', including the ratios $\dot{u}'(t)/\dot{u}(t)$, and $u'(t)/u(t)$, equation (B.50) becomes:

$$X(s)\left(s^2+2\xi\omega_n s+\omega_n^2\right)=U(s)\left[\left(\omega_n^2\left(1-\frac{A'}{A}\left(\cos\phi+\frac{s}{\omega}\sin\phi\right)\right)\right)+s2\xi\omega_n\left(1-\frac{A'}{A}\left(\cos\phi-\frac{\omega}{s}\sin\phi\right)\right)\right] \tag{B.51}$$

Taking the frequency response of the transfer function and calculating the magnitude of this function one arrives at the following equation, which gives the frequency response transfer function or transmissibility of the isolated payload to a harmonic base disturbance.

$$\left|\frac{X}{U}(j\omega)\right|=\left\{\frac{\left(1-\frac{A'}{A}\left(\cos\phi-2\xi\frac{\omega}{\omega_n}\sin\phi\right)\right)^2+\left(2\xi\frac{\omega}{\omega_n}\right)^2\left(1-\frac{A'}{A}\left(\cos\phi+\frac{\omega_n}{2\xi\omega}\sin\phi\right)\right)^2}{\left(1-\left(\frac{\omega}{\omega_n}\right)^2\right)^2+\left(2\xi\frac{\omega}{\omega_n}\right)^2}\right\}^{1/2}. \tag{B.52}$$

Equation (B.52) depicts the feedforward inertial cancellation approach to offsetting the attenuation profile of a second order spring mass damper system. In the previous formulation the spring and damper elements were assumed constant. However, the approach explored, and documented in this work, has the advantages of a closed loop active magnetic system, where the relative spring and viscous elements are variables dependent on controller loop gains. The error terms in equation (B.52) model non-ideal input sensors and solves the transfer function giving the frequency shaped transmissibility curve shown in Figure B.9. These error terms can be viewed as shaping functions which could be introduced into the closed loop control as frequency weighted terms to give specific response performance dependent on excitation profiles or user requirements. Figure B.9 illustrates the advantage of inertial cancellation for a modeled system. The solid curve gives the frequency response of the single degree of freedom system with a viscous damping factor $\xi = 0.1$, and a natural frequency of $\omega_n = 2\pi(0.6\ \text{Hz})$. The dashed line is comparing the same relative based system with the addition of inertial cancellation using an inertial stiffness and damping amplitude ratio of 1.0 with no error assumed in the inertial position and a phase shift of 0.4 radians in the inertial velocity.

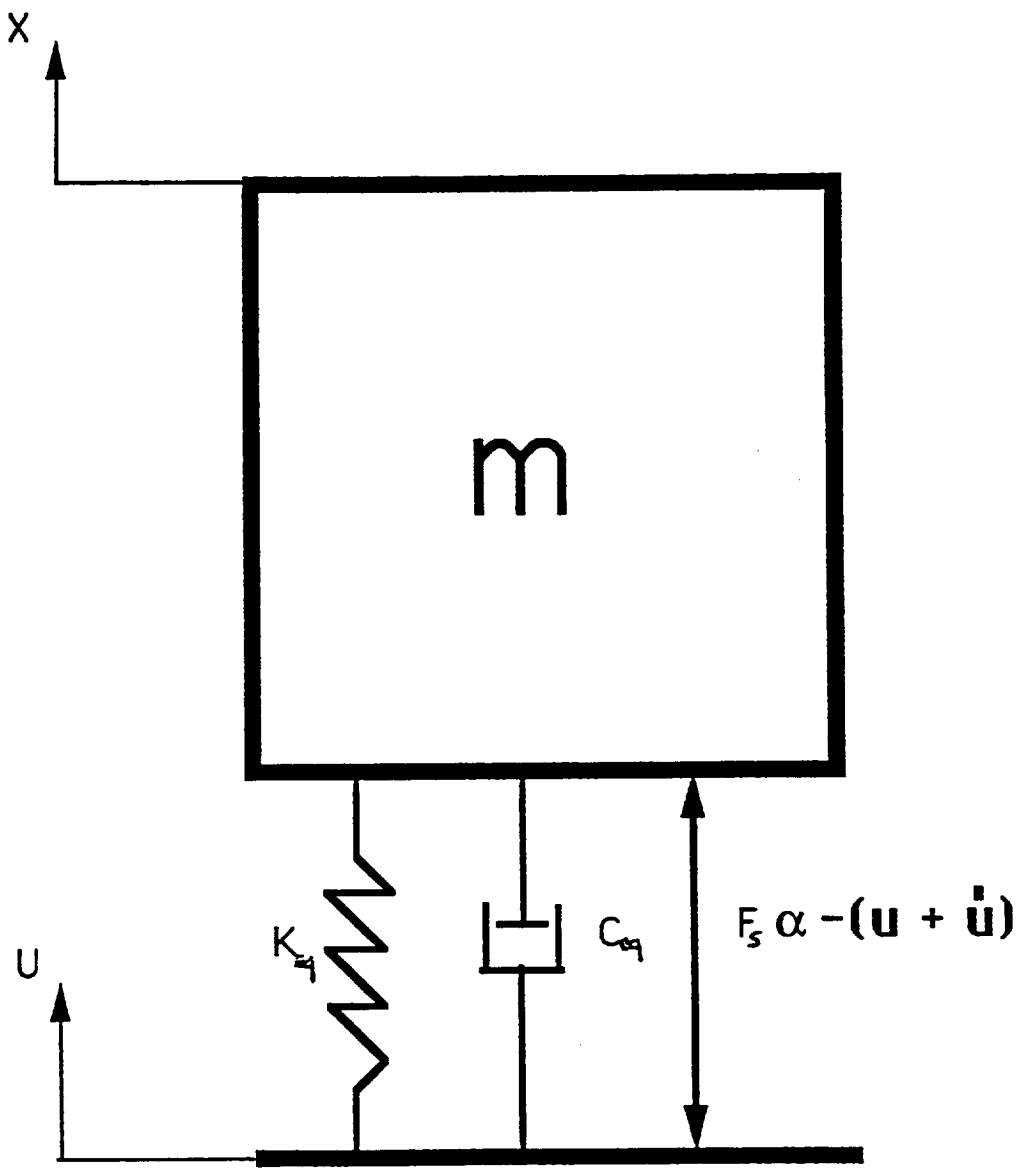

Figure B.8: One degree of freedom inertial feedforward configuration.

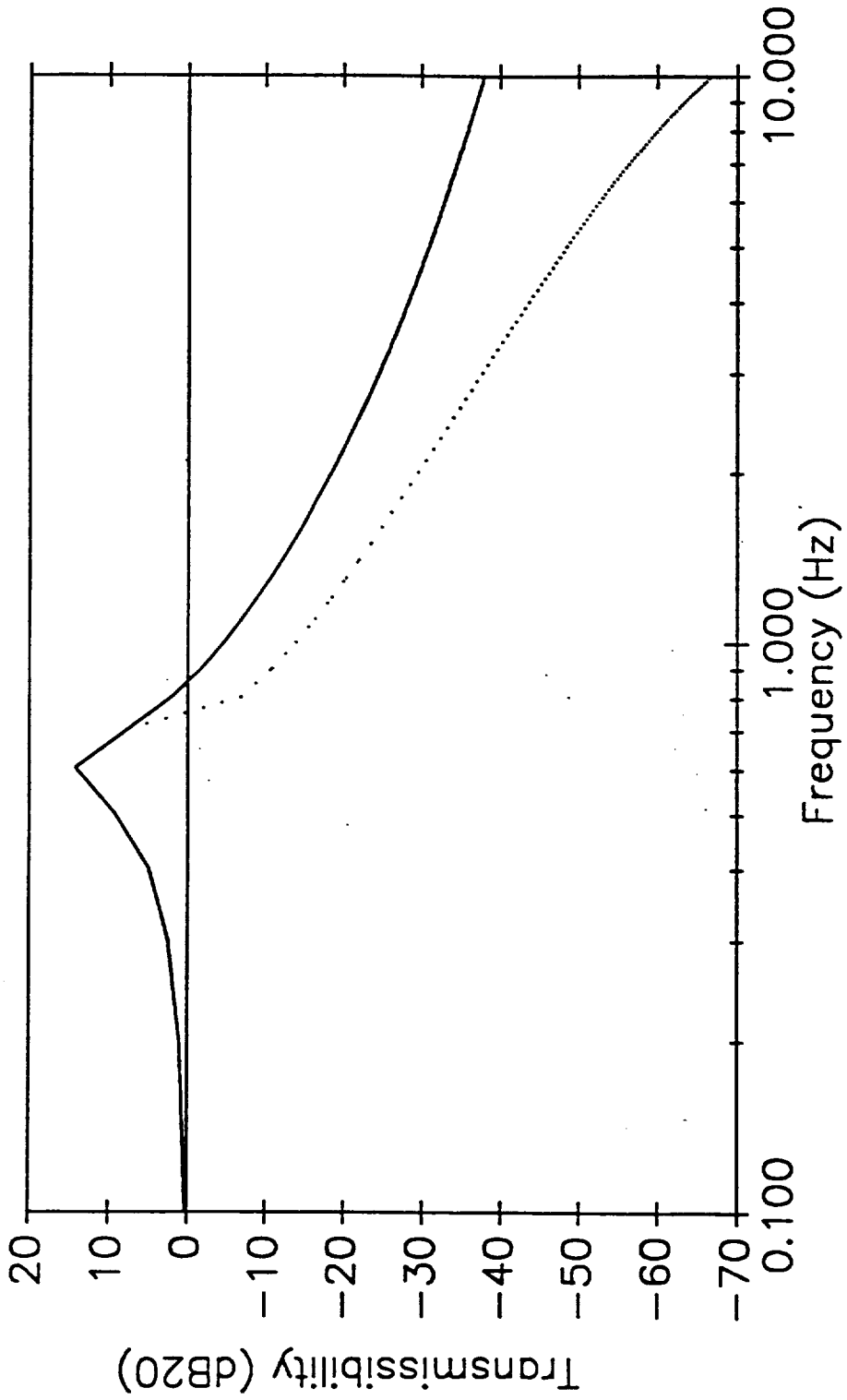

Figure B.9: Frequency response of inertial and relative based one DOF configurations.

Appendix C

One-Degree-of-Freedom Magnetic Circuit Actuator Suspension

The purpose of this appendix is to support the summary of the attractive relative suspension system presented as background for the prototype feedforward/feedback isolation system. The formulation of the relative suspension equations for an isolation system are very similar to equivalent formulations for rotating magnetic bearing systems. Such derivations can be also found in many papers on the subject of magnetic bearings [e.g., 24].

In analyzing a one degree of freedom attractive relative magnetic actuator suspension system, as shown in Figure C.1, small motions are assumed about some center position so a linearized approach can be taken. We also assume the flux levels in the core and armature of the electromagnetic circuit are below saturation. The total magnetic flux in an air gap [24] is

$$\phi = \frac{\mu_o A N i}{h} \tag{C.1}$$

Neglecting leakage and fringe effects in the magnet, the force exerted by the magnet is

$$F_p = \frac{\phi^2}{2\mu_o A} \tag{C.2}$$

Therefore, substituting the relation for the magnetic flux in an air gap gives the relation

$$F_p = \frac{\mu_o A N^2 i^2}{2h^2} \tag{C.3}$$

For both air gaps, the total force exerted is thus

$$F = 2F_p = \frac{\mu_o A N^2 i^2}{h^2} \tag{C.4}$$

Then the actual gap h and current i, for the system shown in Figure C.1, have the form

$$h = h_o - l_1\theta \tag{C.5}$$

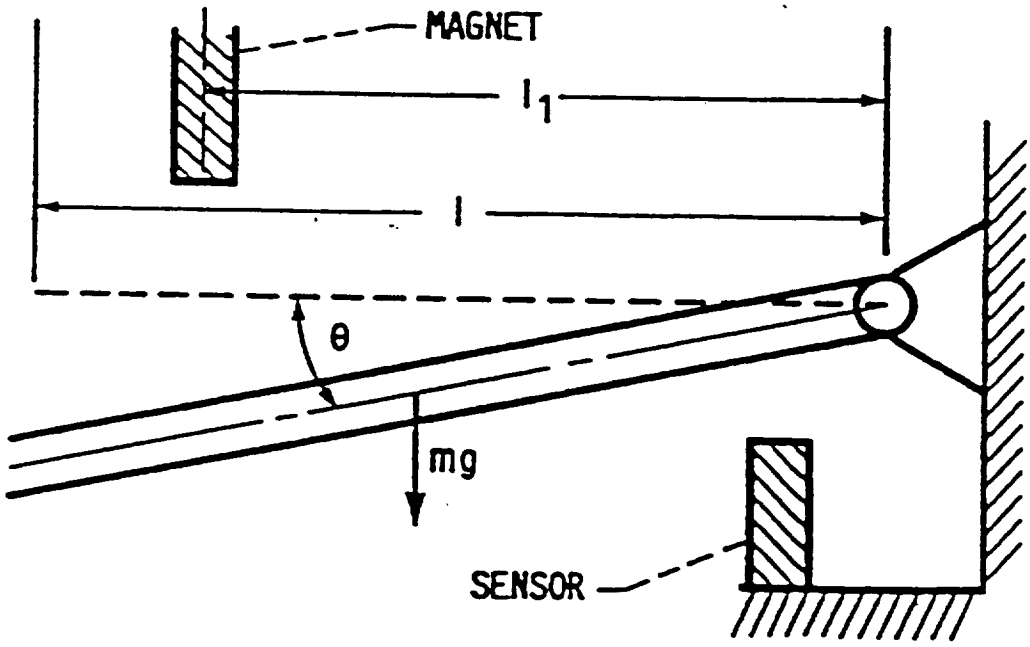

Figure C.1: Physical description of relative one degree of freedom suspension.

$$i = i_b + \Delta i \tag{C.6}$$

The negative sign occurs in h because as the mass of the system moves up, the clearance in the gap decreases. Therefore, substituting these relations for h and i into the force relation for an electromagnetic circuit one arrives at the following equation:

$$F = \frac{\mu_o A N^2 (i_b + \Delta i)^2}{(h_o - l_1\theta)^2} \tag{C.7}$$

By assuming both l_1 and i are small, equation (C.7) can be approximated by a binomial expansion about the bias current i_b, and the gap h. This then gives a linear relationship between the force F and i, making it possible to use a linear control scheme. The binomial expansion of equation (C.7) becomes

$$F = \frac{\mu_o A N^2 i_b^2}{h_o^2}\left(1 + \frac{2l_1\theta}{h_o} + \frac{2\Delta i}{i_b}\right) \tag{C.8}$$

The static equilibrium equation for the one DOF system as shown in Figure C.1 is

$$mg\frac{l}{2} = F_o l_1 \tag{C.9}$$

Thus,

$$F_o = mg\frac{l}{2l_1} = \frac{2\mu_o A N^2 i_b^2}{h_o^2} \tag{C.10}$$

Then by setting i in the linearized force equation to zero, one arrives at

$$F = mg\frac{l}{2l_1} - k_\theta \theta l_1 = \frac{\mu_o A N^2 i_b^2}{h_o^2} + \frac{2\mu_o A N^2 i_b^2 \theta l_1}{h_o^3} \tag{C.11}$$

Therefore, the position stiffness is, from equation (C.11),

$$k_\theta = -\frac{2\mu_o A N^2 i_b^2}{h_o^3} \tag{C.12}$$

A position displacement l_1 toward the magnet increases the force in that same direction. An actual spring would apply a force tending to restore the initial position of the beam at h_o. Now setting in the linearized force equation to zero one gets a linearized force component proportional to the bias current. This has been called a current stiffness by many [24]; however, a change in i does not tend to restore the beam to its original position, but an increase in current will tend to force the beam away from its steady state value always towards the magnet. The following relation demonstrates this proportionality constant which arises from linearizing the force around a bias current:

$$F = mg\frac{l}{2l_1} - k_i\Delta i = \frac{\mu_o AN^2 i_b^2}{h_o^2} + \frac{2\mu_o AN^2 i_b \Delta i}{h_o^2} \tag{C.13}$$

Therefore this proportionality constant becomes

$$k_i = -\frac{2\mu_o AN^2 i_b}{h_o^2} \tag{C.14}$$

The dynamic equation for the system of interest can be written as

$$mg\frac{l}{2l_1} + \Delta F = \frac{\mu_o AN^2 i_b^2}{h_o^2} + k_i\Delta i + ml_1\frac{d^2\theta}{dt^2} + k_\theta\theta l_1 \tag{C.15}$$

Since, from the static equilibrium case, F_o was set equal to the force needed to support the beam at its equilibrium position,

$$F_o = mg\frac{l}{2l_1} = \frac{\mu_o AN^2 i_b^2}{h_o^2} \tag{C.16}$$

then dynamic equation of this system around its static equilibrium position, which is set by the amount of bias current, can be represented by

$$\Delta F = k_i\Delta i + ml_1\frac{d^2\theta}{dt^2} + k_\theta\theta l_1 \tag{C.17}$$

By assuming the current $i = i_b + i_c$, where i_b is the bias current and i_c is the control current, then $\Delta i = i_c$. And assume that at equilibrium, or at $\theta=0$, $h=h_0$. The dynamic response equation becomes

$$\Delta F = k_i i_c + m l_1 \frac{d^2\theta}{dt^2} + k_\theta \theta l_1 \tag{C.18}$$

In order to stabilize the system one needs to take the derivative of the position signal and use both position and velocity to control the system. This portion of the control circuit can be modeled as a position constant k_g and a velocity constant k_T. These gains are adjustable and effect the stiffness and damping coefficients acting on the system. The transfer function of this portion of the circuit can be modeled as

$$\begin{aligned} \frac{v_c}{v_p} &= k_g + \frac{k_r \tau_2 s}{1+\tau_2 s} \\ &= \frac{k_g + (k_g + k_r)\tau_2 s}{1+\tau_2 s} \end{aligned} \tag{C.19}$$

Then current amplification is described by a constant as follows:

$$\frac{i_c}{v_c} = k_a \tag{C.20}$$

A block diagram can be formed as shown in Figure C.2, using force as the input and position as output. The transfer function becomes

$$\frac{\theta}{F}(s) = \frac{\dfrac{1}{ms^2 + k_\theta}}{1 + \dfrac{1}{ms^2 + k_\theta}\left\{\dfrac{k_i k_a k_p \left[k_g + (k_g + k_r)\tau_2 s\right]}{(1+\tau_2 s)(1+\tau_1 s)}\right\}} \tag{C.21}$$

In order to determine the theoretical stiffness and damping coefficients, the dynamic equations of the one DOF system are written and compared to a lumped second-order model. By

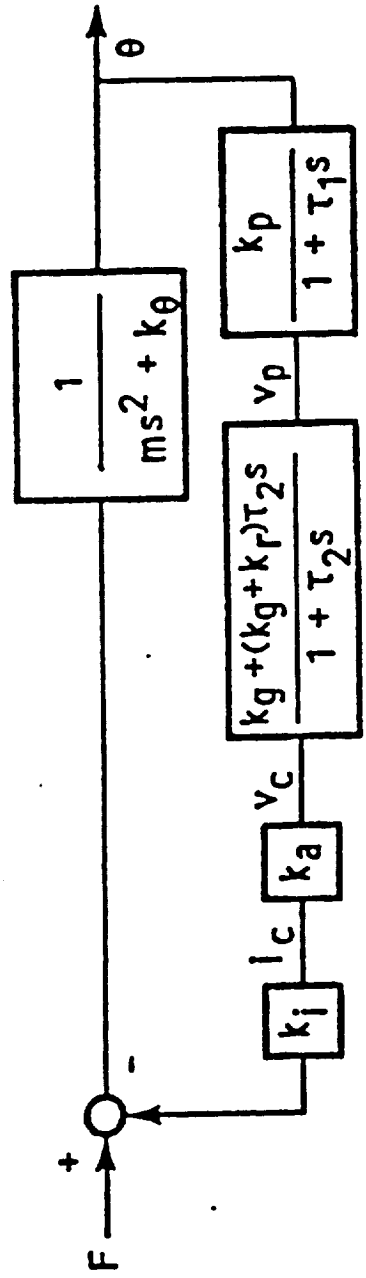

Figure C.2: Control block diagram.

using the block diagram, Figure C.2, an equation can be written involving position θ and control current i_C as follows:

$$i_c = \theta \frac{k_a k_p \left[k_g + (k_g + k_r)\tau_2 s\right]}{(1+\tau_2 s)(1+\tau_1 s)} \tag{C.22}$$

By using the relation

$$\Delta F = k_i i_c + (ms^2 + k_\theta)\theta \tag{C.23}$$

this system of equations can be put into matrix form as follows:

$$\begin{bmatrix} \Delta F \\ 0 \end{bmatrix} = \begin{bmatrix} ms^2 + k_\theta & k_i \\ \dfrac{k_a k_p \left[k_g + (k_g + k_r)\tau_2 s\right]}{(1+\tau_2 s)(1+\tau_1 s)} & -1 \end{bmatrix} \begin{bmatrix} \theta \\ i_c \end{bmatrix} \tag{C.24}$$

Then in solving this matrix formulation of the system dynamic equations for θ, one arrives at the following equation for θ(s):

$$\theta(s) = \frac{\Delta F}{\left(ms^2 + k_\theta\right) + \dfrac{k_i k_a k_p \left[k_g + \left(k_g + k_r\right)\tau_2 s\right]}{(1+\tau_2 s)(1+\tau_1 s)}} \tag{C.25}$$

where

$$\Delta F = k_i i_C + (ms^2 + k_\theta)\theta. \tag{C.26}$$

Thus

$$\theta(s) = \frac{k_i i_c + (ms^2 + k_\theta)\theta}{\left(ms^2 + k_\theta\right) + \dfrac{k_i k_a k_p \left[k_g + \left(k_g + k_r\right)\tau_2 s\right]}{(1+\tau_2 s)(1+\tau_1 s)}} \tag{C.27}$$

Setting this relation equal to the lumped second-order system of a spring dashpot configuration one can get the theoretical stiffness and damping values for the closed-loop magnetic circuit configuration:

$$\theta(j\omega) = \frac{k_i i_c + (k_\theta - m\omega^2)\theta}{(k_\theta - m\omega^2) + \dfrac{k_i k_a k_p \left[k_g + (k_g + k_r)\tau_2 j\omega\right]}{(1+\tau_2 j\omega)(1+\tau_1 j\omega)}} = \frac{f(\omega)}{(k_{eq} - m\omega^2) + j\omega c_{eq}} \tag{C.28}$$

Thus, from the equality given in equation (C.28), one obtains the following relations:

$$f(\omega) = k_i i_C + (k_\theta - m\omega^2)\theta, \tag{C.29}$$

$$k_{eq} = k_\theta + \mathcal{R}_e\left\{\frac{k_i k_a k_p \left[k_g + (k_g + k_r)\tau_2 j\omega\right]}{(1+\tau_2 j\omega)(1+\tau_1 j\omega)}\right\} \tag{C.30}$$

and

$$c_{eq} = \frac{\mathcal{I}_m}{\omega}\left\{\frac{k_i k_a k_p \left[k_g + (k_g + k_r)\tau_2 j\omega\right]}{(1+\tau_2 j\omega)(1+\tau_1 j\omega)}\right\} \tag{C.31}$$

Therefore, in evaluating the equivalent stiffness and damping for the closed-loop system one comes up with the following relations:

$$k_{eq} = k_\theta + \frac{k_i k_a k_p \left[k_g(1-\tau_2\tau_1\omega^2) + (k_g + k_r)(\tau_2 + \tau_1)\tau_2\omega^2\right]}{(1-\tau_2\tau_1\omega^2) + (\tau_2 + \tau_1)^2\omega^2} \tag{C.32}$$

$$c_{eq} = \frac{k_i k_a k_p \left[(1-\tau_2\tau_1\omega^2)(k_g + k_r)\tau_2 - k_g(\tau_2 + \tau_1)\right]}{(1-\tau_2\tau_1\omega^2) + (\tau_2 + \tau_1)^2\omega^2} \tag{C.33}$$

Appendix D

Transfer Function Determination

This appendix will describe how the signal analyzer used extensively in the design and development of the active isolation systems determines the transfer function of signal conditioning filters or any other system. The generation of random noise by the signal analyzer is described first and then the processing accomplished by the analyzer is discussed.

The signal analyzer generates an exponentially time-correlated random process with a correlation time, T, and mean-square value of σ^2. This process is effectively Gauss-Markov, which implies wide-sense stationarity and ergodicity, and therefore has properties which make the mathematics tractable. The autocorrelation function, $R_{nn}(\tau)$, of this process, $n(\tau)$, is shown in Figure D.1 and can be described by

$R_{nn}(\tau) = \sigma^2 e^{-\tau/|\tau|}$.

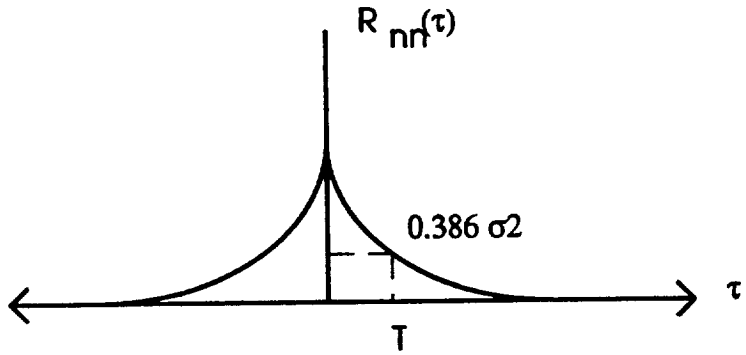

Figure D.1: Autocorrelation of an Exponentially Time-Correlated Process

The analyzer obtains the autospectral (or power spectral) density of this random process by taking the fast Fourier transform of the autocorrelation function. In the frequency domain, the autospectral density, $G_{nn}(\omega)$, of the random process, $n(\tau)$, is illustrated in Figure D.2 and is given by

$$G_{nn}(\omega) = \frac{2\sigma^2 / T}{\omega^2 + (1/T)^2}. \qquad \text{(D.1)}$$

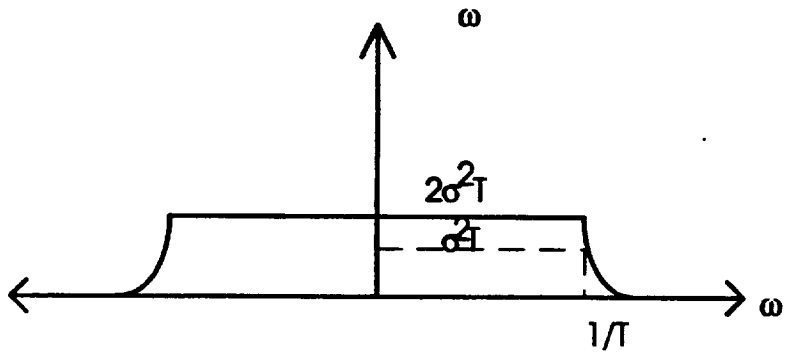

Figure D.2: PSD of Exponentially Time-Correlated Process.

The result is a band-limited process, displaying equal power at all frequencies within the band of interest. The half-power point occurs at 1/T, which corresponds with the highest frequency selected through the analyzer span control. Through judicious selection of the frequency span, a random process displaying the desired characteristics is obtained.

For analytical purposes, white noise as opposed to wideband noise, is desirable to work with for a number of reasons. It is easily manipulated with engineering tools and the theory is complete and practical. Whiteness implies that the noise value is not correlated in time and that the noise has equal power in all frequencies. Since this would result in a noise with infinite power, a white noise process does not realistically exist. Although this concept does not exist it is useful to consider. Any physical system has a certain frequency bandpass, i.e., a frequency range of inputs to which it can respond. Above this range, the input either has no effect or the system attenuates the effect and essentially the input does not exist beyond a certain stopband.

Typically a system will be driven by wideband noise, one having constant power at frequencies within the passband. On this plot, a white noise would merely extend this constant power

level across all frequencies. Within the bandpass of the system, the fictitious white noise looks identical to wideband noise.

In some instances, the noise power level is not constant over all frequencies within the system bandpass, or the noise may be time correlated. For such cases, a white noise put through a small linear filter can duplicate virtually any form of time-correlated noise. This is the case of the random process generator in the signal analyzer.

To obtain a random process exhibiting the desired autocorrelation and autospectral density, the analyzer drives a first order lag system with a zero mean, white Gaussian noise of strength Q, where $Q = 2\sigma^2/T$. After applying the white noise to the lag circuit and allowing transients to die out, a steady state process with the desired statistics results.

It may be obvious why it is necessary for the analyzer to alter the half power point of the random process it generates, when alternatively it could generate a single process with an exceptionally wide band. In actuality, the analyzer can only generate a process that makes the integral of the PSD constant. Reducing the half power point (increasing the correlation time) results in a higher power level distributed over the frequency band. Likewise, increasing the half power point, decreases the power level. When exciting a system across its bandpass, it is desirable to distribute the highest amount of power within the frequency band of interest. Therefore, it is necessary for the analyzer to provide for the adjustment of the random process statistics through the selection of the proper frequency span value.

The data processing performed by the analyzer in seeking to determine a test item's transfer function requires the basic setup shown in Figure 3.13. The random noise process is injected into the system and sampled by a channel of the analyzer. The system output is sampled by a second channel. Prior to digitization, both channels of data are filtered to prevent aliasing. Because processing is accomplished in real time, biases and trends are not removed. Using the data collected from the random process, $x(\tau)$, the autocorrelation function $Rxx(\tau)$ is calculated. The random process data,

together with the data collected from the system output, y(τ), allow the calculation of the cross correlation function Rxy(τ). Both of the correlation functions are then fast Fourier transformed, using side love suppression techniques, to give the autospectral density, Gxx(ω), and the cross spectral density, Gxy(ω). Using complex forms of these densities, the system transfer function is computed by

$$H(\omega) = \frac{G_{xy}(\omega)}{G_{xx}(\omega)}. \tag{D.1}$$

The magnitude and phase result is displayed on the analyzer screen.

D.1 Autocorrelation and Crosscorrelation Functions

Given an accelerometer output measuring the random vibrations of some structure, the voltage output from the accelerometer, x(t) will be a random signal. If two voltage measurements, v_1 and v_2 are taken at two different times, t_1 and $t_1 + \tau$ respectively, and this process is repeated many times giving multiple pairs of measurements $\{v_1,v_2\}$, where in each pair, v_1 is measured τ seconds before v_2. If the time interval τ is extremely small, then v_1 and v_2 are statistically likely to be nearly the same value.

For most random processes, an increase in the time duration τ results in a lower probability that v_1 and v_2 become less interdependent, or correlated as the time interval τ, is increased. The autocorrelation function may be described as a measure of the correlation between two successive measurements, as a function of the time elapsed between these two measurement. It follows that the autocorrelation function is also an indication of how rapidly the function is changing with time. If the function changes very rapidly, then the time duration τ, will have to be extremely small in order to obtain good correlation between the voltage measurements v_1 and v_2.

The expressions for the autocorrelations of two random processes x(t) and y(t) are shown below for the special case in which the process means μ_x and μ_y, and the autocorrelation functions

themselves are not changing with time. If this is not the case, the autocorrelation functions become functions of both time t, and the time interval between measurements, τ. It is assumed that the process means and the autocorrelation functions process for a certain length of time do not change. Such processes are often called stationary processes. It is also assumed in the expressions below that the random processes are both zero mean.

$$R_{xx}(\tau) = E\{x(t)x(t+\tau)\} = \underset{T \to \infty}{Lim} \frac{1}{T}\int_0^T x(t)x(t+\tau)dt \tag{D.2}$$

$$R_{yy}(\tau) = E\{y(t)y(t+\tau)\} = \underset{T \to \infty}{Lim} \frac{1}{T}\int_0^T y(t)y(t+\tau)dt \tag{D.3}$$

In these expressions the operator E{ } is used to denote the arithmetic mean of the set of values enclosed by the brackets. For example, in the expression for $R_{xx}(\tau)$, all elements of the time history x(t) which form pairs separated by a fixed time interval τ, are identified. The elements of each pair are multiplied together, and the arithmetic mean of all of these products is then calculated. The process is repeated for the next value of τ, until all values of τ have been exhausted.

The crosscorrelation function is closely related to the autocorrelation function. The only difference between the two functions is the source of the measurement v_2 in the above discussion of the autocorrelation function. The first voltage measurement v_1 is a measurement of the random process x(t) as before, but the second measurement v_2, is a measurement of some other random process, y(t). As before, the two measurements are taken within τ seconds of one another. The expression for the crosscorrelation function between x(t) and y(t) is shown below. As was assumed in the presentation of the autocorrelation functions, the two random processes are zero mean. In addition, the process means and the crosscorrelation function are not changing with time.

$$R_{xy}(\tau) = E\{x(t)y(t+\tau)\} = \underset{T \to \infty}{\lim} \frac{1}{T}\int_o^T x(t)y(t+\tau)dt \tag{D.4}$$

D.2 Autospectra and Autospectral Density Functions

A random process which has a mean and an autocorrelation function that are not changing with time is said to be stationary. The signal content in the frequency domain, of a stationary random process is given by the Fourier transform of the autocorrelation function as

$$S_{xx}(j\omega) = \frac{1}{2\pi}\int_{-\infty}^{\infty} R_{xx}(\tau)e^{-j\omega\tau}d\tau \tag{D.5}$$

where: j = imaginary operator = $\sqrt{-1}$, and ω = frequency in rad/s. $S_{XX}(j\omega)$ is called the two sided autospectrum of the random process x(t). This function is said to be two sided because it is symmetric about the $\omega = 0$ axis. The spectrum equation is modified by dividing by the bandwidth of interest, and by changing the limits of integration to reflect this bandwidth. If the signal has units of volts, then the division by the bandwidth gives the spectrum units of V^2/(rad/s). The modified spectrum having the units of V^2/(rad/s) is a measure of the density of signal per unit frequency increment. For this reason, the modified autospectrum is called an autospectral density function. The limits of integration in an autospectral density function must also be consistent with the bandwidth. For example, if an autospectral density is to be calculated for a signal over the frequency band $\omega_i \le \omega \le \omega_f$, then the limits of integration are from ω_i to ω_f. Notice that the resulting function is not symmetric about the $\omega = 0$ axis. This function, defined over the above frequency band is said to be one sided. In order to reflect all the energy in the signal over to the right hand side of the $\omega = 0$ axis, the spectrum must also be multiplied by 2. It should be noted that the autocorrelation function $R_{XX}(\tau)$ is also a symmetric function. When the band limited autospectral density function is multiplied by 2, only the portion of $R_{XX}(\tau)$ corresponding to positive values of τ need be included. The complete, one sided autospectral density function, which is the standard for describing spectra is defined below,

$$G_{xx}(j\omega) = \frac{1}{\pi(bw)}\int_{\omega_i}^{\omega_f} R_{xx}(\tau)e^{-j\omega\tau}d\tau \tag{D.6}$$

where bw = bandwidth (rad/s).

D.3 Crossspectra and Crossspectral Density Functions

The one sided crosspectral density function between the random processes x(t) and y(t) is given below. This function differs from the one sided autospectral density function in that the crosscorrelation function $R_{xy}(\tau)$ is used rather than the autocorrelation function $R_{xx}(\tau)$.

$$G_{xy}(j\omega) = \frac{1}{\pi(bw)} \int_{\omega_i}^{\omega_f} R_{xy}(\tau) e^{-j\omega\tau} d\tau \qquad \text{(D.7)}$$

Appendix E

Input and Output Spectra for Multi-Dimensional Transfer Function Calculations

The following figures are given as reference to the transfer functions calculations from Chapter 4 for the multi-dimensional Learjet transfer functions calculated for the relative and inertial control cases. Figures E.1 through E.4 (a) and (b), give the input and output spectral densities for the X direction for the single input reference locations one through four for both trajectories, relative and inertial, respectively. Figures E.5 through E.8 (a) and (b), give the input and output spectral density functions for the Y direction, and Figures E.9 through E.12 (a) and (b) give the input and output spectral density curves for the Z direction, for the single input reference locations one through four for both relative and inertial control cases, respectively. Figures E.13 and E.14 (a) and (b) give the input and output spectra for the θ_X rotation for the trunnion location and the aircraft location, respectively. Figures E.15 and E.16 (a) and (b) give the input and output spectra for the ϕ_Y rotation as defined in equations (4.17) and (4.18), and Figures E.17 and E.18 (a) and (b) are the input and output spectra for the β_Z rotation as defined in equations (4.19) and (4.20). These spectral density functions have been plotted with the same minimum and maximum values for both relative and inertial control cases.

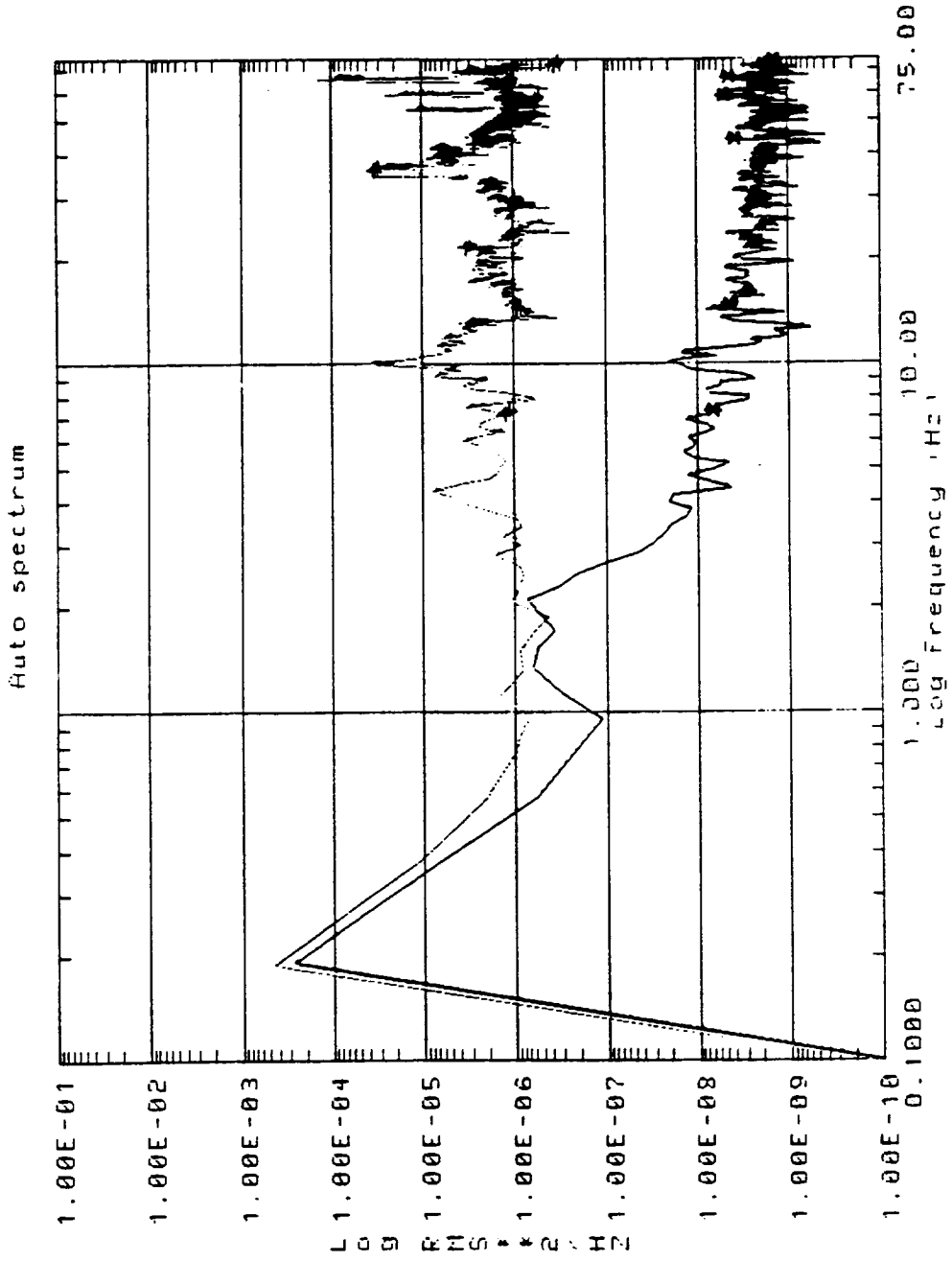

(a) Payload under relative control.

Figure E.1: Output and input power spectra for platform x and aircraft location 1 x.

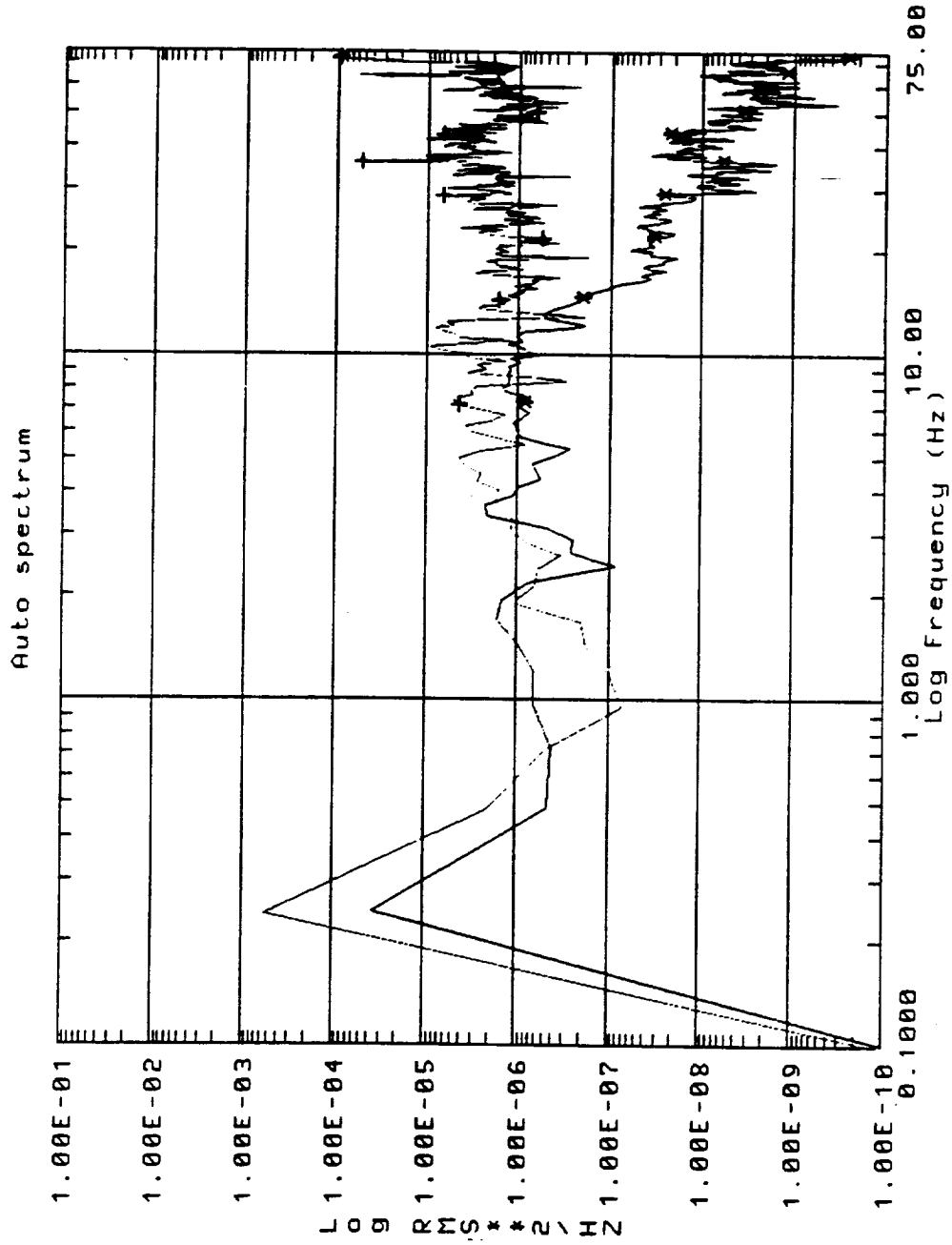

(b) Payload under inertial control.

Figure E.1: Output and input power spectra for platform x and aircraft location 1 x.

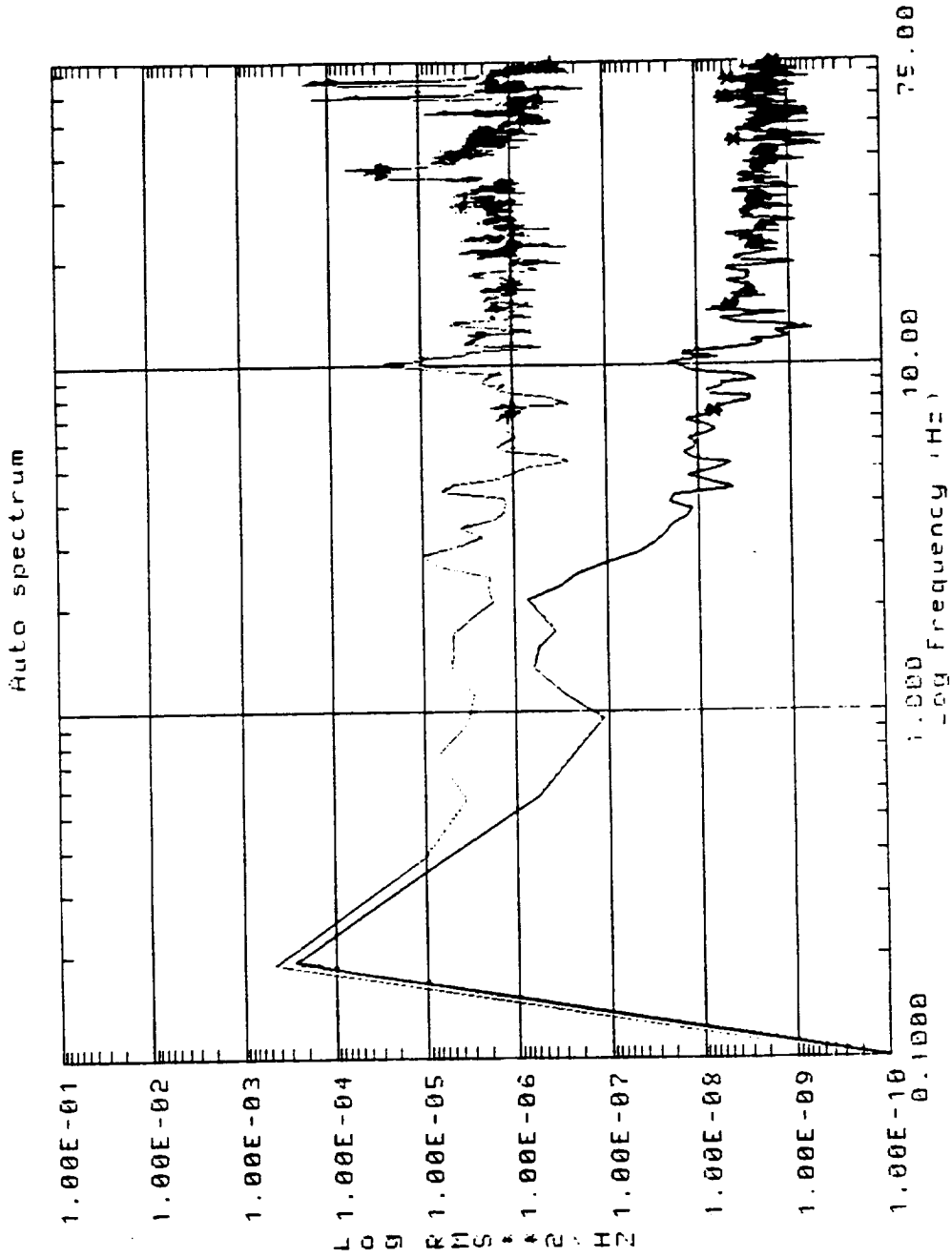

(a) Payload under relative control.

Figure E.2: Output and input power spectra for platform x and aircraft location 2 x.

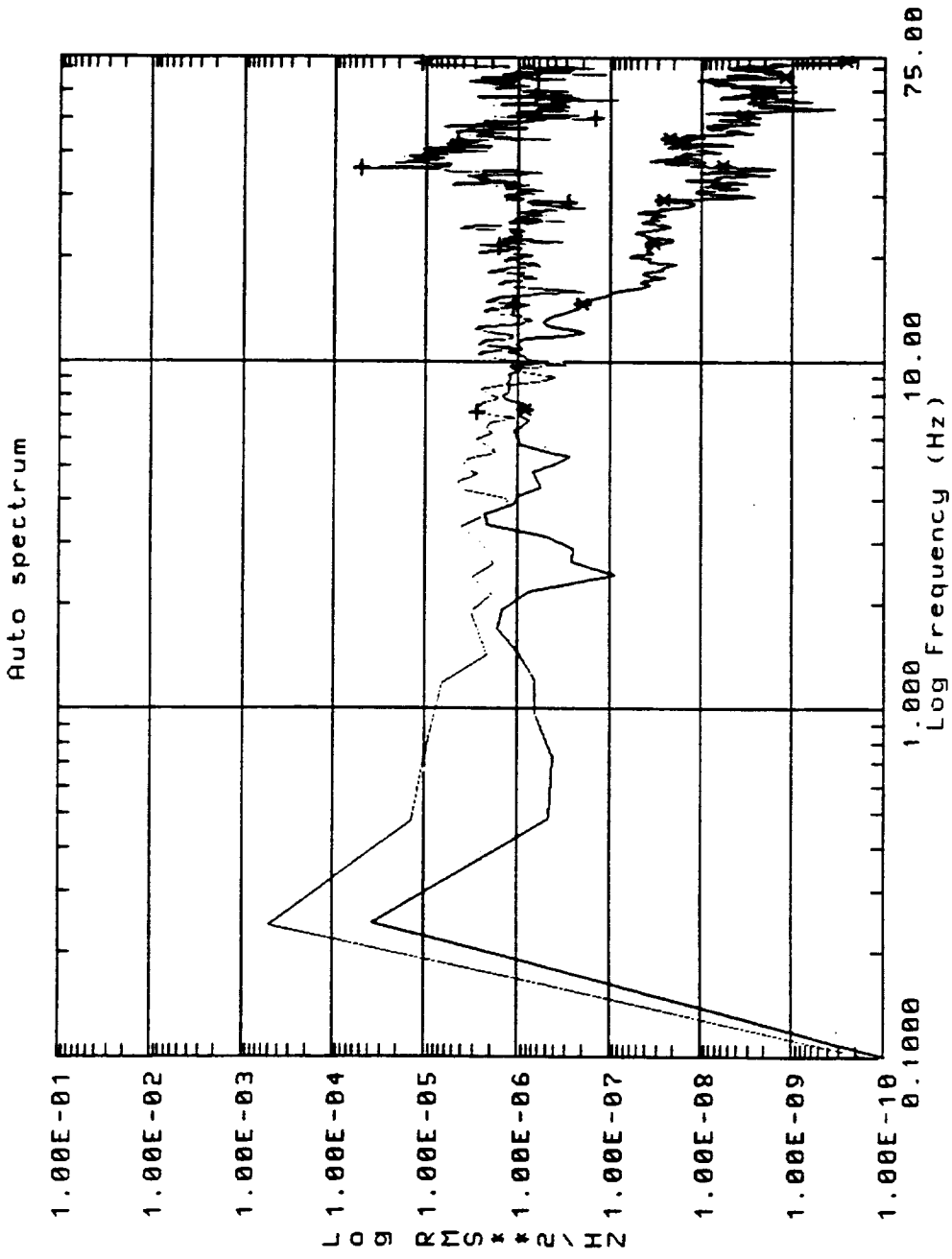

(b) Payload under inertial control.

Figure E.2: Output and input power spectra for platform x and aircraft location 2 x.

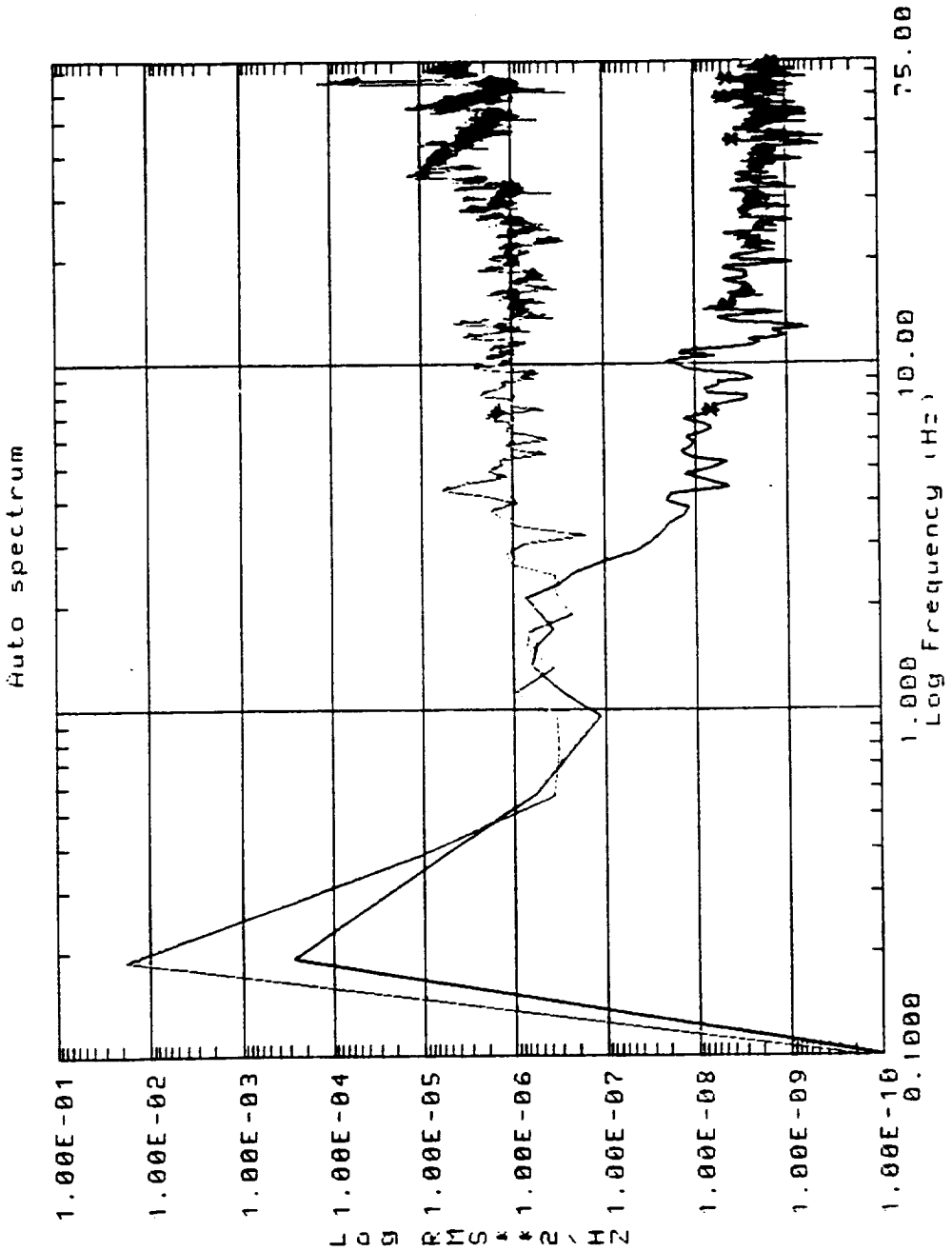

(a) Payload under relative control.

Figure E.3: Output and input power spectra for platform x and aircraft location 3 x.

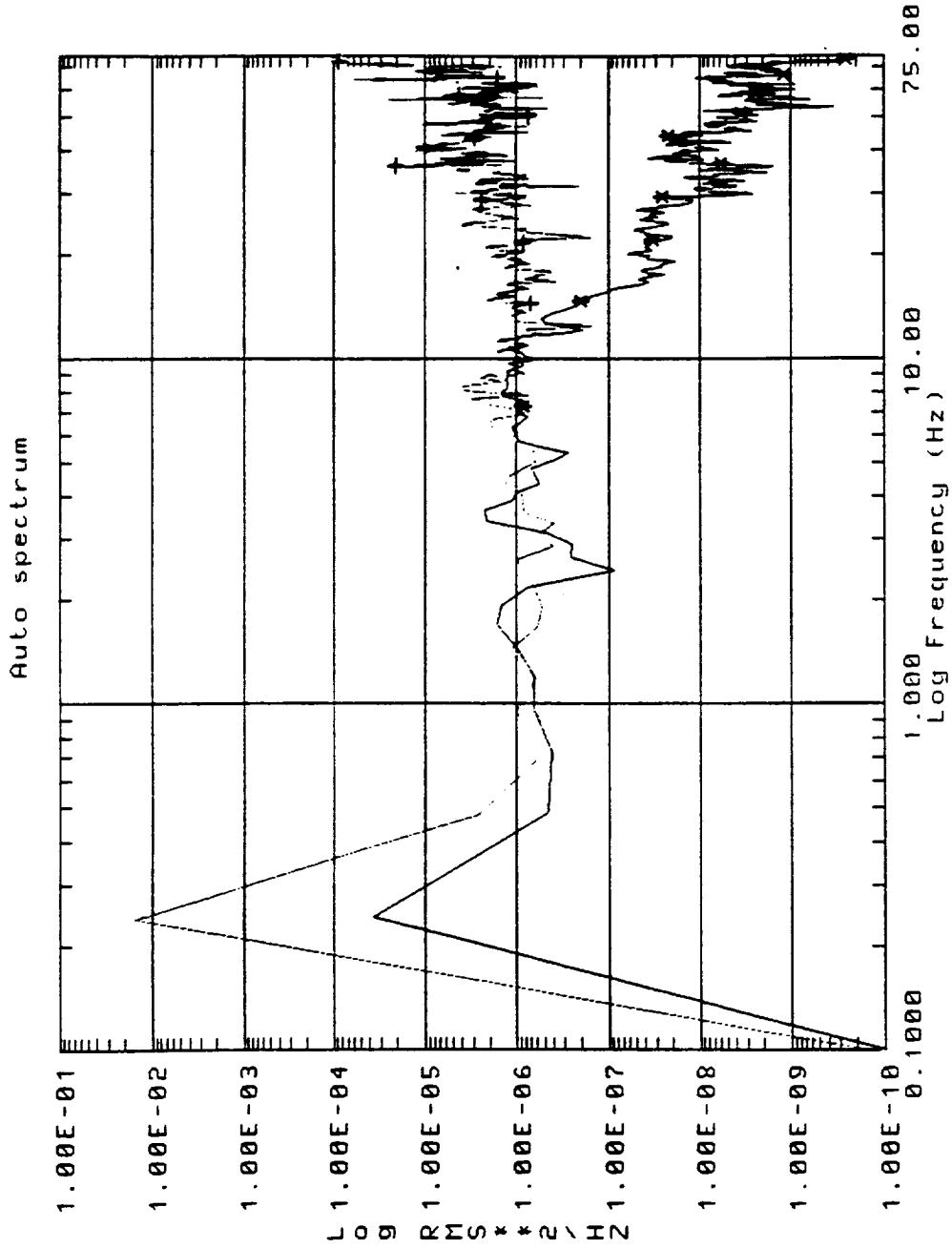

(b) Payload under inertial control.

Figure E.3: Output and input power spectra for platform x and aircraft location 3 x.

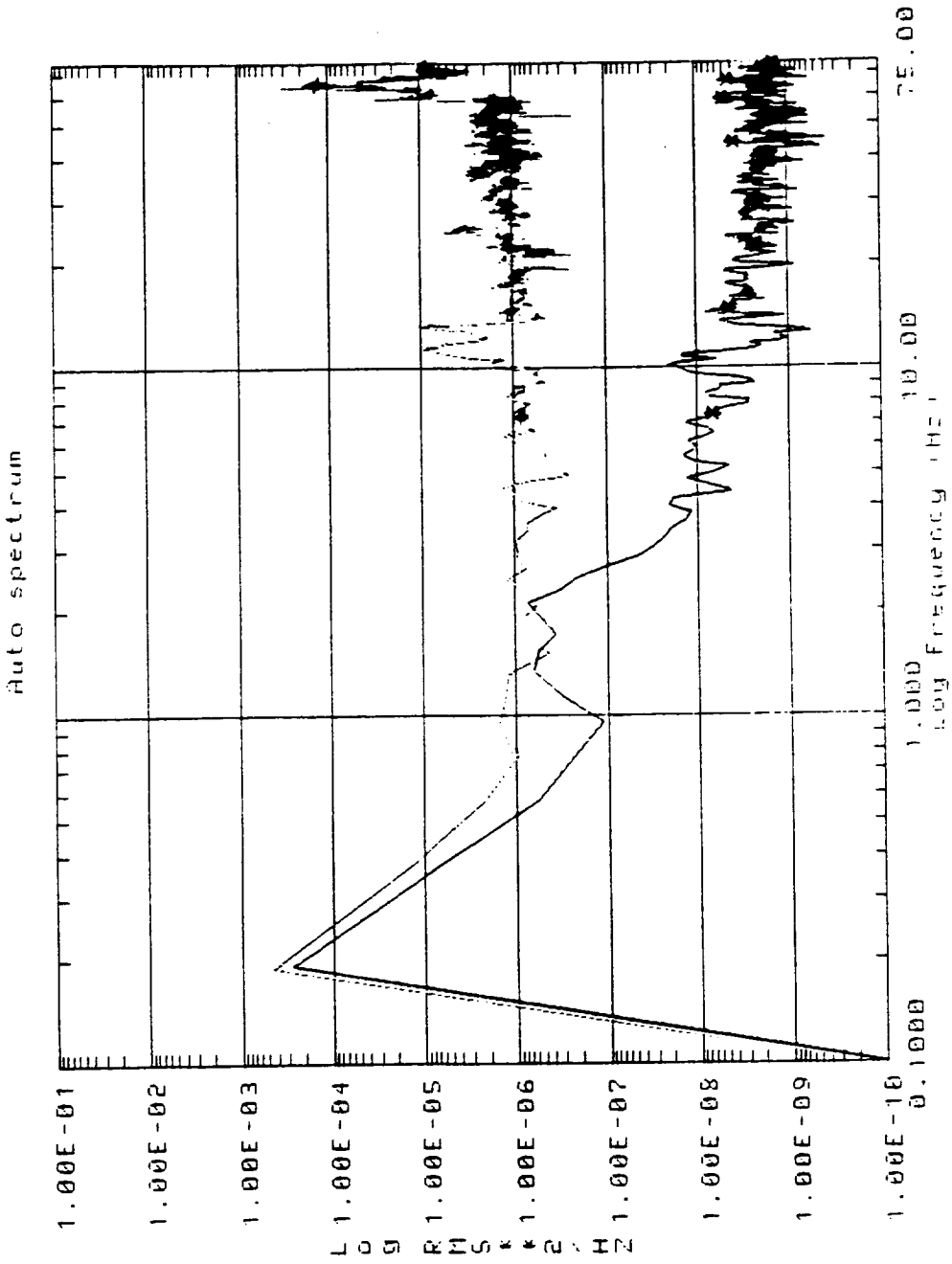

(a) Payload under relative control.

Figure E.4: Output and input power spectra for platform x and aircraft location 4 x.

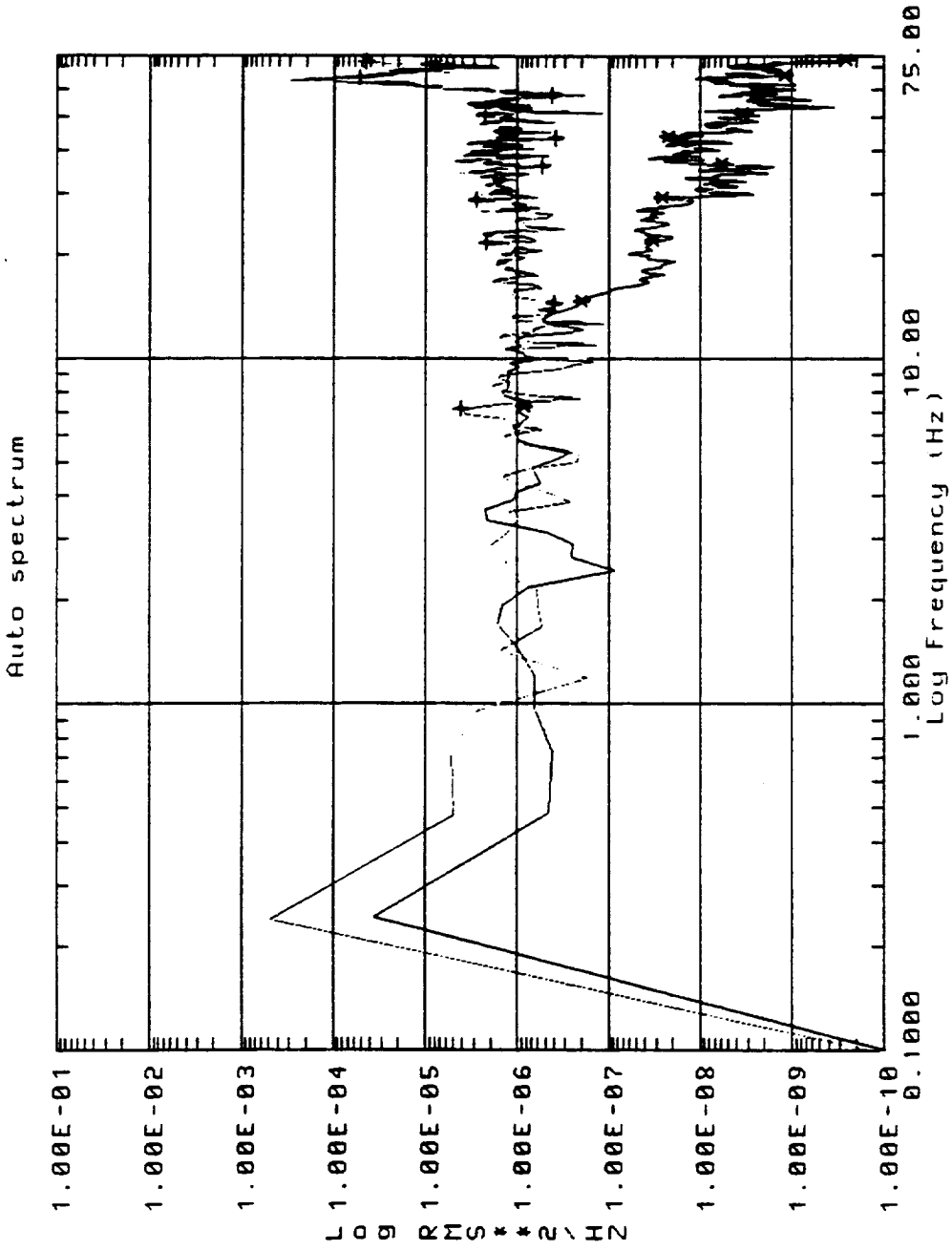

(b) Payload under inertial control.

Figure E.4: Output and input power spectra for platform x and aircraft location 4 x.

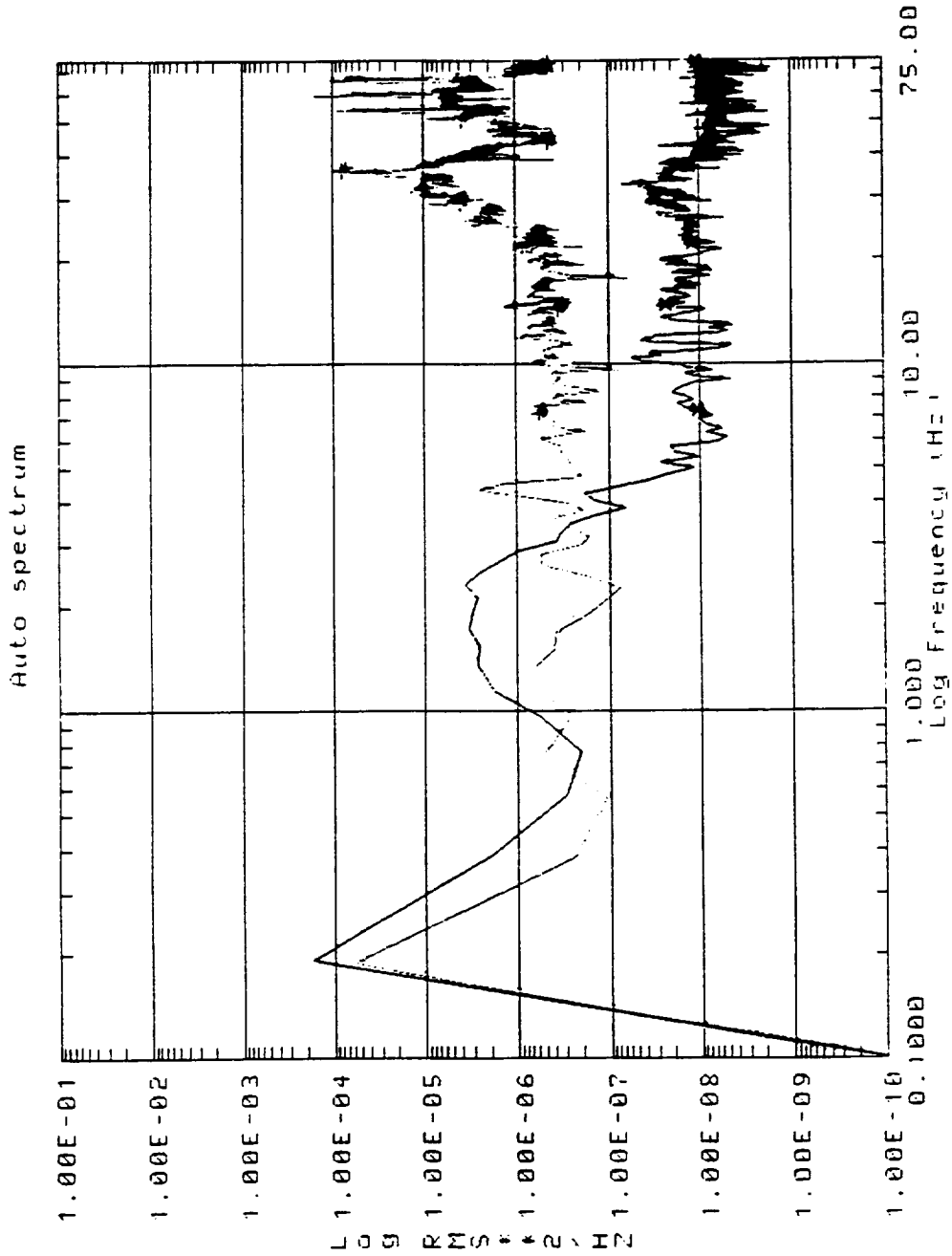

(a) Payload under relative control.

Figure E.5: Output and input power spectra for platform y and aircraft location 1 y.

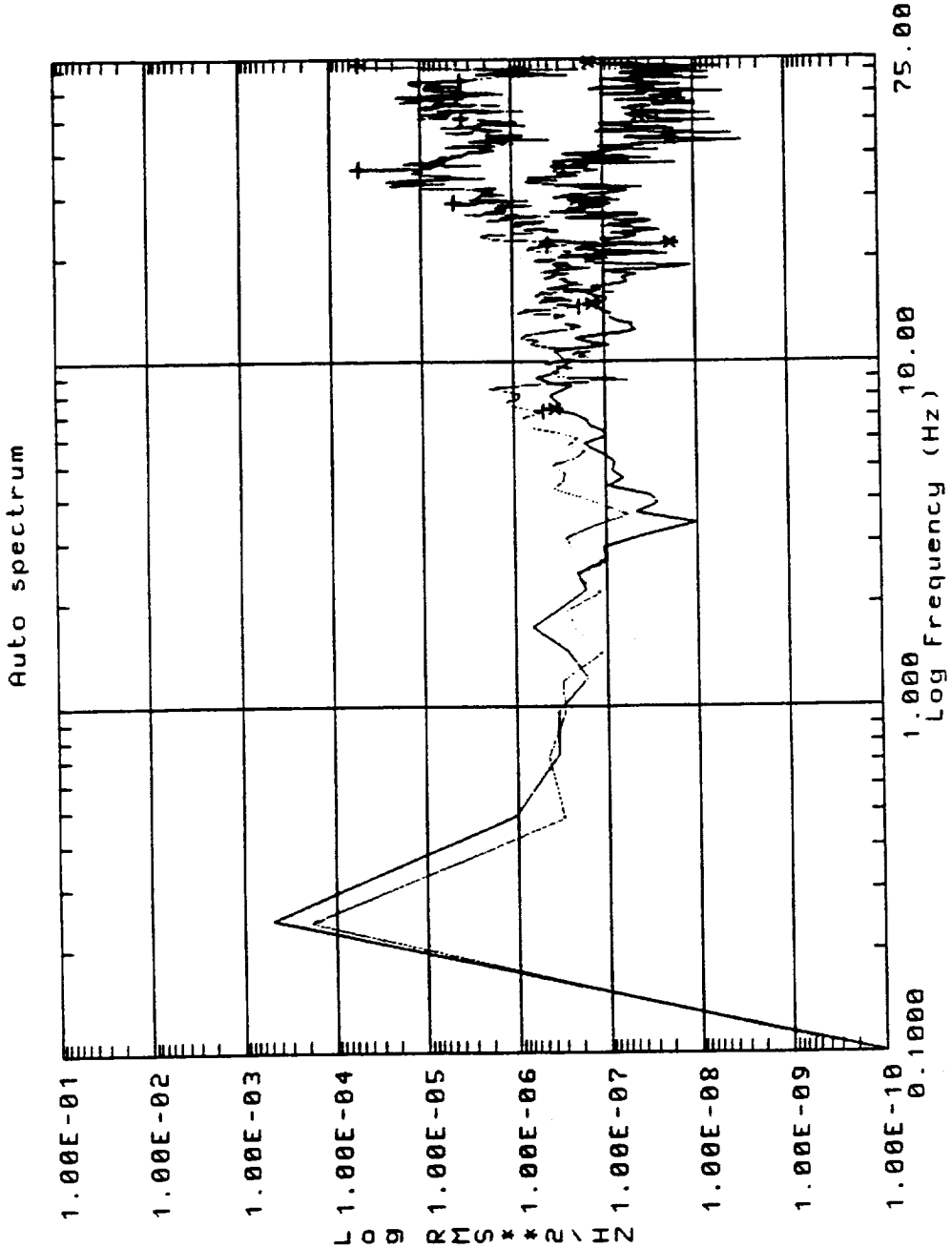

(b) Payload under inertial control.

Figure E.5: Output and input power spectra for platform y and aircraft location 1 y.

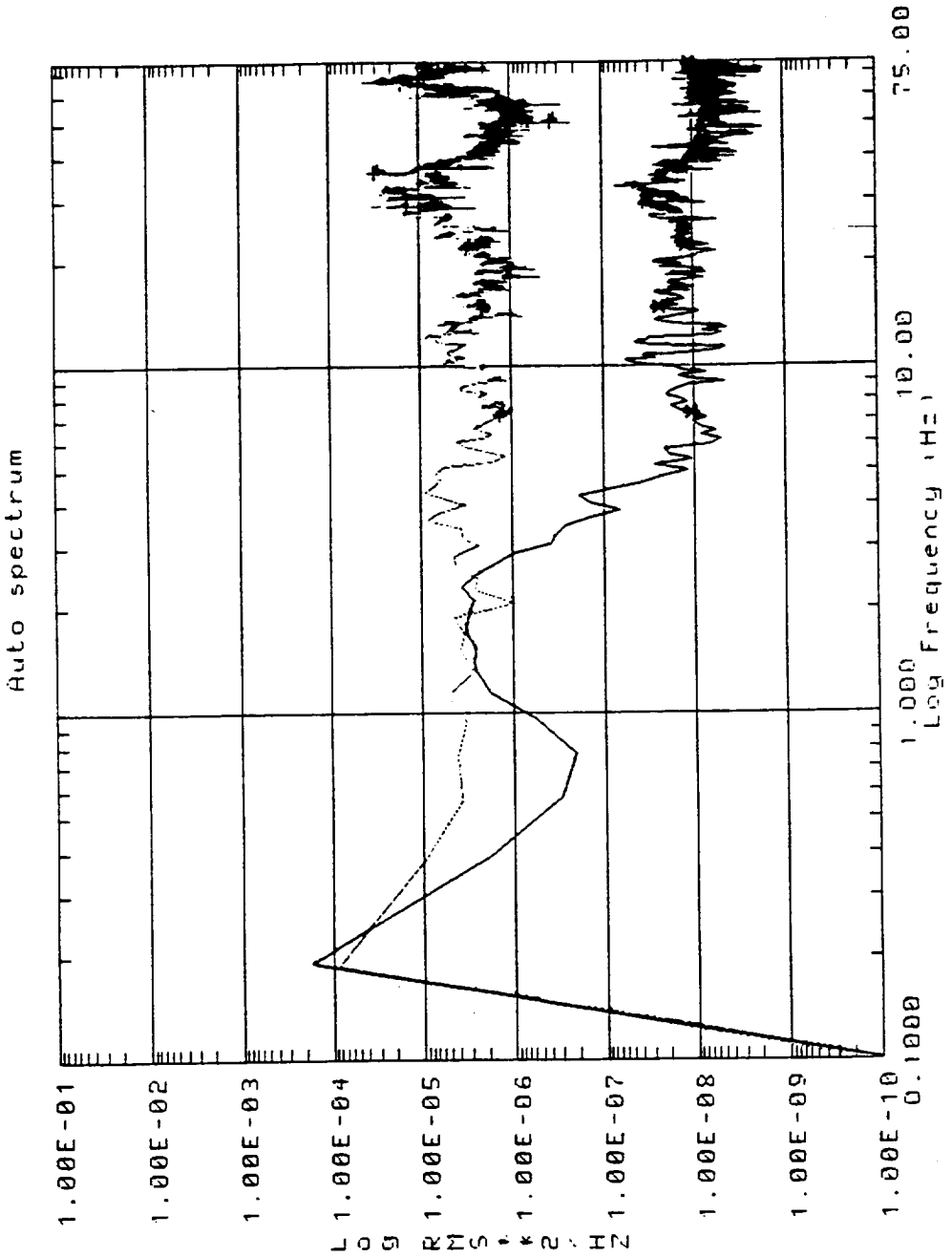

(a) Payload under relative control.

Figure E.6: Output and input power spectra for platform y and aircraft location 2 y.

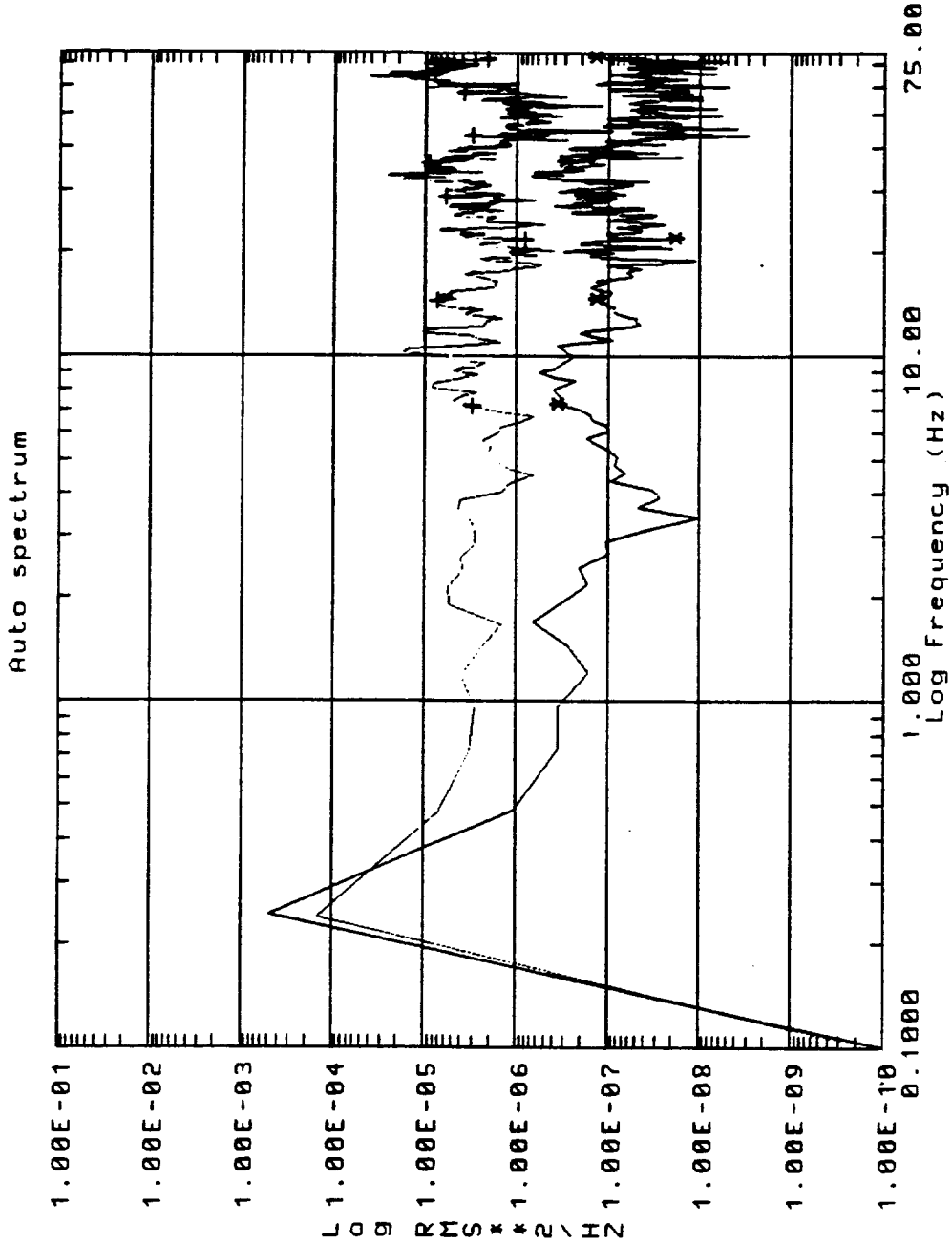

(b) Payload under inertial control.

Figure E.6: Output and input power spectra for platform y and aircraft location 2 y.

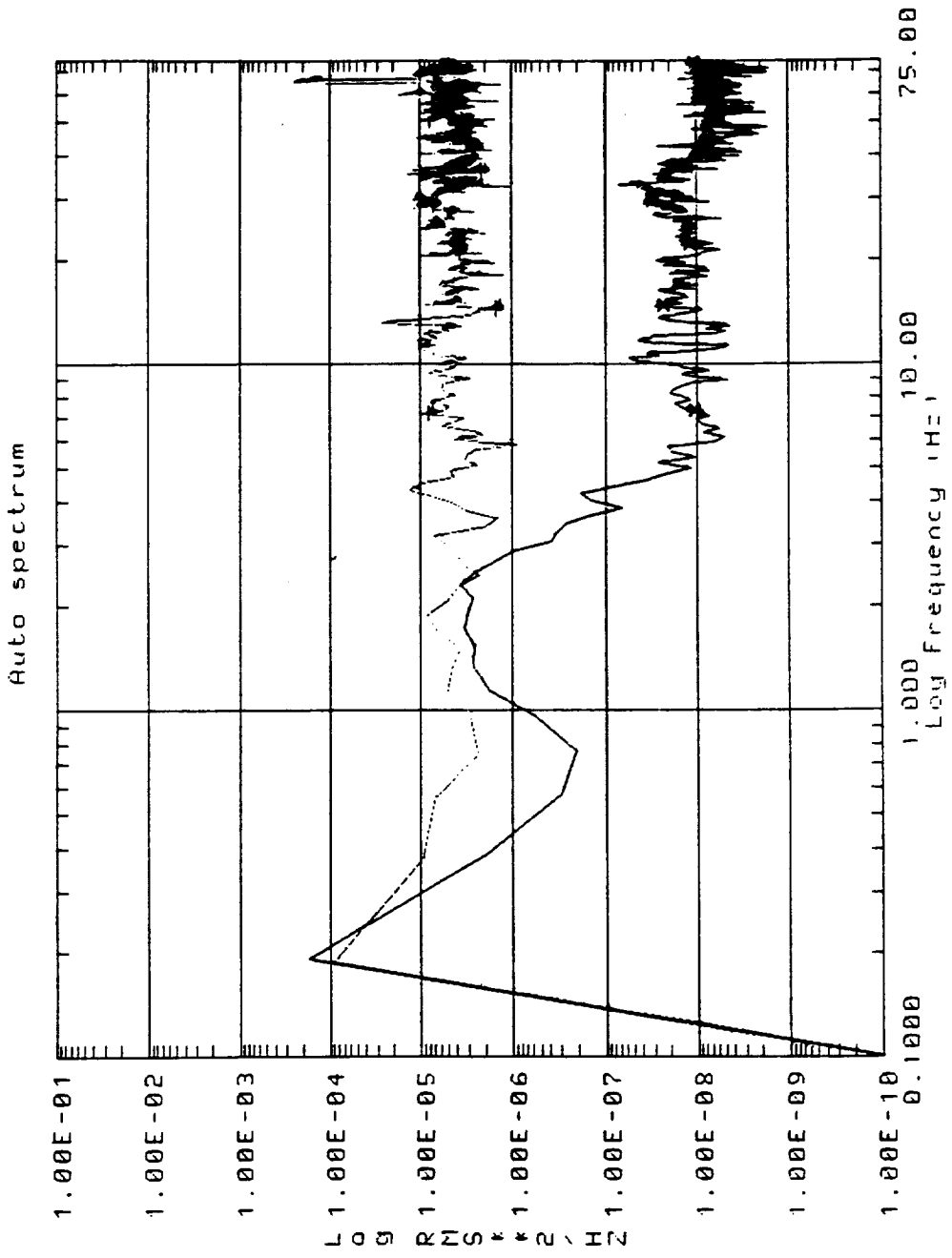

(a) Payload under relative control.

Figure E.7: Output and input power spectra for platform y and aircraft location 3 y.

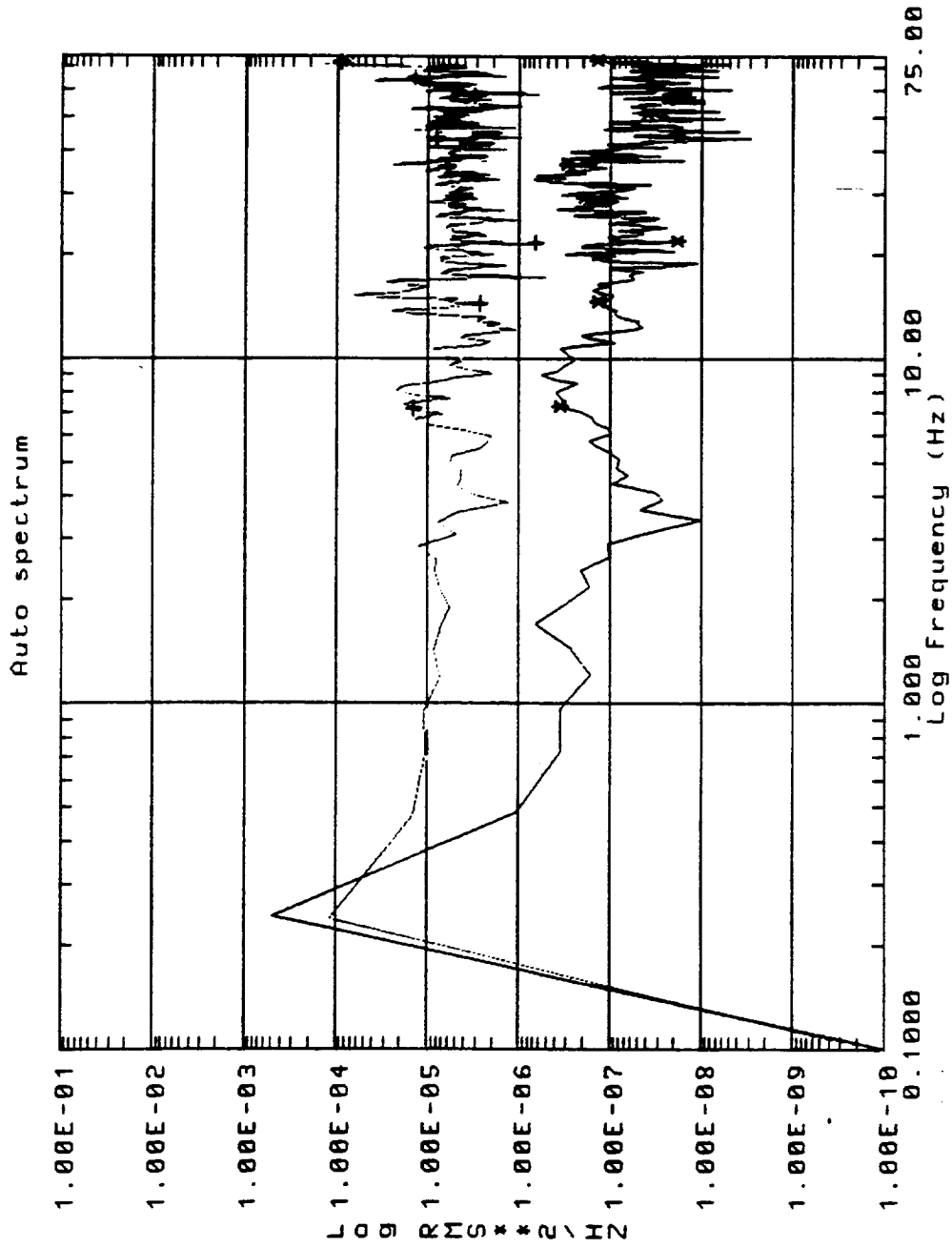

(b) Payload under inertial control.

Figure E.7: Output and input power spectra for platform y and aircraft location 3 y.

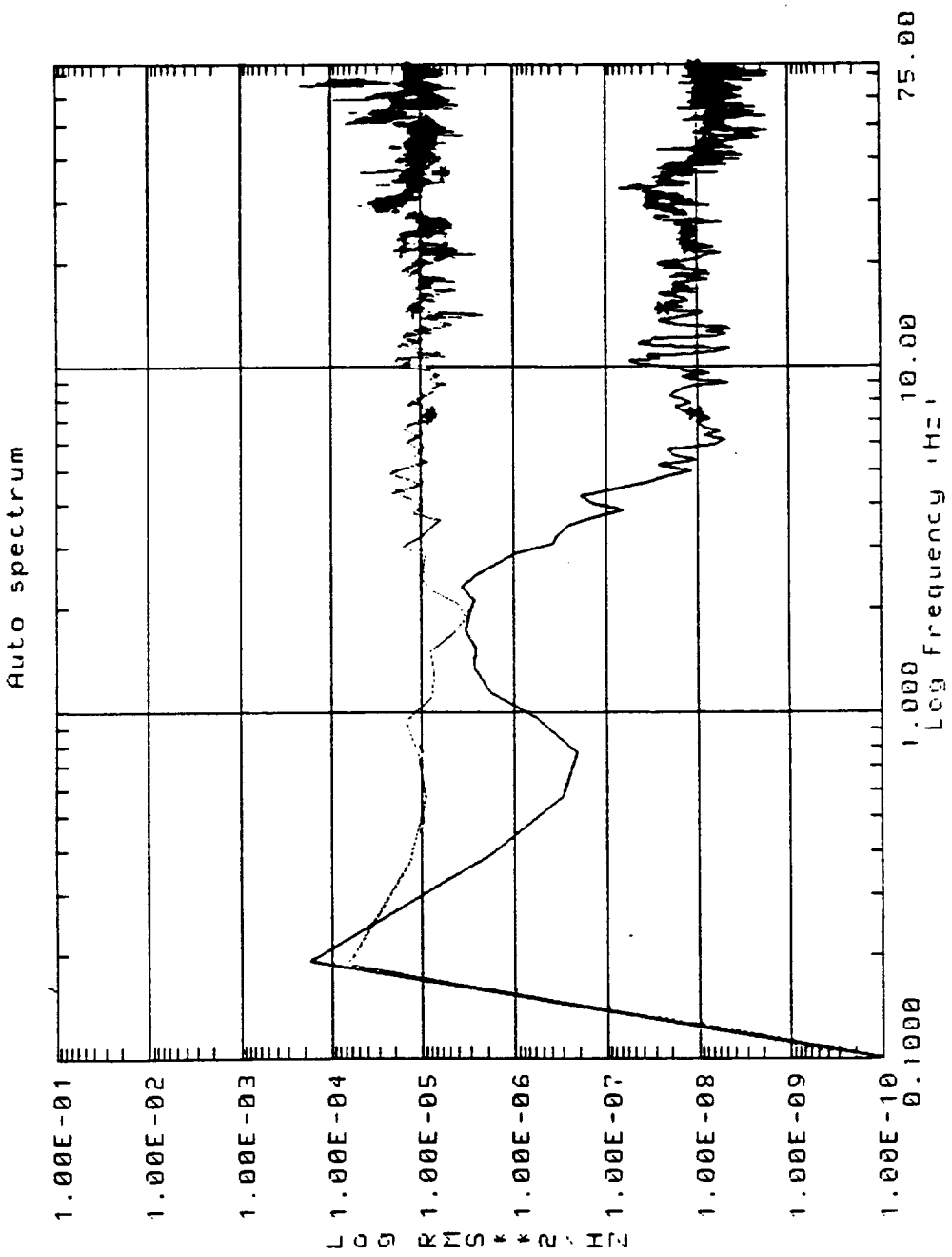

(a) Payload under relative control.

Figure E.8: Output and input power spectra for platform y and aircraft location 4 y.

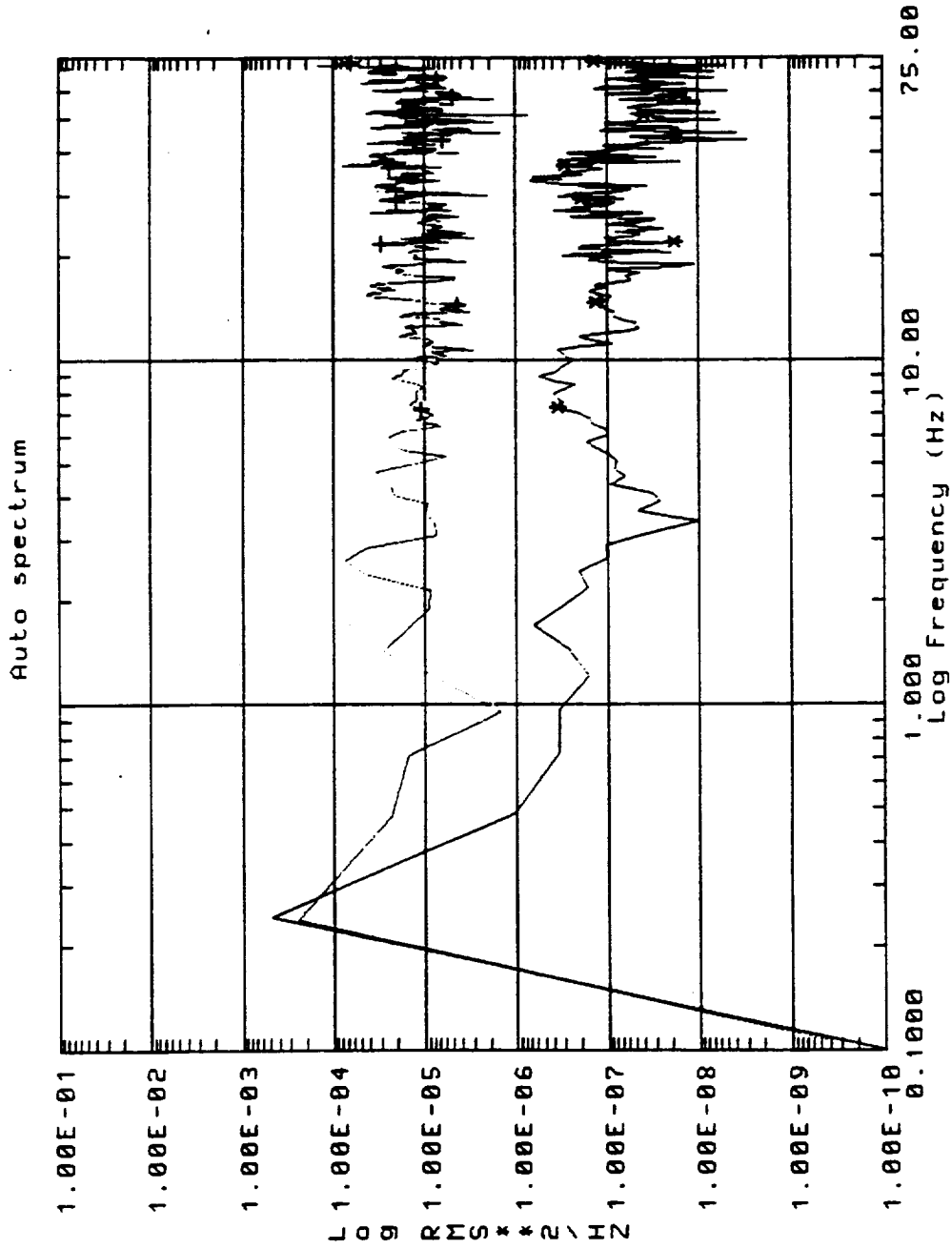

(b) Payload under inertial control.

Figure E.8: Output and input power spectra for platform y and aircraft location 4 y.

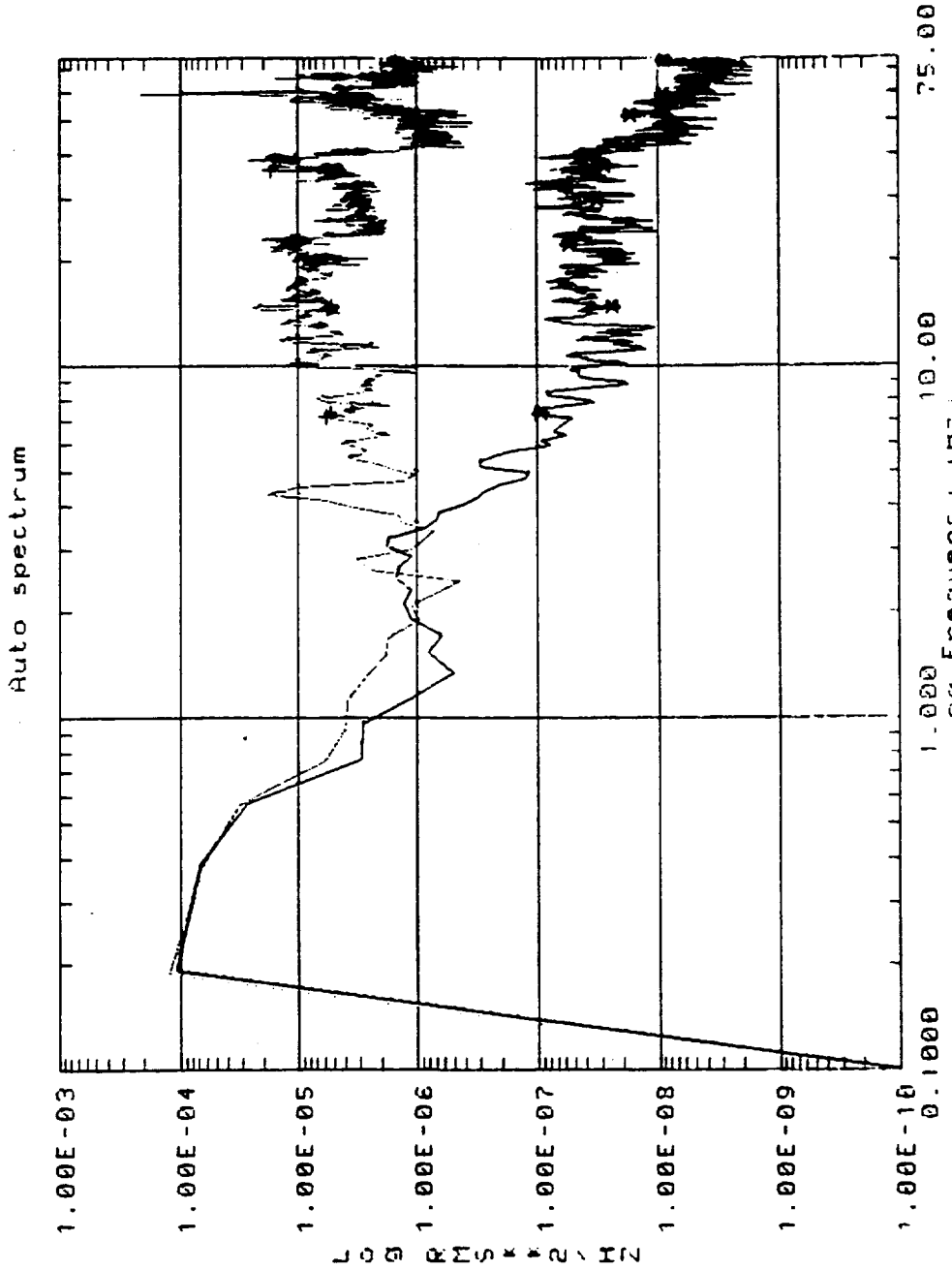

(a) Payload under relative control.

Figure E.9: Output and input power spectra for platform z and aircraft location 1 z.

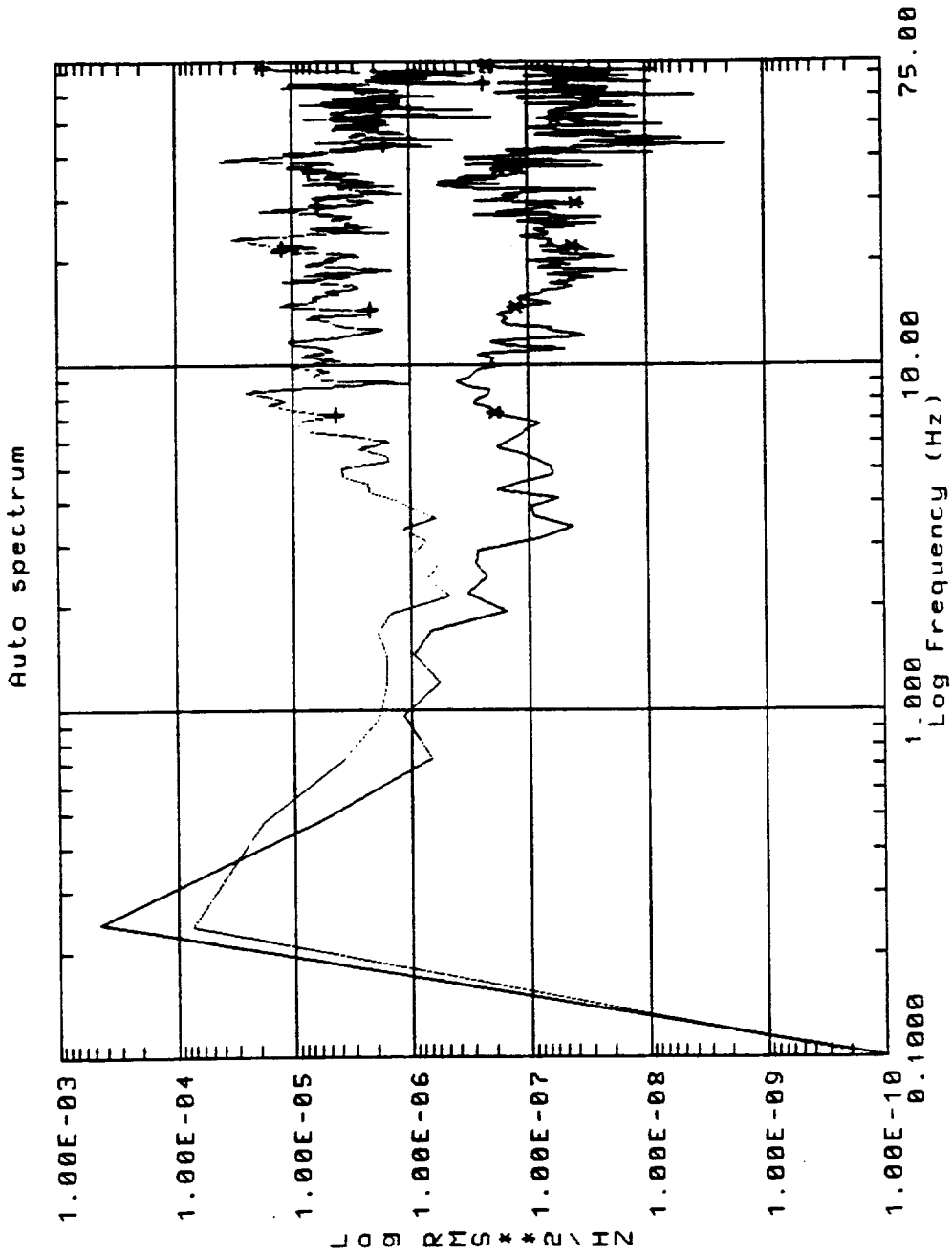

(b) Payload under inertial control.

Figure E.9: Output and input power spectra for platform z and aircraft location 1 z.

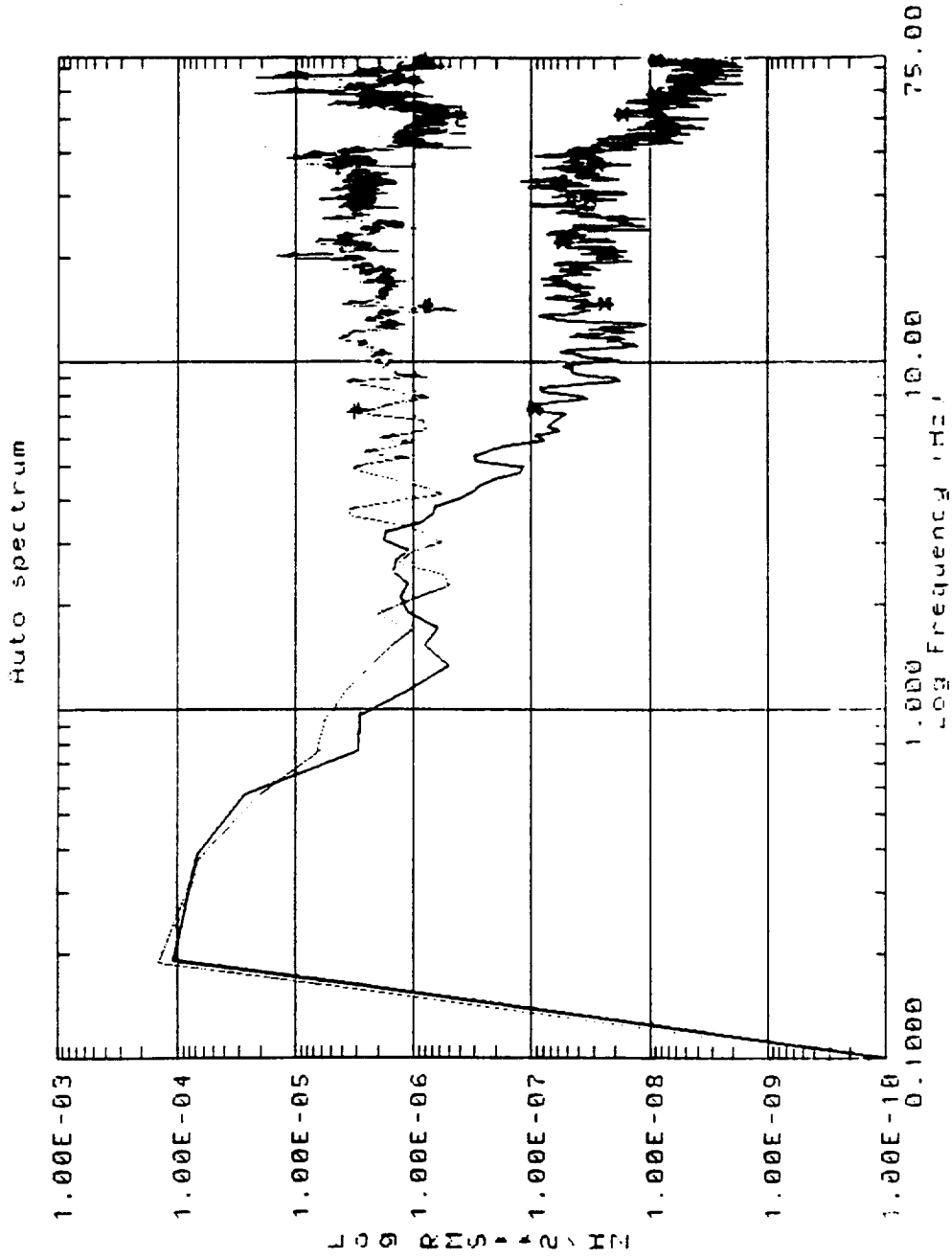

(a) Payload under relative control.

Figure E.10: Output and input power spectra for platform z and aircraft location 2 z.

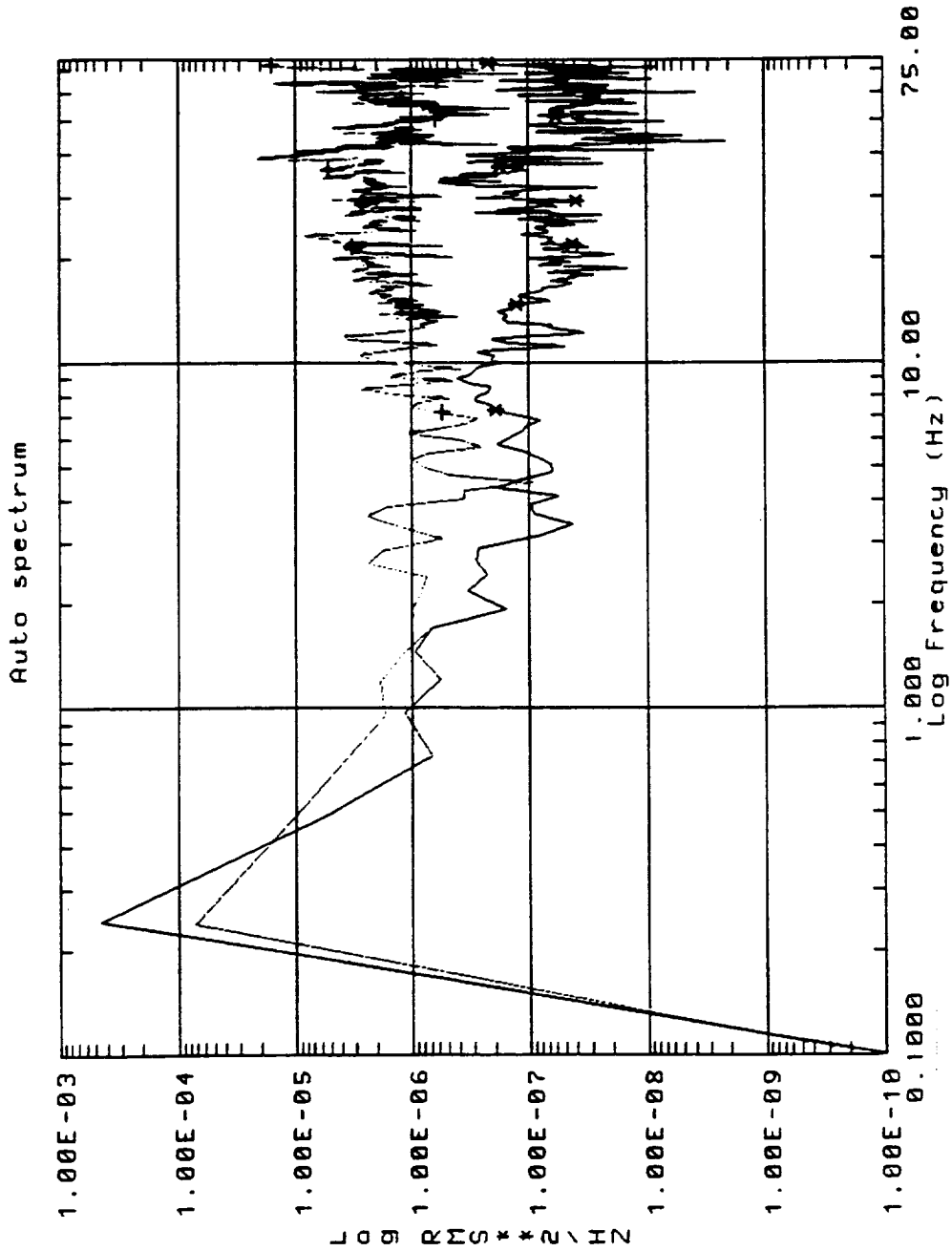

(b) Payload under inertial control.

Figure E.10: Output and input power spectra for platform z and aircraft location 2 z.

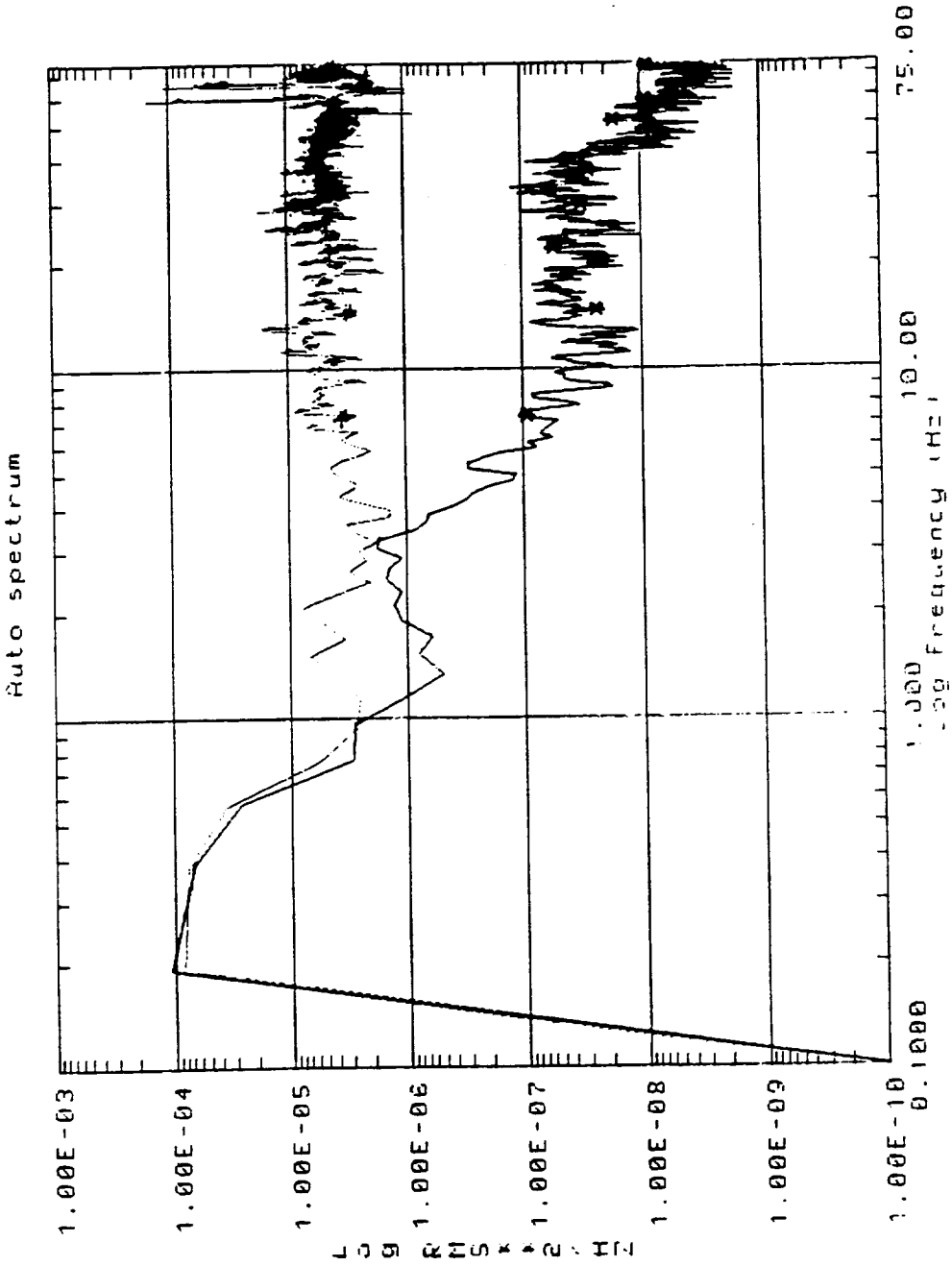

(a) Payload under relative control.

Figure E.11: Output and input power spectra for platform z and aircraft location 3 z.

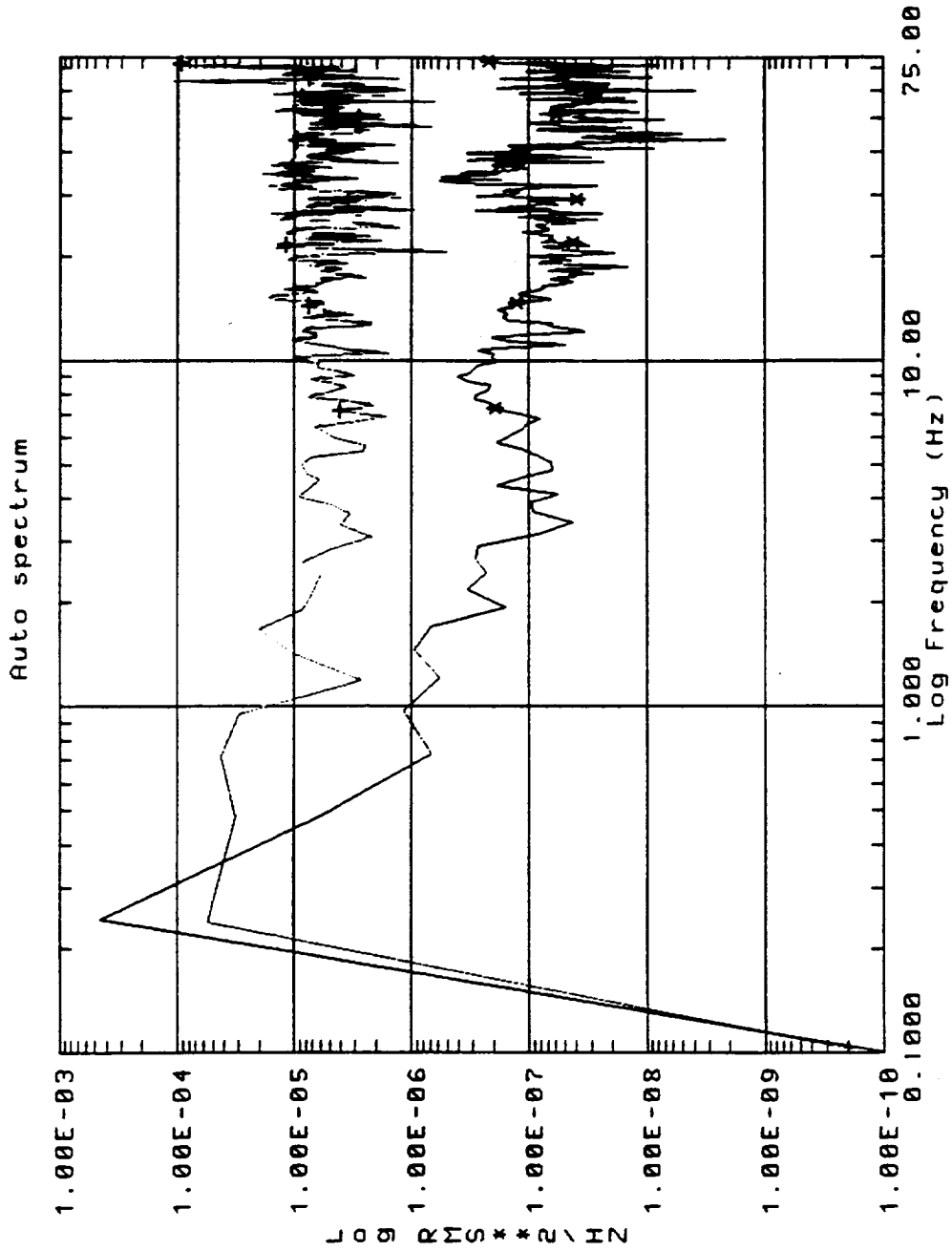

(b) Payload under inertial control.

Figure E.11: Output and input power spectra for platform z and aircraft location 3 z.

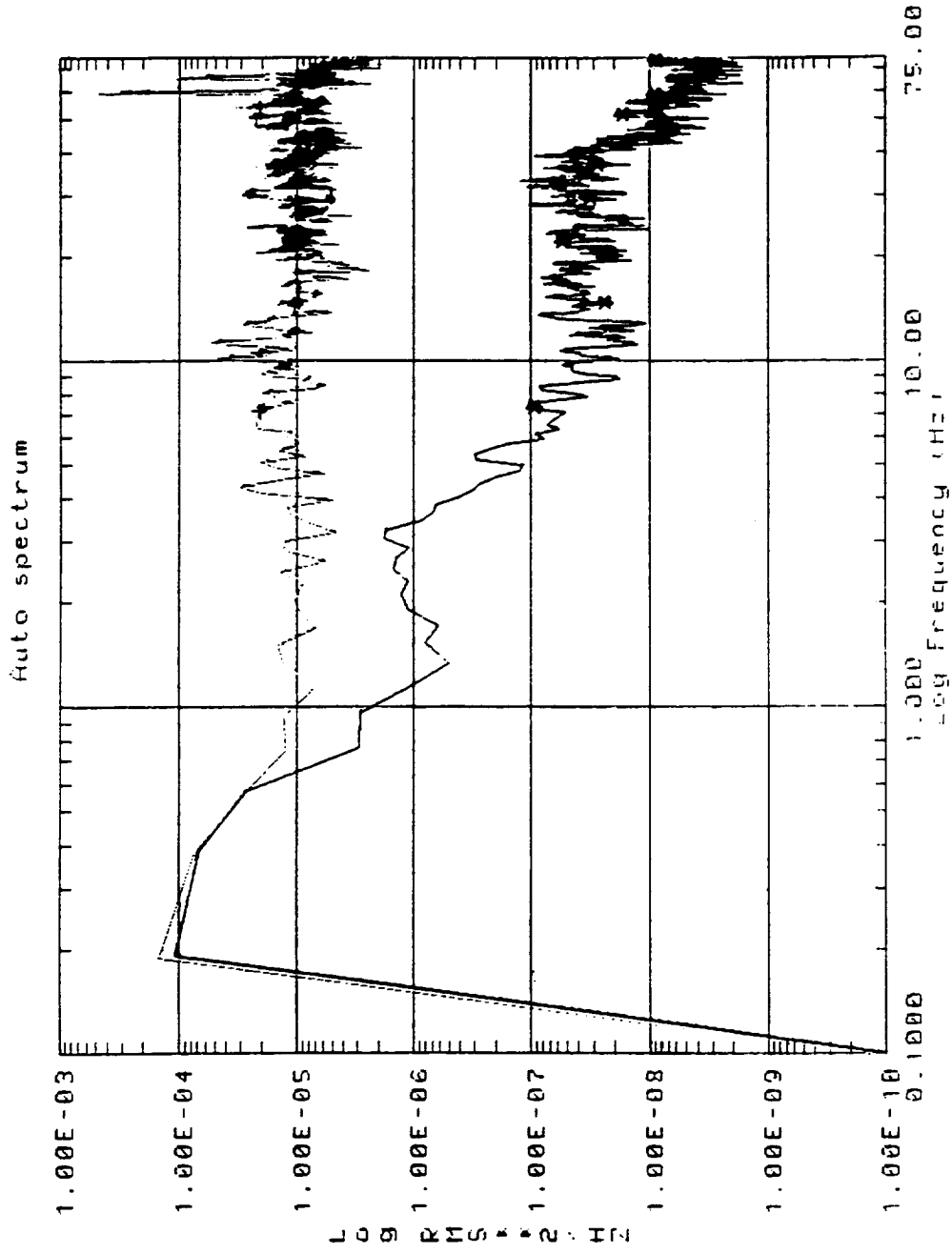

(a) Payload under relative control.

Figure E.12: Output and input power spectra for platform z and aircraft location 4 z.

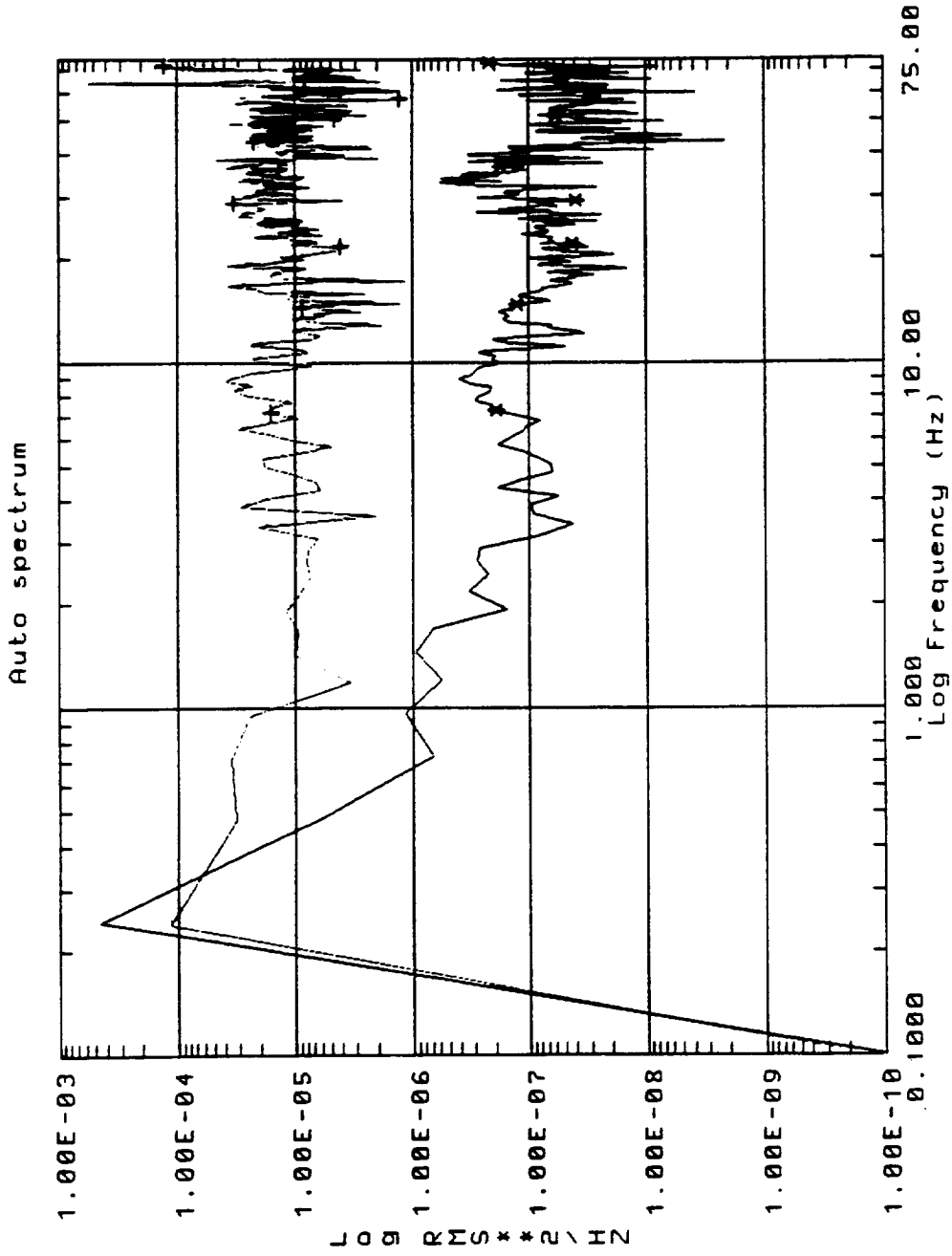

(b) Payload under inertial control.

Figure E.12: Output and input power spectra for platform z and aircraft location 4 z.

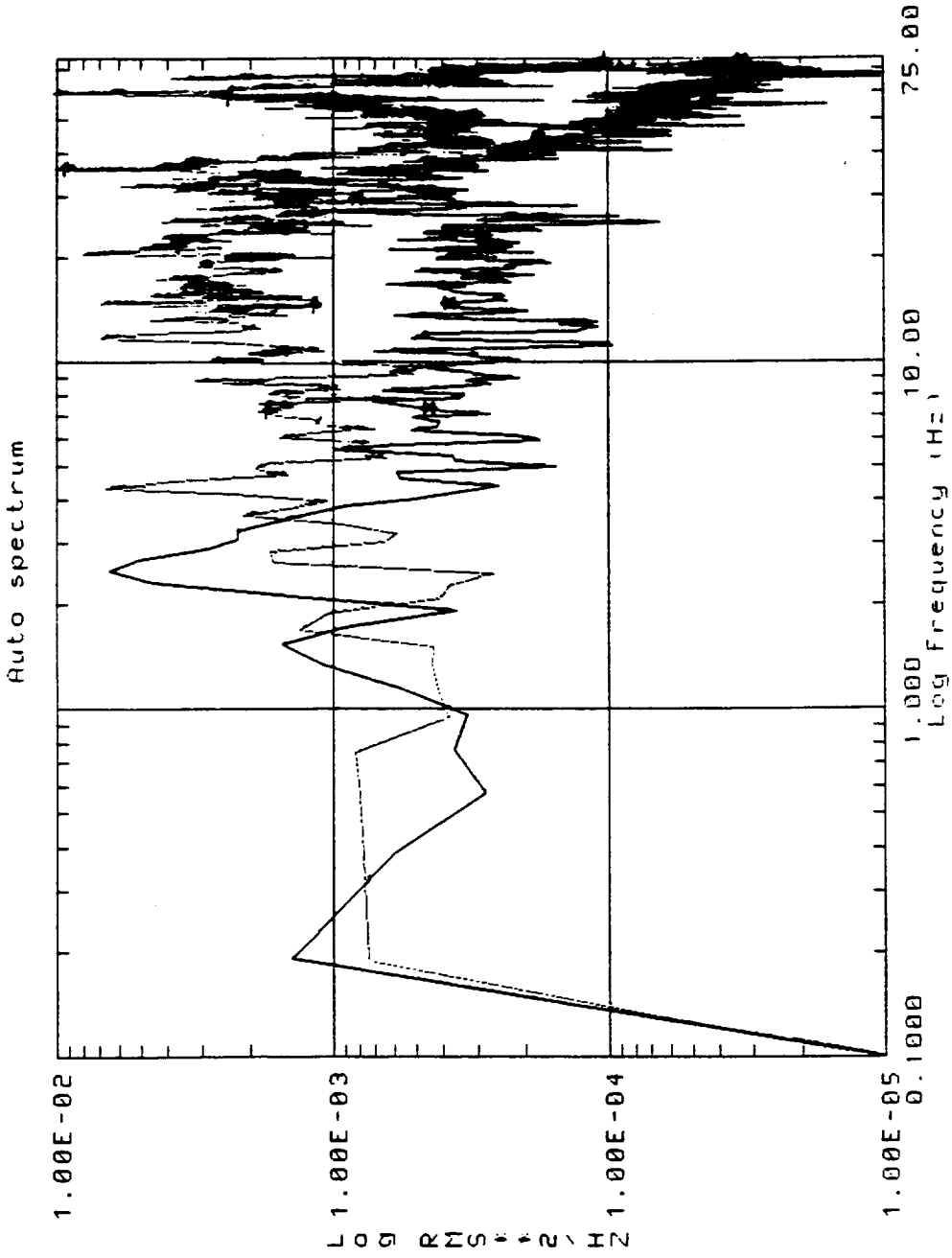

(a) Payload under relative control.

Figure E.13: Output and input power spectra for platform θ_x and trunnion θ_x

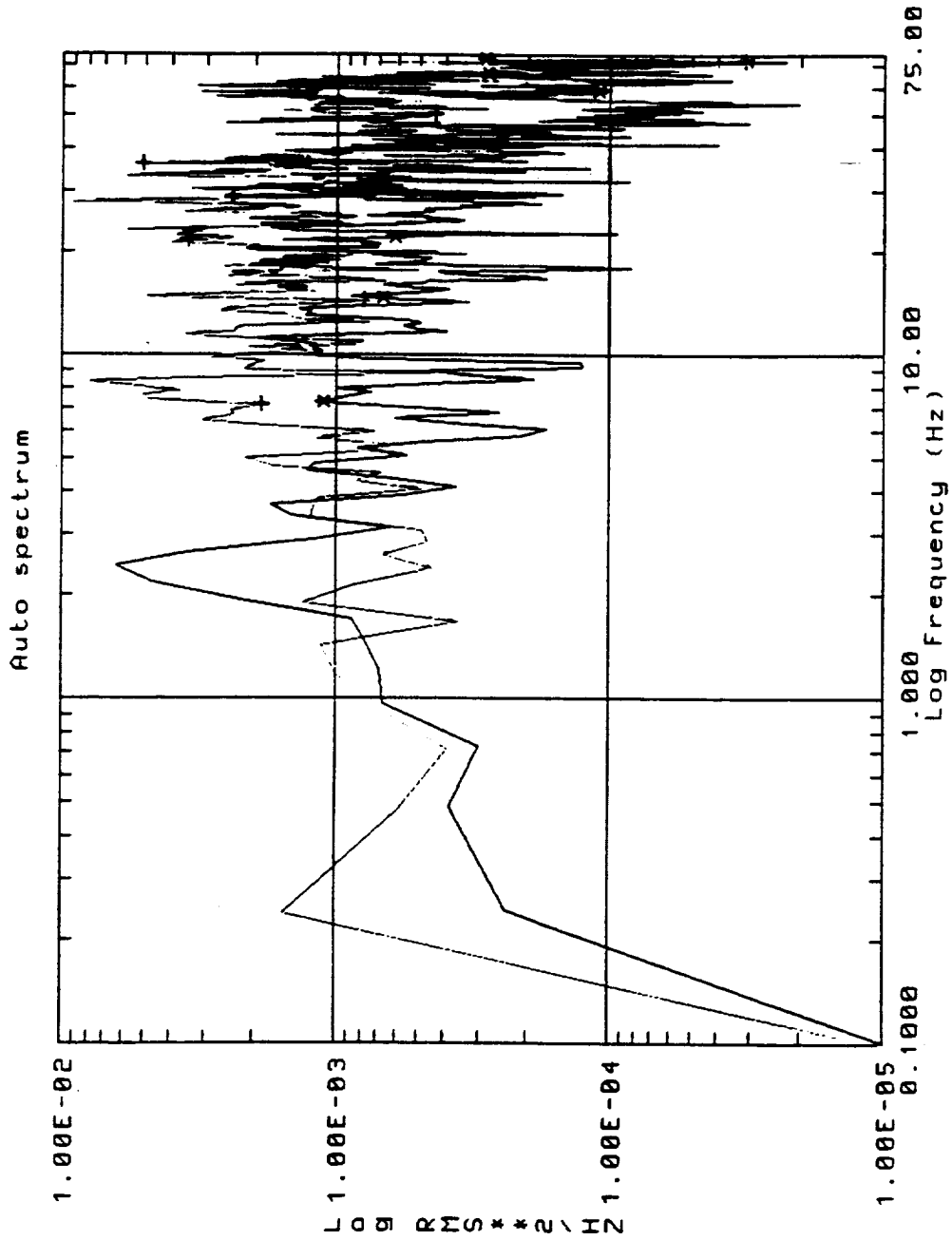

(b) Payload under inertial control.

Figure E.13: Output and input power spectra for platform θ_X and trunnion $\theta_{X'}$

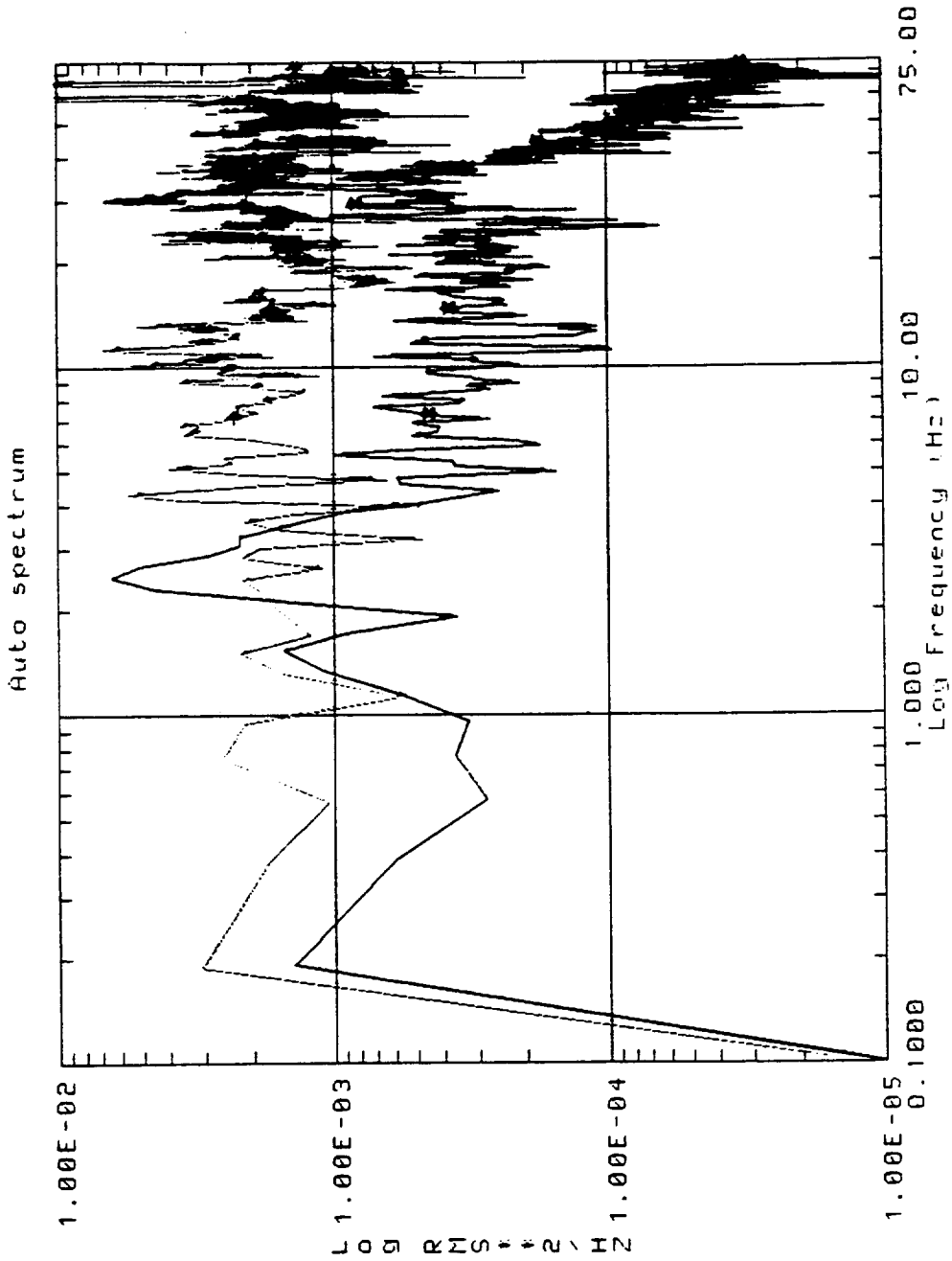

(a) Payload under relative control.

Figure E.14: Output and input power spectra for platform θ_x and aircraft θ_x.

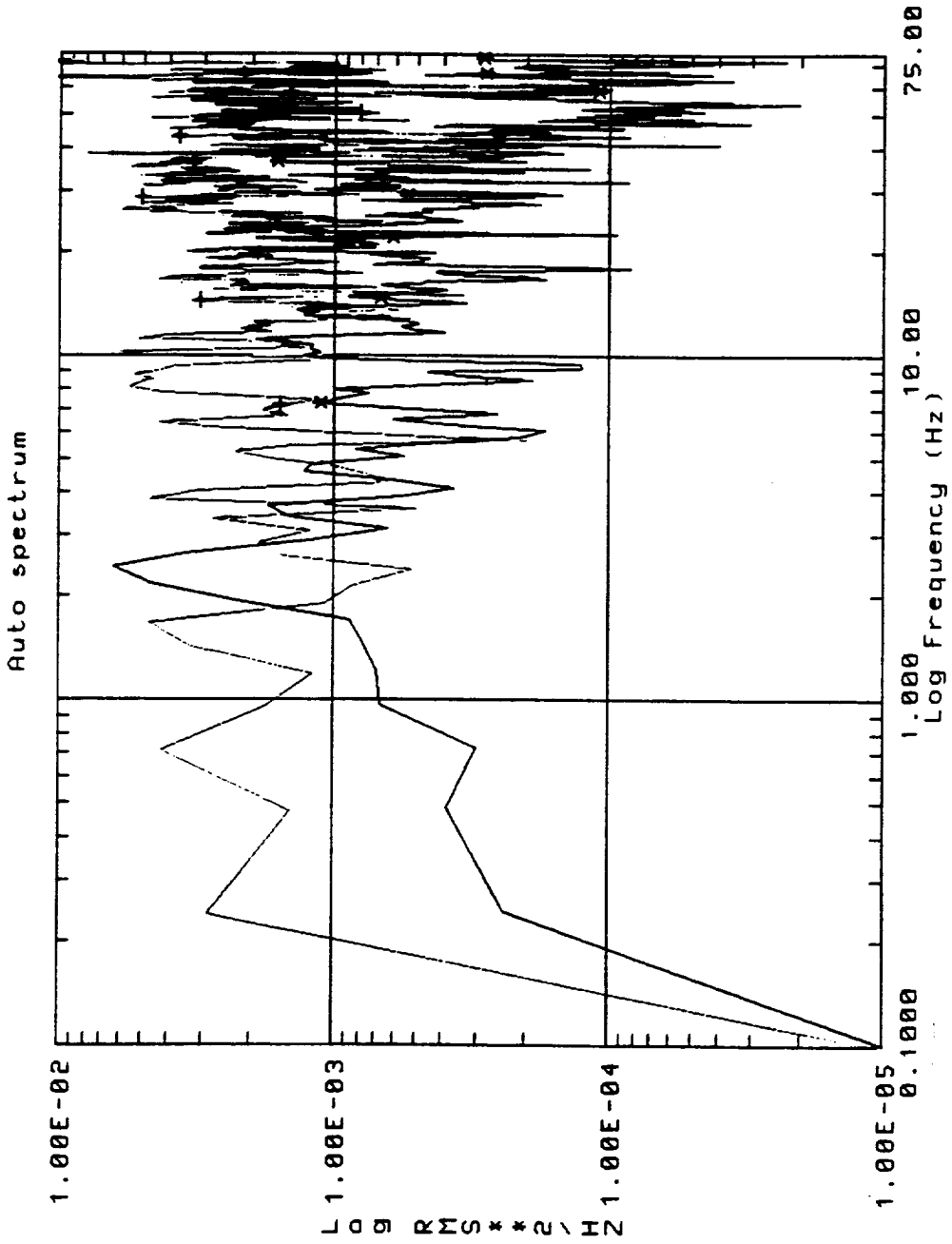

(b) Payload under inertial control.

Figure E.14: Output and input power spectra for platform θ_x and aircraft θ_x.

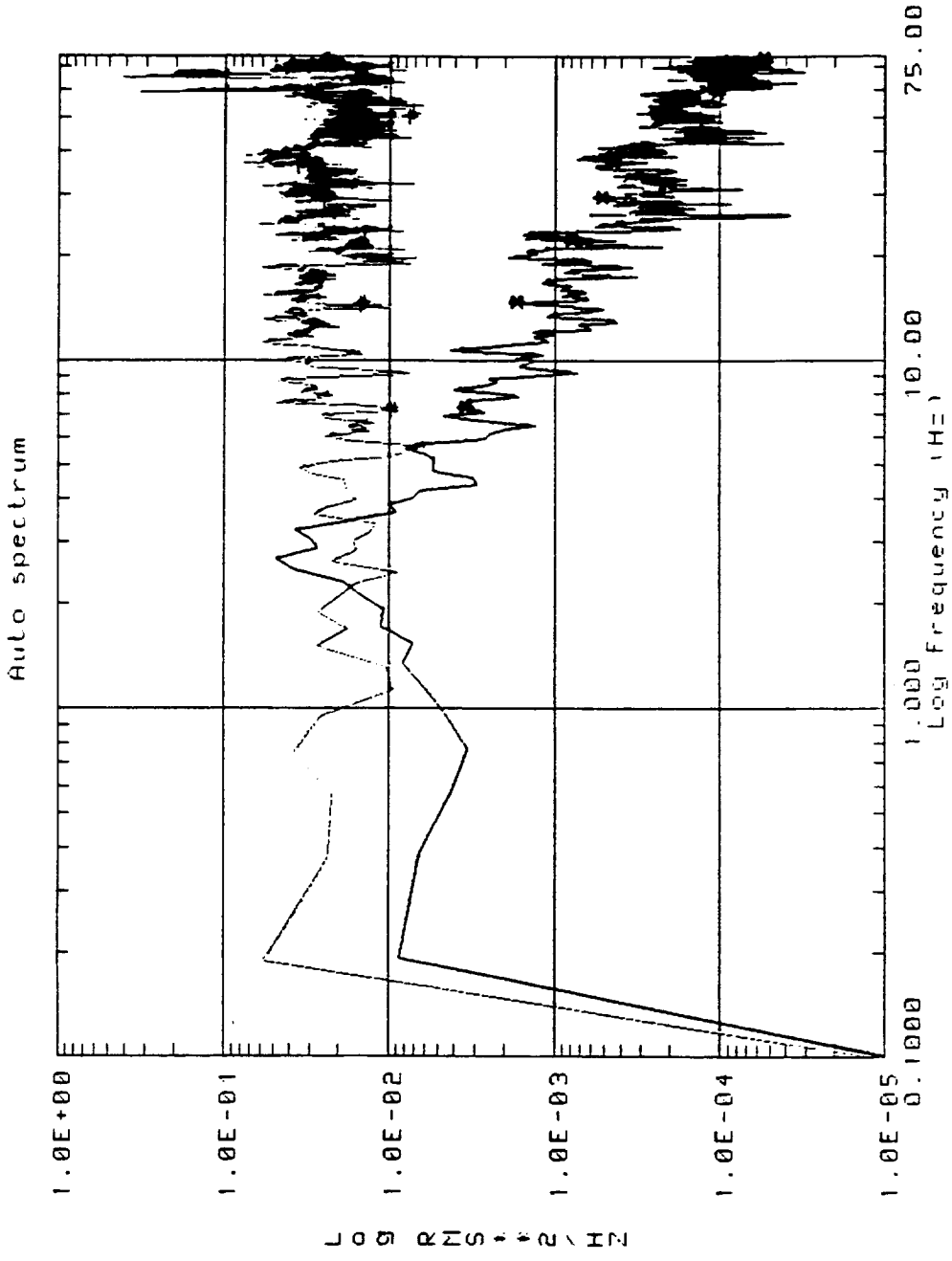

(a) Payload under relative control.

Figure E.15: Output and input power spectra for platform ϕ_y and aircraft $\phi_{y2\text{-}3}$.

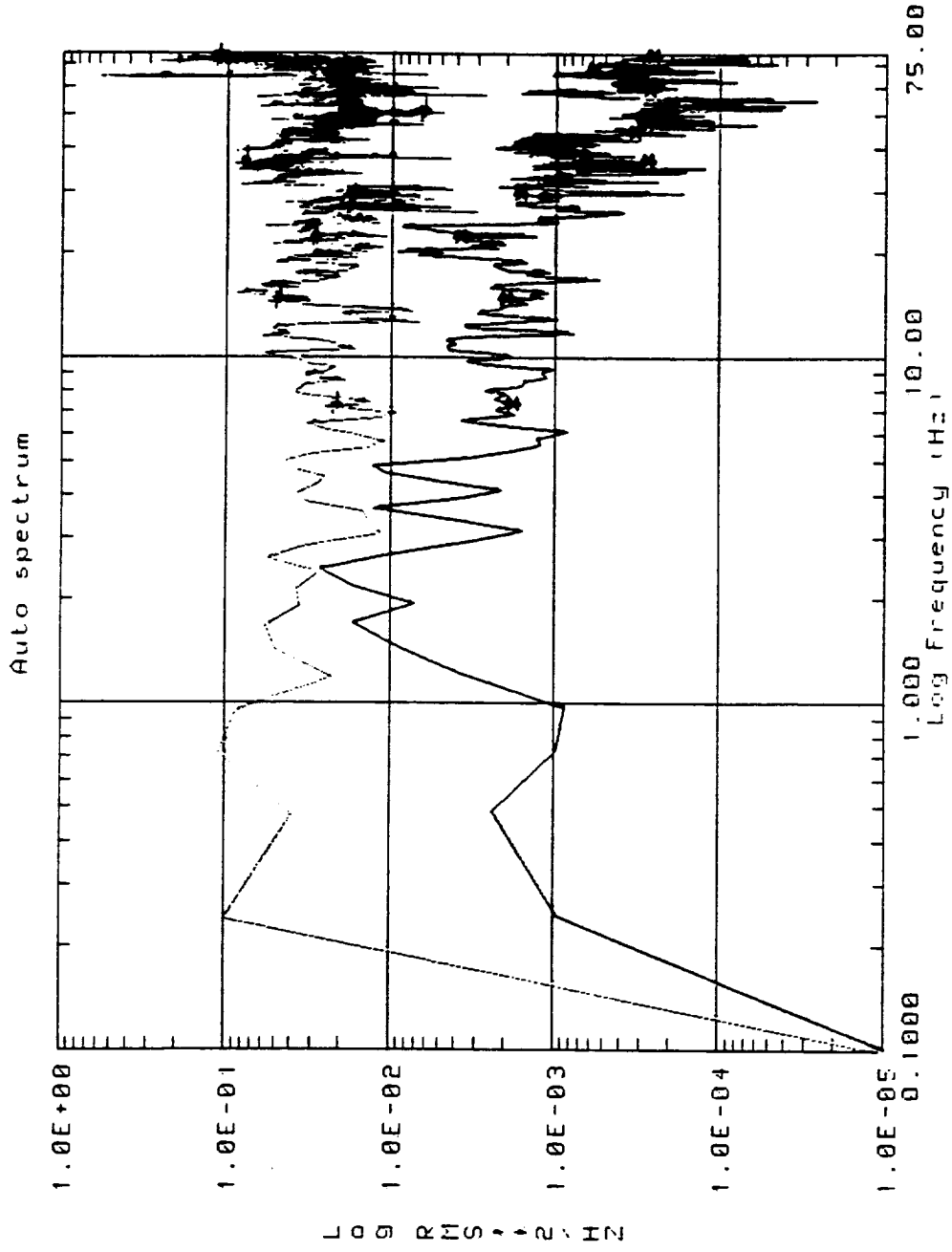

(b) Payload under inertial control.

Figure E.15: Output and input power spectra for platform ϕ_y and aircraft $\phi_{y2\text{-}3}$.

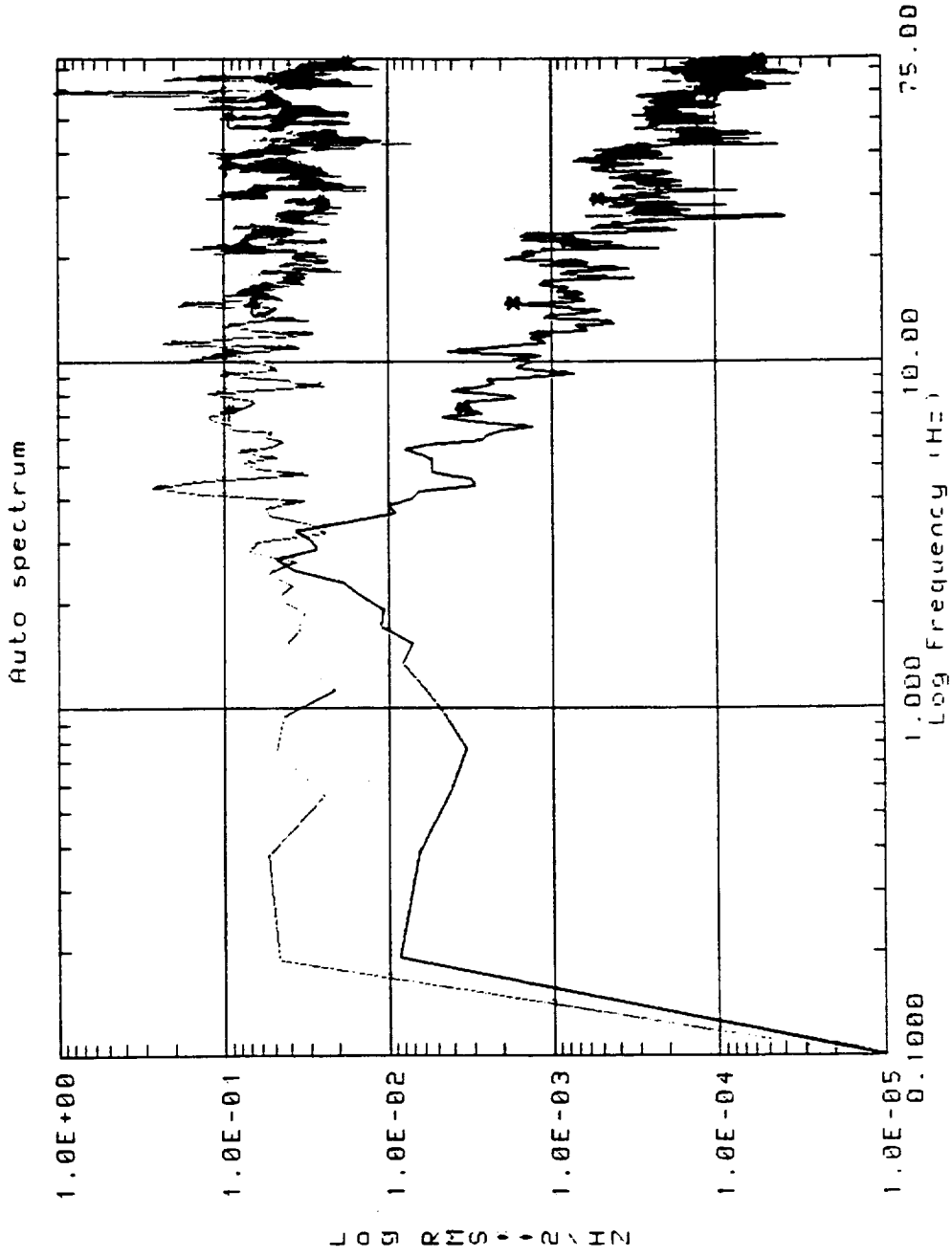

(a) Payload under relative control.

Figure E.16: Output and input power spectra for platform ϕ_y and aircraft $\phi_{y1\text{-}4}$.

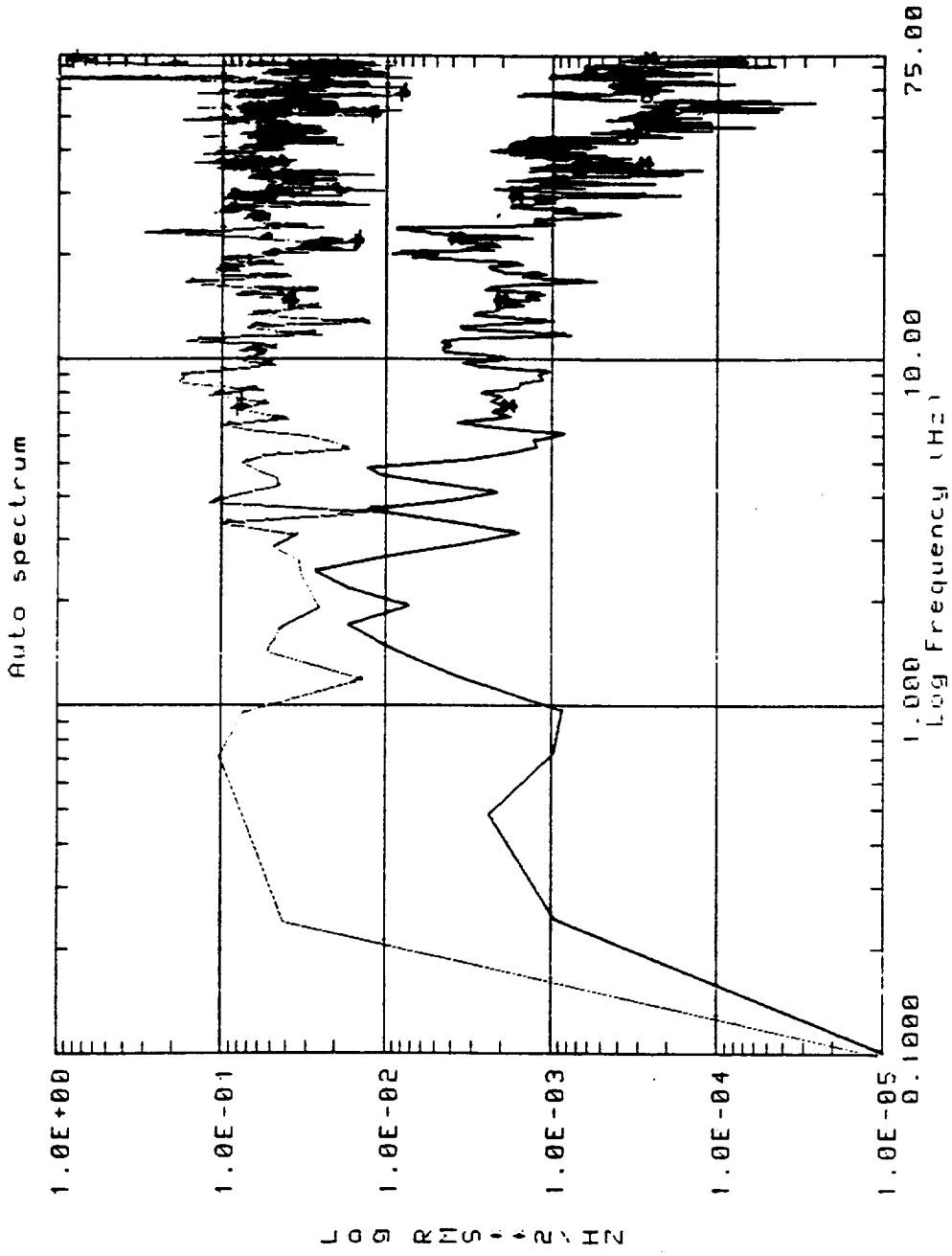

(b) Payload under inertial control.

Figure E.16: Output and input power spectra for platform ϕ_y and aircraft $\phi_{y1\text{-}4}$.

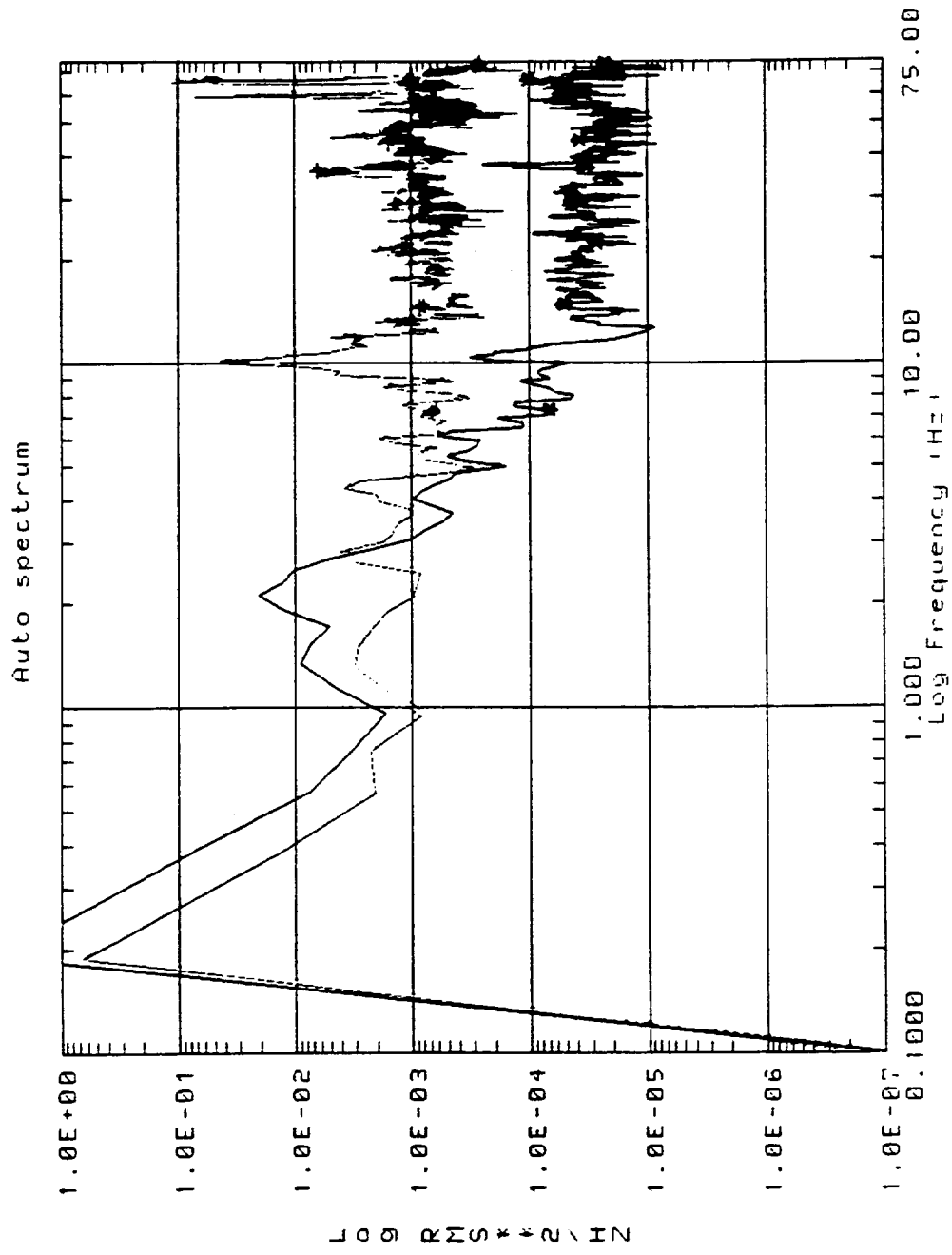

(a) Payload under relative control.

Figure E.17: Output and input power spectra for platform β_Z and trunnion β_Z.

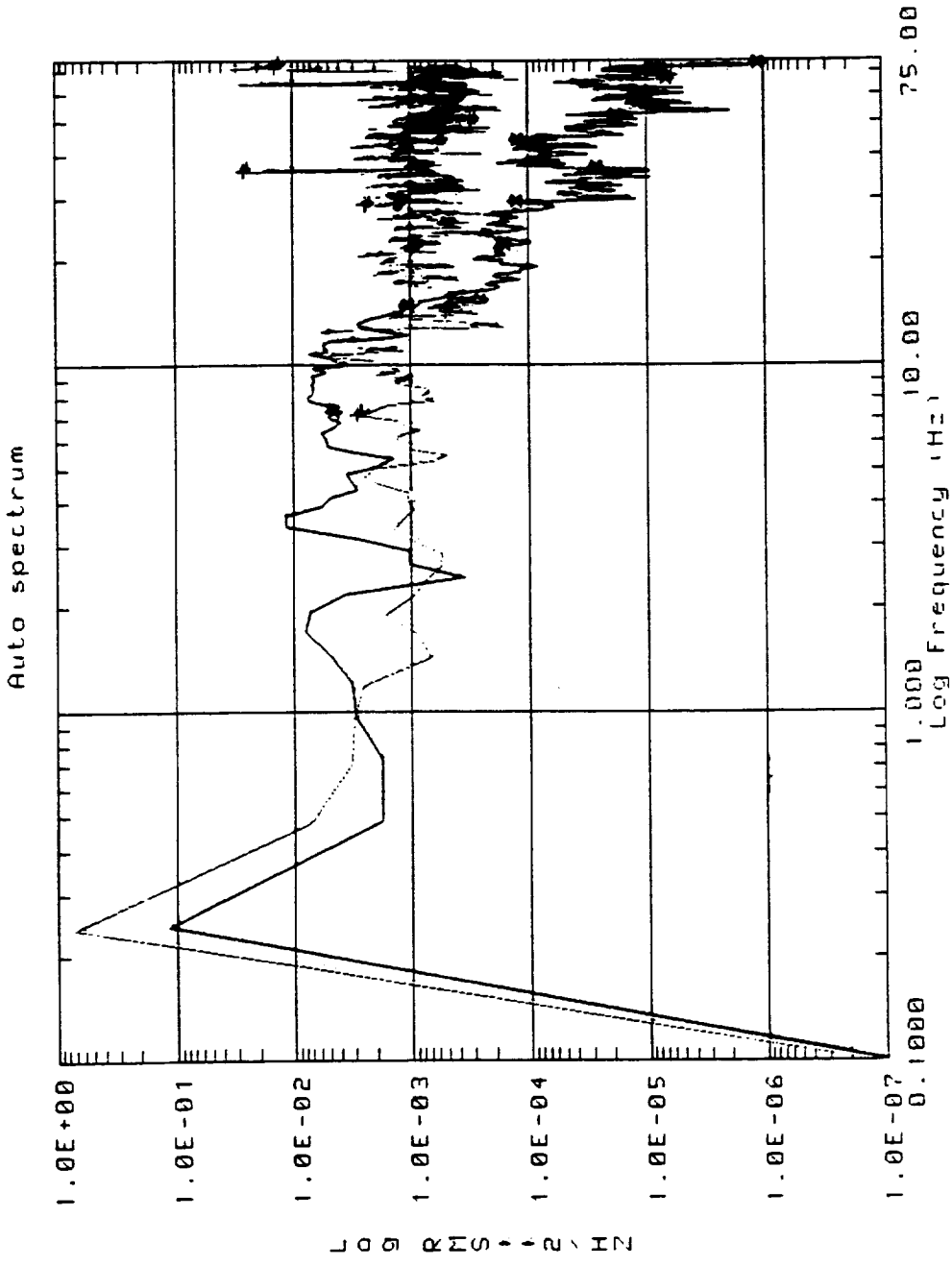

(b) Payload under inertial control.

Figure E.17: Output and input power spectra for platform β_z and trunnion β_z.

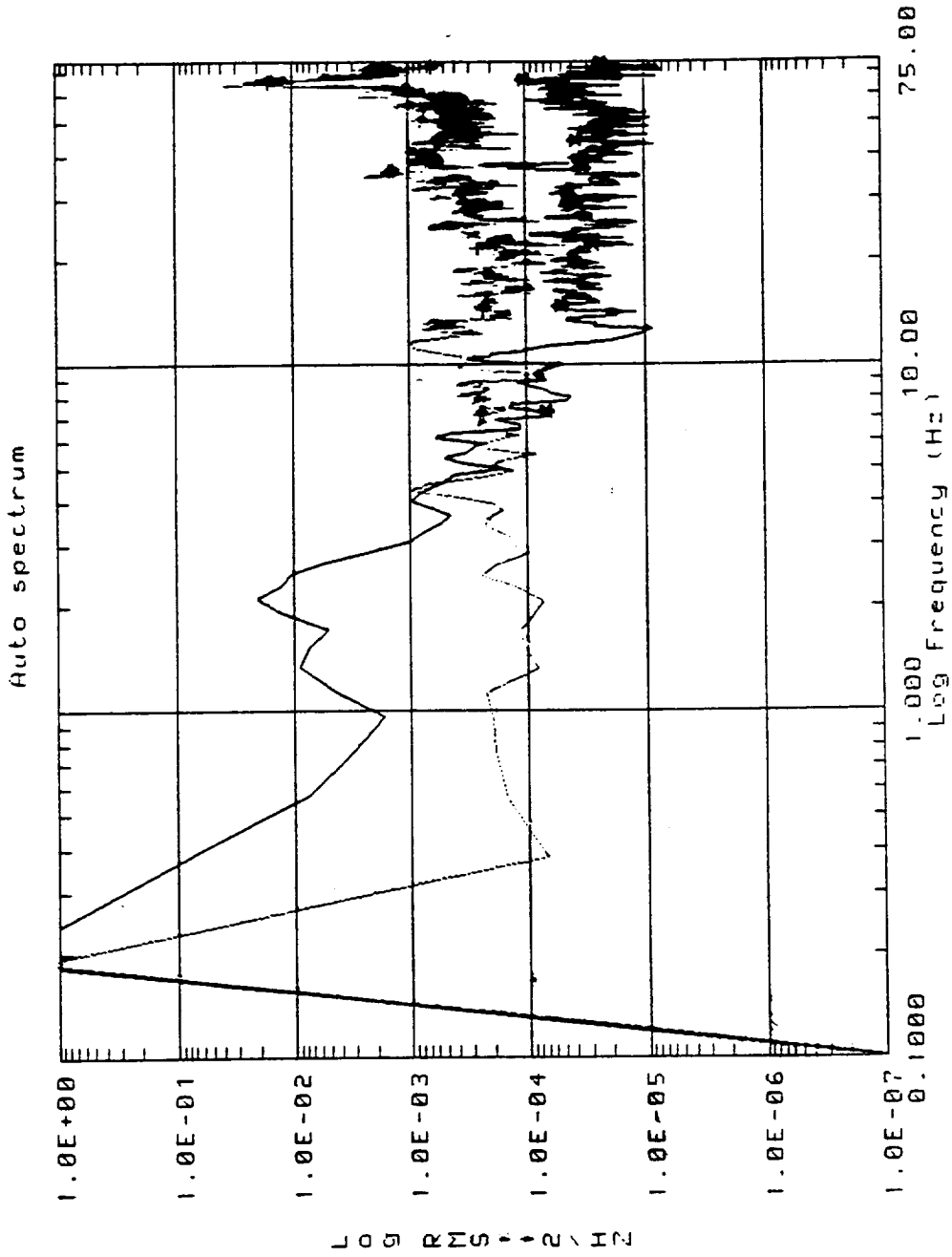

(a) Payload under relative control.

Figure E.18: Output and input power spectra for platform β_z and aircraft β_z.

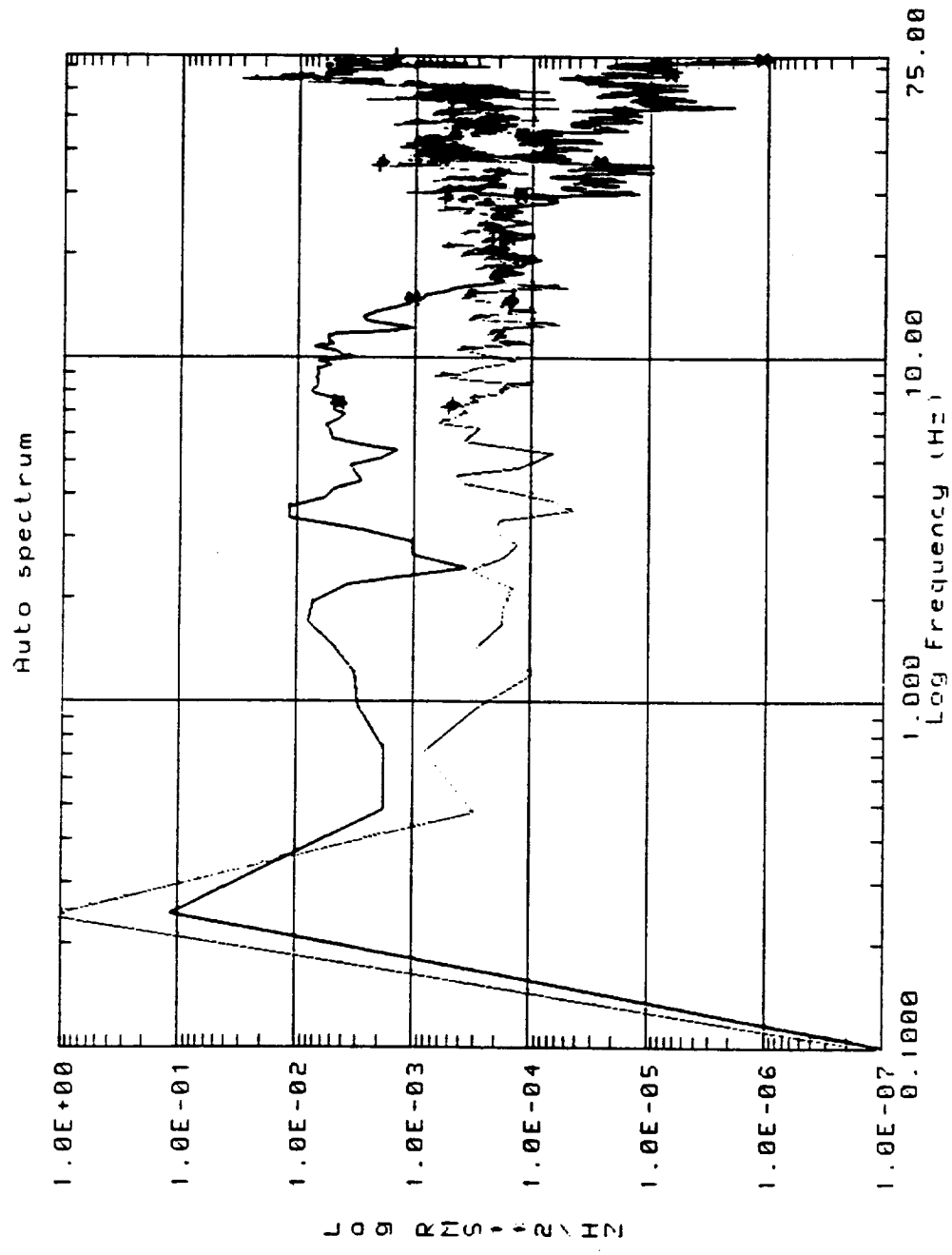

(b) Payload under inertial control.

Figure E.18: Output and input power spectra for platform β_z and aircraft β_z.

REPORT DOCUMENTATION PAGE

Form Approved
OMB No. 0704-0188

1. AGENCY USE ONLY (*Leave blank*)	2. REPORT DATE	3. REPORT TYPE AND DATES COVERED
	September 1993	Technical Memorandum

4. TITLE AND SUBTITLE

Microgravity Vibration Isolation Technology: Development to Demonstration

5. FUNDING NUMBERS

WU-694-03-03

6. AUTHOR(S)

Carlos M. Grodsinsky

7. PERFORMING ORGANIZATION NAME(S) AND ADDRESS(ES)

National Aeronautics and Space Administration
Lewis Research Center
Cleveland, Ohio 44135-3191

8. PERFORMING ORGANIZATION REPORT NUMBER

E-8067

9. SPONSORING/MONITORING AGENCY NAME(S) AND ADDRESS(ES)

National Aeronautics and Space Administration
Washington, D.C. 20546-0001

10. SPONSORING/MONITORING AGENCY REPORT NUMBER

NASA TM-106320

11. SUPPLEMENTARY NOTES

This report was submitted as a thesis in partial fulfillment of the requirements for the degree Doctor of Mechanical and Aerospace Engineering to Case Western Reserve University, Cleveland, Ohio. Responsible person, Carlos M. Grodsinsky, (216) 433-2664.

12a. DISTRIBUTION/AVAILABILITY STATEMENT

Unclassified - Unlimited
Subject Category 01

12b. DISTRIBUTION CODE

13. ABSTRACT ***(Maximum 200 words)***

The low gravity environment provided by space flight has afforded the science community a unique area for the study of fundamental and technological sciences. However, the dynamic environment observed on space shuttle flights and predicted for Space Station Freedom has complicated the analysis of prior "microgravity" experiments and prompted concern for the viability of proposed space experiments requiring long term, low gravity environments. Thus, isolation systems capable of providing significant improvements to this random environment have been developed. This dissertation deals with the design constraints imposed by acceleration sensitive, "microgravity" experiment payloads in the unique environment of space. A theoretical background for the inertial feedback and feedforward isolation of a payload was developed giving the basis for two experimental active inertial isolation systems developed for the demonstration of these advanced active isolation techniques. A prototype six degree of freedom digital active isolation system was designed and developed for the ground based testing of an actively isolated payload in three horizontal degrees of freedom. A second functionally equivalent system was built for the multi-dimensional testing of an active inertial isolation system in a reduced gravity environment during low gravity aircraft trajectories. These multi-input multi-output control systems are discussed in detail with estimates on acceleration noise floor performance as well as the actual performance acceleration data. The attenuation performance is also given for both systems demonstrating the advantages between inertial and non-inertial control of a payload for both the ground base environment and the low gravity aircraft acceleration environment. A future goal for this area of research is to validate the technical approaches developed to the 0.01 Hz regime by demonstrating a functional active inertial feedforward/feedback isolation system during orbital flight. A NASA IN-STEP flight experiment has been proposed to accomplish this goal, and the expected selection for the IN-STEP program has been set for July of 1993.

14. SUBJECT TERMS

Active inertial isolation; Vibration isolation; Low frequency isolation; Active magnetic suspension

15. NUMBER OF PAGES

262

16. PRICE CODE

A12

17. SECURITY CLASSIFICATION OF REPORT	18. SECURITY CLASSIFICATION OF THIS PAGE	19. SECURITY CLASSIFICATION OF ABSTRACT	20. LIMITATION OF ABSTRACT
Unclassified	Unclassified	Unclassified	

National Aeronautics and
Space Administration

Lewis Research Center
Cleveland, Ohio 44135